1972

Aspects of forces on charged particles in electrostatic precipitators

Owen J. Tassicker
Wollongong University College

Thesis for the Degree of
DOCTOR of PHILOSOPHY

ASPECTS OF FORCES ON CHARGED PARTICLES IN ELECTROSTATIC PRECIPITATORS

Submitted by:

Owen J. Tassicker; MEE(Melb), FIE Aust, FIEE, CEng.

Department of Electrical Engineering
Wollongong University College
University of New South Wales

July, 1972

811457

Synopsis

An electrostatic precipitator comprises a number of electrodes whose geometry, hopefully, has optimum corona generation properties. Flue gas flowing through the interelectrode space is ionised and corona currents are distributed over the earthed receiving electrode. Solid particles in the gas being charged, are accelerated to the receiving electrode where they deposit in layers.

In this dissertation, the basic processes of gas ionisation; particle charging, collection and final disposal, are reviewed and some problem areas identified. The word "particle" in the thesis title is used in a broad sense to include both solid dust particles and ions.

Effective dislodgement of deposit by rapping of collector electrodes is shown to depend upon the adhesive strength of the layer. This in turn is shown in the dissertation to depend upon the particle size, shape, composition, compaction and surface properties. Force components comprise Van der Waal, Debye dipole, capillary and electrostatic. When corona currents flow, the additional forces due to this cause are repulsive for low resistivity and attractive for high resistivity materials.

The design, construction and commissioning of a unique device, the Precipifuge, is described. Capable of determining the adhesive strength of a layer of deposit, under precipitator conditions, it is in fact a combination of centrifuge and precipitator.

A new kind of active probe termed the Micro Area Boundary Electrode is described by which a small volume, say 1 mm^3, of ionised gas at a point on the electrode surface may be interrogated. Using either d.c. perturbation or an a.c. diagnostic signal, the value of E, J and σ and the complex dielectric constant may be determined.

By means of MABEL, the coronas produced by a number of electrode geometries are examined. Some conclusions of a fundamental and others of an applied nature are drawn. The visible corona tufts known to emanate from the surface of a smooth wire at negative high potential, have been shown to penetrate right through the corona gas space, appearing as current discontinuities over the whole of the anode. Dust deposition follows corona power density on the boundary. For equal power inputs to a precipitator, collection efficiency depends strongly on electrode configuration.

The complex permittivity of a dispersoid, fundamental to the determination of adhesive forces, has been examined for fly-ash over a range of temperatures and frequencies.

THESIS CONTENT

PRINCIPAL SYMBOLS

α_s = density of a solid or particulate, kg m^{-3}

α_b = density of composite bulk solid particles & voids

a = radius of corona discharge electrode, m

A = van der Waal constant of attraction between spheres

A = cross sectional area of test cell; precipitator receiving electrode area, m^2

A_c = cross sectional area of precipitator perpendicular to gas flow, m^2

A_o = area of probe, m^2

A_{o1} = area of probe and screen, m^2

b = radius of cylindrical receiving electrode; spacing wire-duct electrodes, m

C_o = capacitance between active probe face and surrounding electrode; vacuo free space capacitance of concentric test cell, F

$\bar{c}$ = average ion velocity, m s^{-1}

d = particle diameter, m

d' = contact diameter between particles, m

D = electrostatic flux density, C m^{-2}

D_i = diameter of probe, m

D_m = mean diameter of insulation surrounding probe, m

D_o = diameter of hole containing probe, m

δ = volume fraction of a composite dielectric of spheres and voids ($=1-\phi$)

ΔF = force between a pair of particles, N

$\tan\delta$ = loss angle of dielectric

e = electronic charge, C

E = electric field strength, V m^{-1}

E_τ = tangential electric field on the surface of a particle, V m^{-1}

E_l = electric field on surface of a charged particle, V m^{-1}

E' = electric field strength on a boundary in absence of space charges, V m^{-1}

E_z = electric field in gap between particles, V m^{-1}

E_c = electric field charging particles; or electric field over contact area of adjacent particles, V m^{-1}

E_f = activation energy, ev

E_g = electric field in a gas at the interface, V m^{-1}

E_i = breakdown strength of gas, V m^{-1}

$E_{av} = E_\ell$ = average electric field in a dispersoid layer

E_o = electric field strength on a boundary, or distant from a charged particle, V m^{-1}

η = viscosity of a gas; or efficiency of a precipitator; efficiency of rapping, (viscosity N s m^{-2})

ε = complex dielectric constant = $\varepsilon'-j\varepsilon''$, F m^{-1}

ε_ℓ = composite dielectric constant, (solid + voids)

ε_g = dielectric constant of a gas, F m^{-1}

ε_o = permittivity of free space, F m^{-1}

γ = surface tension of fluid, dyne/cm, N m^{-1}

G = $(D_o - D_i)/2$, gap around probe, m

G = conductance, Ω^{-1}

h = planck constant, J s

I = current in probe or alternating current in dielectric

I_1 = quiescent direct current in screen, A

I_2 = total corona current in pseudo guard, A

I' = total corona current, A

I_o = quiescent direct current in unbiased probe, A

J = current density, A/m^2

J_o = current density at boundary, A/m^2

k = Boltzmann constant, $J°K^{-1}$

K = electrical mobility of gas, $m^2s^{-1}V^{-1}$

K^+ = mobility of +ve ions, $m^2s^{-1}V^{-1}$

K^- = mobility of -ve ions, $m^2s^{-1}V^{-1}$

L = annular gap of test cell; length of precipitator; length of corona receiving electrode; emitting electrode, m

n = density of ions, or gas molecules, m^{-3}

n_o = density of ions in gas, distant from particle, m^{-3}

n_p = density of particles, m^{-3}

n^+ = density of positive ions, m^{-3}

n^- = density of negative ions, m^{-3}

N = no. of singly charged ions

$(N_s e)$ = saturation charge on a particle, C

ϕ = porosity = (void volume)/(total volume); potential in an electric field

ψ = electrostatic flux, C

Q = fractional loss of particles from a precipitator

q = (Ne) = charge on a particle, C

q_s = surface charge density at interface, $C\ m^{-2}$

P = pressure or tensile stress, Nm^{-2}, dyne/cm^2 or grm wt/cm^2

r = a radius variable, m

R = a radius, m

R' = resistance at the interface of a pair of particles, Ω

ρ = space charge density by ions, $C\ m^{-3}$

ρ' = space charge density by gas-borne dust, $C\ m^{-3}$

$\overline{\rho}$ = resistivity, Ω m

$\overline{\rho}_i$ = intrinsic resistivity of dielectric material, Ω m

$\rho_{d.c.}$ = resistivity to direct current, Ω m

S = specific surface area of aerosol, cm^2/cm^3

σ = surface charge density, $C\ m^{-2}$

$\overline{\sigma}$ = conductivity, $\Omega^{-1} m^{-1}$

T = absolute temperature, °K

τ = time constant, s

V = alternating potential applied to dielectric; potential in an electric field, V

V_a = potential applied to corona system, V

V_b = probe bias voltage or corona breakdown voltage (flashover), V

V_o	=	corona inception voltage, V
v_d	=	drift velocity, m sec^{-1}
w	=	particle migration velocity, m/s
ω	=	angular velocity, /s
χ	=	co-ordination number in particle packing

0. RELATIONSHIP OF THE DISSERTATION TO THE ELECTROSTATIC PRECIPITATOR

This dissertation concerns itself with some aspects of the forces on charged particles in electrostatic precipitators. Here, the work 'particle' is used in a broad sense to include ions, small dielectric and conducting spheres. The forces considered are electrostatic, London-Van der Waals intermolecular attraction, gravitational, and capillary in origin.

The contributions described in subsequent chapters relate to coronas, electrostatic boundary probes, dielectric constant of an ionised gas, particle charging time constants, complex dielectric constant of powders, tensile strength of a compacted powder, and the development of a special centrifuge. Such topics cover several disciplines and are therefore of interest to a variety of workers. However, the development of these various ideas has all been undertaken with an eye to their applicability to the electrostatic precipitator. Indeed, without such a frame of reference, the various topics may appear to be entirely unconnected. The fascinating combination of fundamental engineering and physics concepts embodied in the electrostatic precipitator, provides the thread binding the several chapters of this dissertation together.

A substantial introductory chapter now follows, in which the principles of operation of electrostatic precipitators are formulated. Some problem areas are identified. The several original contributions to be made in later chapters are noted as that aspect of technology is described, and are briefly summarised in paragraph 1.6.

CHAPTER 1

FUNDAMENTALS OF ELECTROSTATIC PRECIPITATOR TECHNOLOGY AND SOME UNSOLVED PROBLEMS

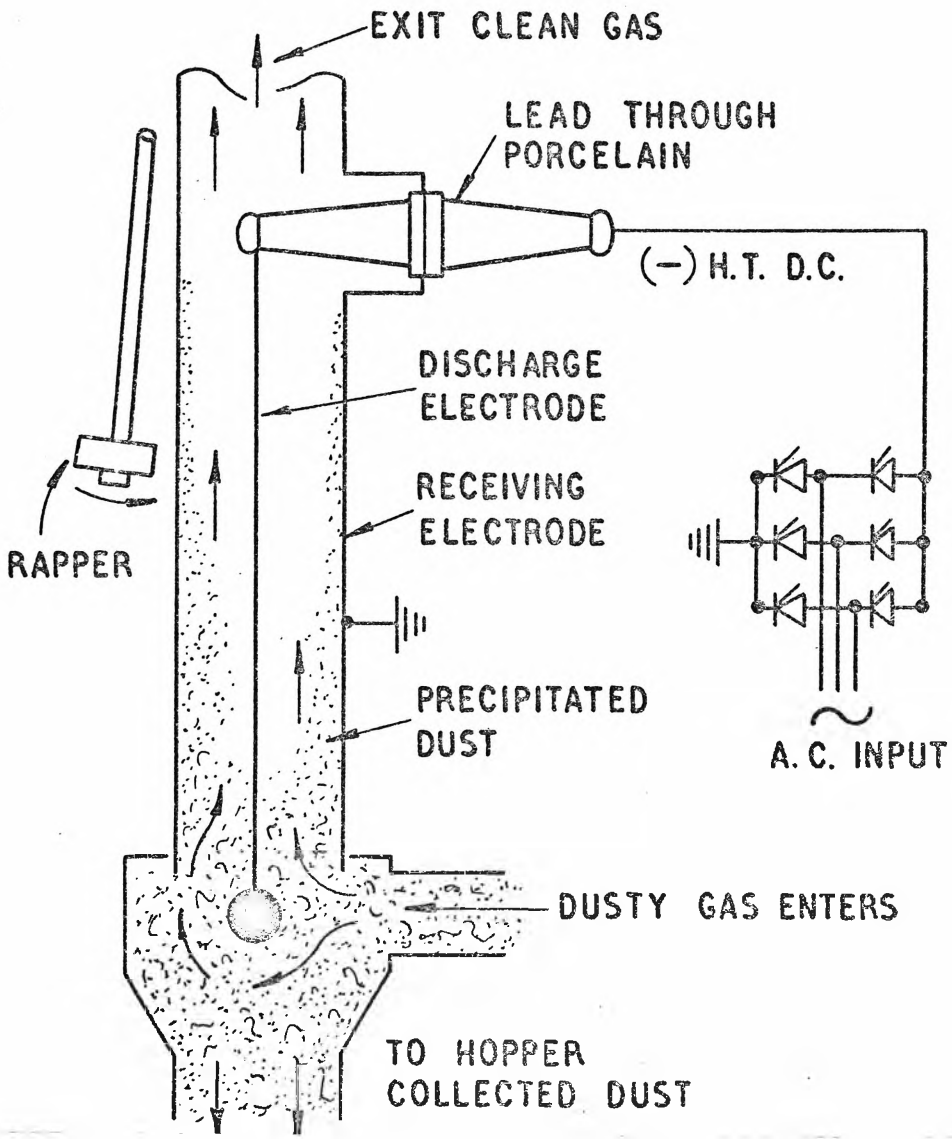

FIG. 1.1 THE TUBULAR SINGLE STAGE PRECIPITATOR

1. FUNDAMENTALS OF ELECTROSTATIC PRECIPITATOR TECHNOLOGY AND SOME UNSOLVED PROBLEMS

Building on early experimental work by Gilbert, Hohlfeld and Guitard (1600-1850), in which they observed that smoke and fogs could be removed from jars by the application of static electricity, Lodge and Walker took out patents on electrostatic precipitators (1885-1903). The first commercial electrostatic precipitator was designed by Cottrell (1906), and the Berkely, U.S.A., installation collected sulphuric acid and noble metals from smelter fume.

In the Cottrell single stage precipitator shown in Fig.1.1, dust laden gas enters at the base and flows upward through a concentric electrode system. At the surface of the central (discharge) electrode, the gas is ionised due to the high negative d.c. potential of the wire. The whole region is filled with negative ions at a typical density of 10^9 ions cm^{-3}. Within several milliseconds of entering the charged volume, particles receive a saturation charge proportional to their surface area and to the field strength in which they are situated. Typically, for a 1μ diameter particle, the saturation charge is equivalent to 250 electrons. Impelled by the force of the radial electric field, the particles move towards the receiving (earthed) electrode. This motion is resisted by viscous forces and a terminal velocity known as the 'migration velocity' is quickly reached. As the particle diameter population typically may vary from 1μ to 30μ, so the migration velocity will vary from about 0.03 to 0.5 m/sec. On reaching the receiving electrode, the particle is electrically discharged, adhering to the previously captured substrate. Periodical rapping of the receiving electrode causes agglomerates of particles to detach and drop into the hopper below. Aerodynamic as well as electrical design of the electrode system is required if particles are not to be re-entrained

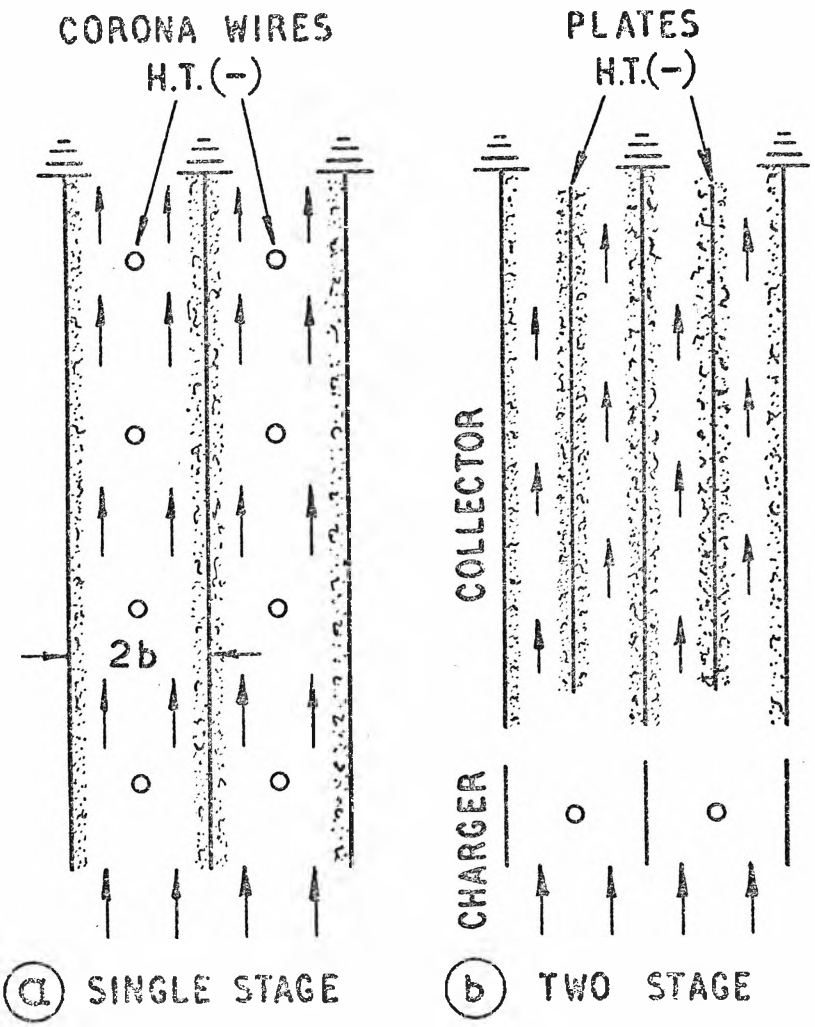

FIG. 1.2 WIRE IN DUCT ELECTRODES

(a) Single stage (b) Two stage

in the gas stream. The three phases of particle charging, collection and removal are now complete.

The collection efficiency of a precipitator is defined as the ratio of the mass of dispersoid removed from the system to the total quantity entering. Such efficiencies vary in practice from 90 to 99.9%.

All design and engineering effort is directed towards the improvement of precipitator efficiency. For example, duct type electrodes, Fig.1.2A are used for large volumes of gas. The two stage precipitator of Fig.1.2b in which the particle charging and collecting functions are separated, finds application in 'electronic' air cleaning for small scale application.

Electrostatic precipitators are effective in recovering useful by-products which would otherwise be lost to the atmosphere. Applied to smelters, valuable copper, lead and zinc oxides are recovered. Most industrial countries now have 'clean air' legislation limiting the amount of solid fume or smoke which may be discharged to the atmosphere. For example, in the State of New South Wales, new plants may not exhaust gas with a concentration of dust greater than 0.25 grm/Nm^3. Dispersoids first captured because of health hazard or aesthetic offence have frequently been found to have commercial value. The largest single user of precipitators, the power generating industry, collects enormous quantities of fly-ash. This has but recently found a small use as an additive to cement. As a means of cleaning industrial flue-gas, precipitators are now firmly entrenched in the smelters, blast furnaces, open hearth furnaces, cement mills, in the gasification of solid fuels, and in the chemical, paper and electric power production industries.

In order to give some idea of the scope of performance of precipitators, the following table[1] is presented:

Table 1

Typical Range of Precipitator Performance (after White)

Gas Flow	.05 to 100,000 m^3/min
Gas temperature	to 650°C
Gas pressure	10 atmospheres
Gas velocity	typically 1.0 to 5.0 m/sec.
Pressure drop	0.2 to 1.0 Torr
Particle size	0.1 to 300 micron
Particle concentration	.0002 to 200 grm/m^3
Particle composition	solid, liquid, corrosive
Treatment time	1 sec to 10 sec.
Efficiency	90% to 99.9%

The literature relevant to electrostatic precipitators is dispersed widely among the professional journals. This is in keeping with a technology which spreads over many disciplines. Chemical engineers have perhaps shown more courage in the past than other professional groups in coming to grips with this difficult art and their journals contain many of the best contributions.

Two books in the English language dealing with electrostatic precipitators have appeared. The first by Rose and Wood[2] (2nd ed. 1966) is a valuable introduction to the art. The work by White[1] (1963) is a substantial treatise which not only places the whole series of interlocked disciplines into perspective, but which also contains an extensive bibliography. Any worker in the area of electrostatic precipitators is bound to look closely at the valuable material contained in these two works.

1.1 BASIC ELECTRIC FIELDS AND SOME METHODS OF MEASUREMENT

For effective electrostatic precipitation, there must be a copious supply of ions available in the gas to charge the suspended particles. In addition, a strong electric

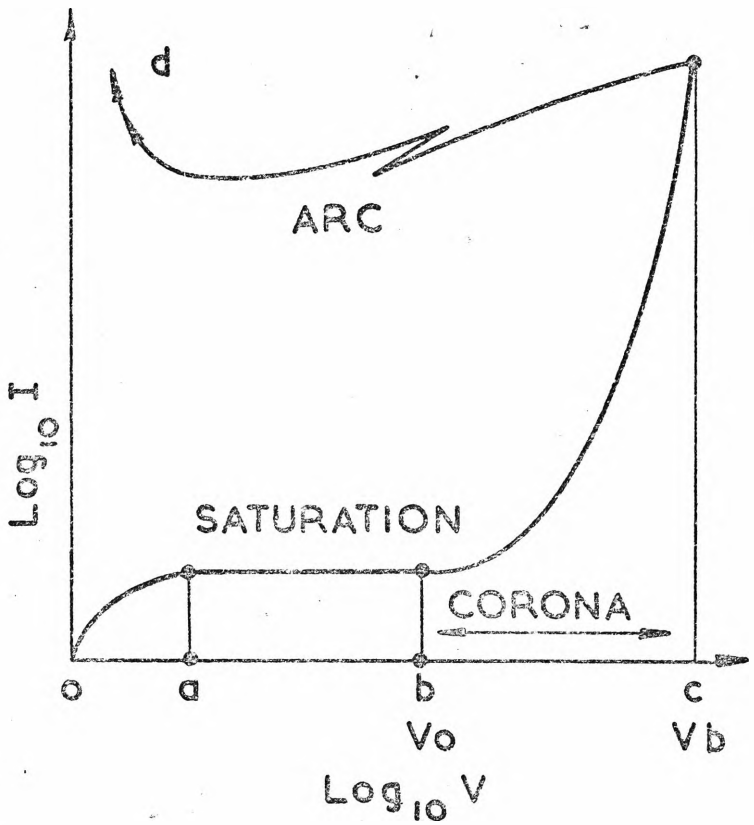

FIG. 1.3 CORONAS IN PRECIPITATORS

(a) Corona regimes

oa Faraday currents
ab Saturation currents
bc Self sustained corona
cd Arc.

field is needed to accelerate the charged particles to the receiving electrode. In two stage precipitation, depicted in Fig.1.2b the functions of charging and collecting are separated. In single stage precipitation, the same field is used for both functions. In either case, the strongest possible field is desired, so the voltage between the electrodes is raised to a value just short of overt breakdown (as distinct from stable corona) in the gas.

The complete corona current/voltage characteristics have been studied systematically by a host of workers from the time of Townsend[3] through to the present day[4,5] . Such a typical relation is shown in Fig.1.3a. From O to a there is a small Farady current, measurable only be sensitive instruments. Natural ionisation allows only a saturation current indicated by a-b. Over the regime b-c, the discharge becomes self-sustaining, commencing at corona onset V_o, after which the current increases closely parabolically for most discharge geometries. At V_b, breakdown of the gas occurs and the voltage falls to the arc value. From c to d the arc current increases with a small voltage drop across it. In precipitator technology, the area of interest is from b to c. The currents below b are too small to be useful. Above c, the arc short-circuits the electrode system and precipitation stops. A precipitator does, however spend about 5% of its time in the arc region. In Fig. 1.3b is shown that part of the corona characteristic which is useful in precipitator technology. It has been determined for those mixtures of N_2, O_2, CO_2, H_2O, SO_2 occuring in industrial flue gases in a cylindrical electrode geometry.[4,5,6,7]

Two types of corona may be distinguished, viz: positive and negative. Negative corona, in which the high tension discharge electrode is held negative with respect to the earthed receiving electrode is by far the more effective

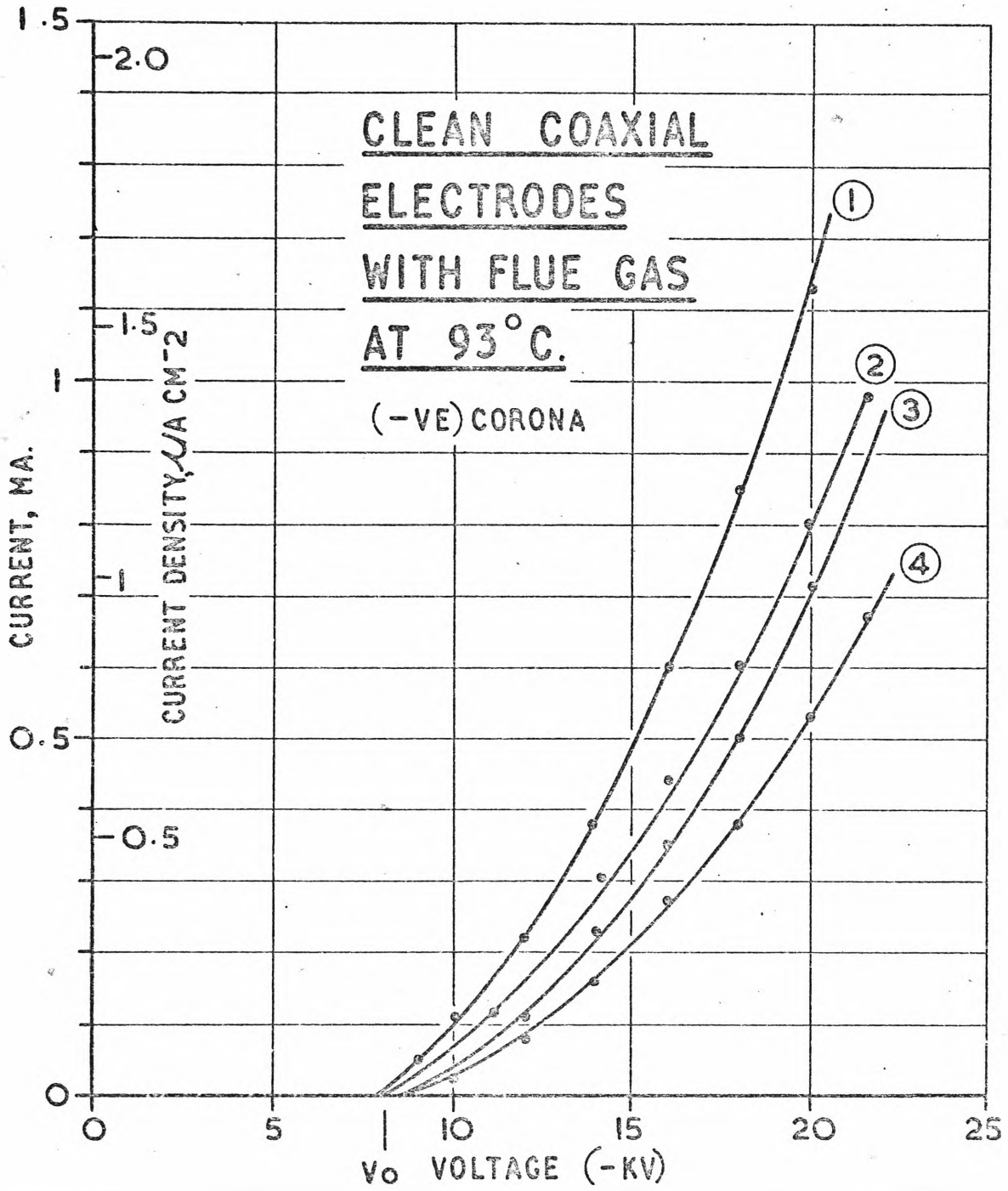

FIG. 1.3(b) CORONA IN COAXIAL GEOMETRY EFFECT OF WATER VAPOUR

Increasing H_2O decreases ion mobility and increases sparkover.

Vo = corona onset.

(i) Dry air 0.0% H_2O

(ii) Atmospheric Air 1% H_2O (by wt.)

(iii) Flue Gas: H_2O = 5% (by wt.)

(iv) Flue Gas: H_2O = 10% (by wt.)

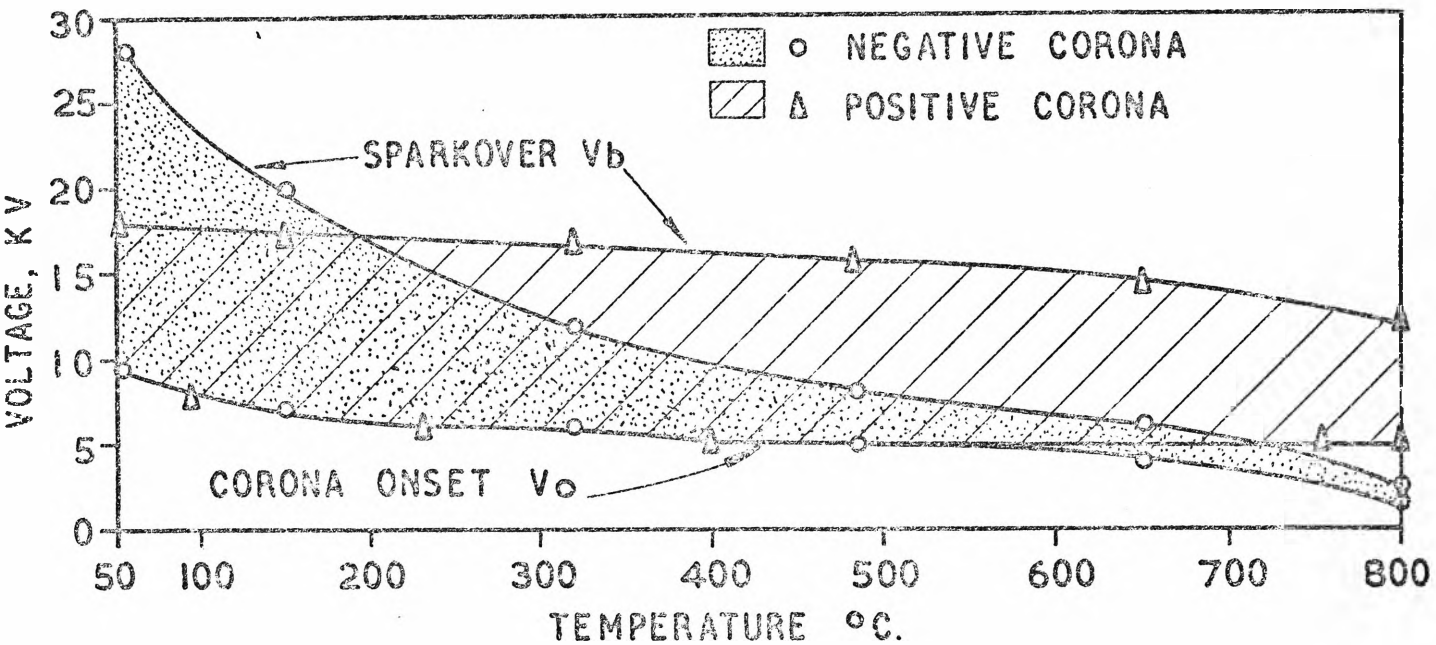

FIG. 1.4 POSITIVE AND NEGATIVE CORONA

Showing V_o and V_b for positive and negative corona in air as a function of temperature at atmospheric pressure. Concentric cylindrical electrodes, $2a$ = 0.5mm, $2b$ = 5cm. (after Shale)[10]

at normal temperatures and pressures and is almost exclusively used in practice. The nature of the two discharges is rather different, positive corona being the more amenable to rigorous mathematical analysis. In positive corona a steady smooth glow surrounds a smooth regular discharge wire[8]. In negative corona (possible only in the presence of electronegative gases), the discharge emanates from sharp tufts which are stationary in space only for the point-to-plane geometry. On a smooth wire, they may move about over the electrode, but generally space themselves regularly and stably[9].

It is an original contribution of this dissertation, that such discontinuities visible on a smooth wire negative emitting electrode actually penetrate the whole of the gas space to the anode. In Chapter 6, is given a description of previously unsuspected discontinuities in J over the whole of the anode surface.

Individual tufts from negative corona are not in a steady state in time, the intermittent currents being known as Trichel pulses. Such high frequency pulses are not of direct concern to precipitators since it is the average of many which are effective in practice.

For high temperature operation, positive corona is more promising than negative. Shale,[10] in experiments on air from atmospheric pressure to 80 psig and temperatures to 900°C, found the corona data shown in Fig.1.4 for cylindrical electrodes. For positive corona, sparkover and onset were simply dependent upon gas density considerations. Negative corona sparkover fell rapidly with increasing temperature so that above 200°C, $(V_b-V_o)_+ > (V_b-V_o)_-$. The zone of stable precipitator operation favoured positive corona at such temperatures, a criterion applying whether the electrodes were clean or contaminated.

As shown in para. 1.2, the migration velocity of a solid particle is proportional to the square of the electric field strength E in which it is situated. Therefore the electric field E in a precipitator is a most important parameter in the evaluation of performance.

In any space-charge limited discharge Poisson's equation applies, viz:

$$\nabla^2 V = -\rho/\varepsilon_o \qquad .....(1.1)$$

which for a cylindrical electrode system[13] as depicted in Fig. 1.1 or Fig. 4.8 reduces to:

$$\frac{d^2V}{dr^2} + \frac{1}{r}\frac{dV}{dr} + \rho/\varepsilon_o = 0 \qquad .....(1.2)$$

Now the ionic current density

$$J = \rho V_d = (ne)\ K\ E \qquad .....(1.3)$$

where V_d = drift velocity and K = gas ion mobility. For a cylindrical electrode system of length L, and total current I'

$$(I'/L) = (2\pi r)\ \rho K\ E \qquad .....(1.4)$$

which gives the (steady state) charge density as a function of E and I'.

The derivation is considered more fully in appenxix 1.1 because the results are important in several places in this dissertation.

There it is shown that:

$$(I'/L) = 4\pi\varepsilon_o\ K \left[\frac{(V_a - V_o)^2}{2b^2} + \frac{V_o(V_a - V_o)}{b^2 \ln(b/a)} \right] \qquad ..(1.5)$$

from which the parabolic dependence of I' upon V_a is clear,

(vide Fig.1.3b & 4.9a). Tassicker[5] and Henry[6] have used this expression to determine the mobility of various industrial flue gases. The electric field in the same cylindrical geometry is given by (see appendix 1.1):

$$E^2 = \frac{2(I'/L)}{4\pi\varepsilon_o K}\left(1-\left(\frac{a}{r}\right)^2\right) + \left(\frac{V_o}{r\ln(b/a)}\right)^2 \quad .....(1.6)$$

from which E at any radius is seen to depend upon the superposition of the usual electrostatic field, upon a field due to space-charges present only when a current flows.

The important features of this equation are shown in Fig.4.9 where a slight amount of ionisation (I'/L = 1μA/cm) increases the boundary electric field E_o from 0.37 to 1.55 kv/cm. Further, the effect of the space-charge is to establish a constant electric field over a large part of the interelectrode space. Pauthenier and Moreau-Hanot[11] have verified eq.1.6 experimentally.

Eq.1.1 has not been solved for corona geometries other than cylindrical and point-to-plane. An approximate solution for the important wire-in-duct electrode geometry depicted in Fig.1.2a, has been obtained by Cooperman[12] as:

$$(I'/L) = V_a(V_a-V_o)\frac{4\pi K\varepsilon_o}{b^2 \ln(4b/\pi a)}$$

which is similar to eq.1.5 for small currents.

The point-to-plane corona geometry has long been studied[13] and the quadratic relationship between I' and V known.

It appears then, that the three common geometries all show a corona onset voltage V_o and thereafter a quadratic relationship between current and voltage. In other practical precipitators whose electrode geometry is not amenable to analysis, the same quadratic relationship is inferred by

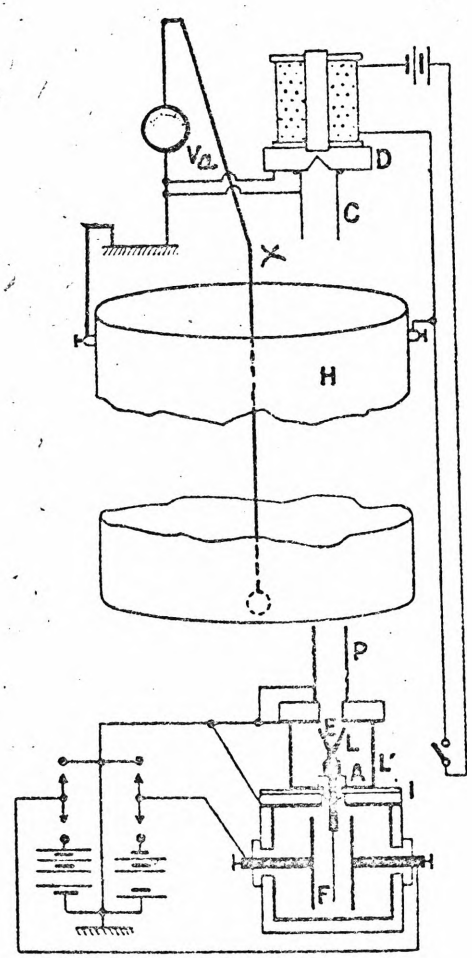

FIG. 1.5 CHARGING OF SPHERE IN A CORONA

The Pauthenier/Moreau-Hanot falling ball experiment. Corona is set up in the cylindrical electrodes H-X. A sphere released from the container D falls through the guards C, traverses the corona H-X and enters the Faraday Cage E via the guards P. Electrometer F measures the charge.

anology and found to hold reasonably.

In order to determine electric fields and corona current distribution in electrostatic precipitators by experimental means, various probes have been used. Booth[14] used a fairly crude insulated wire probe.

Using a long, thin, exposed conductor (such as that indicated by X-Y in Fig.4.8) which he traversed through the ionised gas, Sato[30] (1933) used a null technique to determine potentials. In this way, he verified the distribution indicated in Fig.4.9b and obtained some figures for charge density.

In a long series of definitive experiments Pauthenier[11] and his co-workers (1932-1960) examined the cylindrical geometry (Fig.1.1 and 4.8) exhaustively. They then used these results as a basis upon which to develop the theory and practice of spherical particle charging in an ionised gas, a matter discussed in para.1.2. Considering the case for spherical particle charging proved, they then dropped precision steel balls through an axially-symmetric ionised gas into a Farady cage, measured the charge, and from eq.1.7, computed the field through which it passed. In this way, the falling ball was considered to be a sort of probe. Pauthenier and Moreau-Hanot also used a hot wire probe, connected to earth via an electrometer, to determine fields. Beyond the cryptic comment; "La mesure des potentiels aux différents points du champ est plus délicate"; they give no description of the basis of this method, so that it is impossible to form an opinion about it.

Penney and Matick[15] used a variation of the Sato fine wire probe to document the field distribution in the axially symmetric wire-in-duct corona (Fig.1.2a) obtaining such important results as that shown in Fig.1.6.

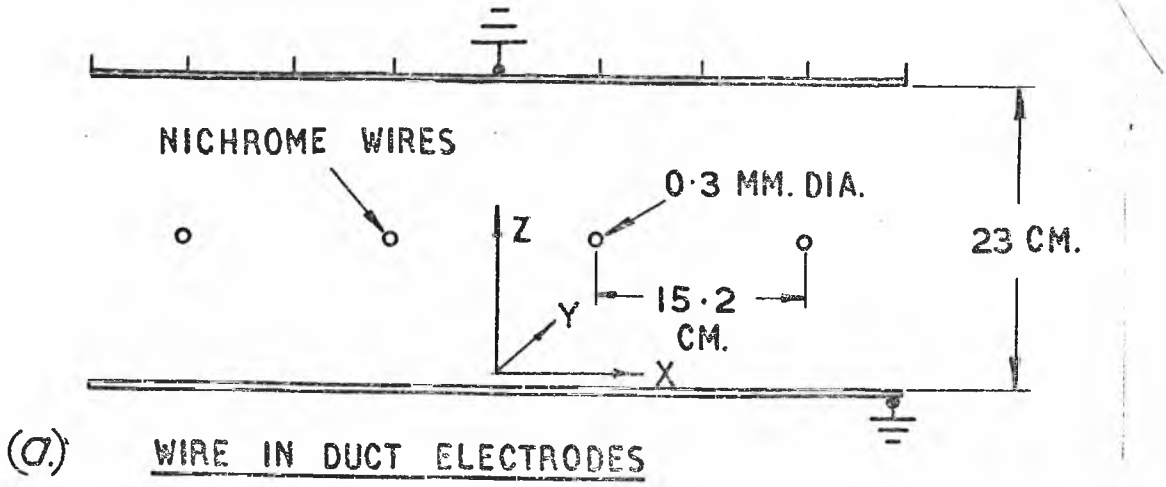

(a) WIRE IN DUCT ELECTRODES

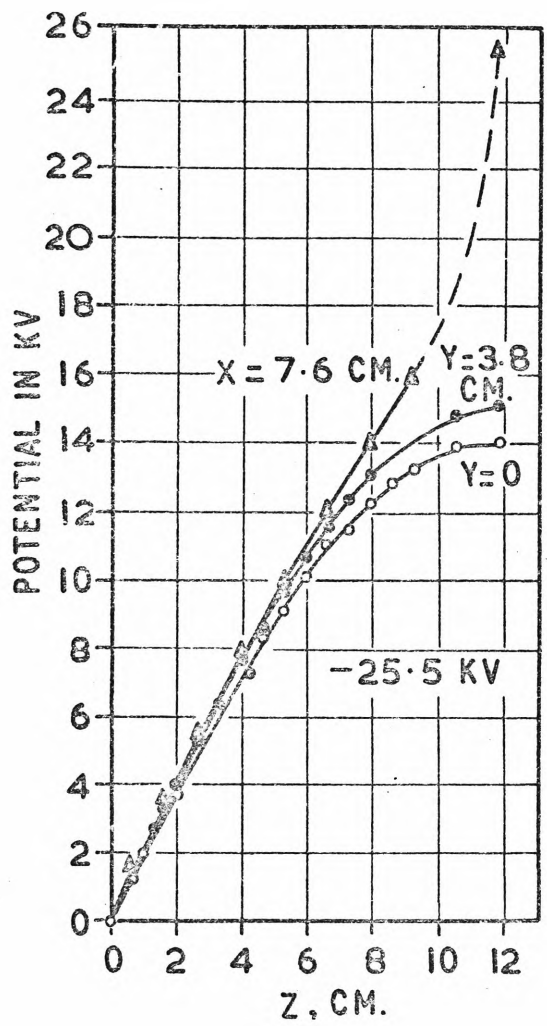

(b)

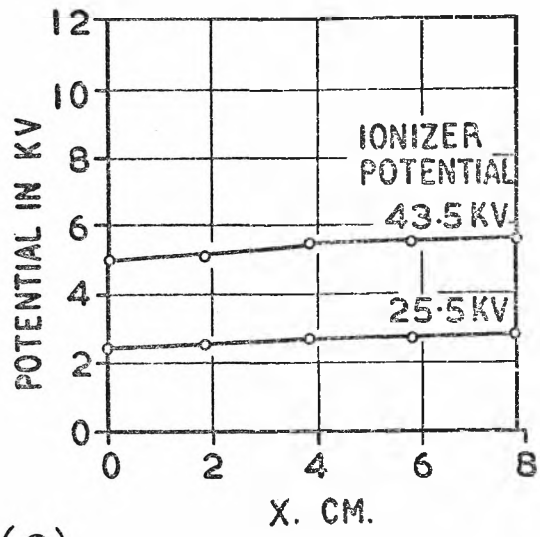

(c)

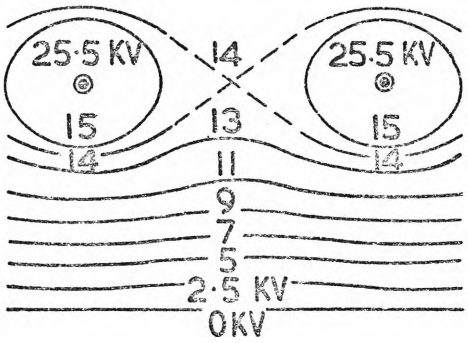

(d)

FIG. 1.6 FIELDS IN WIRE-IN-DUCT ELECTRODE CORONAS (after Penney & Matick[15])

Ioniser potential 25.5 kV and I' = 1.47μA/cm/wire

(a) Electrode configuration (b) Measured potentials in Z direction (c) Potentials in X direction and Z = 1cm (d) Equipotential plot

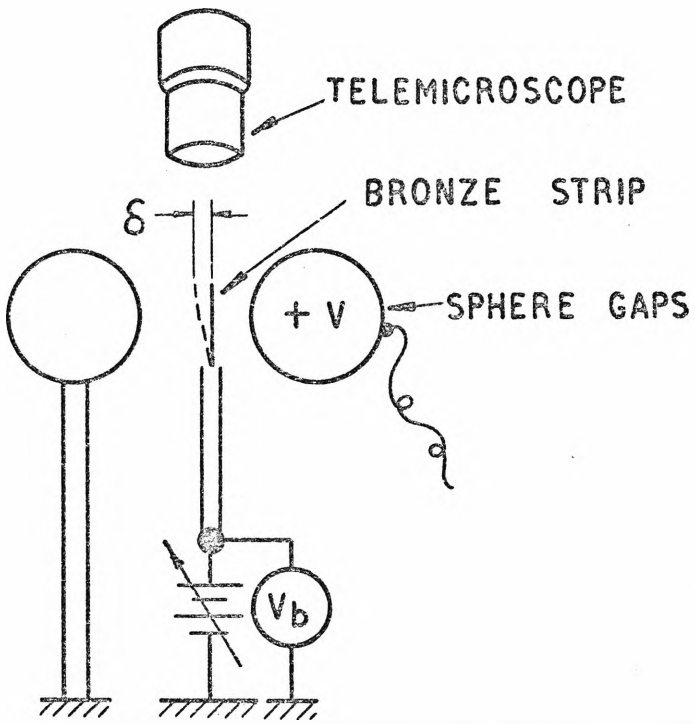

FIG. 1.7 THE DEFLECTING REED PROBE (after Gosho[18])

A thin flat phosphor bronze strip inserted along an equipotential into the field to be measured, is observed by a telemicroscope. V_b is adjusted until the strip deflection δ reaches zero.

Cooperman[16] used a variation of the Pauthenier technique by firing metallic spheres as projectiles in order to determine field strength and current density in concentric cylindrical and wire-in-duct geometry. The object of projecting the spheres was to avoid troublesome deflection by electrostatic forces during transit. His results, unfortunately conflict with those of Penney and Mattick[15] and Lagarias[17]. It appears that errors in individual readings of E ±10% and J ±30% (especially in regions of light ionisation) were largely the result of the short transit times of the projectiles. The writer will take sides in the dispute by presenting his own data in C6.

Lagarias[17] utilised the free falling ball technique in a commercial precipitator both with and without dust loading. Though encountering some difficulty with ball deflection, he presents results which are both self-consistent and in harmony with those of Penney and Mattick. These two sets of results when read together with White (ibid p.108) constitute the best account of wire-in-duct corona available.

The probe due to Gosho[18] has the attractive capacity to measure electric field strength with or without the presence of corona. A fine phosphor bronze strip illustrated in Fig.1.7, is inserted into the field along an equipotential, and is so deflected. An outside voltage applied to the strip, (which is observed by a telemicroscope) is adjusted until the deflection is zero. The potential so applied is the potential at that point in the field. The probe, unfortunately, suffers from vibration due to ripple voltage, Trichel pulses or transmitted from other moving apparatus in the neighbourhood.

Rose and Wood[19], however, in surveying (1966) the various probe results available, express strong reservations about them all because of the disturbing effect of the probe itself.

There is however a fundamental weakness in all of the probes described, namely that they all require a wholly, or substantially, axi-symmetric field. The writer has developed an entirely new probe described in C4 and 5, which meets several of the objections levelled at existing probes. It is capable of measuring J, $\bar{\sigma}$ and E in the gas on a boundary of the discharge. Since it is mounted flush on the receiving electrode, it eliminates the mechanical perturbation objected to by Rose and Wood. Since it is extremely small in size ($\simeq$ 1mm dia) it provides excellent spatial discrimination no matter how irregular the corona field. No degree of symmetry is needed in the field for its effective operation. It should be emphasised that many discharge electrodes in practical precipitators consist of a series of barbs or points, for an examination of which the writer's probe is well suited, whereas none of the other probes are applicable.

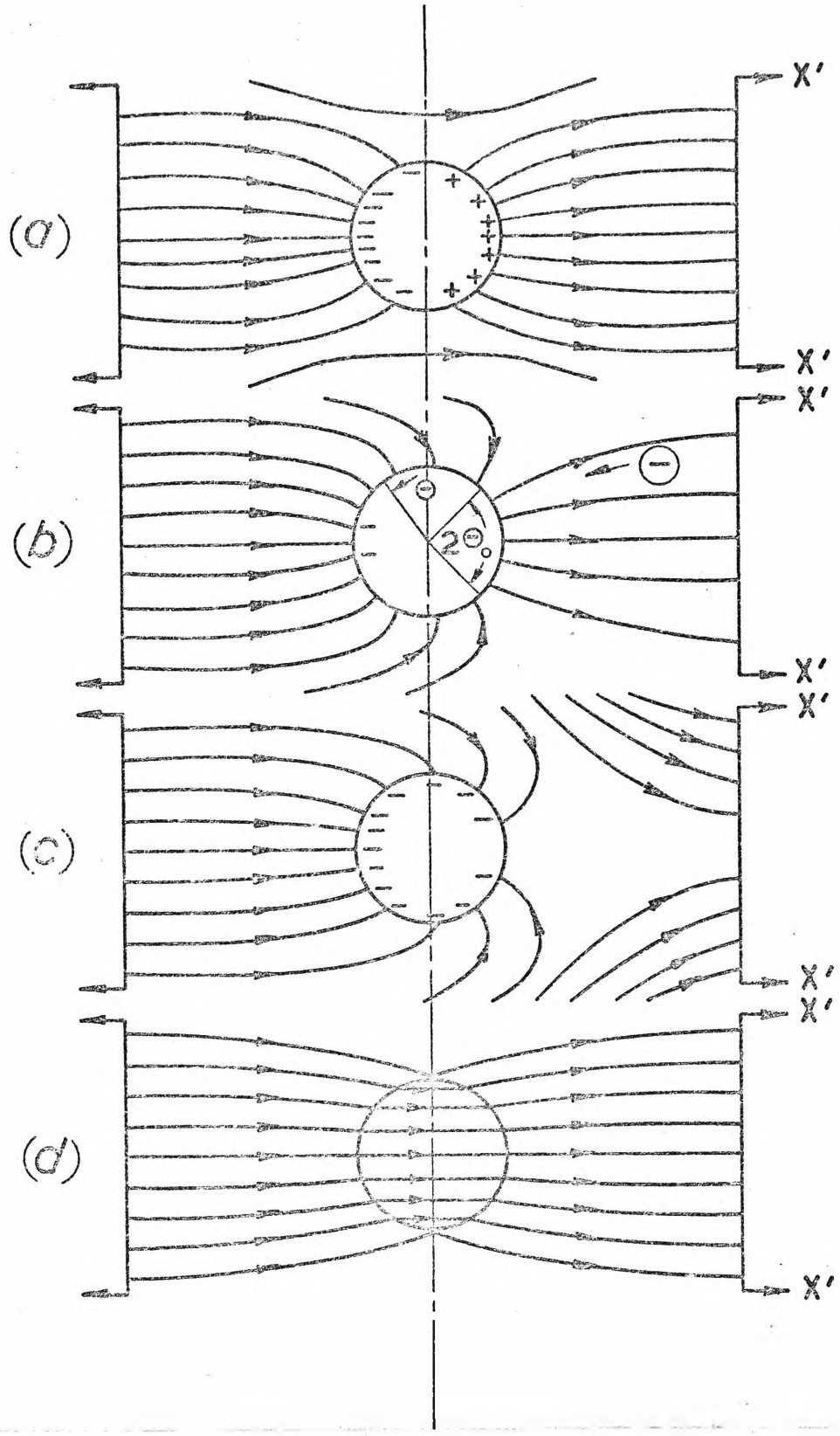

FIG. 1.8 CHARGING OF A PARTICLE

(a) A conducting sphere with no nett charge

(b) Negative ions enter the sphere, distorting the field.

(c) Charging ceases when no positive flux leaves the sphere

(d) A dielectric uncharged sphere

1.2 Charging of Particles

Particles carried by the gas as it passes through the electrode system are now rapidly charged. It should be noted that even in the absence of a corona field, most natural particles carry some charges as the result of friction, fracture during grinding, contact with flame or exposure to photoelectric emission. However, such casual charges would by themselves be insufficient to produce the efficiencies sought in a modern electrostatic precipitator. Charging of particles in the corona field occurs by two distinct processes known as Field Charging and Diffusion Charging. Field Charging, in which ions alight on the surface of the particle by drifting down lines of flux, is the dominant process for particles above 0.5 μm. Diffusion charging, in which ions arrive at the particle by random thermal motion, is the effective process at NTP for particles below 0.2 μm. In the intermediate region both processes are effective.

The process of Field Charging was first properly defined by Rohman[20], and extensively developed by Pauthenier and Moreau-Hanot[11]. White[21] has refined the derivation as follows.

Provided the spacing between particles is greater than about 10 diameters (almost always the case in practice), then a single spherical metallic particle situated in an electric field will appear as in Fig.1.8. In the absence of a nett charge on the particle, the field E_1 around the surface of the sphere is;[22] a well known result:

$$E_1 = 3E_o\cos\theta \text{ V/m}$$

where E_o is the initial undisturbed field taken to be uniform and θ is defined in Fig.1.8b.

One now posulates a uniform flux of (-ve) ions some distance from the particles which drift through the cross section x-x', finally arriving on the particle.

As the gas ions impart charge to the sphere, the local field is distorted in the manner shown in Fig.1.8b, the rate of charge collection consequently diminishes.

It may be shown that ion ingress ceases when a saturation charge of

$$(N_s e) = 3\pi\varepsilon_o E_o d^2 \qquad .....(1.7)$$

is attained. The particle charge at any instant is,

$$N(t) = N_s/(1+\tau/t) \qquad .....(1.8)$$

where

$$\tau = 4\varepsilon_o/(n_o eK)\ (s) \qquad .....(1.9)$$

which is a sort of charging time constant. It is to be noted from eq.1.7 that the saturation charge on a particle is proportional to its surface area and the field strength in the charging region. The charging time constant however is dependent only on the gas conductivity

$$(n_o eK) = \bar{\sigma}\ \Omega^{-1}m^{-1}$$

In the case of a dielectric sphere, eq.1.7 instead becomes:

$$(N_s e) = 3\varepsilon_r/(\varepsilon_r+2)\ \pi\varepsilon_o E_o d^2 \qquad .....(1.10)$$

It is common to generalise eq.1.7 and 1.10 as

$$(N_s e) = p\pi\varepsilon_o E_o d^2 \qquad .....(1.11)$$

where

$$p = 3\varepsilon_r/(\varepsilon_r+2)$$

When $\varepsilon_r \to \infty$, for metals, the dimensionless parameter p reduces to 3. Taking the saturation charge on a fully conducting particle as 1.0, the saturation charge on other particles becomes:

TABLE 1.2.1

Saturation Charge on a Particle

	ε_r	$(N_s e)$
Metallic	∞	1.0
Quartz	7	0.78
Oil	2.2	0.52

The difference in charging behaviour is thus quite limited for the whole range of possible dispersoids.

The second type of particle charging process due to random thermal agitation was first analysed by Arendt and Kallman[23]. The concise analysis by White[21], is outlined as follows.

From the well known law from the kinetic theory of gases, the rate of ion flow to the surface of a particle is

$$\frac{n\bar{c}}{4}(\pi d^2) \text{ ions/sec} \qquad .....(1.12)$$

where $\bar{c}$ = average ion velocity, and n = local ion density, which, assuming complete ion capture, leads to:

$$\frac{dN}{dt} = \frac{\pi}{4} d^2 n\bar{c} \qquad .....(1.13)$$

Since the ion density n at the surface of the particle is

$$n = n_o \varepsilon^{-Ne^2/(2\pi\varepsilon_o dkT)} \qquad .....(1.14)$$

then a relation for N(t) follows:

$$N(t) = \frac{2\pi d\ kT}{e^2} \log\ (1 + \frac{d\bar{c}n_o e^2}{8kT}\ t) \qquad .....(1.15)$$

This equation indicates that the charge increases slowly without limit in time, but is directly proportional to diameter and the absolute temperature. Diffusion charging is thus more effective in a hot precipitator. In practice, the actual charges found are about double those predicted by eq.1.15. Important improvements have been made by Murphy, Adler and Penney[24] by considering diffusion and drift together in a set of finite difference equations. Other improvements and measurements have also been reported.[25,26,27]

Some idea of the comparative magnitudes of field and diffusion charging is given by the following table by Lowe and Lucas[28] who based their calculations on:
$T = 300°K$, $n_o = 5 \times 10^7$ ions/cm^3, $E_o = 2$kV/cm and $p = 1.8$

TABLE 1.2.2

Particle Charging

Particle Radius (μm)	Ion Drift				Ion Diffusion			
	Period of Exposure (sec)				Period of Exposure (sec)			
	0.01	0.1	1	∞	0.01	0.1	1	10
0.1	0.7	2	2.4	2.5	3	7	11	15
1.0	72	200	244	250	70	110	150	190
10	7200	20,000	24,000	25,000	1100	1500	1900	2300

(after Lowe and Lucas[28])

So far, we have only considered the charging process in a gas with ions of one sign, since in a precipitator operating normally, there is a plasma sheath of mixed ions around the discharge electrodes occupying no more than 1 or 2% of the interelectrode space. The remaining 98% of the gas space contains ions of the one sign. In the unhappy situation where back corona occurs, the pores in the precipitated layer on the formerly passive receiving electrode break down and emit positive ions. The gas space now becomes a plasma containing ions of both signs, a situation discussed in para. 1.4. Corona V-I characteristics are profoundly altered, and obviously, particle charging suffers. Pauthenier[29] analysed the drift charging process in such a bi-ionised gas, disclosing the highly significant relations:

$$(N_s e) = [3\varepsilon_r/(\varepsilon_r+2)]\ \pi\varepsilon_o d^2 E_o(\gamma-1)/(\gamma+1) \qquad \ldots(1.16)$$

where $\varepsilon_r \to \infty$ for conducting particles, and

$$\gamma = \sqrt{(k^+n^+e)/(k^-n^-e)} \qquad \ldots\ldots(1.17)$$

For conducting particles only:

$$(Ne)/N_s e) = \frac{1 - \varepsilon^{-\alpha t}}{1-(\frac{1-\gamma}{1+\gamma})^2\varepsilon^{-\alpha t}} \qquad \ldots\ldots(1.18)$$

where $\alpha = 4\pi\sqrt{(k^+n^+e)\ (k^-n^-e)}$ $\qquad \ldots\ldots(1.19)$

These equations merit close scrutiny. The traditional eq.1.11 for a mono-ionised field results on placing $\gamma = 0$ or ∞ (depending on polarity) in eq.1.16 and 1.17. When (k^+n^+) approaches zero (back corona suppression) the charging

eq.1.18 reduces to eq.1.8 for the traditional mono-ionised field. A study of eq.1.16 and 1.17 shows that the saturation charge is likely to be drastically reduced in the bi-ionised field - a result noted in para.1.4 and found only too commonly in the state of New South Wales.

In precipitator technology it has been usual to regard the particle charging time as being very short (20 to 100 m.sec) compared with its residence time in the precipitator (e.g. White ibid p.137, Lowe and Lucas ibid p.43). In recent sustantial study[31], this assumption has been strongly questioned. The factor determining charging time constant is, from eq.1.9 or 1.18 , the conductivity of the gas $\bar{\sigma} = (n_o Ke) = 4\varepsilon_o/\tau$.

The present writer makes his own contribution to this dispute in Chapter 5 by presenting a new experimental technique by which the important parameter, $\bar{\sigma}$, may be determined quickly and accurately in a bench scale or technical scale apparatus.

1.3 Collection of Particles

The electric force on a particle with total charge q in an electric field is given by

$$F = q\,E \quad N \qquad .....(1.20)$$

and for the particles in question,

$$F = p\pi\varepsilon_o E_o d^2 E_c \quad N \qquad .....(1.21)$$

where we must now distinguish between the 'charging' field E_c and the 'collecting' field E_o. Since for a large portion of the interelectrode space, the field strength is roughly constant (eq.1.6 and Fig.4.9b), it is common to write

$$F = p\pi\varepsilon_o E^2 d^2 \quad N \qquad .....(1.22)$$

The particle quickly reaches its terminal velocity, and in precipitator theory, it is common to neglect the acceleration period.* The electrical force is balanced by the viscous friction as given by Stokes' Equation in which η is the gas viscosity and w the velocity

$$w = p\varepsilon_o E^2 d/(3\eta) \qquad .....(1.24)$$

For non-spherical particles, the value of the numerical factor p is adjusted, but not the form of the expression Eq.1.24. For very fine particles, the viscous drag must be reduced by the Cunningham correction factor which takes account of the mean free path of the gas molecules. Thus, the migration velocity is increased by the factor $(1+A\lambda/d)$ where λ is the mean free path of the gas molecules. For typical temperature conditions and a 0.5μ particle (White, ibid p.157)

$$(1+A\lambda/d) = 1.34$$

---

* This has recently been called into question by Seman and Penney.[32]

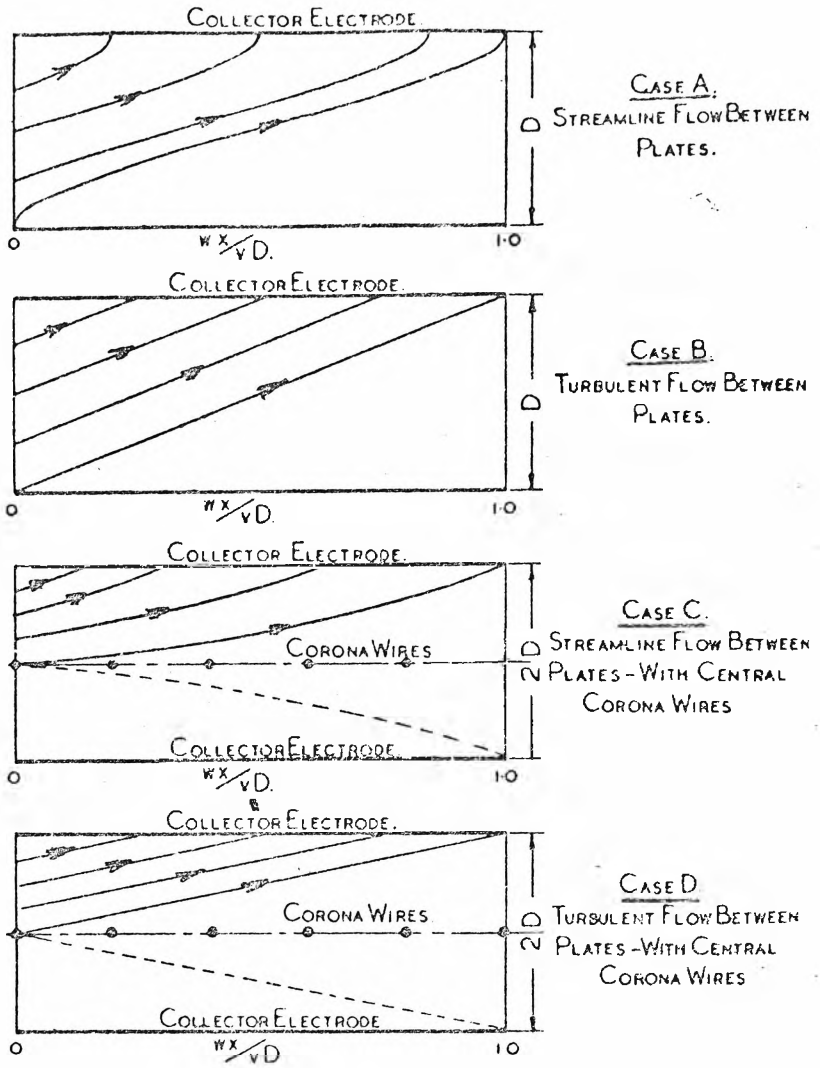

Particle trajectories in plate precipitators under various flow conditions.

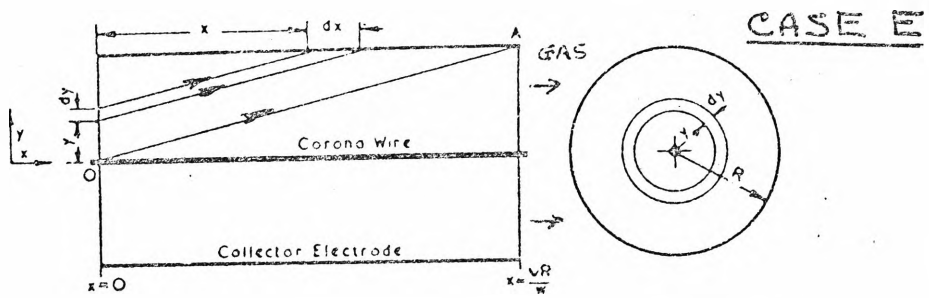

Particle trajectories in a tubular precipitator under turbulent flow conditions.

FIG. 1.9 PARTICLE TRAJECTORIES (after Rose and Wood[33])

When the velocity of the particle is high, streamline flow around the particle breaks down and Stoke's law fails. Using an approximate value of viscosity for flue gas (2.4×10^{-4} poise) calculation shows that serious deviations from Stoke's Law do not occur except for very large particles in abnormally high fields.[33]

In practice then, the migration velocity as given by Eq.1.24 holds and the velocity is seen to be proportional to the particle diameter.

In the Table(1.3.1),typical velocities are shown for average precipitator fields E_c = 5kV/cm and E_o = 4kV/cm.

TABLE 1.3.1

(after White[1])

Particle diameter μm	Gas Temperature °C	Gas Viscosity Poises*	Particle Velocity cm/sec
.5	20	1.8×10^{-4}	6.4
5.0	20	1.8×10^{-4}	48.5
50	20	1.8×10^{-4}	485
.5	350	3.0×10^{-4}	3.95
5.0	350	3.0×10^{-4}	30.5
50	350	3.0×10^{-4}	305

$$* \text{ 1 poise} = \frac{\text{MKS unit of Viscosity}}{10}$$

If the gas flow in the precipitator is non-turbulent corresponding to low Reynolds numbers, then the charged particle has a readily calculable trajectory. When applied to the cylindrical electrode precipitator, two types of trajectory will result as illustrated in Fig.1.9. In the case of the plate-type precipitator, similar trajectories are found for streamline and turbulent flow. It will be

observed from these figures that there is a particle-free region adjacent to the corona wires and downstream of the gas flow. Photographs of particle trajectories ($d > 5\mu m$) by Rose and Wood; by Pauthenier, Demon and Varshney[34], and the measurements of Hignett[35] support those exhibited in Fig.1.9. These photographs also indicate that, at least for all but the smallest particles, there is a dust free zone near the downstream corona wire.

On reaching the receiving electrode, by whatever trajectory the particle approaches it, in the simple theory, it is assumed to adhere and then to be electrically discharged. The mechanism of this final capture and deposition in the hoppers, in reality a complex matter, is taken up later in Para. 1.5.

It is now possible to define the efficiency of a precipitator as

$$\eta = \frac{\text{weight of particles collected by precipitator}}{\text{weight of particles entering the precipitator}} \qquad .....(1.25)$$

since the efficiency of an electrostatic precipitator is close to 100%, the efficiency may be more conveniently expressed as:

$$\eta = 1 - \frac{\text{weight particles lost}}{\text{weight particles entering precipitator}}$$

$$= 1-Q \qquad .....(1.26)$$

Other definitions of efficiency are possible, for example, based on the total number of particles entering and escaping.

The trajectories indicated by Fig.1.9 suggest that 100% particle capture is possible for a precipitator of a certain length. For the tubular system shown in Fig.9e, but

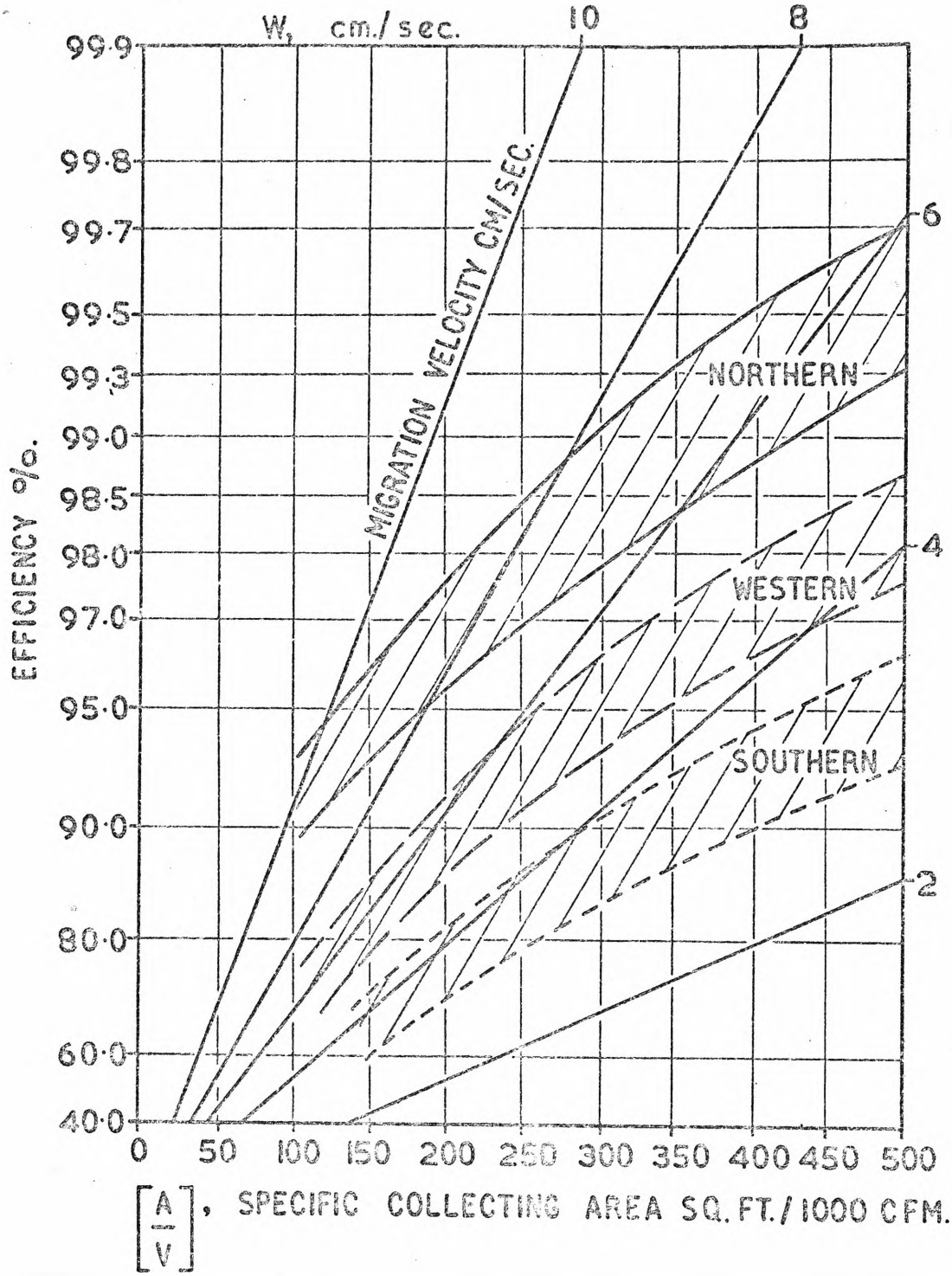

FIG. 1.10 EFFICIENCY, MIGRATION VELOCITY AND SPECIFIC COLLECTION AREA (after Watson and Blecher[50])

Results of a pilot precipitator installation collecting fly-ashes from parent coals of different sulphur content. Southern coals have low sulphur and extremely high resistivity, northern coals have low sulphur and high resistivity.

laminar flow, Rose and Wood show that all particles will be captured in a length of tube given by:

$$L = \frac{4}{3} \frac{V\ b}{w}$$

where V is the gas velocity and b the tube radius.

However, in practice efficiencies of 100% are rarely observed, instead an exponential relationship of the form:

$$\eta = 1-\varepsilon^{-\alpha L} \qquad .....(1.27)$$

is widely reported. This relation was derived by Deutsch[36] who found that

$$\eta = 1-\varepsilon^{-\frac{A}{V} w} \qquad .....(1.28)$$

where

A = total collecting area of electrode. m^2
$= 2\pi bL$ for a tubular precipitator
$V = A_c v$ = rate of gas-flow m^3/s

The Deutsch eq.1.28 in spite of its inadequacies, has been used as the basis for precipitator design and for the analysis of full-scale and pilot-scale plant tests for fifty years. In a given installation, the area A of the receiving electrodes is fixed, but the gas load V m^3/s is often a variable. The mean migration velocity w depends (eq.1.24) on the particle material, electrical energisation, gas viscosity and particle diameter. Typical tests results and the method of plotting an exponential η scale are shown in Fig.1.10. The bands of performance shown for the southern, western and northern ashes are indicative of the usual scatter found in test results in practice. The Deutsch equation is not followed exactly, for the bands of performance are not parallel to the lines of equal migration velocity. In this case, most of the deviation from the

exponential law is due to the mixed particle population[43,44,45] being presented to the precipitator - larger particles being generally collected first and the more difficult fines later, (i.e. in accordance with eq.1.24). In the absence of severe disturbing effects, the exponential law is followed well for small particles of a single size, and fairly well for large particles.

The physical grounds upon which the Deutsch equation and various improved[37] derivations of it are based are as follows:

(i) At any cross section of the precipitators perpendicular to the direction of gas flow, there is complete mixing of the particles and the gas. Extreme turbulence and the effects of the electric wind[38] are believed to account for such mixing.

(ii) Except for boundary layers, gas transport velocity is constant. (Implied in Fig.1.9b).

(iii) Particle migration velocity w is constant at the boundary layers.

(iv) All particles arriving at the collector plate are captured and there are no re-entrainment or back corona effects.

It will be seen at once that complete particle mixing (assumption (i)) is in conflict with such trajectories as Fig.1.9 and with the supporting photographs and measurements. Much debate and effort has been, and is currently taking place in order to resolve the conflict.

The two phenomena being invoked to this end are gaseous eddy diffusion leading to partial remixing and particle re-entrainment.

The writer believes there has been some confusion over the concept of the motion of a small particle subject simultaneously to an electrical drift force and to strong gas turbulence. The matter has been clarified for the writer by considering an analogous situation, i.e. the movement of

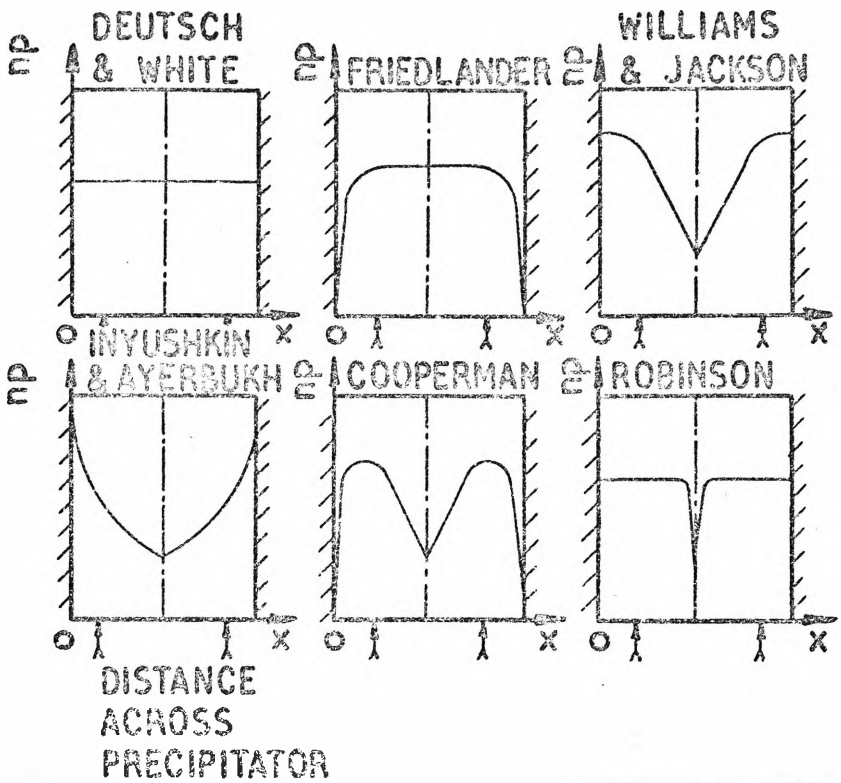

FIG. 1.11 TURBULENT DIFFUSION IN PRECIPITATOR GAS STREAM (after Robinson[39])

Turbulent eddies continually re-distribute particles which the electric field tends to concentrate near the walls. Particle concentration profiles calculated or observed by various authors for qualitative comparison only - no re-entrainment being assumed.

——— – ——— – *Discharge electrode*

n_p = *Particle concentration*

x = *Transverse distance across precipitator.*

an ion in a stationary gas. In the adjacent sketch, (a) the ion moves, in the absence of an external electric field

(a) 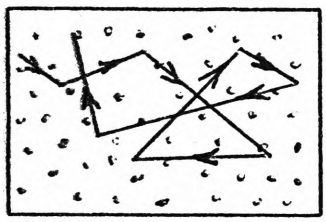 (b) 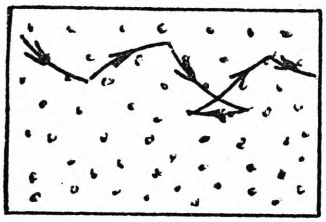

Random Ion Motion

Random Ion Motion with Superimposed Drift

in a random manner, subject to collisions, and with a mean velocity dependent on the temperature. When subject to an electric field, the ion now shows a slow drift velocity superimposed on the much higher thermal velocities. A small (say $\leq$ 1μm) charged particle, though too large to exhibit substantial thermal velocities, nevertheless suffers violent velocity changes when situated in a turbulent gas (Reynolds Number > 5000). Such a particle nevertheless still shows average transport in the direction of the electric field due to drift. A single large particle (> 10μm) shows little response to turbulence of the gas on present photographic evidence. It therefore discloses a regular deterministic trajectory; a resultant of the electrical drift velocity and the mean gas flow.

Robinson[39] in recently summarising the theories of various workers on the effects of turbulent diffusion shows the illustration of Fig.1.11. The Deutsch/White theory assumes complete diffusive re-mixing over each cross section, so that n_p the particle density is constant over a cross section but decreases steadily longitudinally. The Williams/Jackson approach leads to a comparatively clear space around the corona wire with maximum density at the

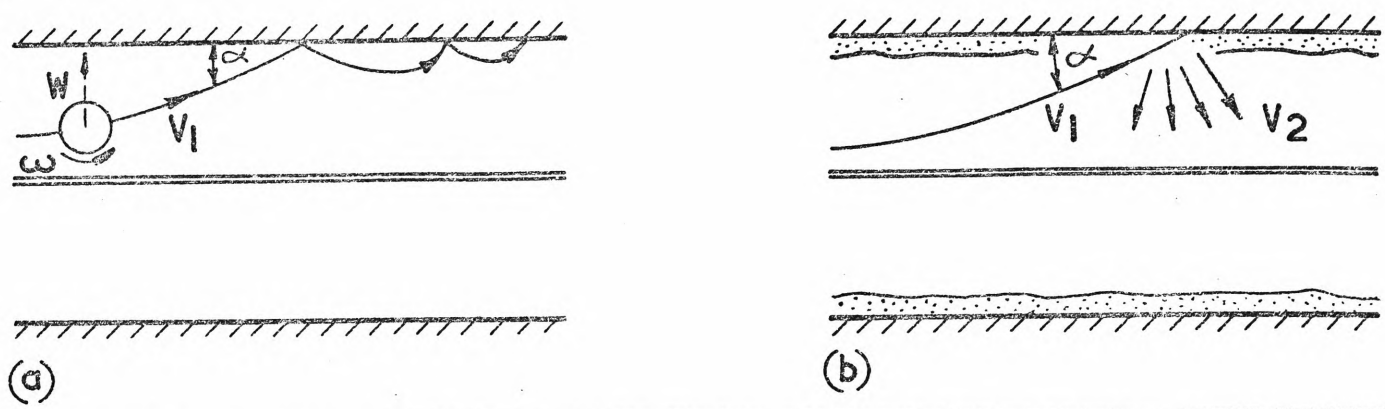

FIG. 1.12 PROBABILITY OF ATTACHMENT OF A PARTICLE

(a) A particle on striking the substrate has a probability of attachment h < 1, dependent upon incident velocity, Adhesive force etc.

(b) A large particle dislodges others on impact such that

$$\Sigma(m_2\bar{v}_2) = \gamma(m_1\bar{v}_1)$$

dislodged *impact* *where*

γ = *'secondary emission' coefft.*

walls. It may well be that the Cooperman/Robinson treatments express the behaviour of small particles rather well. Summarising then, for small particles in turbulent flow, diffusive mixing leads to exponential-type collection efficiency. In a purely laminar flow gas (in which re-entrainment has been prevented by use of a wet collector) efficiencies of 100% have actually been recorded[40], verifying the Rose and Wood contention (Fig.1.9) that complete collection is possible.

Both Rose and Wood[2] and Lowe and Lucas[28], quite early, suggested re-entrainment of particles after their initial impact as being responsible, at least in part, for the exponential Deutsch equation*[42] The writer unreservedly supports this view, particularly as regards large particles, advocating the use of a 'coefficient of attachment' of much the same form as that used in the kinetic theory of ionised gases. In this view, and making reference to Fig.1.12, the probability of attachment per collision, $h < 1$, between a particle and the substrate would depend upon:

Angle and velocity of impact
Mass of particle
Resistivity of particle
Force of adhesion between particle and substrate

The writer also suggests the use of a 'dislodgement coefficient' to account for dislodgement of small particles upon impact by a larger one (akin to secondary emission) to be denoted by $\gamma < 1$

where:

$$\Sigma(m_2\bar{v}_2) = \gamma(m_1\bar{v}_1)$$

dislodged material — impacting particle

---

* White: "Industrial Electrostatic Precipitation" 1963, P331 makes some pertinent notes on erosion by gas velocity, describing test procedures and results. However the recent study by Oglesby et al[30] found little evidence for re-entrainment by gas velocity erosion..

In support of such notions, low resistivity carbon particles have been commonly observed to 'hop' after impact, along the length of the precipitator. The writer has carried out an elegant experiment illustrating the 'hopping' of low resistivity particles in which carbon in fly-ash was separated out with nearly 100% efficiency. The photographs of particle trajectories by Penney[41,32] et al unmistakably show particles rebounding on impact. They also show scouring of a previously deposited layer by impact of larger particles.

In this dissertation, no particular contribution is made to the topic of particle collection, nor are the two parameters h and γ describing attachment and dislodgement developed. The state of the theory of collection efficiency cannot be said to be either satisfactory or final. The mean migration velocity w as calculated by the theory given is found in practice to be generally too large by a factor of 2 to 3. No serious worker in the field of electrostatic precipitation can be very satisfied with such a state of affairs. One aspect of the collection process stands out strongly as being at least in part responsible for the discrepancy between theory and practice, and that is the role of adhesion and re-entrainment.

The part played by adhesion in high efficiency precipitation is stressed as being important and not so well understood. The matter is taken up more fully in Chapters 2 and 3.

1.4 Particle Properties and Back Corona

The electrical and physical properties of the particles to be collected influence the electric field, the corona, the adherence to the collecting electrode, the efficiency of precipitation and finally, the optical appearance of emitted smoke.

Firstly, all naturally occuring particles are distributed in size and shape. For an irregularly shaped particle,, it is necessary to define what is meant by its size. Several definitions are possible and useful.[46,47]

(mainly after White[1])

Equivalent Diameter	Qualitative Definition	Mathematical Definition
Length Diameter	Diameter Measured in a Specified Direction	$d = \ell$
Mean length diameter	Arithmetical Average of Several Specified Dimensions	$d = \frac{1}{n} \sum_{1}^{n} d_k$
Surface area diameter	Diameter of Sphere having same surface area as particle	$d = (\frac{A}{\pi})^{\frac{1}{2}}$
Volume diameter	Diameter of sphere having same volume as particle	$d = (\frac{6V}{\pi})^{\frac{1}{3}}$
Stokes diameter	Diameter of a sphere having same density and settling speed as particle	$d = \{\frac{18v\eta}{(\delta_1 - \delta_2)g}\}^{\frac{1}{2}}$
Vol/surface mean	volume particle/surface area	$d = (\frac{V}{A})$

For example, consider a cubical particle of side 1μ, then:

Average dia. based on three dimensions = 1μm
Diameter of equivalent sphere of same volume = 1.24μm
Diameter of equivalent sphere of same surface area = 1.38μm
Vol/surface mean = 1/6μm

On choosing a method of defining a particle diameter,

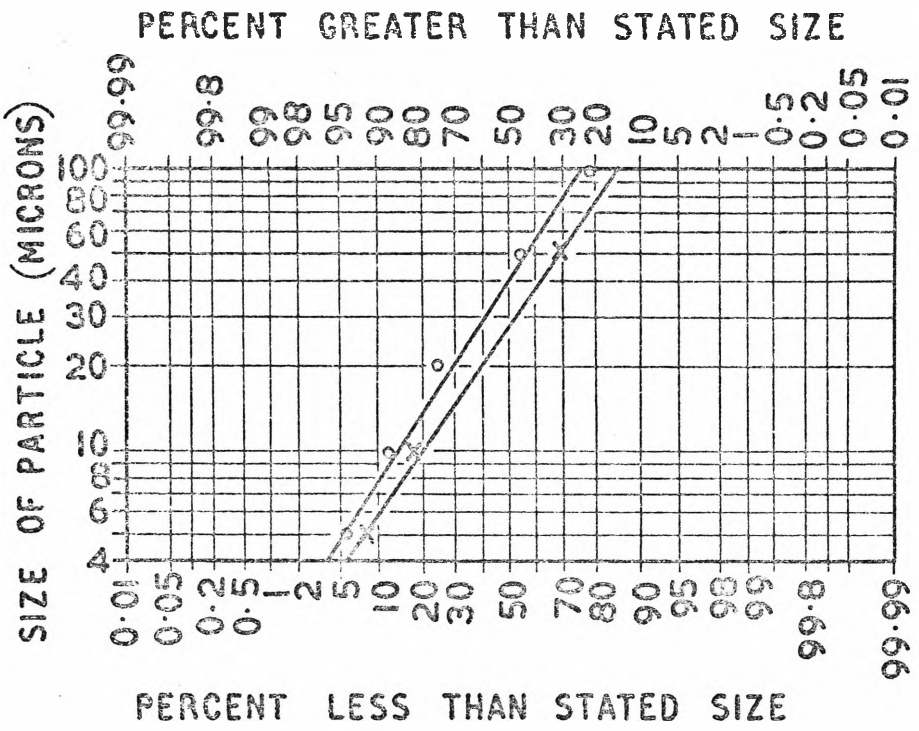

FIG. 1.13 PARTICLE DISTRIBUTION SIZE

Log normal probability distribution curve plots as a straight line.

o Wyoming low sulphur coal after pulverising

+ The ash after firing the coal

then a given population may be expressed in terms of normal statistics. The size-frequency distribution function $\gamma(x)$ is defined by noting that the proportion of particles lying within the size interval (dx) is $(\gamma(x)dx)$. The cumulative-distribution function

$$y(x) = \int_0^x \gamma(x)\, dx = \text{proportion of particles lying between 0 and x.}$$

Typical distribution curves for pulverised coal and fly-ash are shown in Fig.1.13 following the Rossin-Rammler (log-normal) straight line relationship.

The Deutsch efficiency equation, only applicable to particles of a single size has been amended by Troost[43], Allander and Matts[45] and White[44] for dust with a log-normal particle size distribution.

The public nuisance of a smoky stack is often judged by its appearance against the skyline, rather than by the mass of particles exhausted. The appearance is governed by the dispersion and reflection of light, so that fine particles have the appearance of being more dense than the same weight of coarser particles. Rayleigh's law of scattering applied to particles much smaller than 0.5μ, i.e. the wavelength of light exhibit true reflection, and scattering follows a second power law[48]. These facts are also made use of in the design of many commercial smoke-density meters which use a light source and photocell.

The dielectric constant ε_r of a non-conducting particle has some bearing on the process of electrostatic precipitation. The quantitative effect on particle charging was noted in Eq.1.10 and illustrated by the table which followed. When a particle is captured on the collecting electrode, it adds to the layer already present. The forces of adhesion are subject to detailed investigation in this dissertation in C2 where it is demonstrated that the dielectric constant is an

important factor in electrostatic forces. The complex dielectric constant, examined over a large frequency range may disclose properties of the particle important to electrostatic precipitation. For example, absorption bands from the ultra-violet to radio frequencies might throw light on the surface properties of dispersoids which are known to be very complex. At power or audio frequencies, absorption time constants indicate the presence of inter-facial polarisation as demonstrated in C7. Dzyaloshinskii[72] et al have already shown the importance of such frequency response data in the calculation of Van der Waal forces of adhesion between small particles. It is submitted that much valuable information on the properties of dispersoids could be obtained from systematic studies of the complex dielectric constant. In this comparatively unexplored area, the writer makes a vigorous incursion in C7.

When in the form of a layer adhering to the collector electrode the resistivity becomes very important. The ionic currents reaching the surface of the layer either as gas ions or as charged particles must discharge through the layer. If the resistivity of this layer is low, say $\rho < 10^{+4}$ ohm-cm, precipitation of solid particles (as distinct from liquid droplets) becomes difficult because the particles rebound on contact. It is supposed that large particles of low resistivity, on reaching the previously deposited layer, part rapidly with their charge, acquiring a sub-stantial charge of the same sign as the receiving electrode. They are repelled from the surface and are attracted back in the direction of the field. Davidson and Whittet[49], working with soot (carbon) particles, report that no difficult-ies were experienced provided the precipitate was damp (adhesive). When a dry patch developed, particles were thrown back with such vigour that they were finally collected on the corona wire opposite.

When the resistivity of the precipitate is between 10^4 and 10^{18} ohm-cm, no special difficulties occur and electrical precipitation is most effective. The charge on incoming particles is able to leak away through the precipitate and adhesive forces are able to hold them in position.

When the average voltage gradient in the substrate given by $E_{av} = J\bar{\rho}$ exceeds about 10 to 50 kV/cm, the layer breaks down, steady ionisation takes place in the pores, and precipitation becomes difficult because of the phenomenon known as 'back ionisation'. As developed by the writer's colleague[73] McLean, (eq.2.7 and Fig.2.2d), stress magnification E_z = (10 to 100) x E_{av} occurs in the pores of the dielectric with resultant electron field emission across small gaps. These energetic electrons are in the writer's view almost certainly responsible for ionising nearby gas molecules by collision and thereby initiating the process of back ionisation . Positive ions released in cells of 'reverse ionisation' move back into the gas space which now becomes bi-ionised and in the manner described in para.1.2, particle charging falls severely.

Since the phenomena of back ionisation due to high resistivity particulates leads to disastrous performance of precipitators in the field,[50,51,52,53] it has been the subject of many investigations. The fundamental origin of back corona has received attention[54,55,56] followed by studies of the changed electric field and modified particle charging.[29,54,58] The value of the contribution by the writer's colleague Herceg, is in showing the criteria for an applied voltage waveshape which eliminates back corona.

Since the current density in practice varies from 0.01 to 0.1 $\mu A/cm^2$, so the value of dispersoid resistivity at which back corona commences varies from about 10^{10} to 10^{12} ohm-cm. Much effort has therefore been expended in an

examination of the conditioning agents to be added to the flue gas in small quantities which will reduce resistivity values below the threshold of back corona.[58,59,60,75] Water is regarded as the primary conditioning agent, being added in quantities to some 30%.[60,61,62,63] Sulphurous acid and ammonia in some 5 to 90 ppm are also used to lower fly-ash resistivity.

A rather interesting illustration of the effect of back corona in a cylindrical geometry with an extremely difficult fly-ash is described by the writer.[5] Filtered flue gas was first admitted to the cylindrical electrode (Fig.1 ref.5) system, leading to the clean electrode corona characteristic (Fig.5 ref.5). After ½ minute of exposure to dusty flue gas, the corona characteristic has been markedly distorted due to reverse ionisation. After 4 minutes of deposition, the corona characteristic has become severely distorted; sparkover being reduced by 25% while currents increased to 250%. It is a salutary reflection that a high resistivity deposit only a fraction of a millimetre thick could be so damaging. Meanwhile both the pilot precipitator and the main plant collection efficiencies fell to that of a settling chamber, so that the electrical energisation might just as well have been switched off. Field and laboratory resistivity tests on the same dust yielded the characteristic shown in Fig.(2)[5] of the same paper. In the 'bone dry' test, log ρ when plotted as a function of 1000/(T+273) yields a straight line relation reflecting the well known relation for intrinsic semi-conductors:

$$\rho = A\epsilon^{+E_f/kT}$$

where E_f, the activation energy and slope of the straight line is typically 0.6 to 0.8 eV for fly-ash. With synthetic laboratory flue gas containing 4.8% H_2O and all other constituents apart from SO_3, the resistivity is of the same

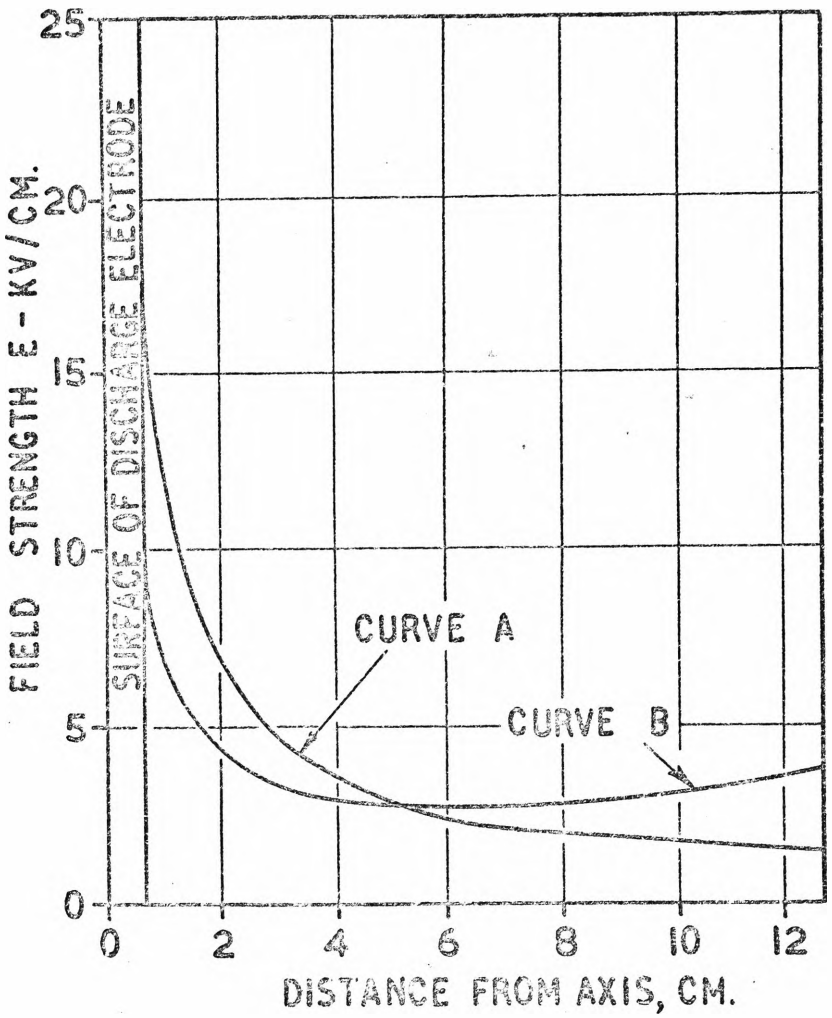

FIG. 1.14 EFFECT OF DUST BURDEN ON CORONA

(after Rose and Wood[2])

A tubular precipitator operating at 40kV without dust loading has corona current of 0.8μA/cm length.

Curve A = no dust loading

Curve B = dust loading, S = .083cm^{-1}

shape, but higher in magnitude than the in-situ test - a difference attributed to the absence of SO_3.

Efforts to cope effectively with the precipitation of high resistivity particulates, occupy a substantial proportion of many precipitator research programmes. The efforts focus on electrical conductivity of a particulate layer which is a complex function of the bulk resistivity, particle shape, degree of compaction, surface chemistry, and the presence of adsorbed gases.

We conclude this paragraph by reference to the effect on the corona current of dust burden in the gas.

A charged dust particle bheaves in much the same way in the corona field as does an ion, except that, because of its low mobility, it is quite sluggish. It therefore remains as a slowly moving cloud, able to retain considerable space charge due to the dust of:[64,65]

$$\rho' = p\varepsilon_o E\Sigma(\pi d^2/\text{vol}) \qquad \text{from eq.(1.7)}$$

placing S = surface area dust/($cm^3$of gas)
then

$$\rho' = p\varepsilon_o ES$$

and eq.2 becomes

$$\frac{d^2V}{dr^2} + \frac{1}{r}\frac{dv}{dr} + (\rho/\varepsilon_o + pES) = 0 \qquad .....(1.29)$$

The parameter S, the dust area per unit volume is readily determined from a knowledge of the dust loading in the precipitator. For a somewhat high fly-ash loading of $18g/m^3$, the surface area is $.083cm^2/cm^3$ of gas. When eq.1.29 is solved[64,65] it shows the electric field to be increased at the outside radius reaching a definite minimum near the discharge electrode. The corona current I' per unit length of discharge electrode is reduced. This situation, depicted in Fig.1.14, is commonly quite marked in

the first stage of a precipitator in the field. The specific surface area S is very much dependent upon the mean particle size, fine fume of sub-micron size having considerable capacity for storing charge as a space cloud.

Those properties of a particle enabling it to agglomerate and adhere are so important in this dissertation that they are considered in introductory fashion in the next paragraph.

1.5 Rapping and Forces of Adhesion

As noted in para.1, the final capture of a particle is complete only when it has been rapped from the receiving electrode and deposited in the hopper as an agglomerate. It is this phase of the collection process which is probably least capable of precise formulation, and which is most subject to empiricism. Knowledge is fragmentary with the picture only slowly being filled in.

In those wet-type precipitators where the receiving electrode is irrigated, final capture and removal of particles in the form of a slurry is almost 100%.

In dry-type precipitators, receiving electrodes are given blows by hammers every few minutes. Revolving hammers, electromagnetic hammers, pneumatic hammers and electromagnetic vibrators all find a place in practice. The blow must be heavy enough to overcome the various forces of adhesion to be considered in C2, but it must not be so great as to cause fragmentation of the agglomerates with dispersion of the dust back into the gas stream. The blows must not be too frequent, for insufficient dust mass will have accumulated to break the tensile strength in the layer; nor must they be too infrequent or plates, becoming excessively fouled, will suppress corona current or dust will drop off in an avalanche.

In a recent paper, Sproull[74] illustrates the almost overiding importance of rapping losses in large high efficiency plant. Apparatus designed for 99.5% efficiency was failing to meet design specifications. A search of the gas space by a special probe[67] revealed that most loss occured during rapping. By optimising, in-situ, the rapping blows in frequency, magnitude and duration, the loss Q was reduced to 10 or 15% of its former value. For such a plant, the problem is to so rap the electrodes, that some hundreds of tons of dust per hour are deposited in the hoppers

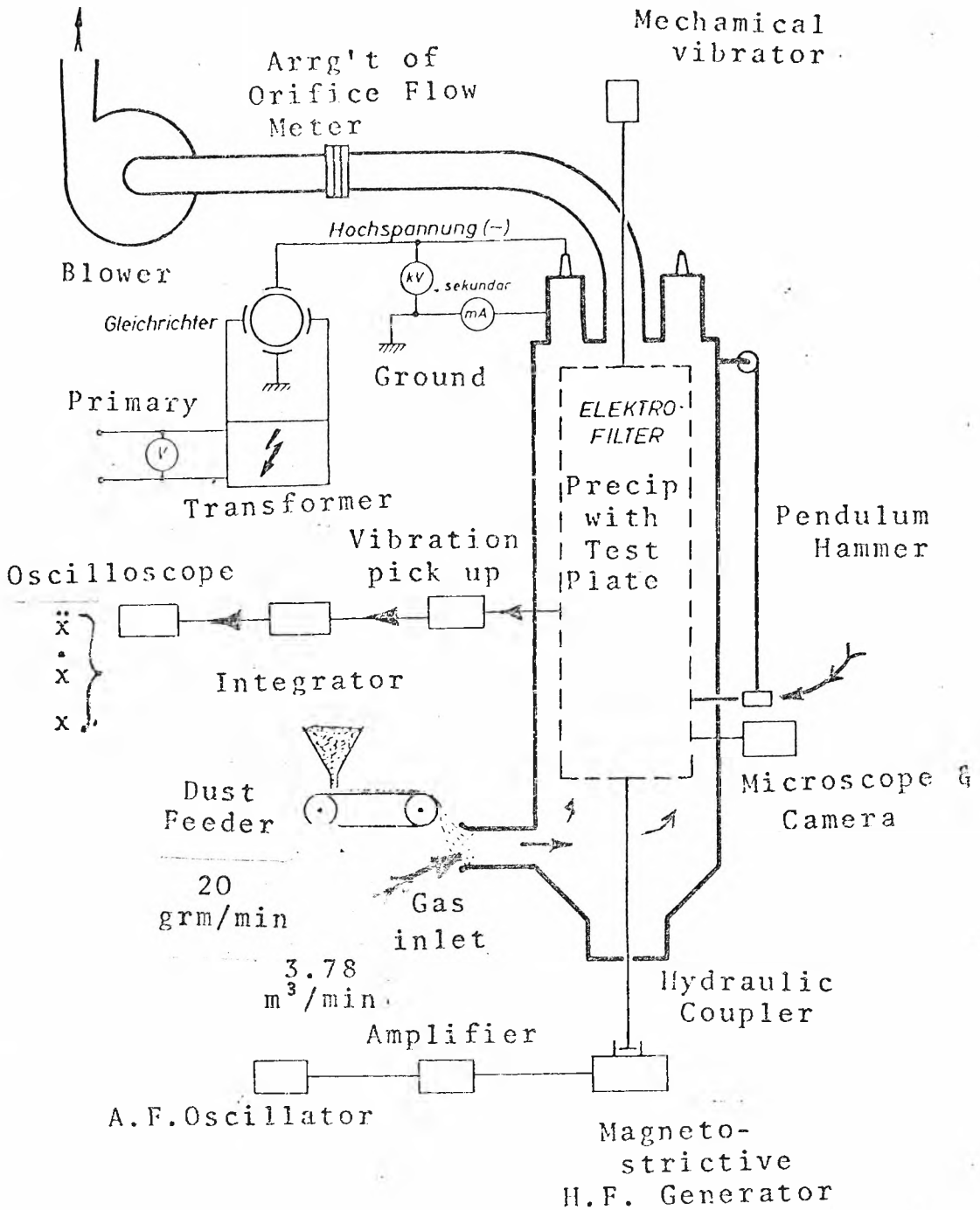

FIG. 1.15 TECHNICAL SCALE APPARATUS FOR DETERMINATION OF RAPPING CHARACTERISTICS (after Ruckelshausen[69])

with much less than ½% being re-entrained, for there will always be some loss in accordance with the Deutsch expressions.

Unquestionably then, serious losses result from inefficient rapping, while valuable dividends will be gained from proper attention to this operation.

The literature dealing with fundamental forces of agglomeration and cohesion in powders is sparse and widely scattered. It is only with painful toil that such scraps as there are may be found at all. At the other end of the scale, only a few papers have appeared dealing with rapping in precipitators at a technological level.

Plato[68] describes the work on a small precipitator in similar fashion to Sproull[74].

Watson and Blecher[50] placed 16 piezo-crystal transducers over the surface of a (2 x 4)m receiving electrode, recording the vibrations induced in (x,y,z) directions (illustrated in Fig.2.7a) for blows in the plane of the electrode of 20 and 40 foot-pounds. They found a natural oscillation frequency of about 500 Hz and maximum accelerations normal to the plate of 600g 250g and 250g going from top, middle and bottom. Excessive dust build-up severely damped down the accelerations. By observation through special windows, they concluded that a normal acceleration of at least 40g was necessary to keep these particular plates adequately clean.

Ruckelshausen[69] in collaboration with Stuttgart University conducted a long series of investigations (1952-56) on rapping and adhesion in the Lurgi laboratories at Frankfurt. Strong chemical, physical and electronic laboratory support was provided by Metallgesellschaft A.G. The effort invested in this work merits some description of it. The technical scale precipitator shown in Fig.1.15 comprised wire emitters with a plate-type receiving electrode (1 x .366)m. Two fly-

ashes were separately investigated, one with 48% carbon and of low resistivity and the other with 7.8% carbon and medium resistivity $\simeq 10^9$ ohm cm. The plates could be rapped with a hammer, vibrated mechanically or vibrated at audio-frequency via a magneto-strictive generator and hydraulic generator. Transducers registering accelerations, velocities and displacement were closely placed over the entire plate surface. Microscopic examination of dust in-situ was carried out.

Considering the degree of effort invested in this project, the results were meagre. Some information of an applied mechanics nature was obtained concerning magnitudes and modes of vibrations in the plate. Accelerations perpendicular to the plate were by far the most important in the dislodgement of dust. It was inferred that while tangential acceleration produced shearing action which did not alter forces of adhesion, normal acceleration, as soon as it produced any movement, instantly lowered adhesive forces. Vibration which was below the threshold of dislodgement, actually consolidated and strengthened the layer of dust. Large particles were frequently observed to detach first, from which it was concluded that small particles adhered more tenaciously. A useful parameter relating residual dust deposit to acceleration mode, was:

$$\int_o |\ddot{z}|dt \quad \text{to a certain minimum threshold.}$$

In vibration rapping, most dust detached in the first second.

Ruckelshausen observed an interesting phenomena concerning the electrical component of the adhesive force during rapping. For the carbonaceous dust ($\rho \simeq 10^3 \Omega$-cm) the residual dust layer was about 50% less with the power on than with the power off. With the higher resistivity ash ($\rho \simeq 10^9 \Omega$-cm), there was a 25% greater thickness of residual layer when the H.T. power was on than when it was switched off. This confirms,

quantitatively that the corona current may loosen a low resistivity deposit and strengthen a high resistivity layer. Unfortunately, no corona current densities were given.

The German workers could find no correlation using the relation: rapping efficiency = (residual dust)/(total initial dust) which is rather interesting considering that Sproull[70] used this very index as the basis of a substantial paper in 1965 (to be discussed in C2) on rapping.

The general lack of fundamental data emerging from the Ruckelshausen work is no reflection on either the worker or his supporting resources; but rather underlines the extreme difficulty of this aspect of precipitator technology. It is a pity that mixed particle populations were exclusively used rather than sieved specimens. Also, in assessing rapping efficiency in terms of the residual mass, no account appeared to be taken of the possibility that some of the mass detached was actually re-dispersed into the gas stream. Unless dust was detached in such a fashion that if fell as agglomerates, then it could be argued that the rapping mode was useless.

However, a fatal weakness in this particular study appears to be contained in some data concerning plate dust burdens, which when analysed, disclose that the depth of initial dust deposit could not have been greater than (10 to 25) μm. Such an incredibly thin dust layer could not have averaged more than two to four particles deep according to the particle sizing stated. Hence the layers were neither thick nor thin. Therefore no conclusions could be reached regarding the adhesive force of single particles, nor the tensile strength of thick layers. Perhaps it is a case of being wise by hindsight.

Ruckelshausen concludes by remarking: "The quantitative dependence of the adhesion forces on particle size as well as the physical character of the adhesion forces are at present insufficiently known."

In a major review of rapping and adhesion five years later by Brandt[71] the recognised German authority, not a great deal of new fundamental knowledge was added. Some earlier conclusions were confirmed viz; acceleration normal to the plates is the effective dislodgement parameter, small particles adhere more tenaciously than large, and vibration, the least effective of the dislodgement modes may actually compact the deposit. Brandt noted that it was often the high harmonic mode of induced vibration that was effective, rather than the fundamental. Some definite thickness of layer was needed so that the dust would fall as agglomerates when finally detached. Uneven deposits due to patches breaking loose, quickly fill in with fresh dust (akin to electropheritic painting) so that boundaries between thick and thin areas continually merge. The fundamental origins of interparticle adhesive forces were said to be: Adhesion, cohesion, electrostatic, mechanical and chemical. One could well quarrel with his table listing the order-of-magnitude estimates of the various forces. For example, electrostatic forces were calculated by assuming a particle in a layer retained its full saturation charge received in the corona field, no leakage whatever being assumed!. Such an assumption is not attractive - in any case Herceg[56] has demonstrated that no space charges exist in such a layer. Brandt rather vaguely speaks of "mechanical" forces when apparently he means London - Van der Waal forces. In conclusion, this author affirms that it is forces normal to the collecting electrode which are the important ones, but adds: "As to the magnitude of these forces in a direction perpendicular to the surface, nothing is known (about them)".

It is against such a rather sparse background of information dealing with the fundamentals of adhesion in a particulate layer that we begin Chapter 2. Even when the papers by Sproull[70], Lowe and Lucas[28] and Penney et al (to

be discussed in C2) are added, knowledge on the subject is decidedly fragmentary. Work on adhesive strength carried out by electricians with an interest in precipitation being so limited, one must search elsewhere for data. In any case, since there are so many gaps in data, one will have to develop one's own experimental techniques, a task undertaken in C3 where the writer describes his own invention, the Precipifuge.

1.6 Original Contributions in this Dissertation

Finally, then, to complete this introductory chapter, the writer summarises what he believes to be his own particular new contributions in this dissertation.

Fundamental origins of forces of adhesion are examined in some depth in C2. Research work from several different disciplines is brought together, some sort of synthesis being attempted. Some generalisations are advanced. New ground is broken in the paragraphs dealing with electrostatic forces of adhesion.

A new device, the Precipifuge, which as the name suggests is a combination centrifuge and precipitator is described in C3. It is capable, with considerable precision, of measuring the tensile strength of a layer of precipitate under most of the conditions existing in an electrostatic precipitator. Since it can operate under a high vacuum, forces related to adsorbed layers of gases may be identified.

A new transducer, the micro area boundary probe is described in C4 by which the entire current density profile J_o over a receiving electrode in a corona system may be mapped, considerable precision, even in an irregular field. The probe is also used to measure the conductivity $\bar{\sigma}$ of the ionised gas at a point on the boundary together with the boundary electric field strength E_o. By means of this device maps of E_o and J_o are produced for several important practical corona geometries.

This probe, essentially a d.c. device as presented in C4, is further developed in C5 using an a.c. diagnostic signal. It thus emerges as a device of modest elegance with obvious uses in plasma physics and electropheritic processes. A contribution to particle charging dynamics is also made here. With the micro area boundary probe as developed, several important emitter geometries are investigated in C6. Discontinuities over the anode, noticed during

development of the Precipifuge in C3 to be associated with negative corona are described in some detail in C6 as they are investigated using the micro area boundary probe together with a precision a.c. impedance bridge.

In C7, new ground is broken in the investigation of the properties of particles subject to electrostatic precipitation, by an examination of the complex permittivity as a function of temperature and frequency. A common dispersoid, fly-ash is documented over the range $20<f<50KHZ$; $20°C<T<200°C$ wherefrom it is shown that important aspects of behaviour may be anticipated.

CHAPTER 2

ORIGIN OF ADHESIVE FORCES IN A PARTICULATE LAYER

2. ORIGIN OF ADHESIVE FORCES IN A PARTICULATE LAYER

The writer left para 1.5 of C1 following a consideration of the importance of rapping in the electrostatic precipitator technology. There he endeavoured to make clear the general state of empiricism of the topic and of the need for considerable attention to fundamentals. The few published works by precipitator researchers are valuable as far as they go, but effectively speaking they leave the subject largely untouched. In this chapter, one attempts to piece together an assortment of works by powder technologists, surface chemists, pharmaceutical technologists, tribophysicists, food technologists, and various works on soil mechanics, that have a bearing on the topic.

There is no assembled body of information relating to generalised tensile forces in a powder upon which a precipitator researcher may draw.

The fairly recent statements by Brandt and Ruckelshausen who both concluded after some years of work that little or nothing was known about normal forces of adhesion, must be borne in mind.

It is, no doubt a difficult topic as the writer has found to his cost, but one well worthy of a concentrated effort. Beginning then on more familiar ground, we consider in para 2.1, a theory of electrostatic forces.

2.1 Stresses from Electric Fields

The electro-mechanical forces on a dielectric particulate layer due to electric fields will be examined, noting that they comprise two components. When the voltage on the discharge electrodes in a precipitator is raised, but below corona onset, an electric field of about 3 kV/cm appears at the receiving electrode. Above onset, the corona currents flowing through the particulate layer to the electrode underneath cause a further average voltage gradient, which in the case of high resistivity materials may typically

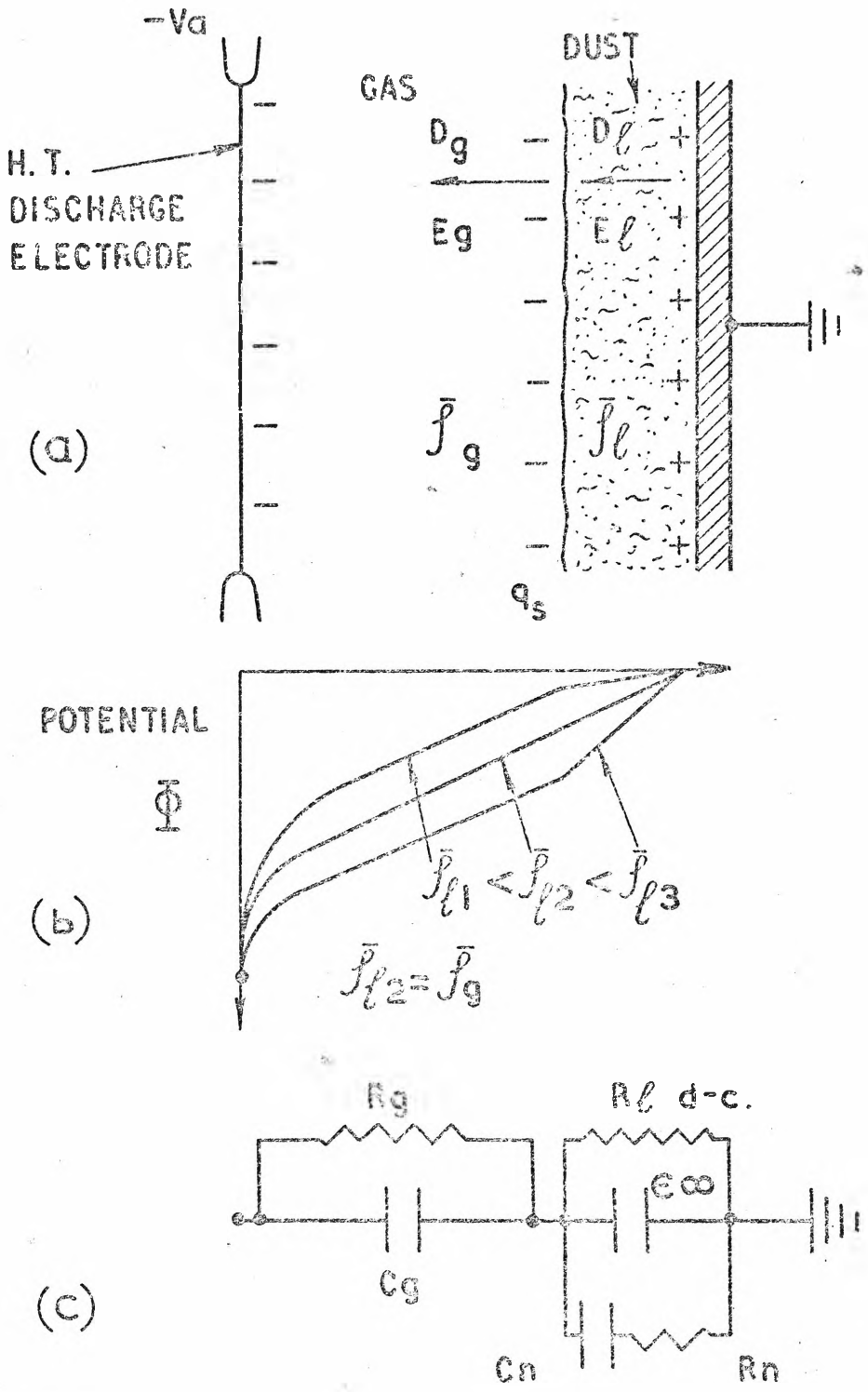

FIG. 2.1 ELECTRIC FIELDS AT THE DUST/GAS INTERFACE

(a) At the dust interface there are changes in electric field due to surface charges and also to differing resistivities.

(b) The electric field $\nabla\bar{\Phi}$ is the same in the two phases only for equal resistivities.

(c) Nominal equivalent circuit showing that resistivities determine d.c. gradients while capacitances determine a.c. gradient.

amount to 5 kV/cm or more.

Components of force on the dielectric from these electric fields may be calculated by classical methods. In the para 2.1.1 we shall consider the dielectric to be homogeneous. In para 2.1.4 the dielectric will be regarded as composed of a regular array of spheres. The consequences of the microscopic model will be compared with those following the macroscopic model.

2.1.1 Forces at the boundary of two homogeneous Dielectrics

The situation existing in the electrostatic precipitator is shown in Fig.2.1a where:

E_ℓ = electric field in the dispersoid layer
ε_ℓ = relative permittivity of the composite dispersoid (solid + voids)
E_g = electric field in the gas at the interface
$\bar{\rho}_\ell$ = resistivity of the composite dispersoid
$\bar{\rho}_g$ = resistivity of the gas at the interface
q_s = surface charge density at the interface
J = current density common to gas and dispersoid.

Then considering the action at the interface, the adhesive pressure tending to hold the dispersoid to the plate is (see appendix 2.1):

$$P = \frac{\varepsilon_o}{2} (\varepsilon_\ell E_\ell^2 - E_g^2) \quad N/m^2 \qquad .....(2.1)$$

since the real part of the gas relative permittivity is 1.

Due to the interstices, $\varepsilon_\ell <$ (ε for solid material).

The current density at the interface being continuous, there is also:

$$E_\ell = \bar{\rho}_\ell J \quad \text{and} \quad E_g = \bar{\rho}_g J$$

$$\text{hence} \quad P = \frac{\varepsilon_o}{2} (\varepsilon_\ell (J\bar{\rho}_\ell)^2 - (J\bar{\rho}_g)^2) \qquad .....(2.2)$$

By application of Gauss' Law at the interface, a surface charge must be present:

$$+q_s = (D_g - D_\ell) = (\varepsilon_o E_g - \varepsilon_o \varepsilon_\ell E_\ell)$$

$$= \varepsilon_o J(\bar{\rho}_g - \varepsilon_\ell \bar{\rho}_\ell) \qquad \ldots\ldots(2.3)$$

The surface charge is positive for dispersoids of low resistivity, becoming zero and then negative with increasing resistivity.

Equations 2.1 with 2.2, indicating that a high-resistivity deposit on a receiving electrode should adhere more tenaciously with the HT corona switched on, has been commonly reported from practice[69,70] and already noted in para.1.5.

Examples of Adhesive and Repulsive Pressure

	Case 1	Case 2	Case 3
E_g kv/cm	5	5	5
ε_ℓ	4	4	4
J $\mu A\ cm^{-2}$	.05	.05	.05
$\bar{\rho}_g$ ohm cm	10^{+11}	10^{+11}	10^{+11}
$\bar{\rho}_\ell$ ohm cm	10^{+9}	5×10^{10}	5×10^{11}
P grm wt/cm^{+2}	-.011	0	+1.1
P N/m^{+2}	-1.1		+110

Consider, by means of examples, the transition from repulsive to attractive pressures on the dispersoid as the resistivity is progressively increased. Typical value for J, ε_ℓ and E_g and $\bar{\rho}_g$ are chosen in the following table: In case 1, the pressure P tends to detach the dust, in case 2 the pressure is zero and in case 3 the dust is attracted to the receiving electrode. Ruckelshausen[69]

has noted, without explanation, this change from repulsion to attraction*. Also the presence of the negative surface charges ($-q_s$) has been frequently observed, slowly leaking to earth after the HT is switched off and retaining the implicit adhesive forces for several seconds.

The sort of potential distribution expected in the precipitator between the H.T. and L.T. electrodes is shown in Fig.2.1b for each of the three cases considered above. The voltage gradient in the gas and dielectric layer will be the same only if $\bar{\rho}_g = \bar{\rho}_\ell$.

Two other workers have applied themselves to this problem. Lowe and Lucas[28] by intuitive reasoning rather than exact analysis put forward an expression for the pressure of:

$$P = + (cEi\rho - \frac{E^2}{32}) \text{ CGS}$$

without defining c or E nor including ε_ℓ. In spite of the inadequacies of the expression, they did appreciate that for a low resistivity material, the force could become negative.

Penney and Klingler[81] advance the expression

$$P = + \tfrac{1}{2}\varepsilon_o[(\frac{J\rho\varepsilon\ell}{\varepsilon_o})^2 - E^2] \quad \text{mks}$$

which unfortunately seems to contain printing errors since it is incorrect dimensionally. They probably intended

$$P = + \varepsilon_o/2[(J\rho\varepsilon\ell)^2 - E^2]$$

---

* The recent paper: Dalmon, J and Tidy, D.: "The cohesive properties of fly ash in electrostatic precipitation", Atmospheric Environment, 1972, Vol. 6, pp.81-92 arrived too late for detailed consideration. They found adhesion of high resistivity particles to be doubled with corona currents flowing.

but do not describe any experimental evidence for or against it.

The writer believes that his expression eq.2.2 is the correct one for a homogeneous layer rather than that given by Lowe & Lucas or Penney & Klingler.

2.1.2 Transient Behaviour - Equivalent Circuit

At the present time, for the author and his colleagues, there is special interest in the A.C. pulse energisation of precipitators as a means of overcoming the problems of back-corona mentioned in para 1.4. While it is not in the scope of this dissertation to discuss pulse energisation, it is of interest to draw an approximate equivalent circuit which may be needed for A.C. studies. Such a circuit, shown in Fig.2.1c consists of the gas and particulate phases in series. The particulate is represented by a capacitance with permittivity ε_∞ paralleled by the d.c. resistivity $\bar{\rho}_\ell$, and by the Debye absorption time constants $(R_1 C_1)...(R_n C_n)$ considered in greater detail in C7. The dynamic constants in the gas phase are the subject of a study, separate from this dissertation.

Under steady-state conditions, it is the R_ℓ (d.c.) parameter that dominates behaviour in the dielectric layer. Under transient conditions, the time constants $(R_n C_n)$ some of which are very long, dominate behaviour.

2.1.3 Key Electrical Parameters in Adhesion Studies

From Eqns. 2.1 and 2.2 it is clear that the key parameters determining adhesion are ε_ℓ, $\bar{\rho}_\ell$, $\bar{\rho}_g$ and J. Considerable attention has been paid by investigators to $\bar{\rho}_\ell$, the d.c. resistivity of a dispersoid, as a function of temperature, compaction, gaseous environment, as already noted in para 1.4. The writer's colleague McLean[78] has recently surveyed the literature relating to d.c. resistivity, making a number of contributions himself. The writer, with

colleagues McLean and Herceg have recently patented and developed a new apparatus[76] for measuring $\bar{\rho}_\ell$, outside a precipitator, in the laboratory and in the field.

The current density J is measured in a macroscopic fashion in practice by dividing the total H.T. bus current by the total collecting plate surface area. This is a coarse parameter, as J varies widely over the collecting electrodes. In this dissertation, in C4, a new method for measuring J at a point in an active precipitator, is described.

The parameter ε_ℓ is hitherto an almost completely unknown quantity. Little has been written by the physical chemists or others on the dielectric properties of powders. Nothing at all appears to have been written about industrial dispersoids. A vigorous start has been made in C7, where

$$\varepsilon(\omega) = \varepsilon'(\omega) - j\varepsilon''(\omega)$$

for fly-ash over a range of conditions, is described.

The conductivity $\frac{1}{\bar{\rho}_g} = (neK)$ of the gas in a precipitator has been a rather neglected parameter in the past. Not only is it important in the relation $E_g = \bar{\rho}_g J$ insofar as this affects the present discussion on forces of adhesion; but also in regard to particle charging as already noted in para 1.2. In this dissertation, a new means of measuring $\bar{\rho}_g$ directly on a clean precipitator plate under full corona conditions is described in C5.

2.1.4 Electrical Forces of Adhesion - A Microscopic View

In para 2.1.1 equations were derived describing electrical pressures on a macroscopic dielectric. We now turn to the more onerous task of examining the stresses in a model consisting of spherical particles in regular cubic array.

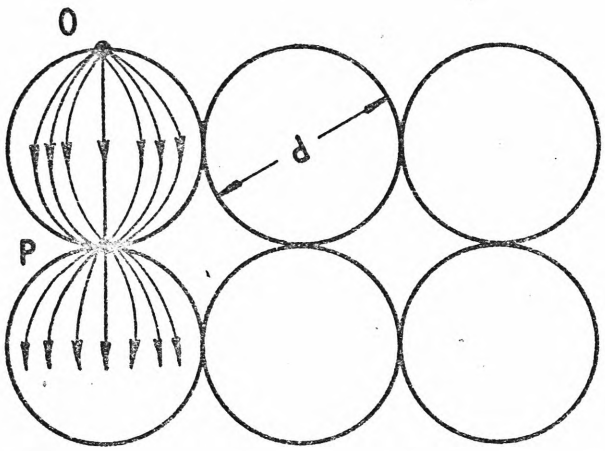

(a) REGULAR SPHERES IN CONTACT

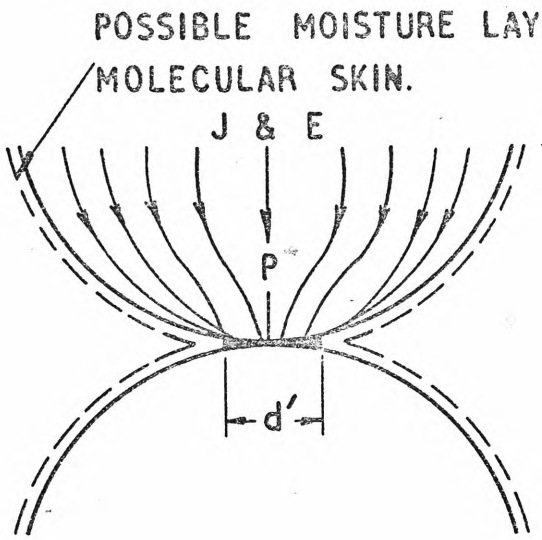

(b) CONTACT POINT

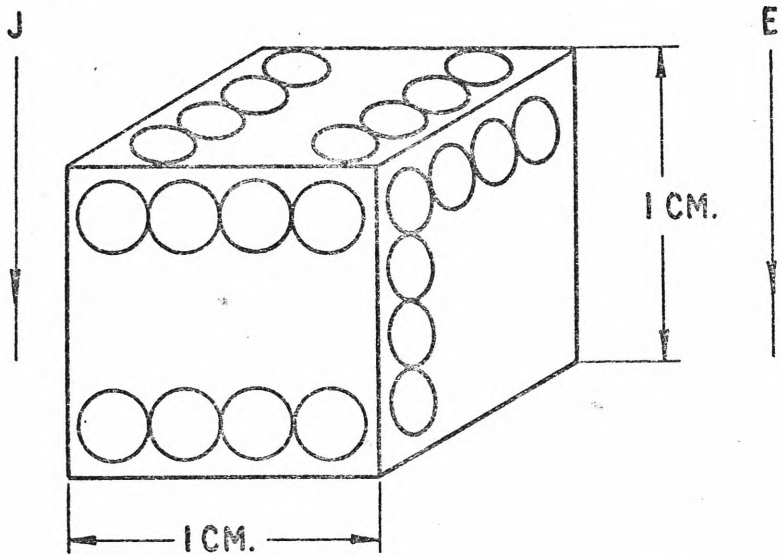

(c) A UNIT CUBE OF PARTICULATE

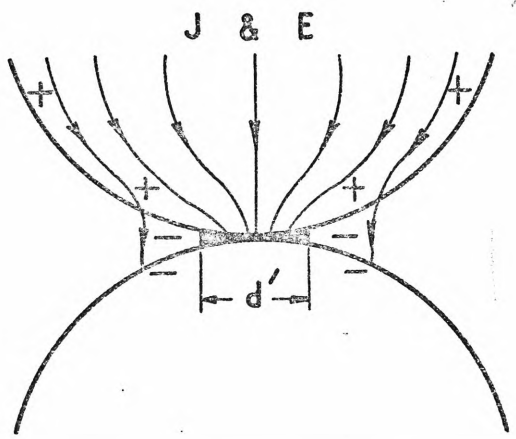

(d) SCHOTTKY FIELD EMISSION ACROSS SMALL GAPS

CONDUCTION IN DISPERSOIDS FIG. 2·2

The electrical fields present in a regular array of spherical particles are depicted in Fig.2.2 McLean[73], by extending the work on electrical point contacts by Holm, has solved the field configurations sufficiently to enable conclusions on resistivity to be made. By a further extension of McLean's work, the writer is able to show that mechanical stress intensification occurs.

As illustrated by Fig.2.2a and 2.2b, most of the resistance of spheres occurs at the point of contact, the diameter of contact being designated as d'.

Since (d/d') is found in practice[73] to be in the range 100 to 1000, in the region of the contact, it is sufficiently accurate to show the surfaces to be flat, vide Fig.2.3. The resistance per contact is shown by Holm-McLean-Masuda to be:

$$R' = (\bar{\rho}_i/d')\ \Omega \qquad .....(2.4)$$

$\bar{\rho}_i$ being the intrinsic resistivity of the dielectric material. By consideration of elastic deformation (following elastic principles by Hertz) at the point of contact, it may be shown[73] that (d/d') is independent of particle size for constant mechanical pressure on the system. In fact $(d'/d) = K \sqrt[3]{P}$ where K is a constant involving Young's modulus for the particle material and the mode of packing, and where P is the mechanical pressure on the particle system, Nm^{-2}. Hence, the total resistance of a cube of material (Fig.2.2c) which contains (1/d) particles in series and $(1/d^2)$ in parallel is:

$$\bar{\rho} = (\bar{\rho}_i/d')(1/d)(d^2) = \bar{\rho}_i(d/d')\ \Omega\text{-cm}$$

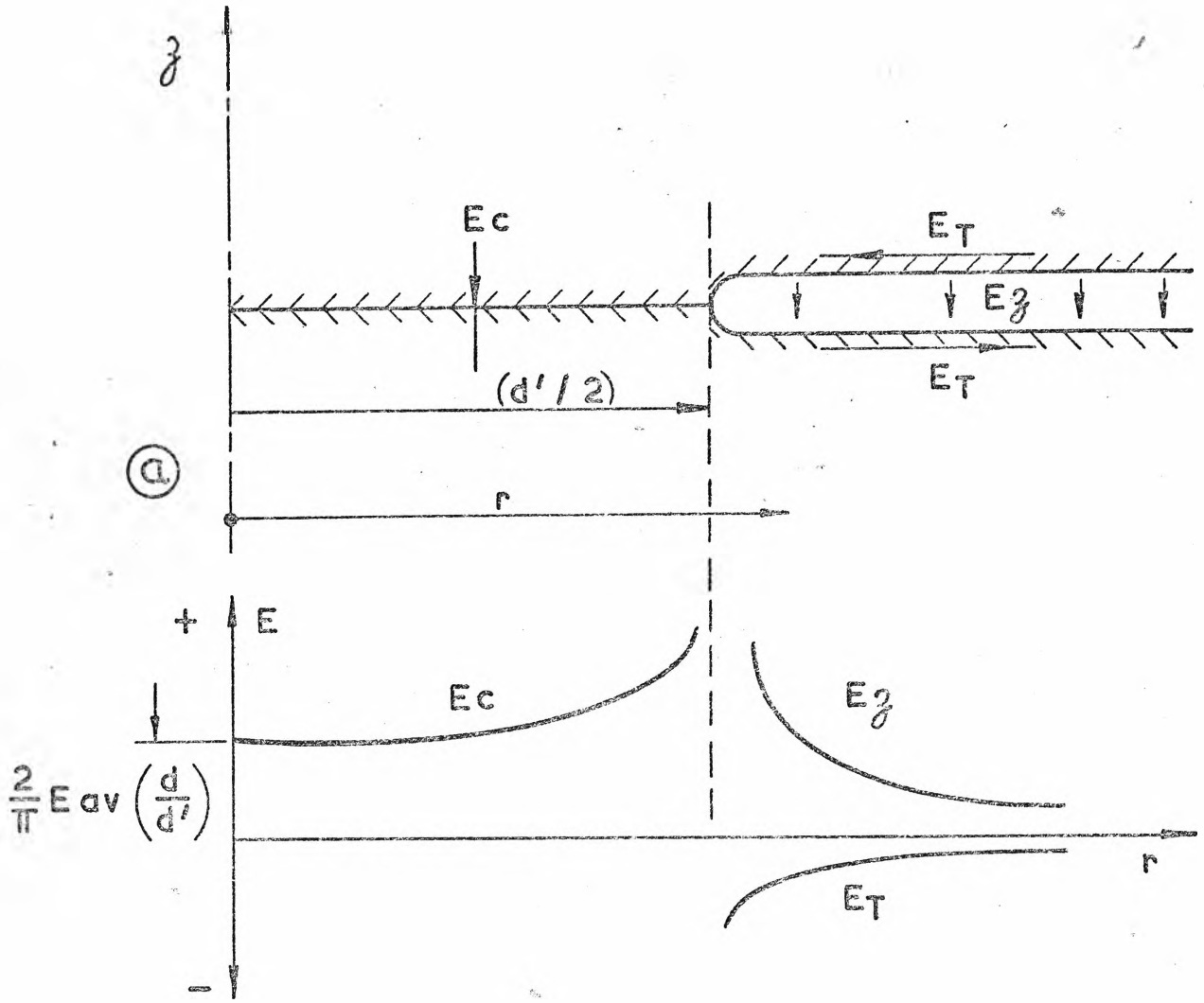

FIG. 2.3 TWO SPHERES IN CONTACT

Due to current conduction, the three electric fields are E_c(contact) E_z(gap) and E_τ (tangential)

By these and other considerations, McLean finds the electric fields in the spheres and around the area of contact, to be as depicted in Fig.2.3.

E_c in the z direction over the contact area is:

$$E_c = \frac{(2/\pi)E_{av}(d/d')}{\sqrt{1 - (2r/d')^2}} \qquad .....(2.5)$$

The tangential stress E_τ over the surface of the particle is:

$$E_\tau = \frac{(2/\pi)E_{av}\ (d/d')}{(2r/d')\sqrt{(2r/d')^2-1}} \qquad .....(2.6)$$

while the stress in the air gap is:

$$E_z = (4/\pi)E_{av}(d/d')^2\ \frac{\arctan\sqrt{(2r/d')^2-1}}{(2r/d')^2-1} \qquad .....(2.7)$$

This field in the gap, E_z, caused by surface current filaments on opposite particle surfaces, may be exceedingly high since the magnification factor (d/d') appears squared.

The value E_{av}, the average electric field is (v/ℓ) obtained by applying a voltage V across a mass of particles separated by ℓ. Then the element of potential appearing across one particle is

$$\Delta V = E_{av}\ d$$

Unfortunately, the fields all tend to infinity at the point of singularity r = (d'/2). This did not prevent valid conclusions in resistance calculations being drawn from eqns. 2.4, 2.5, 2.6 and 2.7. The field magnification occuring may be typified by:

$$E_c\Big|_{r=0} = (2/\pi)(d/d')\ E_{av}$$

For E_{av} = 1 kV/cm and (d/d') = 1000 then $E_c \simeq$ 1 MV/cm. This is approaching the intrinsic electrical strength of pure ceramics, and in any case is certainly high enough to cause the non-linear relation between E and J discussed by Frohlich[77], and frequently measured (para 1.3.). The term (d/d') emerges in all equations as the field magnification factor.

The writer now begins his own analysis of forces as follows.

The mechanical compression across a particle is now determined by:

$$\Delta F = \int P dA = \int \tfrac{1}{2}\varepsilon_o \varepsilon_r E^2 dA$$

with appropriate limits.

Over the contact area the attractive force is, from eq.2.5:

$$\Delta F_c = +\tfrac{1}{2}\varepsilon_r \varepsilon_o \int_o^{d'/2} \frac{(2/\pi)^2 (E_{av} d/d')^2 (2\pi r)\, dr}{1-(2r/d')^2} \quad \ldots\ldots (2.8)$$

putting u = (2r/d'),

$$\Delta F_c = +\tfrac{1}{2}\varepsilon_o \varepsilon_r E_{av}{}^2 d^2\ \frac{1}{\pi} \int_o^1 \frac{-2u}{(1-u^2)}\ du \quad \ldots\ldots (2.9)$$

Though the integration is obvious the integral at the limit as u → 1 tends to infinity. This point will be taken up presently.

As noted in appendix 2.1, lateral pressure between tubes of force leads to a repulsive force from the tangential field E_τ in the z direction of:

putting u = (d'/2r)

$$\Delta F_\tau = -\tfrac{1}{2}\varepsilon_o\varepsilon_r \int_{d'/2}^{\infty} (2/\pi)^2 \frac{(E_{av}d/d')^2(2\pi r)}{(2r/d')^2((2r/d')^2-1)}\, dr \qquad .....(2.10)$$

$$\Delta F_\tau = -\tfrac{1}{2}\varepsilon_o\varepsilon_r E_{av}{}^2 d^2 \frac{1}{\pi} \int_0^1 \frac{-u}{(1-u^2)}\, du \qquad .....(2.11)$$

Obviously taking the limit to ∞ cannot be correct; but since the force falls off rapidly with (2r/d'), the approximation is probably within the region of accuracy of the Holm-McLean equations anyway.

The two integrals are now of the same form, but both diverge at the singularity (2r/d') = (d'/2r) = 1. There appears to be no mathematical artifice which can circumvent the difficulty, so we are lead to seek possible refinements in the physical model. An examination, (to be carried out presently) of the exceedingly high fields E_z in the air gap discloses probable electron field emission at $1 < (2r/d') < 1.03$. In order to obtain some idea of the integral under consideration, we therefore place the upper limit u = 0.97 being the point where electronic emission will probably contribute to conductivity in the model and so to mitigate the singularity.

Algebraically adding the two forces given by eqn.2.9 and 2.11, putting $\varepsilon_r = 6$ (being typical of the solids comprising fly-ash) and placing the upper limit to 0.97;

$$\Delta F_z = (\Delta F_c - \Delta F_\tau) \doteq + \frac{1}{3\pi} \varepsilon_o 6 E_{av}{}^2 d^2 N \qquad .....(2.12)$$

Across a unit square area there will be $(1/d^2)$ particles as illustrated in Fig.2.2c, therefore the pressure is:

$$P_z = (\Delta F/d^2) \doteq \frac{1}{3\pi}\,\varepsilon_o 6E_{av}^2 \quad N/m^2 \qquad .....(2.13)$$

Comparison of this relation with the classical macroscopic relation (in which the composite air/solid dielectric constant for fly-ash is ≃ 3) is illuminating, for:

$$((1/3\pi)\varepsilon_o 6E_{av}^2)/(\tfrac{1}{2}\varepsilon_o 3E_{av}^2) = (4/3\pi)$$

It is a matter for considerable reflection that the ratio is in the region of unity.

Turning now to the forces caused by E_z, the fields across the small air gap, it becomes obvious that we are dealing with an effect on order of magnitude greater than that expressed by eqn.2.13, viz, in

$$\Delta F_z = \int (\tfrac{1}{2}\varepsilon_o \varepsilon_r E_z^2)\, dA$$

Substitute the value for E_z from eq.2.7, put $\varepsilon_r = 1$

and $$u = \sqrt{(2r/d')^2 - 1}$$

and there results:

$$\Delta F_z = +\tfrac{1}{2}\varepsilon_o (d/d')^2\, d^2\, E_{av}^2 (8/\pi) \int_o^\infty \left(\frac{\arctan u}{u^2}\right)^2 du$$

from which the pressure is:

$$P = (F_{gz}/d^2) = +\tfrac{1}{2}\varepsilon_o E_{av}^2 (d/d')^2 (8/\pi) \int_o^\infty \left(\frac{\arctan u}{u^2}\right)^2 du \qquad .....(2.14)$$

Again the integral diverges at the singularity $2r/d' = 1$ or $u = 0$.

By a consideration of the intense stress in the air gap near the singularity, we set the vertical field at which electronic emission from the surface will take place as being in the order of 1 MV/cm. For a value of $(d/d') = 100$ and $E_{av} = 1$ KV/cm we find the critical stress is reached at $u \simeq 4$.

An approximate calculation of the integral taken from $u \simeq 4$ results in finally:

$$P = \tfrac{1}{2}\epsilon_o E_{av}^2 \, (d/5.5d')^2 \quad N/m^2 \qquad .....(2.15)$$

Comparison with the classical equation shows that there is a stress magnification factor of $(d/k\,d')$, predicting much greater adhesive forces.

A full treatment of electronic field-enhanced emission across the gap between articles would require a whole dissertation in its own right. McLean in his work on the resistivity of regular arrays of dielectric spheres, found substantial experimental evidence that field emission does occur, as shown in Fig.2.2d. On theoretical grounds, temperature - corrected Fowler-Nordheim[78] emission is entirely plausible. The gaps between particles are less than molecular mfp in gases at NTP, so that electronic emission could take place with little likelihood of collision. Unfortunately, very little has been written about emission from dielectrics. If the Lyman[79] et al criteria for electrical breakdown in high vacuum small gaps for metallic electrodes could be translated to dielectrics, then breakdown, proportional to the field strength, would occur at about 1 MV/cm.

Finally, we conclude that adhesion within a layer is of the form:

$$P = \tfrac{1}{2}\epsilon_o E_{av}^2 (d/kd')^2 \qquad .....(2.16)$$

which always dominates over that given by 2.13. The

magnification factor (d/kd') remains to be determined accurately but may be of the order of 20. The total force acting on a layer is therefore found by combining eq.2.16 and eq.2.1 as:

$$P = (\varepsilon_o/2)((E_\ell \frac{d}{kd'})^2 - E_g^2) \qquad .....(2.17)$$

since $E_{av} = E_\ell$

This completes our analysis of the pressures in a dispersoid layer subject to an electric field and current conduction. The two new relations proposed for adhesive pressure, viz eq.2.1 and eq.2.17, (the latter being preferred) contain ample material for laboratory investigation.

A major part of this dissertation, C3, describes the design and construction of a unique device - the Precipifuge - to carry out this type of measurement.

2.2 London/Van der Waal Forces

London-Van der Waal forces of adhesion being intermolecular in character, are effective only over very short distances. They act between the molecules of surfaces in contact, being of the same type as those involved in the tensile strength of materials or in surface tension of liquids. Such forces are also believed to be responsible for the tenacious way in which small particles adhere to a clean substrate. Severe rapping fails to remove small particles. Van der Waal forces are mainly instrumental in holding aggregates of gaseous borne particles together. An important review of such forces on single particles has been made by Krupp[80].

2.2.1 Van der Waal forces on a single particle

By integrating the attractive force due to electromagnetic fluctuation phenomena between a pair of molecules,

$$F = \lambda/r^7$$

over two solid spheres, Bradley[83] and Hamaker[84] showed the nett force of attraction to be:

$$\Delta F = (\pi^2 \lambda n^2)/(24 Z_o^2)(d_1 d_2)/(d_1\ d_2) \text{ dyne} \quad .....(2.18)$$

in which λ is a constant of the force law, n the number of molecules/c.c., d_1 and d_2 the respective sphere diameters, and Z_o the separation. The force constant λ is known for very few materials, and can be calculated with great difficulty only for simple molecules under restricted conditions. Unfortunately Z_o is somewhat indeterminate since it cannot be measured directly. It must be greater than a molecular diameter since chemical bonding is not

considered. The best estimate available at the present time is that of Krupp and Sperling[85] who consider:

$$Z_o = 4\text{Å} \pm 30\%$$

For a sphere in contact with a large sphere (plane), eq.2.18 becomes:

$$\Delta F = \frac{\pi^2 \lambda n^2}{24 Z_o^2} d \quad \text{dyne} \qquad .....(2.19)$$

$$\text{or} \quad \Delta F = Ad \quad \text{dyne} \qquad .....(2.20)$$

Using the new and more general theory of Landau and Lifshitz[72,82] Krupp and Sperling[85] show that eq.2.19 may also be derived as:

$$F = \frac{h\bar{\omega}}{16\pi Z_o^2} \cdot d \quad \text{dyne} \qquad .....(2.21)$$

where the constant $(h\bar{\omega})$ may be evaluated, as outlined in appendix 2.2, in terms of the imaginary part $\varepsilon''(\omega)$ of the complex dielectric constant of the materials in contact. Krupp and Sperling calculate $(h\bar{\omega})$ from such data for ε'' as is shown in the sketch for the several pure materials noted in Table 2.1.

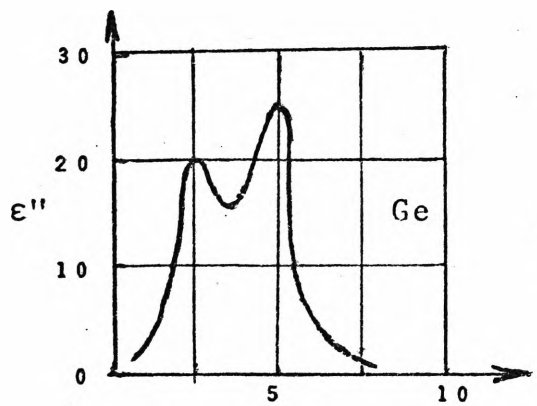

Table 2.1

Materials of Adherents	$(h\bar{\omega})$ ev
Graphite/graphite	7.2
S_i/S_i	7.2
Diamond/Diamond	7.8

For Si/Si and putting $Z_o = 4\text{Å}$, eq. 2.21 becomes:

$$\Delta F = 150\ d \qquad .....(2.22)$$

which as we shall see later is in the right order of magnitude.

To develop eq.2.21 to apply to industrial dispersoids would be attractive; but is frustrated by the total lack of knowledge of the dielectric constant of industrial dispersoids. These are mostly heterogeneous metallic oxides which in powder form have simply not been documented.

A start on the systematic determination over a limited frequency range of:

$$\varepsilon(\omega) = \varepsilon'(\omega) - j\varepsilon''(\omega)$$

for fly-ash has been made by the author and is described in C7.

Though the elegant macroscopic theory by Lifshitz has much to commend it, the inherent disadvantage is that it cannot account for the Born repulsion of molecules in close approach. At a 4Å separation, this could amount to 30%. The older microscopic theory of the Leondard-Jones potential as expounded by Bradley/Hamaker can account for Born repulsion.

Lowe and Lucas[28] sidestep many of the difficulties inherent in the application of eq.2.18 or 2.21, by semi-intuitive use of the tensile strength U of the materials in contact. They reason that, from elementary geometry, two spheres in contact have an opposing area where the molecules are within a distance Z_o of each other of:

$$\text{area} = \pi Z_o d_1 d_2/(d_1+d_2) \qquad .....(2.23)$$

the situation being depicted in the adjacent sketch.

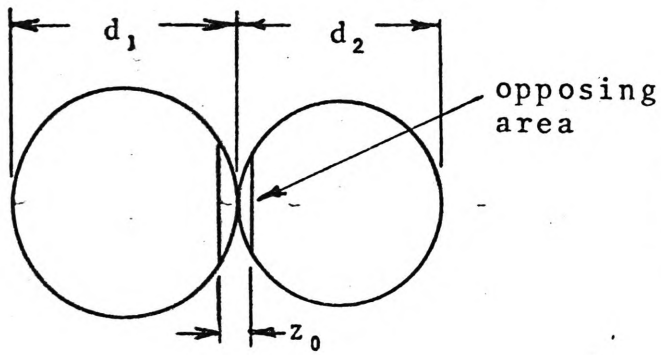

opposing area within Z_o

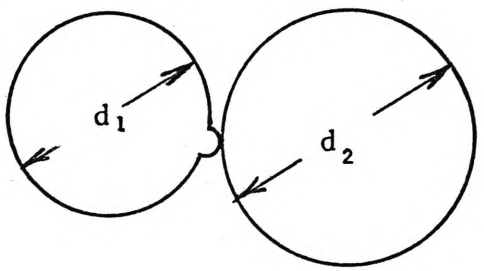

effect of asperite

They suppose the pressure across the area to be much the same as the tensile strength of the material, then:

$$\Delta F = Z_o \pi U d_1 d_2/(d_1+d_2) \quad \text{dyne} \qquad .....(2.24)$$

which is of the same form as the Bradley-Hamaker relation, eq.2.18.

Insertion of $U = 10^{10}$ dynes/cm^2 for quartz fibres - an extremely strong substance - and $Z_o = 1\text{Å}$, leads to the relation:

$$F = 314\ d \quad \text{dyne} \qquad .....(2.25)$$

so that by comparison with eq.2.20, A = 314. This may be compared with Bradley's test figures of A = 212 for quartz spheres. Allowing that the separation Z_o of 1Å used by Lowe and Lucas must be a factor of 4 too low, their force is an order of magnitude too high. It is unattractive, however, to attempt to carry this approach further, at least because of the difficulty of determining the tensile strength U of tiny, irregular, inhomogenous particles. In any case Van der Waal forces cannot be equated with tensile strength.

Both Krupp*and Lowe & Lucas rightly point out that a real particle of nominal size of say 100μm, might make contact at a point on its surface, as indicated in the above sketch, which has an irregularity of say 1μm dia. The actual force of adhesion of any particle, corresponding to its curvature at the contact, must always be less than that suggested by its overall size.

Krupp**further extended the theory of interparticle adhesion by considering both elastic and non-elastic deformation of particles at the point of contact. In this he appealed to the same elasticity principles associated with Hertz, that Holm/McLean used as discussed in para.2.1.4. The result of such deformation is to give the particles a finite area where they are parallel to each other. Creep causes a further increase in force with time.

We turn now to a brief examination of some experimental evidence available.

Bradley[83] found A for quartz spheres to be 212 within the range $.4<d<1$ mm. He constructed a micro-balance comprising a spiral spring whose deflection could be observed with a travelling microscope. The point at which detachment occured between the suspended quartz spheres and a similar substrate, indicated the adhesive force. Close correlation with theory and experiment was obtained. The presence of a perfect gas had no effect on the results, but water vapour increased the attraction.

Beischer[86] found A to be around 3 for iron oxide particles of 0.5μm. Such a constant includes, of course, some unknown value of Z_o. Presumably for a set of particles of given roughness, the A is a valid constant.

Boehme[87]et al used a Spinco Ultra Centrifuge in a long series of carefully conducted experiments to determine the

---

* ibid P.199 **ibid P.182

adhesion of single particles. They photographed the particles which had been gently dusted onto the substrate in the centrifuge head before indexing the speed to a set value. On stopping the machine they re-photographed the same area, counting and measuring the single particles dislodged. The results of several thousand individual measurements on iron oxide spheres $2<d<4\mu m$ are illustrated in Fig.2.4. Examination of the cumulative and frequency distribution curves of this figure discloses:

(i) wide span of forces of adhesion for a particle of single size

(ii) that quite closely, $\Delta F = Ad$

(iii) the most probable value of A for 4μm oxidised/reduced particles is 6.

Electron micrographs of the particles revealed a wrinkled surface, which very likely explains the scatter in the results of Fig.2.4. The results of Beischer and Boehme et al corroborate.

Concluding this paragraph, we find that, by two theories, Van der Waal force of attraction between a pair of particles is given by:

$$\Delta F = Ad \quad \text{dyne}$$

The constant A depends upon the materials, the surface condition and the roughness. The relation has been verified experimentally for single particles of quartz, iron oxide, and reduced iron oxide.

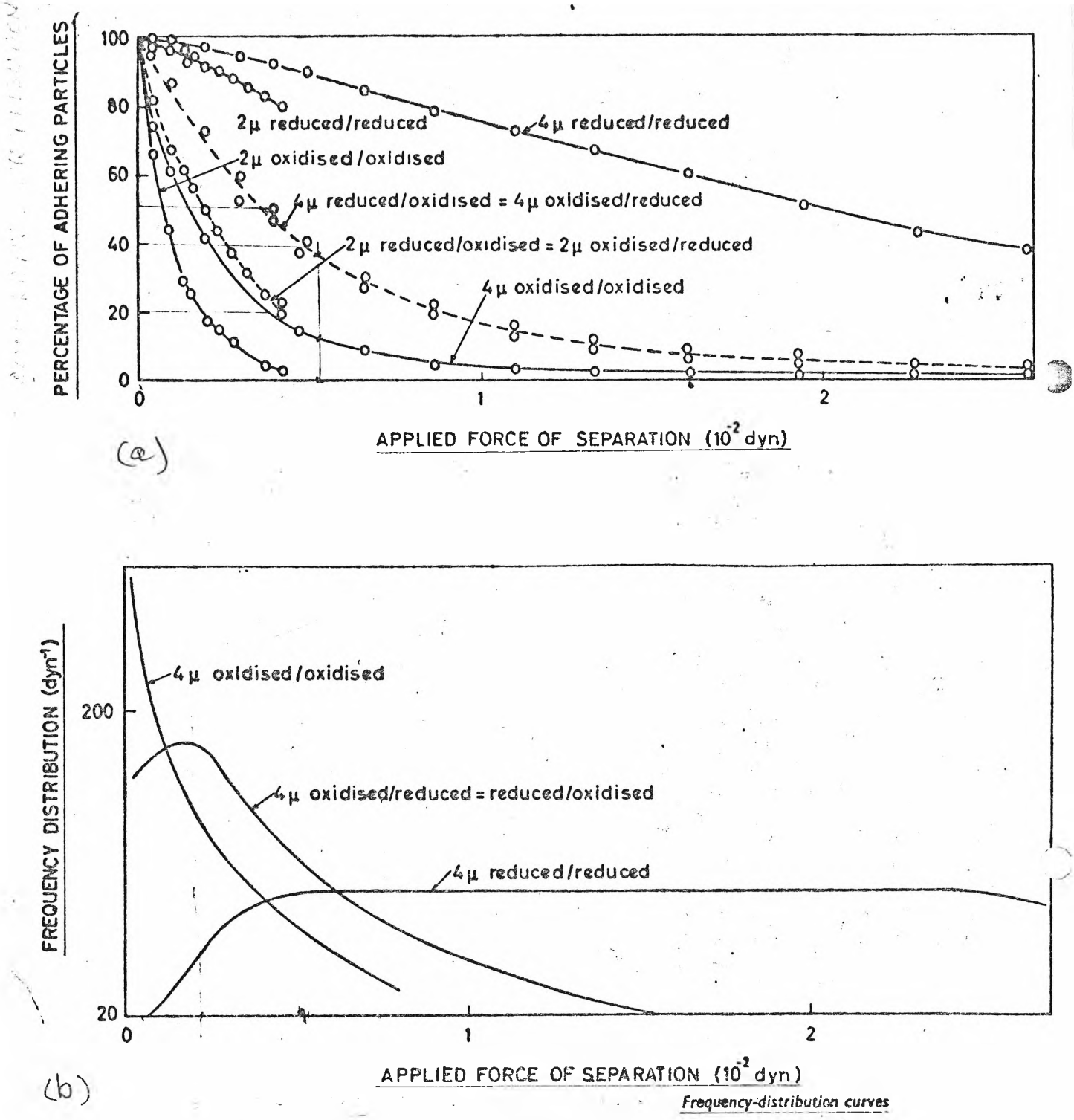

FIG. 2.4 ADHESION OF IRON OXIDE PARTICLES TO SUBSTRATES (after Boehme, Krupp, Rabinhorst and Sandstede[87])

Small iron oxide spheres adhering to a substrate, are detached in a centrifuge.
(a) Cumulative distribution (b) Derived frequency distribution

2.2.2 Tribo-Electrostatic Forces

Two solids in contact generally charge each other electrostatically. Contact potential differences of up to say 0.5V result in a transfer of charge, equilibrium being reached when currents in the two interacting solids become equal. If the solids are separated fairly quickly, then each receive a charge. This well known phenomenon has had several recent reviews, e.g. Loeb* (1958)

These so-called tribo-electrostatic charges are known to be the cause of the charge in clouds of aerosols, sometimes causing explosions in industrial situations. In the present discussion, the Russian school[95] has particularly emphasised the importance of such electrostatic double-layers in causing forces of adhesion. Calculation of charge distribution is of extreme difficulty even in simple cases. The subsequent calculation of force based upon the equation:

$$P = \frac{\sigma^2}{2\varepsilon_{ro}\varepsilon}$$

and the model of Fig.2.2 is more straightforward. The few results to hand indicate that Van der Waal pressures would generally predominate.

Some results reported** appear to be quite strange; e.g. a 2.5μm particle was said to have a total charge of 5000 electrons. If such tribo induced charges were other than very rare, they would have been observed long ago by precipitator investigators. Since such a charge is two times that which could be produced under favourable conditions in a corona field in a precipitator (see Table 1.2.2), drift velocities two times normal would have been observed.

---

* LOEB, L.B.: "Static Electrification", Springer, Berlin, 1958.

** Krupp, ibid p.166

Assuredly they have not.

The matter of tribo-induced electrostatic pressures is far from settled, and judging by the literature, will remain so for a long time to come.

2.2.3 Tenacity of Attachment of a Single Particle

It is now instructive to determine the order of magnitude of Van der Waal forces, comparing them with electrostatic forces, forces due to impact and forces due to aerodynamic drag.

Consider a simple air-borne aggregate consisting of two quartz particles of diameter dμm and separation z_oμm. Using the Bradley data;

$$\Delta F_{vdw} = \frac{212}{2} 10^{-4} d \simeq 1 \times 10^{-2} d \text{ dyne}$$

Supposing two 1μm particles by lucky chance receive maximum charges, of opposite signs due to exposure to a back corona field; then from table 1.2.2:

$$\Delta F \text{ electrostatic} = \frac{(440 \times 1.602 \times 10^{-19})^2}{4\pi\varepsilon_o (Z_o \times 10^{-6})^2} = \frac{4.5 \times 10^{-6}}{Z_o^2} \text{ dyne}$$

where Z_o is the separation in μm.

It is seen at once that the ΔF_{vdw} is of higher order than ΔF_{elect} - for the latter to be equal to the former, the centres of charge separation would have to be as small as .01μm. Thus for an air borne aggregate, the Van der Waal force is likely to dominate.

Bradley[83] has considered the possibility of fragmentation of a small gas-borne agglomerate due to Brownian motion. The smaller the agglomerate, the more violent the motion due to thermal impact. The calculations show that impossibly high temperatures would be needed to disrupt an agglomerate held together under Van der Waal forces.

Forces tending to detach a particle from a surface usually depend upon:

(mass particle) x (normal acceleration)

for example:

$$\frac{1}{6}\pi\ (S.G.)d^3\ddot{z} = m\ a \qquad .....(2.26)$$

A quartz particle would leave the surface when:

$$212d = \frac{1}{6}\pi 2d^3\ddot{z}$$

or $$\ddot{z} = 200/d^2 \qquad .....(2.27)$$

so that if:

$d = 1\mu m$ then $\ddot{z} = 2\times10^7 g$

$d = 100\mu m$ then $\ddot{z} = 2\times10^3 g$

for detachment

To remove such particles would require the plate to be given a very high impact indeed. Arguing that quartz is an exceptional material, and using Beischer's figures for iron oxide particles, a 1μm particle would still need a big bang to move it.

Similar calculations may be made to determine if a particle which impinges on a surface will bounce off or adhere under the influence of Van der Waal forces. By considering the linear and angular momentum and velocity equations for a particle, approaching a hard surface, illustrated in Fig.1.12a, Jordan[88] obtains a criteria for quartz spheres based upon Bradley's force relation. The particle will stick only if:

$$\omega < (30/d)\ \ cm/s \qquad .....(2.28)$$

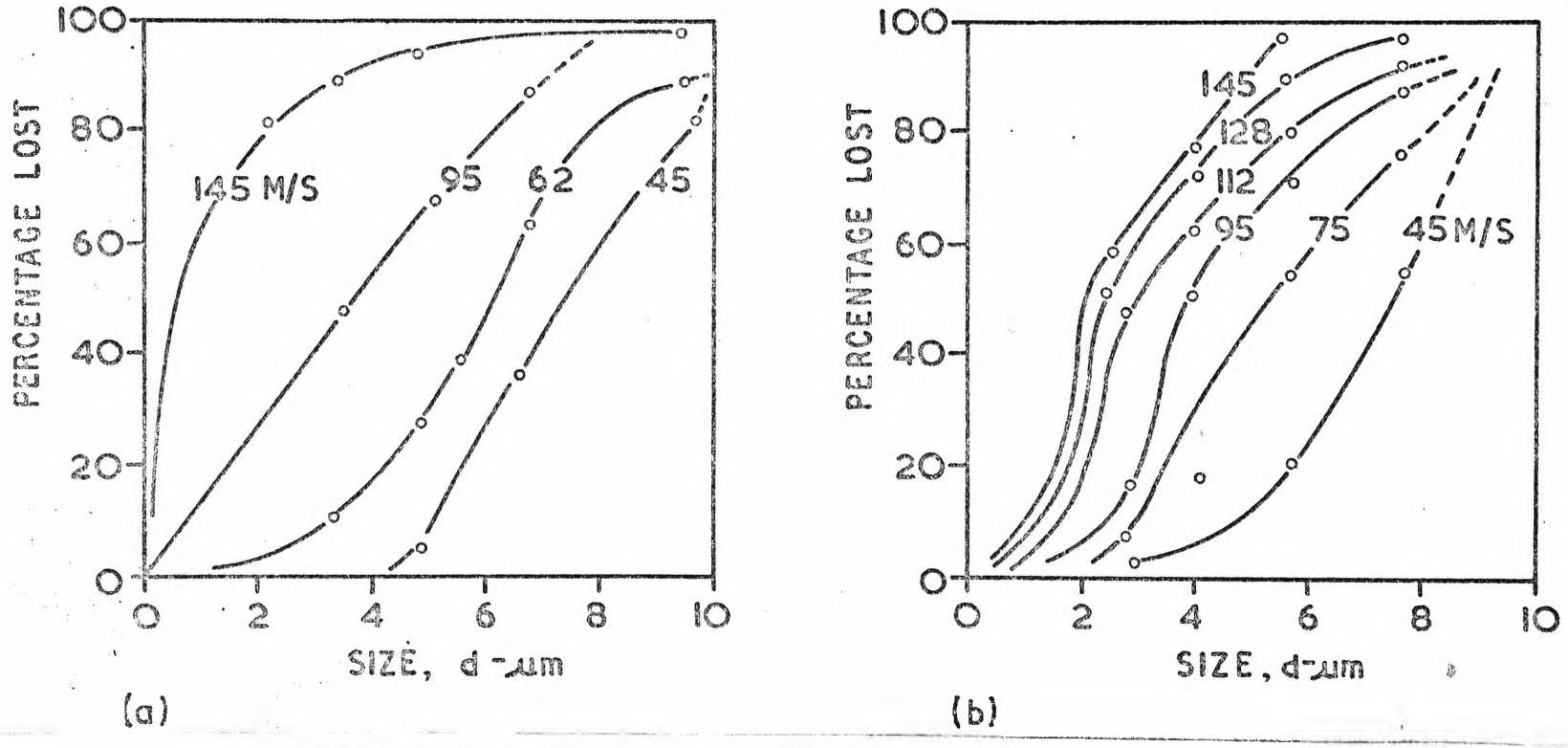

FIG. 2.5 DETACHMENT OF GLASS AND QUARTZ PARTICLES BY AIR STREAM (after Jordan[88])

An airstream directed normally at a surface with adhering (a) Glass and (b) Quartz particles, detaches them in the manner shown. Air velocities in m/s.

where d is the diameter in μm and ω the initial velocity perpendicular to the plate, which in the case of a precipitator is simply the drift velocity. Since the critical velocity is proportional to (1/d), a larger particle is less likely to adhere. Indeed, using this criteria, a 10μm particle will bounce if the initial normal velocity is greater than 3 cm/s. In practice, this is almost always exceeded, as a glance at Fig.1.10 will confirm. The situation will worsen with larger particles. Jordan's analysis is based upon an impact coefficient of restitution of 0.8: a comparable figure for a layer of particles is not known, but since it is probably less than 0.8, higher non-rebound initial velocities are possible in a precipitator. The common assumption in precipitator theory that a particle on touch-down will be captured, is thus far too optimistic. This analysis adds theoretical support for the photographs of Penney et al which, as discussed in para.1.3 show bouncing of large particles. It also adds fundamental validity to the writer's advocacy in the same paragraph of a 'probability of attachment coefficient'.

A particle adhering to a plate subject to a gas stream will experience an aerodynamic force proportional to d^2, tending to detach it. A mention of the work of White and Oglesby on erosion by gas velocity was made in para.1.3. Jordan describes experiments with quartz and glass particles of size $1<d<12\mu m$, adhering in a mono-layer to a similar substrate.

A perpendicular air blast directed at the layer removed particles in accordance with Fig.2.5. The speed of the jet required to overcome the Van der Waal forces is remarkably high. To remove 50% of 8μm quartz particles required a jet of air 45m/s while to remove 50% of 2μm particles required a jet 145 m/s. The situation is, however, somewhat

removed from that obtaining in a thick layer on a precipitator plate.

By whichever means is used to remove particles i.e. either by impact or by aerodynamic pressure, it is clear that small particles hold on more tenaciously than large ones under the influence of Van der Waal's forces. A large particle approaching the substrate is more likely to rebound than a small one.

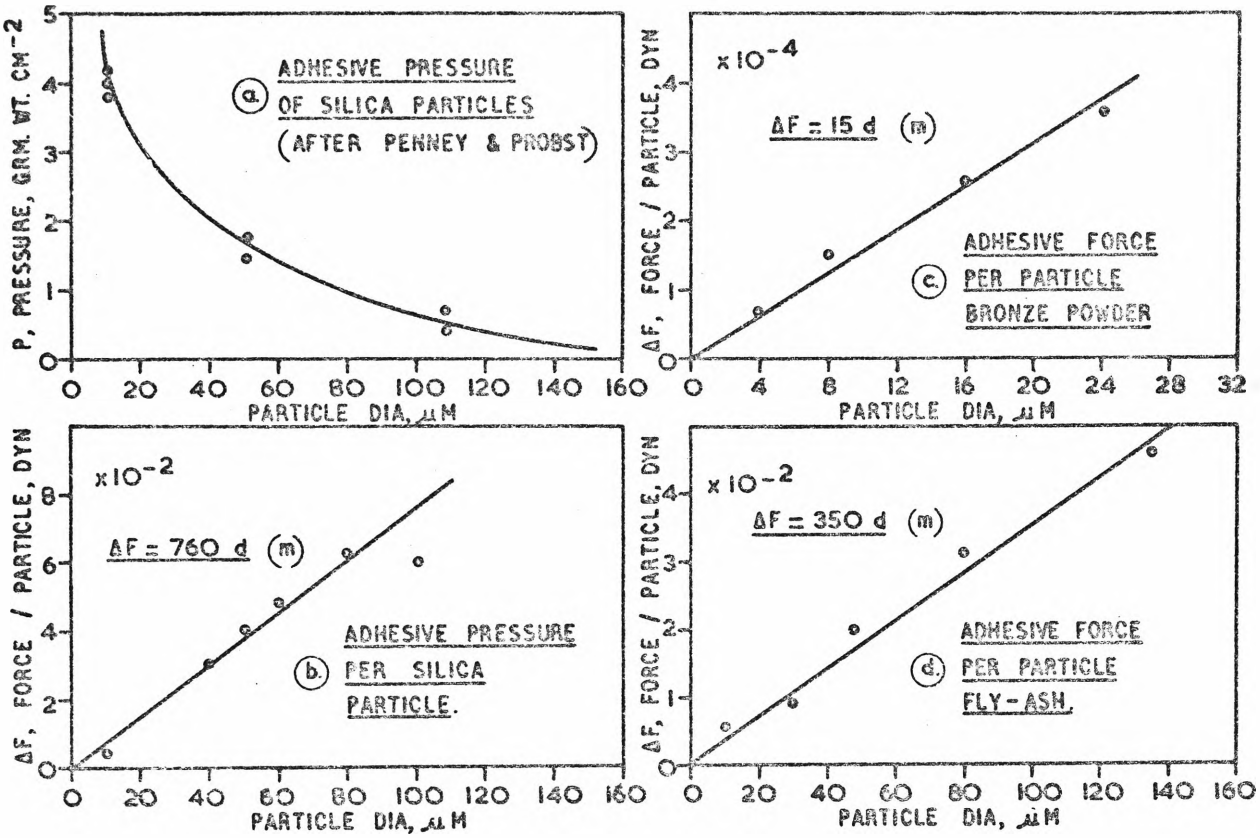

FIG. 2.6 ADHESION FORCES AND PRESSURES

(a) Detachment pressures for a layer of silica particles from centrifuge measurements (after Probst & Penney)[66]

(b) Forces for single silica particles reduced from centrifuge data (by Tassicker)

(c) Forces for single bronze particles reduced from centrifuge measurements (by Tassicker)

(d) Forces for single fly-ash particle reduced from centrifuge measurements (by Tassicker)

2.2.4 London-Van der Waal Forces in an Electrostatically Deposited Macroscopic Layer

Having considered the effect of Van der Waal forces on a single particle, we now turn our attention to thick layers. In this paragraph we shall concentrate upon the tensile strength of thick layers which have been electrostatically deposited.

Penney et al[81,66] (1962-3) measured macroscopic forces of adhesion in layers of particles which had been electrostatically deposited up to a depth of 2mm on a small brass plate in a precipitator. After removal, the specimen was placed on a centrifuge head whose surface they observed by means of a synchronously strobed flash. On acceleration of the rotor, a larger fraction of the dust detached at a definite speed. From a knowledge of the mass detached, the area of substrate, speed and radius of gyration, the adhesive strength as a pressure in grm wt/cm^2 was calculated.

They expressed their results as in Fig.2.6a in which adhesive pressure P is shown as a function of particle diameter d for silica particles. The size fractions appeared to have been obtained by relatively coarse sieving, e.g. 0-5μm, 0-10μm, 44-53μm etc so that their results show understandable scatter. No comment was made concerning the degree of angularity or roundness of the particles. Their results all show a sort of inverse relationship between P and d so that they comment; "The adhesion of electrostatically deposited dust is found to decrease as the particle size increases".

A rather unusual feature of the work by Probst and Klingler is that they make no reference in their publications to adhesion work other than their own, in spite of the fact that there was at that time some current activity on the other side of the Atlantic.

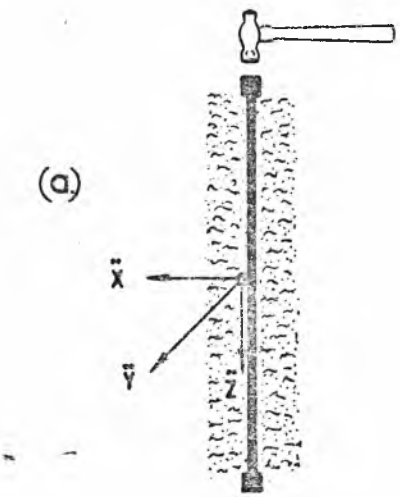

RAPPING A RECEIVING ELECTRODE

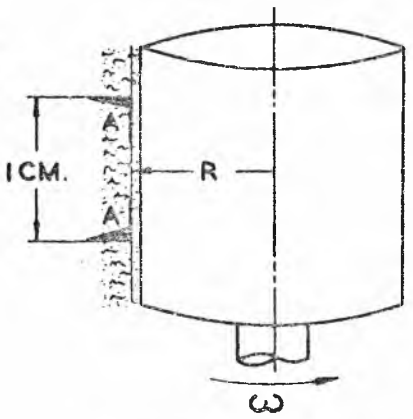

ADHESIVE PRESSURE ON PRECIPITUGE ROTOR

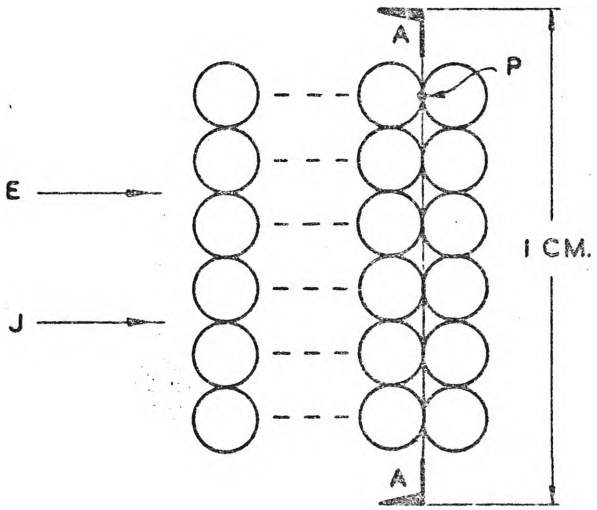

ADHESIVE FORCES IN A LAYER

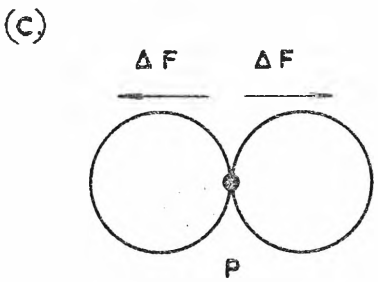

PAIR OF PARTICLES

FIG. 2.7 FUNDAMENTAL ADHESIVE FORCES

Their general conclusion that a layer of fine particles adheres more tightly than a layer of coarse particles appears to agree with the general conclusions reached in the preceding para 2.2.3 for single particles.

The writer now attempts a reconcilliation between the macroscopic data of Penney et al and that of Krupp and Sperling etc for single particles, by making use of a simple packing model; i.e. a cubical array. Making reference to Fig.2.2c or Fig.2.7c where the single particles comprising a layer are illustrated, one observes that across interface AA of unit area, there are $(1/d^2)$ particles. If the force between adjacent particles is ΔF, then the total pressure over the unit cross section is

$$P = \Delta F(1/d^2)$$

hence

$$\Delta F = Pd^2 \qquad .....(2.29)$$

Operating on the data contained in Fig.2.6a in this way, one finds that the adhesive force per silica particle follows roughly the straight line relationship depicted in Fig.2.6b. When data for the bronze powder and fly-ash is treated in the same way, again approximate straight line relationships between ΔF and d follow as depicted in Fig.2.6c and 2.6d. One concludes therefore that the Penney et al macroscopic data, in spite of obvious limitations in the experiments, does indeed harmonise with the more fundamental data on single particles provided by Krupp, Bradley etc.

They made further important observations. The adhesive strength of a layer of electrostatically deposited dust, or dust which had drifted gently onto the substrate from a gas stream, was at least 30 times greater than dust which had been mechanically pressed into position in the bulk. Dusts electrostatically deposited retained their high

adhesivity long after the HT field was switched off. Particles of higher resistivity and subject to higher current densities during precipitation showed denser packing under the microscope and higher adhesion subsequently, but this effect was not quantified.

Sproull[70] in a well referenced and documented study, described adhesion measurements on a number of electrostatically deposited dusts including fly-ash, cement kiln feed, cement dust. A circular flat electrode of 9 in^2 upon which the dust was deposited, could be subjected to controlled impact, giving shear or normal accelerations. These were measured by piezo-crystal and the signal conditioned to provide velocity and displacement. Results were expressed in several ways, one of which is shown in Fig.2.8a. There, the dependent variable is:

Rapping efficiency = (% dust dislodged by a single blow).

Interestingly, as noted in para 1.5, Ruckelshausen stated emphatically that he could make no use of this parameter. With a constant normal rap of 13g, Sproull varied the initial depth of deposit on the plate, using this as the independent parameter. Rapping efficiency improved with depths of deposit up to a certain point, the reasons for which are developed in para 2.6. A given curve in Sproull's results comprised an average of about 100 individual tests, and although standard deviation was not specified, it is clear that scatter in these tests was high. No data was given on sized speciments.

The writer found that it was with considerable difficulty that the results, more oriented to practical uses, yielded up any fundamental data. The data of Fig.2.8a after some manipulation with simple mechanics, can be expressed in the form shown in Fig.2.8b, an inspection of which shows it to be of the same form as the cumulative distribution curve of

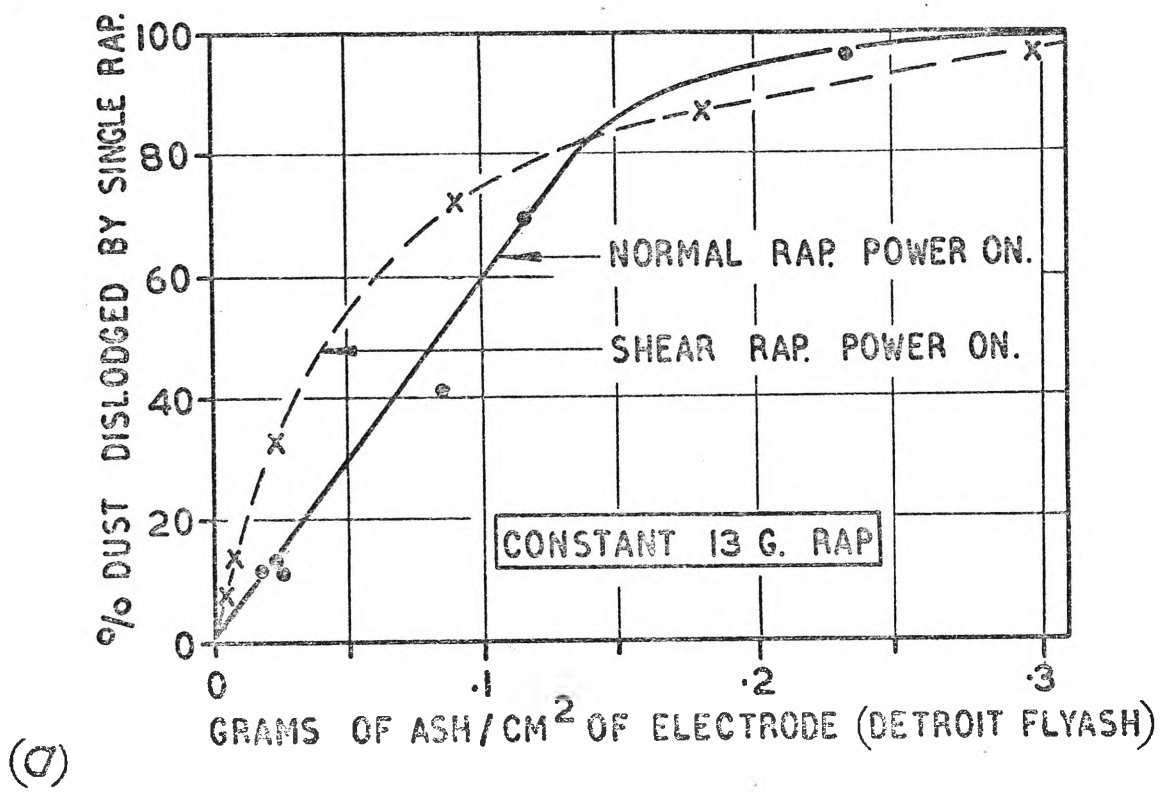

(a)

FIG. 2.8 ADHESIVE STRENGTH OF FLY-ASH

(a) Corona power on in both cases. Mixed particle size populations. Form of data presented by Sproull[70] for Detroit fly-ash. A constant 13g normal rap is applied. Rapping efficiency increases with depth of deposit.

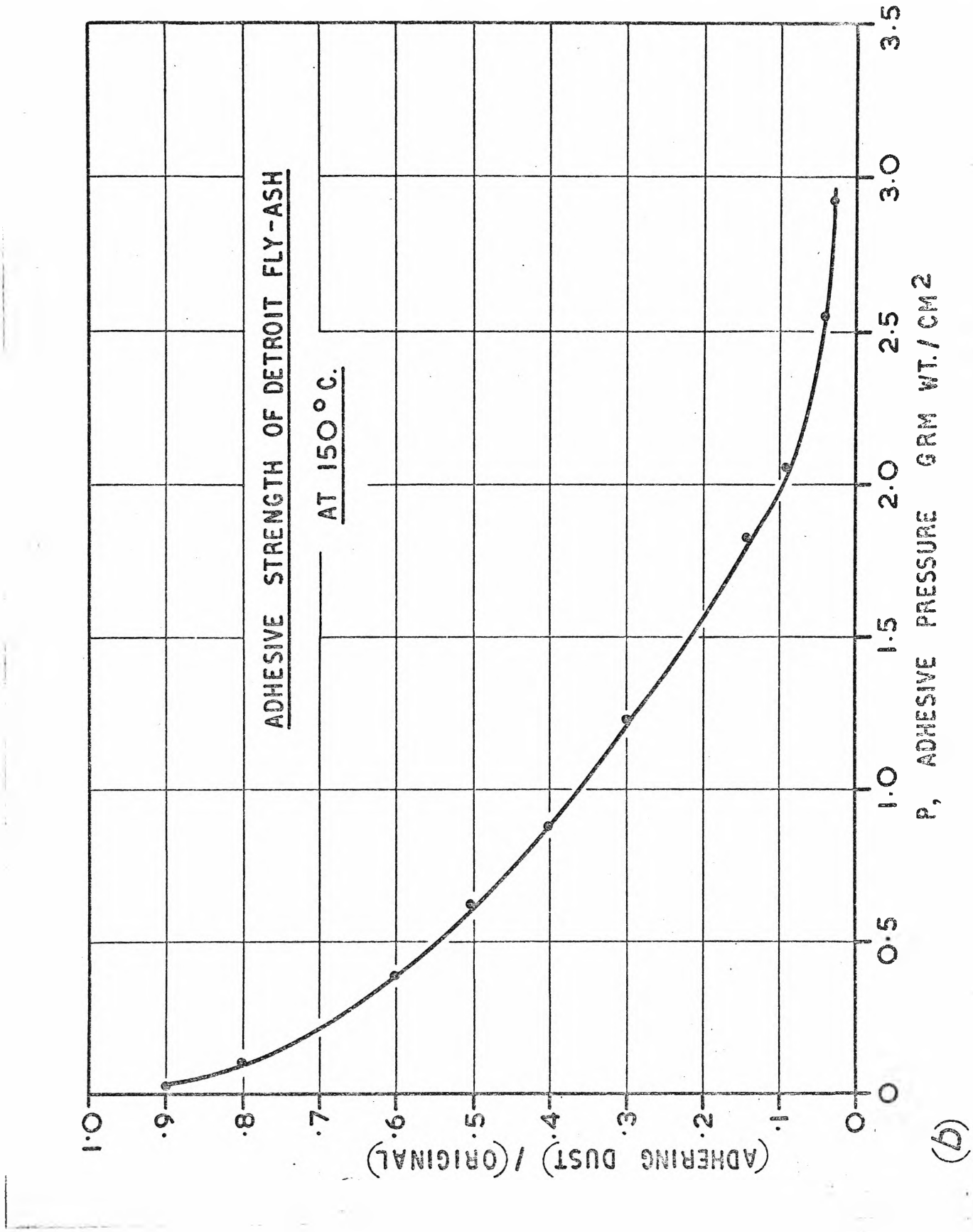

FIG. 2.8 ADHESIVE STRENGTH OF FLY-ASH

(b) Data reduced from Fig. 2.8(a). Effectively a cumulative distribution curve as a function of adhesive pressure P.

the Boehme et al data of Fig.2.4a for single particles. It is therefore seen to be statistical data, expressing both the uncertainty of the modes of vibration induced in the flat plate and variability in the fly-ash deposition. The most probable value of adhesive pressure at 50% detachment is 0.6 grm wt/cm^2, a value which is in order-of-magnitude agreement with earlier data by Penney and Klingler.[81] An alternative interpretation is suggested in para 2.6.

Viewed in the ways described, both sets of results on macroscopic layers by Penney et al and Sproull, are seen to harmonise with the findings described earlier on the behaviour of single particles.

2.3 Tensile Strength of Powders

In this paragraph we consider some of the findings of the powder technologists whose specimens have been compacted or deposited in some fashion other than by electrostatic means. Powder fracture is carried out by these workers in a sort of tensile tester,[92] described briefly in para.2.3.3.

2.3.1 Cohesion and Adhesion

Both of these terms are widely used[89,90,91] to describe the behaviour of powders in hoppers, bins, chutes, orifices; in pelletising and in tabletting.

Cohesion is defined as the ultimate shear stress at zero compressive stress and adhesion as the ultimate tensile stress at zero shear stress. The Mohr Stress Circle, commonplace in the study of the elasticity of solids, is also used for powders to relate cohesion and adhesion.

As a result of some hundreds of tests on different powders, Farley and Valentin[94] produce the data shown in Fig.2.9a. The cohesive strength is found empirically to be twice the adhesive strength.

The writer believes that it is principally the adhesion, i.e. the tensile strength at zero shear, which is the parameter of interest in the rapping of precipitators. The works by Ruckelshausen,[69] Brandt,[71] and Watson and Blecher[50] cited in para.1.5 all emphasise that it is the normal acceleration which is effective in dislodging precipitate. The former two authors, it will be recalled, complained that the corresponding particle parameter, i.e. the adhesive strength, was an unknown quantity.

We now confine our attention in subsequent paragraphs to the one parameter, the adhesive strength as a function of porosity, particle size and moisture content.

2.3.2 The Porosity of a Powder

This important parameter is a measure of the particle packing density. Porosity, is defined as being:

$$\text{Porosity} = \phi = \left(\frac{\text{void volume}}{\text{total volume}}\right)$$

$$= 1 - \frac{\text{density of bulk material}}{\text{density of solid material}}$$

$$= 1 - \alpha_b/\alpha_s \qquad \ldots\ldots(2.30)$$

Both the Porosity ϕ and the related quantity, the relative bulk density (α_b/α_s), are commonly used in powder technology.

The form of packing of a mass of spheres greatly influences the porosity as the table indicates*:

Characteristics of Packings

	Porosity ϕ%	Relative Bulk Density α_b/α_s %
Cubical	47.64	52.36
Orthorhombic	39.54	60.46
Rhomborhedral	25.95	74.05
Chance packing of spheres	35 to 43	65 to 57

The analysis of random packed spheres shows the porosity of 35-43%, to be a weighted average of the rhombohedral and cubical cases.

The porosity or relative bulk density is readily measured by one of the several well-known laboratory techniques.

---

* Professor R.T.Fowler, Uni. of N.S.W., personal communication.

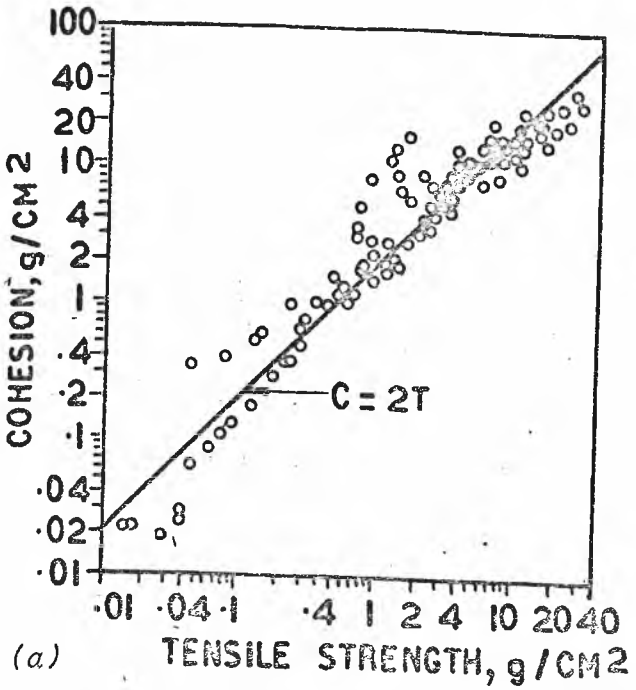

(a)

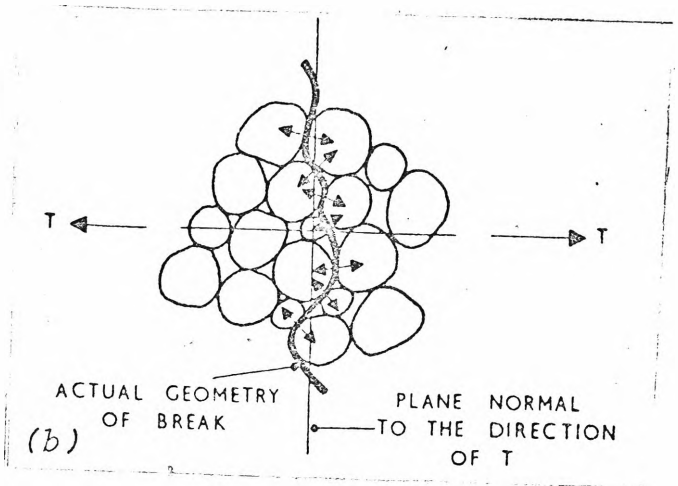

(b)

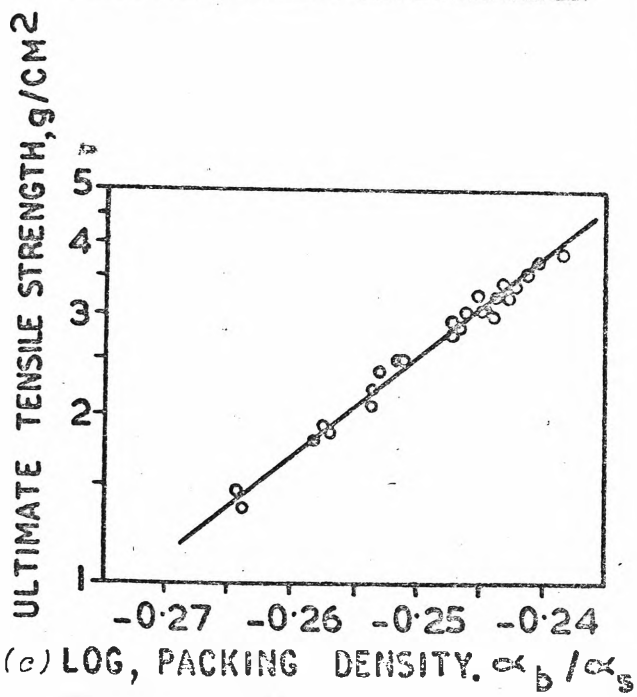

(c)

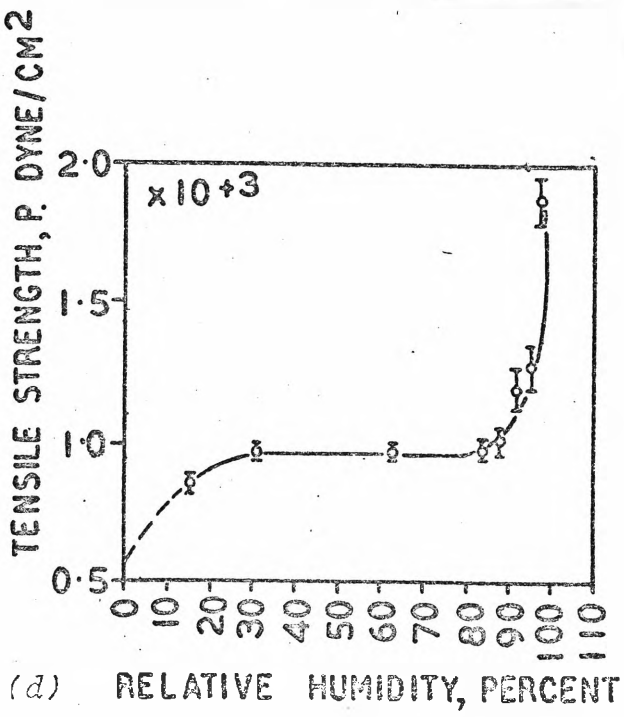

(d)

FIG. 2.9 ASPECTS OF ADHESION

(a) *Relation between tensile strength T and shear strength C for a variety of powders and particle sizes (after Farley & Valentin)*

(b) *Illustrating the non-planar geometry of the surface of a split in a powder compact. The small arrows show that the forces between particle-pairs are inclined to the direction of T. (after Rumpf and Cheng)*

(c) *The relation between adhesive strength and packing density of zinc particles. Coarse from wt at 37 micron (after Farley & Valentin)*

(d) *Effect of relative humidity on the cohesion of limestone dust after an exposure time of 16 hours. (after Eisner, Fogg & Taylor)*

So basic a parameter as the porosity of the particulate on a precipitator plate, has not, so far as the writer can ascertain, been described anywhere in the literature.** It would be very interesting to see how such a porosity compared with that obtained after removing the dust and compacting it in a test cell, in the manner common to powder technology.

2.3.3 Relation between Porosity and Tensile Strength

Rumpf,[99] in a very mature presentation, derives an expression for the adhesive strength of a dry powder in terms of porosity ϕ, and co-ordination number χ defined as being the average number of points of contact between one sphere and its neighbours. Assuming random particle packing and an actual line of cleavage around the mean plane of the break as illustrated in Fig.2.9b, Rumpf derived an expression for the adhesive strength:

$$P = \frac{9}{8} \frac{(1-\phi)}{\pi d^2} \cdot \chi \cdot \Delta F \qquad .....(2.31)$$

which he used later as the basic equation for his considerable experimental work. Obviously the co-ordination number χ and the porosity ϕ must be closely related: one would expect a larger number of points of contact in a powder of lower porosity. In fact, quoting the results of other works, Rumpf states:

$$\chi\phi \doteqdot 3.1 \doteqdot \pi \qquad .....(2.32)$$

Hence combining eq.2.31 and eq.2.32, there follows:

$$P \doteqdot 1.1 \, [(1-\phi)/\phi] \, \Delta F/d^2 \qquad .....(2.33)$$

** Dalmon & Tidy (1972) quote densities.

For the case of cubical packing, $\phi = .4764$

$$\text{and} \quad P = 1.2\ \Delta F/d^2 \qquad .....(2.34)$$

which compares closely with eq.2.29 already found.
Where there are mixed particle sizes, Rumpf uses a mean diameter.

Later, Farley and Valentin[94] also found a definite relationship between porosity and the tensile strength of a given powder as reference to Fig.2.9c shows.

In Fig.2.9c where zinc particles of a certain size were given different relative bulk densities α_b/α_s simply by varying the degree of compaction, the correlation with tensile strength is undoubted. After examination of over one hundred powders, these workers concluded that:

$$P = H(\alpha_b/\alpha_s)^m \qquad .....(2.35)$$

where H and m are constants.

Possibly the data of Farley & Valentin might have fitted eq.2.33 just as well as it fitted eq.2.35. The work of Rumpf and Farley & Valentin is not in disagreement, though the former's is more attractive because it has an analytical basis.

The porosity did not depend to any significant extent upon the particle size of the powder of a given material, provided the same compaction procedure was used. (Some workers[96] have, however, claimed to have found a critical size of powder ≃ 15μm, above which porosity is independent of particle size and below which, porosity increases. They claim to have evidence of repulsion between particles in such cases. More evidence on this point would be welcome.) However from one material to another with fixed compaction, the porosity did vary markedly as follows:

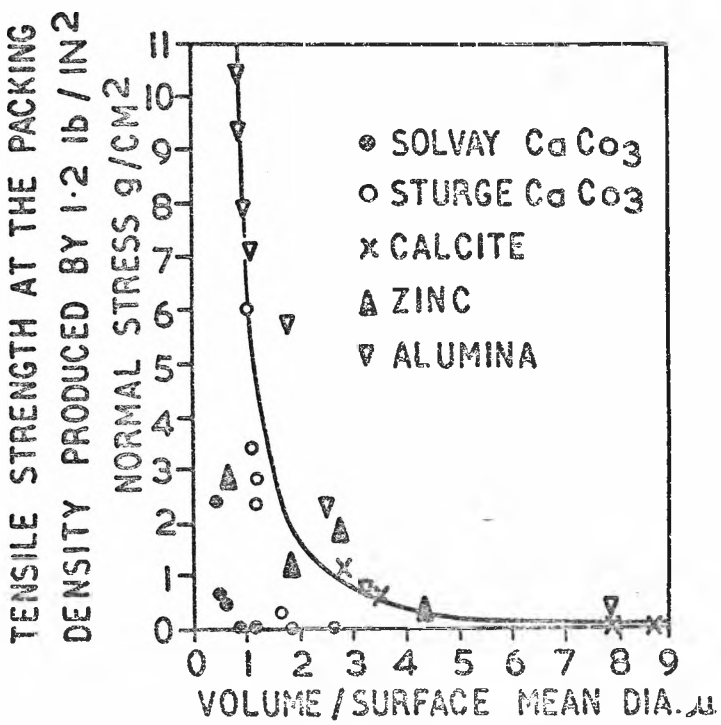

(a)

FIG. 2.10 CORRELATION OF THE STRENGTH OF POWDERS WITH VAN DER WAAL FORCES (Farley and Valentin[94])

(a) Relation between tensile strength (at a constant packing density) and mean diameter for a range of particles.

(α_b/α_s)	Material
.38	Solvay C_aCO_3
.33	Sturge C_aCO_3
.48	Calcite
.26	Alumina

The amount of compression is always limited at one extreme by particle fracture and at the other end by fluidisation.

2.3.4 Tensile Strength and Particle Size

Tensile strength depended very maarkedly on particle size, decreasing with increasing particle diameter in the manner shown in Fig.2.10a. The results though scattered, nevertheless bear some similarity to the centrifuge results for silica particles depicted in Fig.2.6a.

Selecting the two best results shown in Fig.2.10a i.e. for alumina and zinc, one operates upon them in the same fashion as upon the data of Penney and Probst in para.2.2.3. Assuming a simple cubical particle orientation, as before, the writer calculates the force per particle

$$\Delta F = (Pd^2) \qquad .....(2.29)$$

and plots this as a function of particle diameter d, as illustrated in Fig.2.10b and c. Discarding obviously aberrant points, fair correlation with:

$$\Delta F = 450d \text{ for alumina}$$

$$\text{and } \Delta F = 80d \text{ for zinc}$$

is obtained.

Assuming that the experimental work of Penney and Probst and Farley & Valentin was carried out with equal care; it is interesting to speculate upon the reasons for the better

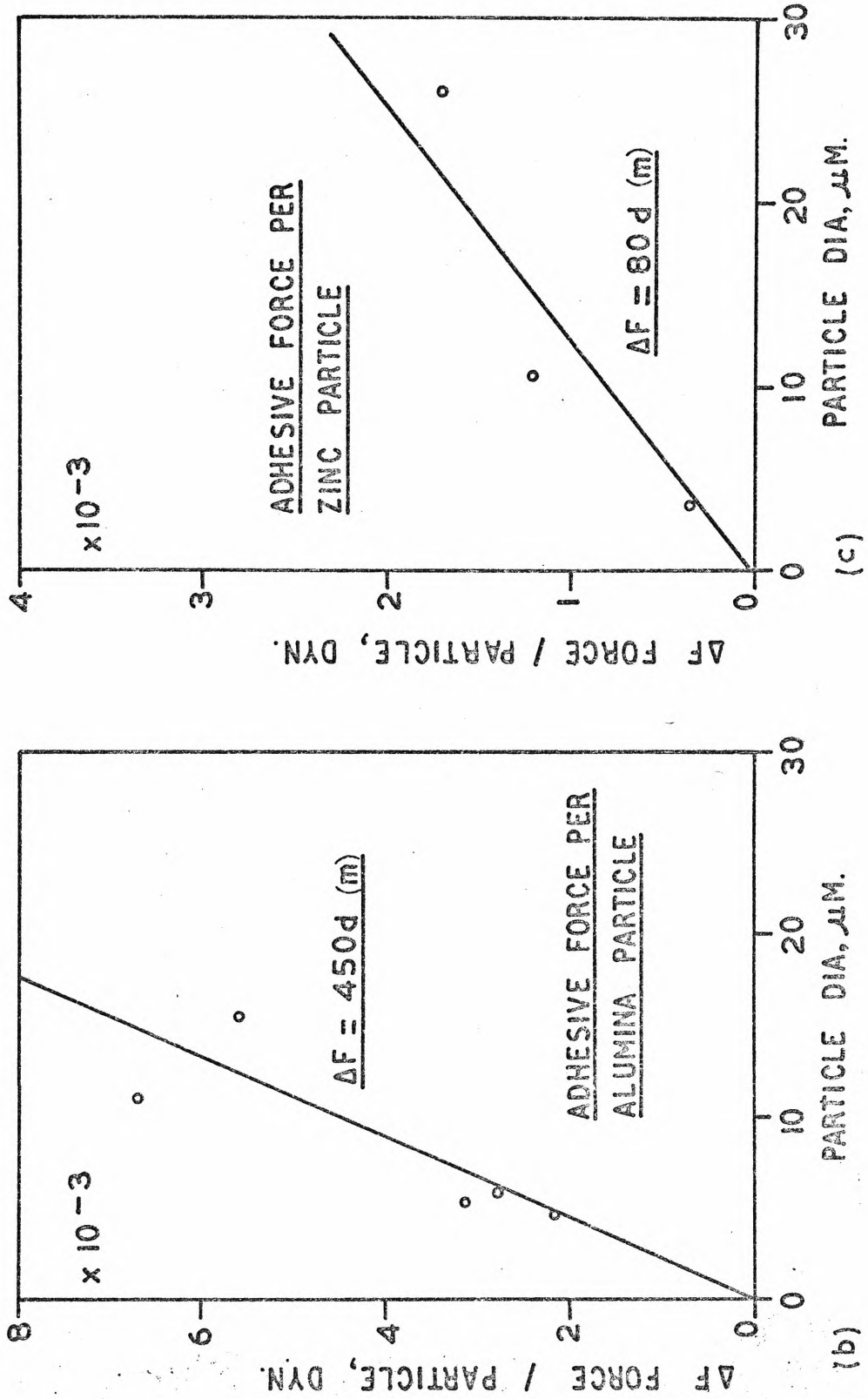

FIG. 2.10 CORRELATION OF THE SERENGTH OF POWDERS WITH VAN DER WAAL FORCES

Data reduced from Fig. 2.10(a) (by Tassicker)

(b) Alumina particles
(c) Zinc particles

correlation of the results of the former than those of the latter with the

$$\Delta F = Ad \text{ relation.}$$

The powder which was precipitated into position may well have had some kind of optimal packing under the action of the electric field. Jenike's remarks on such a matter are pertinent: (Ashton et al, ref.89, P.217 (discussion)) "A certain density can be attained through "Flow" or through "compaction", or through a dynamic condition, e.g. "vibration". While in all three cases, density may be the same, the size and shape of the yield locus is likely to be different. Hence the strength will, in general depend not only on the density but also on the method by which the density has been attained".

The electrostatically deposited dust may represent an important limiting case in the theory of particle packing.

Finally, one concludes by noting that in the work of the powder technologists there is at least some evidence that Van der Waal forces are basic to the strength of powders.

A recent paper by Cheng[93] which attempts a substantial synthesis of studies on the tensile strength of powders, is discussed in appendix 2.3. While it would be premature to attempt to apply these concepts to precipitators at the moment, the work of Cheng and his colleagues merits surveillance.

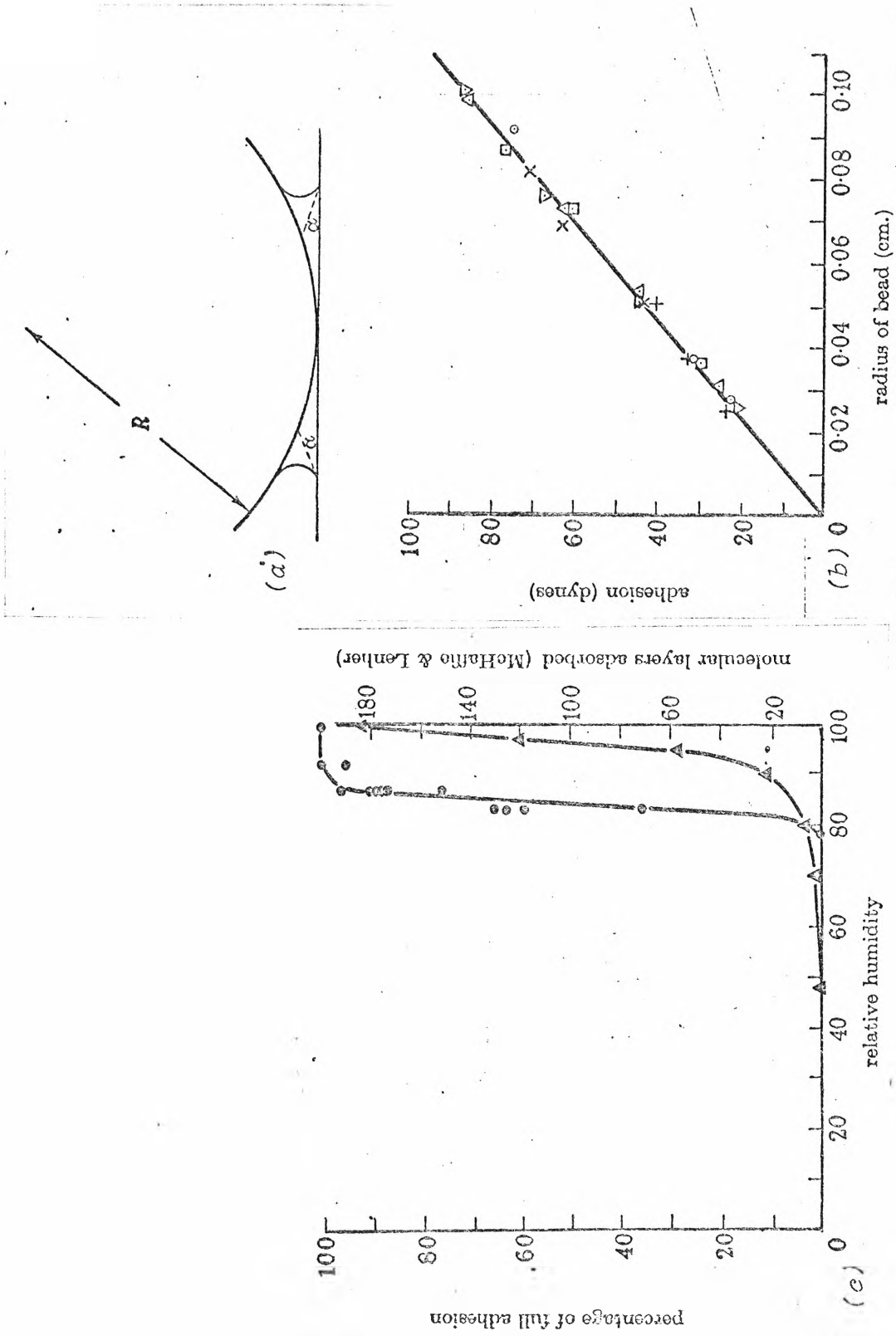

FIG. 2.11 CAPILLARY ATTRACTION OF A SINGLE PARTICLE (after McFarlane & Tabor[97])

(a) A single sphere touching an infinite flat substrate with liquid inclusion

(b) Adhesion of a glass bead on a flat glass surface in a saturated atmosphere of H_2O.

(c) Adhesion of glass surfaces as a function of the atmosphere. There is a close parallel between the adhesion results (curve ●) and the results of McHaffie and Lenher for the thickness of the water film adsorbed on glass surfaces (curve ▲).

2.4 Capillary Attraction and the Effect of Moisture

Since water is present in all flue gases, typically in the order of 5% by weight, and since precipitator operating temperatures may not be that far removed from the dew point, we consider the possibility of capillary attraction.

The writer is indebted to Professor R. T. Fowler of this University who has made available the drafts of five papers in preparation for publication, based upon recent research into powder strength - particularly in wet condition.

2.4.1 Capillary Attraction of Single Particles

The adhesion between single small glass spheres $400 < d < 2000\mu m$ with a flat glass substrate in the presence of H_2O and other surface films, has been investigated by FcFarlane and Tabor.[97] The model for a single glass sphere is shown in Fig.2.11(a) from which the force of attraction due to surface tension is derived as:

$$\Delta F = 2\pi\gamma d \quad \text{dyne} \qquad \ldots\ldots(2.36)$$

for the expected cases of thin layers when $\cos\phi \simeq 1$, and where d = dia. cm, and γ = surface tension of fluid in the surface layer, dyne/cm. The excellent agreement of this relation with measurements is illustrated by Fig.2.11b. The force was found by theory to be independent of the layer thickness for small layers. This was confirmed in practice where the full value of the force given by eq.2.36 was maintained even when the liquid had been so thinned by evaporation as to be much less than 250 molecules thick. The force fell only when the adsorbed layer became so thin that the peaks of surface imperfections must have protruded through the liquid layer.

The thickness of the adsorbed layer, being known to depend upon the relative humidity, it was expected that the force would depend upon humidity. This is illustrated by

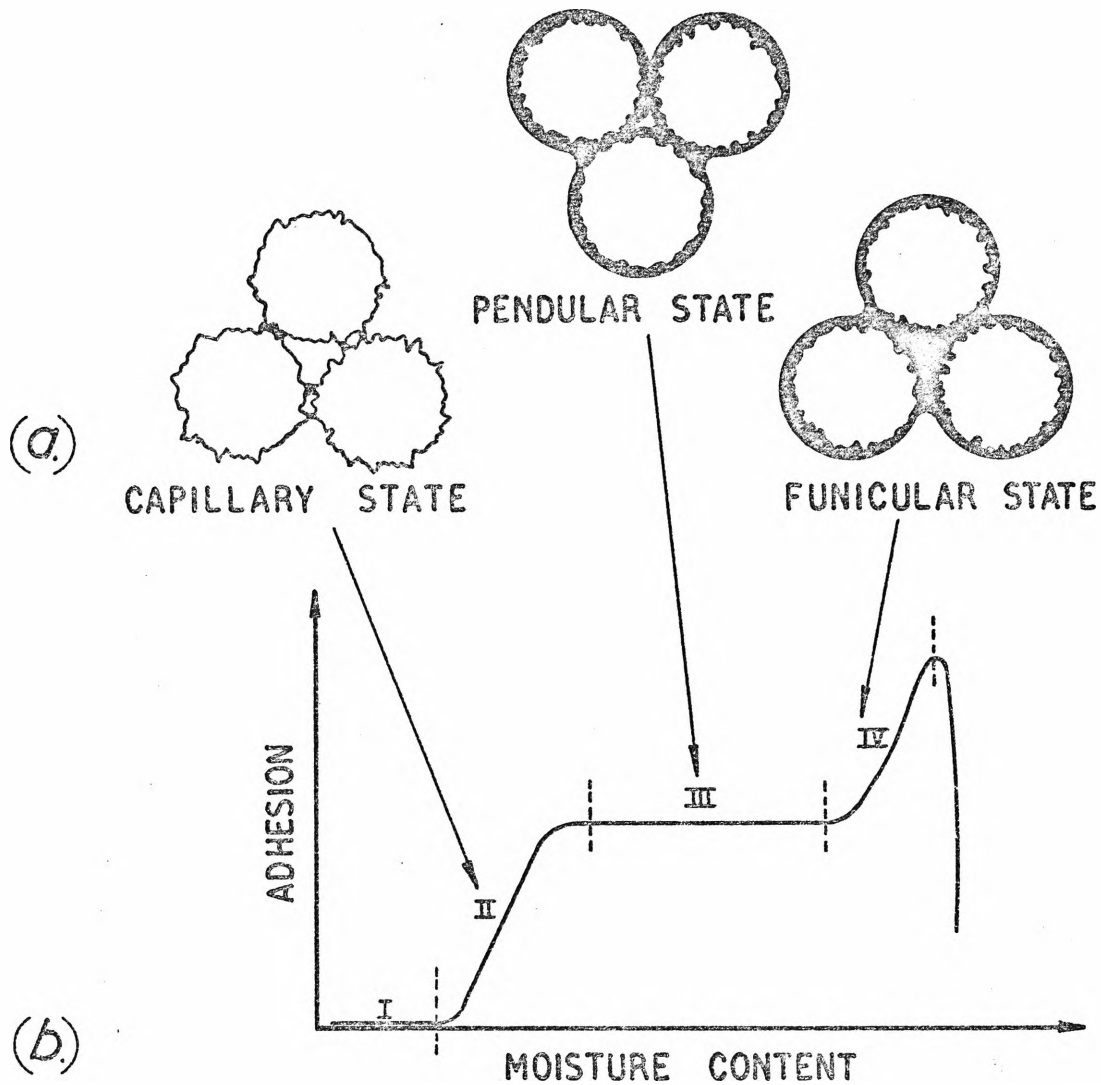

FIG. 2.12 STRENGTH OF A WETTED POWDER (after Radford and Fowler[95])

(a) Three states of wetting - the Capillary, Funicular and Pendular.

(b) Four zones of strength - Chemisorbed, Capillary etc.

Fig.2.11c which shows that the force rises sharply at 80% RH (i.e. with an adsorbed layer > 10 molecule thick) reaching its constant maximum value at 84% RH. The evidence was then, that surface imperfections were about 20 molecules in height. From Fig.2.11b $\Delta F = 430d$ dyne.

Since the theory of capillary attraction for single particles presented by McFarlane and Tabor was so convincingly vindicated by experiment, one seeks now the extension to layers of particles and to imperfect particles.

2.4.2 Wetting of an imperfect particle

The manner in which water molecules attach to, and finally wet, the surface of an irregular particle with asperites has been described by Rumpf.[99]

Making reference to Fig.2.12a and b, four zones are indicated. In zone 1 representing low moisture contents (below 0.01%), typically produced with humidities well below 80%, the particles are covered by the chemisorbed layer of moisture and probably a few physically adsorbed molecular layers.

As the moisture content is increased with gas humidified above 80%, the number of molecular layers rapidly increases due to capillary condensation that occurs both in the pores on the surface of the particles and between particle contact points. The adhesive force rapidly increases in zone II.

The capillary state changes to the pendular state when the thickness of water film covers the asperites. The particles can now be considered as perfectly smooth spheres with moisture forming a continuous film between adjacent touching spheres. This is a common case treated in soil mechanics.

With further increase in moisture content, pendular films coalesce to form continuous filsm through the mass

which becomes the funicular region, zone 4. Finally the mass saturates, performs as a slurry and deform plastically.

This paragraph is added only for completeness. A dry precipitator would only rarely have sufficient water vapour to enter zone 1 at the most - never zone II. A wet precipitator operates past the peak of zone IV.

2.4.3 Strength of a Wetted macroscopic Layer

Radford and Fowler give results for four different groups of particles sieved to the same size.

Here, the mass of water was determined by actual weighting, drying and weighing. In the results, depicted in Fig.2.12c, the four zones described in the preceding paragraph, may be discerned.

In a different type of experiment, a powder was allowed to reach equilibrium with respect to air at various humidity levels.[98]

Eisner, Fogg and Taylor measured the tensile strength of limestone ($CaCO_3$) powder in a humid atmosphere. After dredging the powder onto a glass plate, one half of which was fixed while the other was free to slide on ball bearings, the assembly was slowly tilted and the angle θ at which the specimen broke was noted. If W is the weight in grams of the break-away portion of the dust, then the tensile strength is given by: $P = (W/A)\sin\theta$

$CACO_3$ SIZING

Sieve analysis micron	weight %	Bulk Density (grm-3) cm	Specific surface $m^2 grm^{-1}$
>251	4.5	1.16±.02	.34±.02
124-251	17.8		
64-124	11.8		
64	65.9		

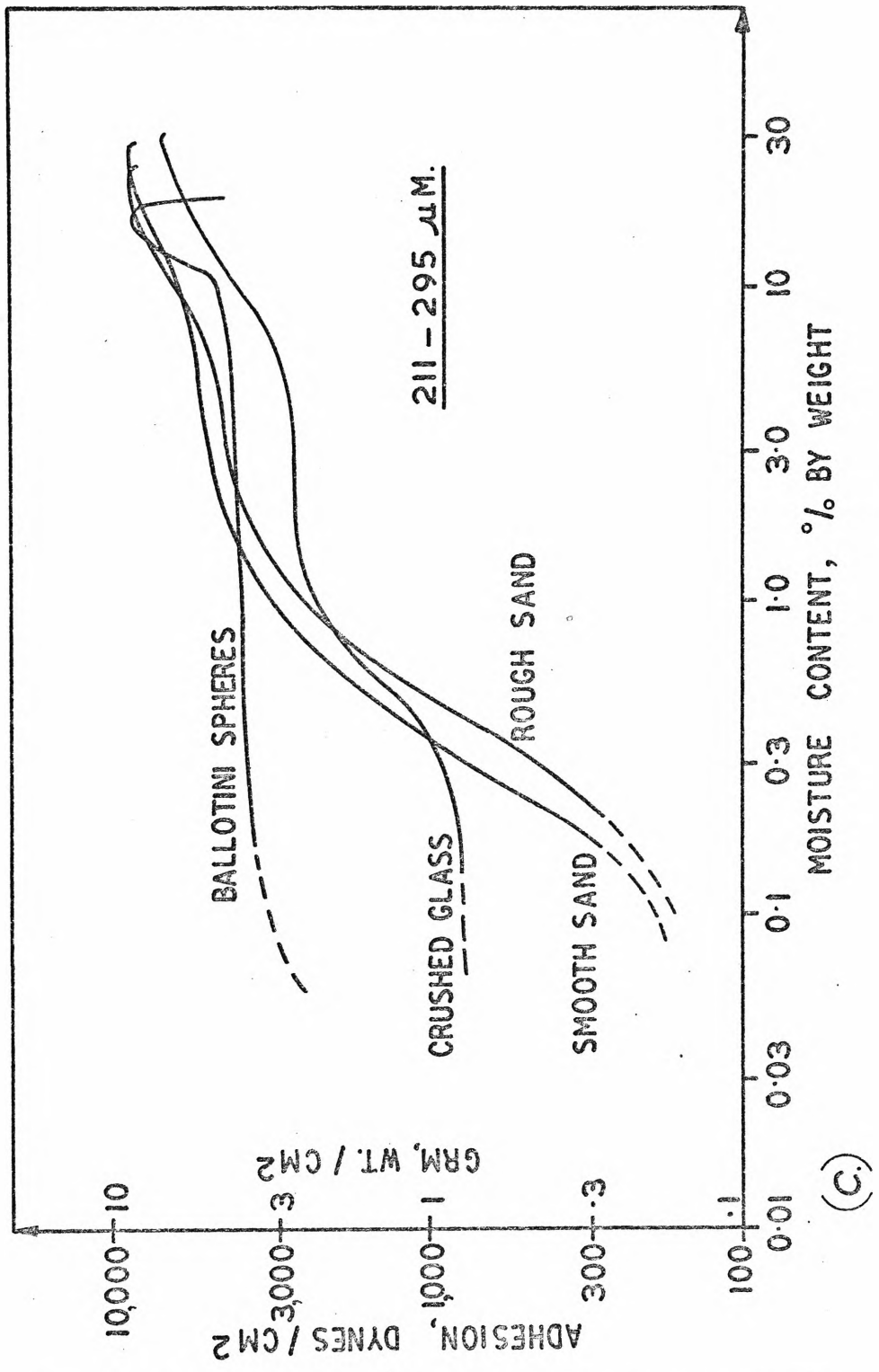

FIG. 2.12 STRENGTH OF A WETTED POWDER

(c) Effect of moisture on the adhesive strength of four different types of particles (after Radford & Fowler[95])

The Eisner et al results, which give an unambiguous tensile strength unaffected by shear considerations - are shown in Fig.2.9d. The initial dry strength doubles with exposure to 30% RH, remains constant at 10^3 dyne/cm^2 until 85% RH when the adhesive strength rises rapidly with humidity to a peak of 2×10^3 dyne/cm^2.

Comparison of this data with that of Fig.2.11c shows a striking similarity in the manner in which the force increases at about 80% RH. There, unfortunately, the similarity ends, for the data of Fig.2.11c when converted to tensile strength by eq.2.29 yields pressures of about* 50×10^3 dyne/cm^2, or some two orders of magnitude higher** than that measured on the limestone dust. Of course, it could be argued that glass and calcium carbonate are different materials. The real reason for the disparity however is almost certainly in the unsatisfactory way Eisner et al prepared their specimen, which (according to Radford and Fowler,) was simply to drop it through 15cm!.

Compaction so obtained must have been very poor and quite unreproducible.

The Eisner et al result is nevertheless of value, in that it gives a hint of harmony between the macroscopic layer dependence upon humidity and the microscopic data of

---

* Actually, 100×10^3 dyne/cm^2 for adhesion to a flat substrate. McFarlane and Tabor do not derive the force for the sphere to sphere case, but inspection of the figure shows that it is probably about half the former.

** On the other hand, Penney & Klingler (para.2.23) found the strength of properly deposited dust to be 30 times that of a crudley mechanically compacted dust. Applying this to the Eisner et al result:

$P = 1.9 \times 30 = 57$ grm wt/cm^2 which is about the same as the reduced MacFarlane & Tabor result of 50 grm wt/cm^2 cited above.

MacFarlane and Tabor.

2.5 Surface Dipole Effects

An investigation in depth of this topic would require so great an incursion into colloid and surface chemistry that it could not possibly be undertaken in a thesis of this format. The problem can be no more than outlined in this paragraph.

In their investigations[81] on the strength of powders electrostatically deposited, Penney and Klingler observed dipole-like action. Dusts deposited electrostatically showed strengths 30 times greater than those pressed into position mechanically, as noted in para.2.2.3. Measurements of surface potential over such a layer of fly-ash, talc and mica, using the electrometer and vibrating electrode technique, disclosed values of 0.1 to 1.0 volts. Dust deposited by falling out gently from a gas stream, showed the same high values of adhesive strength. From this they concluded that dust particles had one or more permanent axes of electrification. During favourable deposition, particles oriented themselves, giving the mass elecret-type properties. Observation of a single dust particle under the action of a reversing electric field showed it to change direction, too, in a way consistent with dipole-behaviour. Penney and Klingler supposed this action to result either from the different work functions across crystal interfaces; or, in view of strong humidity dependence, to mono-molecular layers of adsorbed gases.*

It seems certain that layers of chemisorbed gas only a molecule or two deep can cause additional forces of attraction - or even of repulsion. Alternatively, acting as a screen over the surface of a solid, they may reduce

---

* On the other hand, Dalmon & Tiby (1972) found no evidence of dipole-like action in the dusts they examined.

values of London-Van der Waal forces. Consider three polar gases of interest, viz H_2O and SO_2 which occur naturally in flue gases, and NH_3 which is often added as a conditioning agent, together with other non-polar gases. The polar moment is measured in Debye:

H_2O		1.84×10^{-18}
SO_2		1.60×10^{-18}
NH_3		1.46×10^{-18}
CO		0.1×10^{-18}
CO_2	$<$	0.01×10^{-18}
O_2	$<$	0.01×10^{-8}

Molecules of H_2O will certainly chemisorb on the surface of a homogeneous particle with either the positive or negative pole inwards depending upon the nature of the solid surface thus:

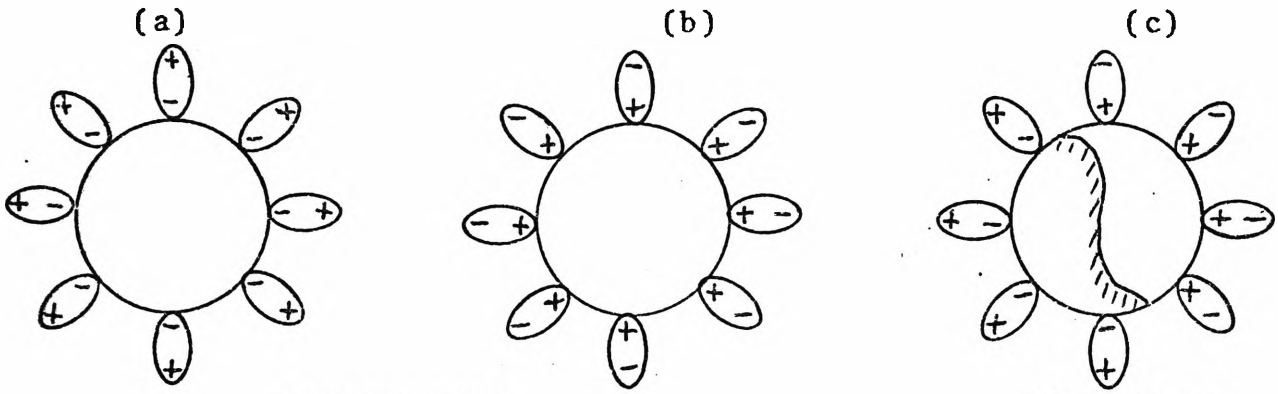

Therefore the outer positive charges of one particle will weakly repel another such particle[100], giving the appearance of diminished overall Van der Waal attraction. If however, the particle has dissimilar surface areas - perfectly possible with industrial dispersoids - then it may, as shown in sketch (c), have patches with negative or

positive ends of ions inward. Two such particles may now very well attract each other more strongly, since unlike poles will attach.

It may be that some of the conditioning agents added to render a resistive dust more conductive, may also act to increase the adhesivity of the dust, by dipole action evinced by a feel of greater 'stickiness'.

These few remarks will have to suffice as a statement of the problem of dipole attraction.

The means by which it may be documented at an experimental level are noted in para.3.5; where such gaseous molecular layers are removed under vacuum. Hopefully, adhesive forces might then be measured without the effect of contaminants.

2.6 Layer Detachment

We are in a position to formulate a general relation for the amount of a layer detached due to acceleration. In the adjacent sketch (a), a layer of deposit T thick has a uniform tensile strength P_t shown in sketch (b). If now the dust is given an acceleration $\ddot{z}$ relative to the solid surface, it is desired to determine how much of the layer will detach.

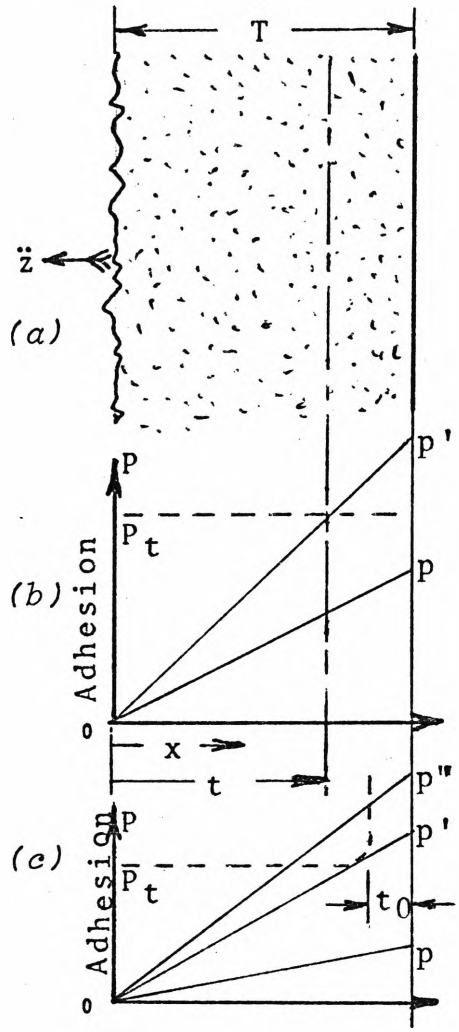

Consider a section x. There is a stress acting on surface x of

$$P = \frac{F}{A} = \frac{M}{A}\ddot{z} = \alpha \times \ddot{z} \qquad .....(2.37)$$

where $\frac{M}{A}$ = mass per unit area between Ox, and α = density of deposit.

Therefore at any section x, the tension in the layer is given by the straight line Op in sketch (b), where the slope is $(\alpha\ddot{z})$. The maximum stress occurs at the solid substrate and is given by $(\alpha\ddot{z}T)$. Since the stress in the deposit (Op) is always less than the strength of the deposit P_t, there is no fracture. For a stress line of (Op'), the whole thickness T should detach, but probably there will be fragmentation from $t < x < T$. There is some evidence that there is a skin of greater tenacity than the average at the solid substrate, so that in such a case, the strength curve is as indicated in sketch (c). There are some theoretical grounds for expecting such an 'underskin' from eq.2.18:

$$\Delta F = \frac{(\pi^2 \lambda n^2)}{24 Z_o^2} \left(\frac{d_1 d_2}{d_1 + d_2}\right)$$

For interparticle forces, the second bracket becomes $(\frac{d}{2})$, while at the interface, $d_2 \to \infty$ and the second bracket becomes d. Thus the innermost particles should adhere twice as strongly. Again considering sketch (c) it is only when the stress line moves from Op' to Op" that any detachment takes place.

The sketches (a), (b), (c) also bring out very clearly that it is harder to remove a thin layer because it has a small mass. For a given slope Op and small thickness, the layer may not detach, but if the layer T should build up, then the same acceleration may enable the deposit to break away.

These simple but important facts may be quantified by saying that until the layer thickness reaches a certain minimum value:

$$T \leqslant (P_t/\alpha\ddot{z}) \qquad \ldots\ldots(2.38)$$

no material at all will detach.

It is possible to interpret Sproull's data of Fig.2.8a in terms of a tough underskin. Suppose there is a layer, t_o, which adheres so tightly that rapping does not dislodge any part of it. Then rapping efficiency = $\frac{t}{T} = \frac{t}{t+t_o}$ which has the form of the sketch below.

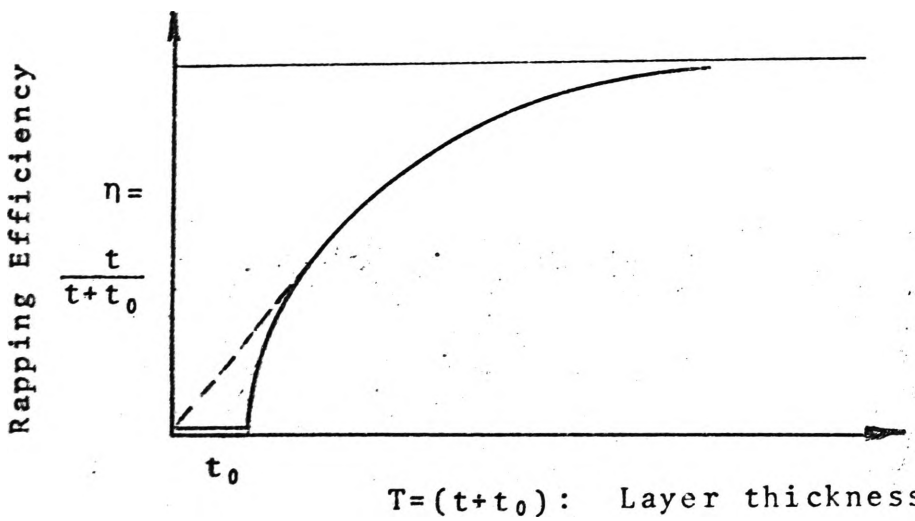

The step at t_o is unlikely to be ever measured in practice, for odd pieces flake away in a random manner, giving rise to the dotted portion of the curve instead. The form of the sketch above then resembles the data put forward by Sproull in Fig.2.8a. This constitutes an extremely simple interpretation of the Sproull data, a plausible alternative to that given in para.2.2.3.

A rather typical case of an 'underskin' may be observed in the photograph of Fig.3.14.

2.7 Towards a General Theory

It is an appropriate time to review and summarise our findings as to the total adhesive stresses in a layer of particles which, combining eqs.2.20, 2.32, and 2.29 there is:

$$P = \left(\frac{A_1 d}{d^2} + \frac{A_2 d}{d^2} + \text{Pelect}\right) \quad \text{dyne/cm}^2$$

$$P = \left(\frac{A_1}{d} + \frac{A_2}{d} + 10^5(\varepsilon_o/2)\left[E_\ell^{\,2}\left(\frac{d}{kd'}\right)^2 - E_g^{\,2}\right]\right)$$

Van der Waal — Capillary — Electrostatic

.....(2.39

where: P dyne/cm^2, total adhesive strength
d cm, diameter particle

We can now summarise what we know numerically about the Van der Waal constant A_1 and the capillary constant A_2 in the following table:

Table 2

Force on a Single Particle

$\Delta F(dyne) = A\ d(cm)$

Source	Quartz	Glass	Alumina	Zinc	Iron Oxide	Silica	Bronze	Fly-Ash
	Dry A_1							
Bradley[83]	66							
Beischer[86]					3			
Boehme et al[87]					6			
Penney & Probst[61,68]						7.6	.15	3.5
Farley & Valentin[94]			4.5	0.8				
	Saturated Water Vapour A_2							
McFarlene & Tabor[97]		215						
Rumpf[99]		202						

The constant A_1 depends upon the particle shape and surface condition. Obviously much more work needs to be carried out on industrial dispersoids, for the present picture is exceedingly sparse.

2.8 FUTURE WORK

We began this chapter dealing with forces of adhesion in a low key, aware that the topic would be onerous. It has however proved possible to piece together a fair theoretical framework from works on soil mechanics, powder technology, and physical chemistry. There are some scattered experimental results, but the picture remains very incomplete. Some recent publications have appeared showing evidence of three or four active groups in Germany, U.S.A. and England who are approaching the problem from the point of view of either the storage and transport of powders, or else the manufacture of powders into pellets and briquettes. So long as these groups remain active, the writer considers it would be inappropriate for electrical engineers to become involved in the general theory of the properties of powders.

There are however certain areas in which the electrical engineer with an interest in electrical precipitation could make a valuable contribution which, the writer believes, would be welcomed by the powder technologists. Deposition by electrostatic precipitation may prove to provide optimal packing. The following topics could profitably be examined:

Porosity of electrostatically deposited powders would be a comparatively easy parameter to document as a function of particle composition, size and corona precipitating field.

Tensile Strength of electrostatically deposited powders as a function of gaseous environment, corona current density and electric field, particle size and composition. It should be noted that there is an immediate need to check the veracity of eq.2.17 which

gives the electrostatic component of force. Penney et al apparently did not conduct this type of experiment. Sproull did conduct experiments with and without the corona power on, but unfortunately has no record* of E, J or $\bar{\rho}$.

Complex Dielectric Constant The general theory of interparticle force by Liftshitz requires information on the complex dielectric constant of the powder material. By using information gained from porosity, permittivity for the bulk material could be related back to the solid particles. Electrical Engineers with facility in microwave/optical techniques could well undertake such studies.

In the next chapter, the writer makes his own modest contribution in the design and construction of a unique machine - the Precipifuge - designed to carry out studies of the tensile strength of powders.

---

* personal communication - Sproull has only a recollection of certain figures.

CHAPTER 3

CONCEPT AND DESIGN OF A PRECIPIFUGE

3. CONCEPT AND DESIGN OF A PRECIPIFUGE

At the conclusion of Chapter 2, the need for much more data on the tensile strength normal to the plane of deposition of precipitated layers of particles was apparent. An extensive experimental programme was therefore indicated, to determine the tensile strength of a layer as a function of:

Manner of precipitation (temperature, current density etc)
Particle composition
Particle size
Applied electric field
Corona currents
Adsorbed gases
Temperature (preferably 0 to 200°C)

A suitable apparatus to compe with all these parameters would obviously be complicated, but an effort ought to be rewarding. It is appropriate therefore to review the methods used by other workers. The basic methods have been reviewed by Krupp et al[85] viz

Pendulum (Bradley para 2.2.1)
Tensile Tester (Ashton, Radford etc. para 2.3.3)
Inclined Plane
Impact on Plate (Ruckelshausen Fig.1.15)
Impact on Solid Plunger (Sproull para 2.2.3)
Centrifuge (Boehme et al, para 2.2.1, Penney et al para 2.2.3)

The pendulum method is suitable only for single particles. The Tensile Tester could not have a high electric field applied in the direction of the extension. The Inclined Plane depends upon finding the shear strength, which in turn involves the uncertain rolling action of some particles. There is so much controversy concerning the inclined plane, that it appeared to be inviting trouble to adopt it. The impacting plate was not considered because the complicated

modes of ensuing vibration make the extraction of fundamental data on the powder very difficult. The impacted plunger used by Sproull, though obviously a marked improvement on the impacted plate, still gave data with a high scatter of results. The centrifuge method appeared to offer the possibility of clearest information with the least ambiguity.

3.1 Corona Electrode Geometry

One has to determine a possible geometry of electrodes which is at the same time compatible with a centrifuge. The criteria for the corona chamber are basic to the whole of this project but the several design considerations tend to conflict. The chamber must provide an earthed electrode and high tension electrode suitable for precipitating dust in the usual way. The receiving electrode upon which dust is precipitated must be convex outward so that the precipitate may then be centrifuged off. For precipitation to occur, the electrode system must be of such a geometry that moderate values of H.T. supply - say 30kV - will be enough to produce adequate corona currents.

A possible geometry is illustrated in Fig.3.1 where the central electrode is positive and becomes the receiving electrode. The negative discharge electrodes are a series of wires parallel to the axis and symmetrically spaced. A glass container, suitable for high voltage and elevated temperature, surrounds the whole to contain heat, to provide mechanical support, to give a measure of safety to personnel and to allow visual observation of the phenomena taking place.

In order that current densities on the receiving electrode may be claculated with some accuracy, a guarded set of earthed electrodes is required, one at each end. Such an arrangement requires high speed slip-rings to pass the corona current to earth via a micro-ammeter.

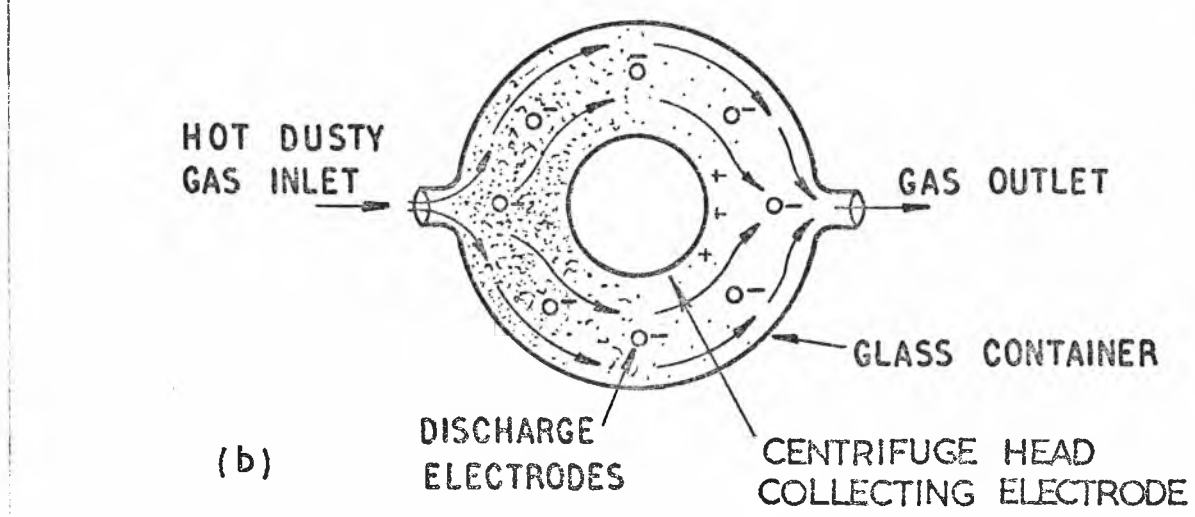

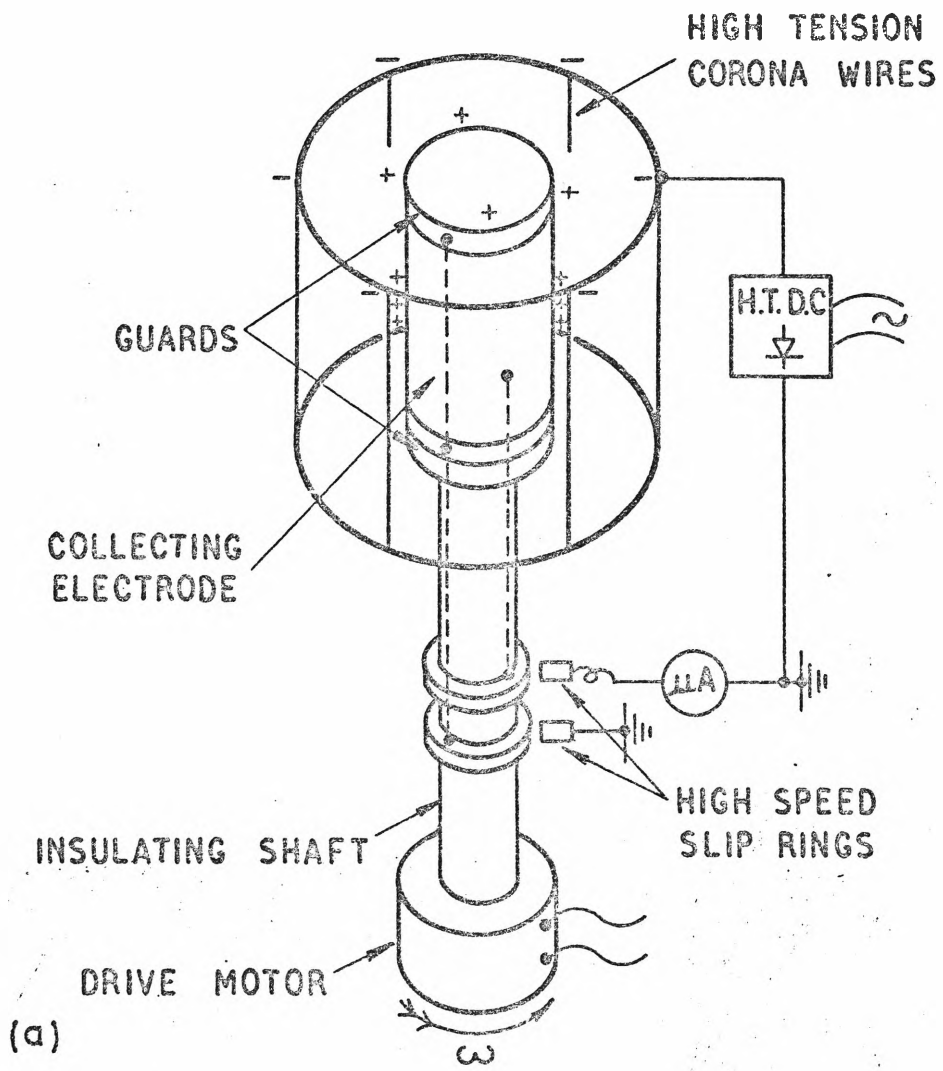

FIG. 3.1 BASIC PRECIPIFUGE GEOMETRY AND CORONA CHAMBER

(a) Six H.T. emitter wires surround a cylindrical receiving electrode, guarded at each end. Slip rings complete the corona circuit to ground.

(b) Glass chamber surrounds electrode assembly, containing hot gas and corona.

3.2 Mode of Operation

The scheme of operation of such a device would be as follows. First, dusty gas would be admitted to the corona chamber with the rotor stationary, and with corona currents flowing. After sufficient dust had been deposited, the gas flow would be stopped. Then the rotor would be spun, with the HT on or off as desired; observing the surface of the dust stroboscopically, the speed at which dust detached would be noted. Finally the adhesive force could thus be calculated at a known current density and electric field.

3.3 Preliminary Adhesion Tests

Since there was no experinece at Wollongong either with the tensile strength of powders or with centrifugal technology, it was deemed prudent, before designing the centrifuge, to gain at least a little first hand experience. Some preliminary local tests were therefore indicated to verify the order-of-magnitude values found by Penney et al and Boehme et al.

The centrifuge chosen for this purpose was a Bechman-Spinco Ultra Centrifuge L2-65 capable of spinning a head, pear shaped and 10 cm dia at base, at 65,000 rpm. The head was of forged aluminium, with a polished, black anodised exterior. The experiments were conducted in the Medical School, Sydney University by courtesy of Dr. A. Pollack. After removing the rotor head from the Spinco, a sparse layer of fly-ash was electrostatically deposited on the outer surface of the rotor head, the object being to measure forces on single particles rather than agglomerates. After placing the rotor head carefully in position, the chamber was sealed and evacuated with an oil-diffusion pump to a pressure of about 6μmHg. Temperature was maintained at 21 to 23°C. The machine was run up to speed, accelerating in 5 minutes, remaining at speed for 5 minutes and then decel-

erating in 5 minutes. The surface was inspected visually for signs of dislodgement of particles after each speed increment. The qualitative results of the tests are as indicated:

Speed	Appearance
10,000	No visible dislodgement
20,000	Slight visible dislodgement
25,000	Marked dislodgement
35,000	Some 50% particles detached

It was therefore concluded that to remove 95% of particles, it might have been necessary to increase the speed to 75,000 rpm. Clearly, the radial acceleration required to detach single particles were in the same order as those reported by Boehme et al.

3.4 Radial Acceleration of the Wollongong Machine

A major decision to be made, was to decide on the radial acceleration to be produced by the Wollongong machine, viz:

$$\text{acceleration} = \omega^2 r/g$$

At the Battelle Institute, as noted in the preceding paragraph, an ultra-centrifuge was used, producing an acceleration of $2 \times 10^5 g$ at 50,000 rpm, at which speed most particles were detached. Later, they used a machine with $10^6 g$ produced at 1 cm radius at a speed of 300,000 rpm.

The acceleration required at Carnegie (Penney et al) to detach macroscopic layers was, predictably, far lower. For fly-ashes, the relevant figures were at most 2250 rpm and 6 cm radius corresponding to 135g.

A decision was made therefore to concentrate studies on thick layers with a machine running at 10,000 rpm, initially with a radius head of 3.18 cm, giving an acceleration of 3500 g.

To have constructed an ultra-centrifuge from first principles would have entailed a very large engineering effort with uncertain return.

When examined carefully, the task of converting a commercial existing ultra-centrifuge to include a high voltage corona chamber and slip-rings would have been exceedingly difficult.

Morover, data from macroscopic tensile data has been shown in para 2.3.3 and 2.2.3, to yield good microscopic data when related to particle size.

It seemed prudent therefore to design a medium speed centrifuge of 10,000 rpm meanwhile, and limit experimentation to thick layers.

3.5 Vacuum Facility

Every serious paper dealing with the adhesion of small particles expresses some concern about the presence of the one or two molecular layers of adsorbed gases, and the uncertainty of the effect they might have. A number of investigators used vacuum to remove some of the contaminants.

The writer decided that it would be worth some effort to provide vacuum facilities on the Precipifuge so as to be able to clear up possible uncertainties about the effect of contaminating gases. Such a facility would also enable any scouring effect on the surface of the dust deposit during centrifuging to be positively assessed.

3.6 Prototype Precipifuge

Rather than meet every technical problem at once, the writer decided to build a prototype precipifuge which would embody all features except the vacuum facility.

3.6.1 General Assembly and Drive

A first assembly is illustrated in Fig.3.2. The supporting framework was cast aluminium alloy. The top bearing was of sealed type to prevent possible ingress of dust into

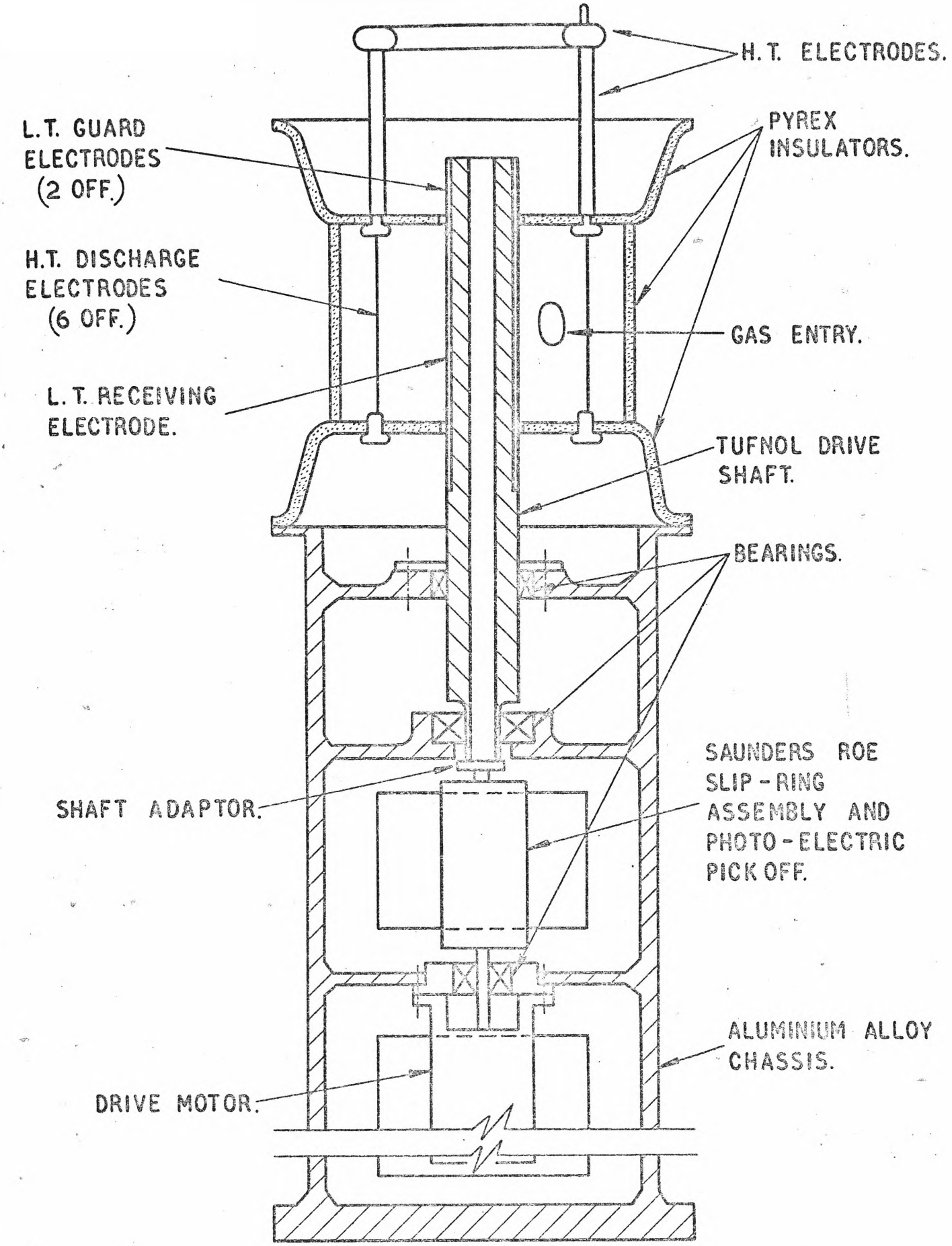

SCALE 1/4 FULL SIZE

FIG. 3.2 GENERAL ASSEMBLY OF PROTOTYPE PRECIPIFUGE

the ball race. The second bearing was of self-aligning type to compensate for any small mechanical misalignment of the bearing housings during boring of the casting. The slip-ring assembly was keyed to the main drive shaft while at the bottom end it was supported by a flexible coupling.

Since the main shaft had to act both as a mechanical member subject to considerable centrifugal forces, as an electrical component supporting the low tension electrode system, and also since it was to be subjected to temperatures exceeding 100°C, considerable care was exercised in its design. The material selected was a bakelised canvas commercially known as Tufnol, possessing excellent mechanical characteristics.

The drive motor was required to be infinitely variable in speed from 100-10,000 rpm. Direct drive was envisaged so as to avoid the loss of power and space entailed with either a step-up gearbox or belt-drive system. Direct drive does however entail special problems, for motors running to 10,000 rpm are comparatively rare.

The only torque from the motor required would be that necessary to overcome bearing friction and wind resistance. Static measurements of friction in the complete system inclusive of all bearings and the slip-ring assembly were carried out. Static torques (of between 0.10 and 0.12 Nm) were consistently measured. If higher torques than static torques were not encountered, then the maximum power required ought not to have exceeded 120 watt.

It will be appreciated that manufacturer's data on bearing friction is sketchy, for in general applications, such bearing torque is a minute percentage of loss. Based upon this estimate, an Evershed Vignoles split-field precision servo-motor of d.c. type with inbuild tachogenerator was incorporated as a drive. It was provided with precision electronic control comprising constant armature current, long-tail pair d.c. amplifier for the field, and speed stabilisation

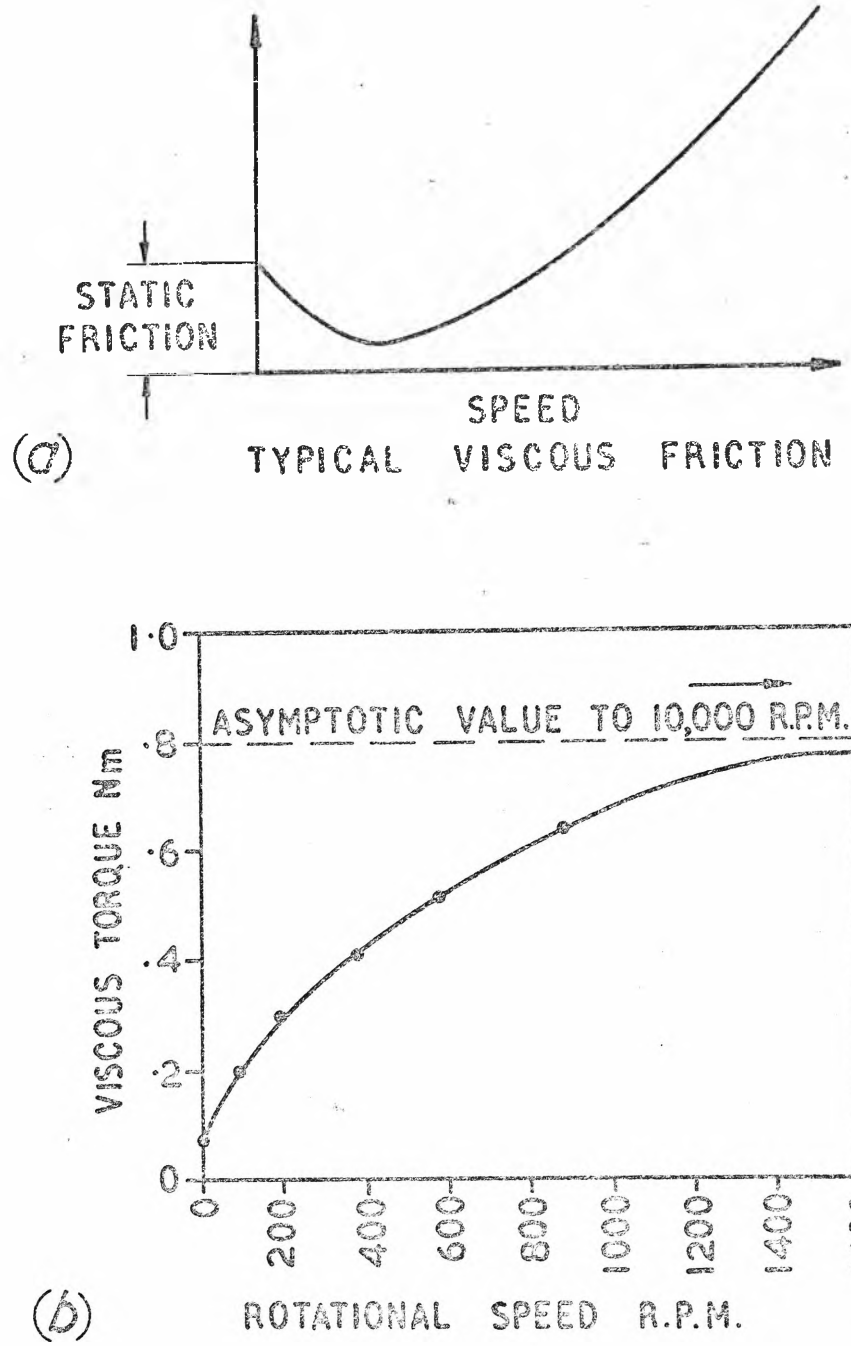

FIG. 3.3 FRICTION LOSS IN THE PRECIPITUGE AS MEASURED

by derivative feedback. Unfortunately this elegant system failed to drive the shaft at any appreciable speed and it had to be abandoned.

A commutator type a.c.- d.c. universal motor, type EAM 106 constructed by Technico Electronics was used. With a power of 360 watt at 8,000 rpm it appeared to be adequate and was again installed, but this expensive system failed to drive the centrifuge at any appreciable speed and accordingly it was discarded.

The largest variable speed commutator motor made by Technico Electronics viz: type OJ9 was inserted into the centrifuge. With a power of 750 watt, it ought to have been adequate. Severe bearing noise developed in the centrifuge attributed to slight misalignment between the second and third bearings. The third bearing was discarded and replaced by a flexible coupling. The resulting easing of friction enabled the speed to be lifted a little but still short of that required.

Each change of mechanical design necessitated a considerable effort of both professional and technician staff. The total number of man-hours being used merely to put the hardware into a working condition, was approaching a serious level.

A critical appraisal of the mechanical losses in the moving system was obviously necessary but hampered by lack of published information on dynamic bearing friction. In spite of the difficulties of measuring the dynamic losses in the system at 10,000 rpm, it was felt that the effort was mandatory. The only explanation for the successive failure of several motors seemed to be that the dynamic friction must be rising very steeply indeed. On general theoretical grounds, viscous friction may be expected to vary as shown in Fig.3.3a. On the grounds that the speed may have taken the friction in the system beyond the minimum and into the rapidly rising region, the dynamic test aimed to investigate this possibility. The results of this test are shown

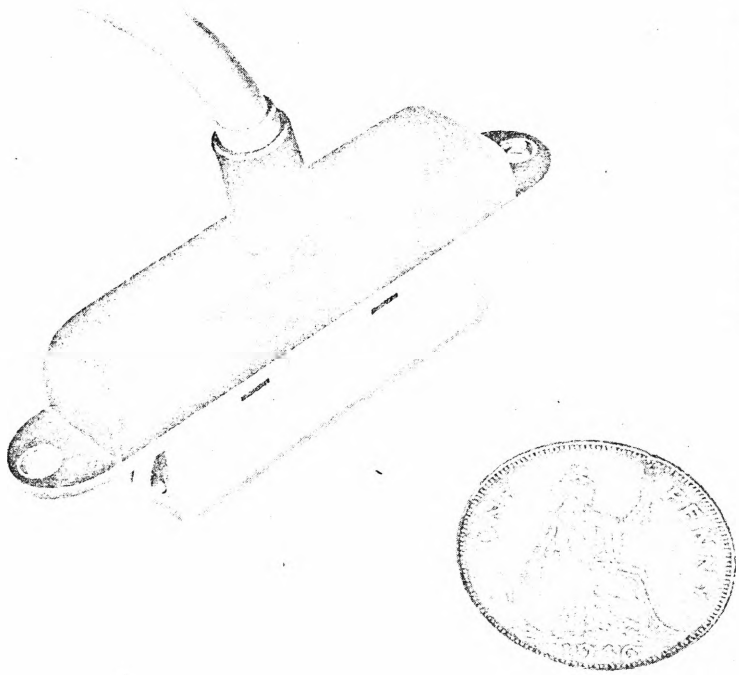

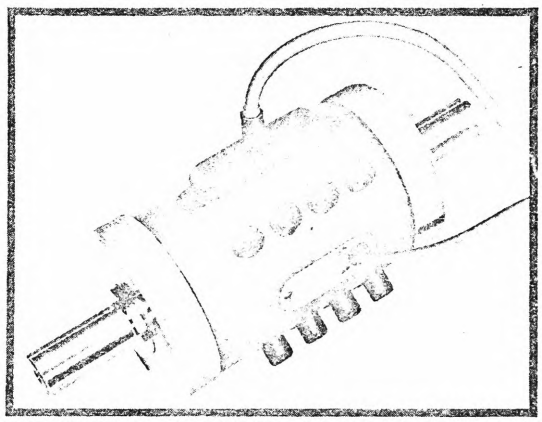

Type 2 Torque Transducer
fitted with Speed Pick-Off

FIG. 3.4 SLIP RING ASSEMBLY

The Saunders Roe 10,000 RPM slip-ring assembly with four independent channels through low noise silver-graphite slip rings. Optical speed pick-off.

in Fig.3.3b.

The power loss is now seen to be ≈ 800 watt. The trouble was traced mainly to a rubber dust seal which when removed allowed a sufficient range of speed for the prototype to function.

3.6.2 Slip Ring Assembly

Since the concept of the present series of experiments is to expose the dust particles being centrifuged to ionic gas current, it is necessary to be able to bring current from the moving to the stationary system. Since the currents are of the order of 1mA, it is important to use slip-rings with a low noise content, and which generate no thermal emfs.

The Saunders-Roe slip-ring assembly, shown in Fig.3.4 has the following data:

Four silver slip-rings
Eight silver-graphite brushes - two per ring, giving two parallel paths per ring.
Speed range 0-10,000 rpm
Temperature range 0° to 60°C
Noise level - random waveform - approx 6μV/mA/1000 rpm
Thermal emf.-below detection at all shaft speeds
Rotor : one piece construction fabricated from a spin moulded dielectric of thermo-setting resin in glass fibre
Stator : supported by the rotor via integral high speed ball bearings.
Optical Speed Pickoff: light source and biassed photo-transistor integral with the remainder of assembly.
Pulse output 6V up to 10,000 rpm.

Thus the slip-ring assembly provides four independent current paths of low noise level and free of thermal emfs. It also

embodies an optical synchronous pulse-generating device which may be used either to actuate a counter or to trigger a stroboscope. In the present situation both functions were envisaged. The device performed within specification under all circumstances.

3.6.3 Heating System

In order to heat the ionising chamber, a 1 kW preheater with a blower was used to direct a stream of hot gas into the chamber. Both the rate of gas flow and the temperature of the heater were continuously controllable so that temperatures of 115°C were easily maintained in the chamber. This was regarded as being the upper limit of allowable temperature because of the organic nature of the drive shaft.

3.6.4 Corona Chamber Design

In Fig.3.5a is shown the first step in the mechanical design of the Corona Chamber. The discharge wires were silver soldered at either end to the substantial electrodes visible in Fig.3.5a whose purpose was to mitigate undesirable corona at the ends of the wires. These latter electrodes were mounted onto flat insulating end plates constructed from the same bakelised canvas material (Tufnol) which was used for the drive shaft. Mechanical rigidity was provided for the end plates by the pyrex cylinder. The corona chamber as a whole rested on top of the aluminium frame casting. Though the Tufnol material has a high resistance to surface tracking, severe arching took place from the bottom of the H.T. electrodes to the earthed frame.

To prevent this tracking from taking place, the bottom end plate was isolated from the frame by means of the porcelain insulators illustrated in Fig.3.5a. These porcelains prevented the surface tracking and the discharge wires generated satisfactory corona currents at room temperature.

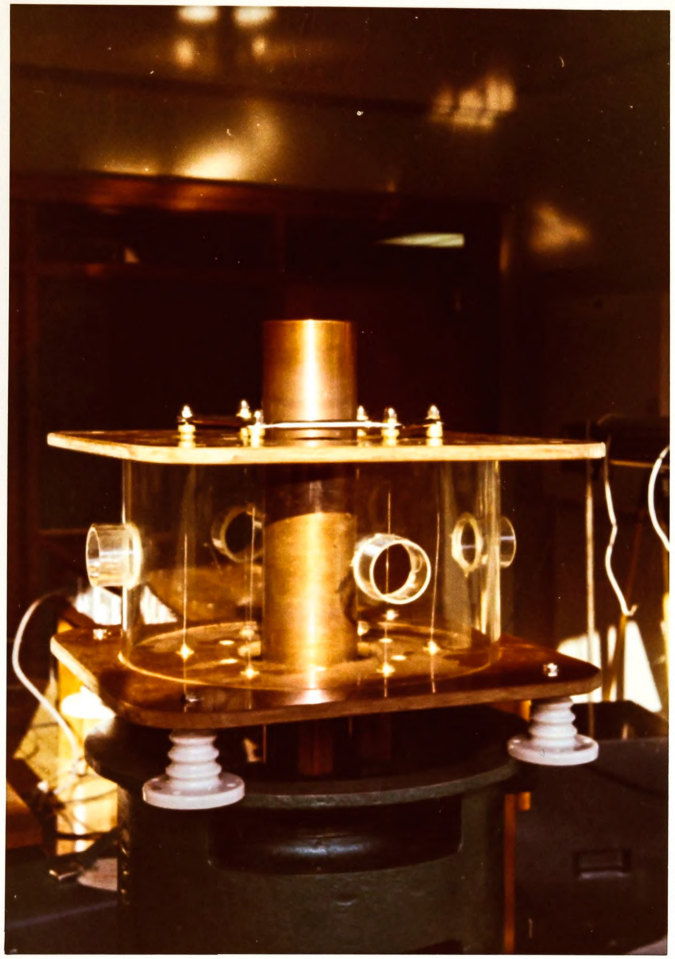

(a) Tufnol end plates and pyrex glass enclosure. Stable at room temperature. Quite unstable at 110°C.

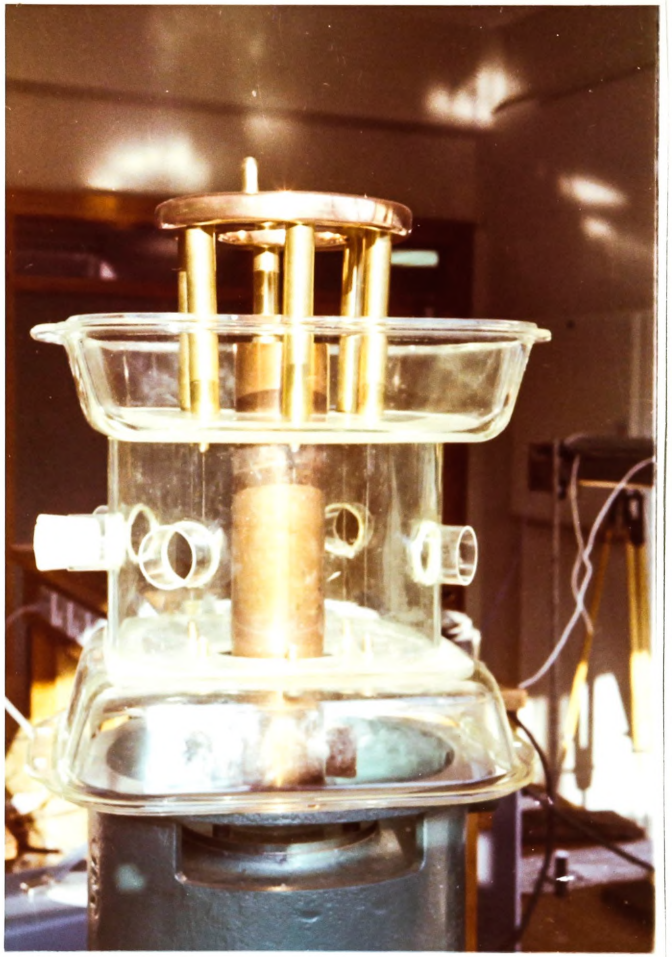

(B) Pyrex glass used throughout. Excellent corona characteristics at all temperatures.

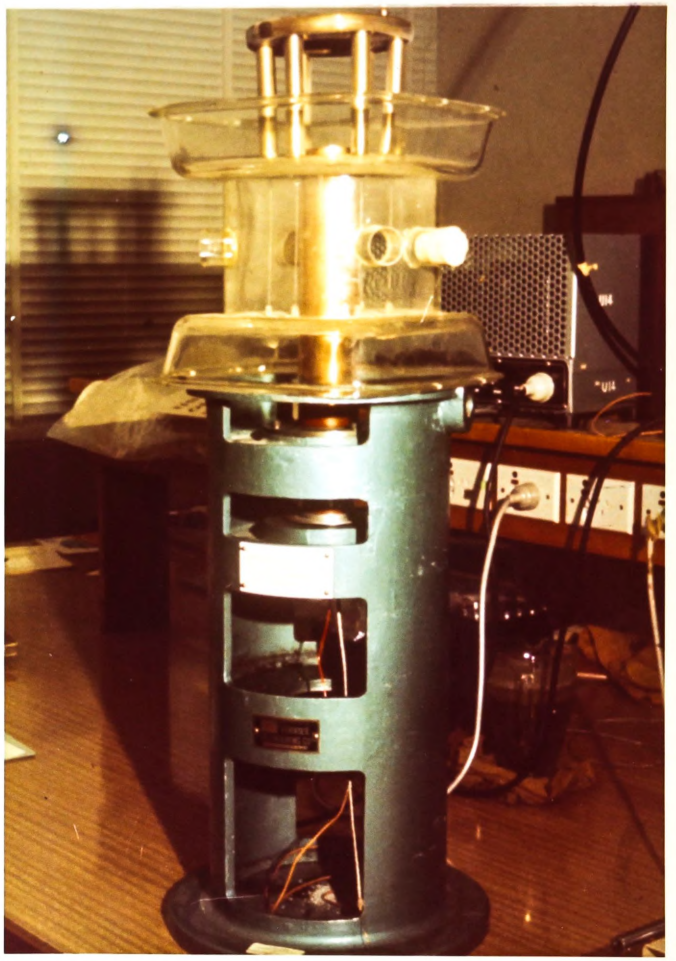

(c) General Assembly

FIG. 3.5 PROTOTYPE CORONA CHAMBERS

Thermal Instability of End Plates

When the chamber was brought up to 100°C, and the electrode system lifted to 10 kV, serious electrical instability of the end plates took place. Strong brush corona appeared in the space between the inside diameter of the end plate and the central earth electrode. Examination of the potential over the surface of the end plates by an electrometer probe showed that the whole area was alive at the full value of the high tension. This situation was regarded as being serious, since the chamber cavity would tend to become an equipotential space. For this reason, it was impossible to generate corona where it was required, viz at the discharge wires. Because of its thermal instability, the bakelised canvas end plates were discarded.

Some four different thermally shock resistant glasses were tested in an endeavour to find a suitable material. Pyrex was the only glass found to be satisfactory, the leakage current at 30 kV being negligible.

Effective Form of the Corona Chamber

The first successful form of the corona chamber is illustrated in Fig.3.5b. No unwanted tracking took place at any voltage up to 30 kV and for temperatures up to 120°C. The electrode assembly passed no measurable current until the applied voltage reached 19 kV when corona discharge began to take place from the stainless steel discharge wires. The corona chamber was now behaving satisfactorily both electrically and thermally.

3.7 Current Density and field Strength within the Chamber - discontinuities apparent

The two most important electrical requirements of the corona chamber are that the corona wires will discharge in a stable fashion, and that the current density and field strength at the inner receiving electrode be uniform.

3.7.1 Current Discontinuities

A very interesting phenomenon was observed within the corona chamber which shed some light on the current densities reaching the central electrode. The central electrode, constructed of recently machined and polished copper, was inserted in position in the chamber and the temperature raised*. Mild surface oxidation took place characterised by a bluish hue typical of subtractive spectra through thin layers. When corona currents were passed through the system it was observed that a clear pattern was etched on the surface of the electrode. The bluish oxide film was no longer visible in some areas. The pattern defied effective photography but is reproduced in Fig.3.6. The corona discharge had obviously reduced the non-stoichiometric copper oxide. The six segments were aligned azimuthally with the six discharge wires. When the system was switched on in total darkness, some of the wires disclosed needle-like tufts of blue light, about two millimetres long and directed radially inward. This behaviour has been observed by many workers studying negative corona, and already noted in par 1.1. In the present situation these needles, spaced regularly along the length of wire at about 1 cm, corresponded to the horizontal etching observed in several of the segments. The most surprising implication of the etched pattern was the zone between each of the segments which remained quite unaffected. If the etching was related to the current density at the receiving electrode, then the pattern disclosed non-uniformity in current density.

3.7.2 Possible Reaction

While the exact mechanism of the disappearance of the copper oxide is uncertain, it is at least possible that the

---

* Very high indeed, due to an overlong coffee break!

following reaction can take place:

$$\left.\begin{matrix} 2(O_2)^- \\ \underline{\text{or}}\ 2(-e) \end{matrix}\right\} + (Cu_2^{++} + O_2^{--}) \rightarrow 2Cu + 3O_2 + 2(-e)$$

The current carriers in air at NTP are mainly singly charged negative oxygen ions (O_2^-) but there are a few high-energy free electrons. It is supposed that either carrier impinges upon the oxide layer with kinetic energy. The copper oxide is in a matrix ionic state in which positively charged copper ions and negatively charged oxygen ions coexist. The impinging negative carrier discharged the copper ion, while the oxygen ion relinquishes its negative charge to complete the electrical circuit. Oxygen molecules diffuse through to the surface of the film and are released as gas. The copper is finally reduced and a spongy matrix of pure copper remains.

For the energy equations to be satisfied, there must be some carriers of such energy that

$$\tfrac{1}{2}mv^2 > \Delta G + hf$$

where ΔG is the total free energy of association in the reaction, and hf is radiation if emitted.

Although the above hypothesis for the reduction of the oxide film is feasible, it must be observed that another mechanism is possible. It is a common practice to clean surfaces by bombarding them with high energy +ve ions derived from a gas at pressures of say, 1 torr.

The possibility that the phenomena could have been due to sputtering may be examined as follows.

The mean free path of molecules in air at N.T.P. is approximately 10^{-5} cm. Taking an energy of 20 eV as being the lowest at which sputtering could possibly occur, we are lead to a field strength at the surface of the collecting electrode of:

$$E = \frac{20}{1 \times 10^{-5}} = 2 \times 10^6 \text{ V/cm}$$

Such a high field strength is impossible. Hence we may infer that sputtering is unlikely to account for the etched pattern observed.

Finally, we may conclude that of the two mechanisms examined, the former, in which a reduction of the oxide layer is proposed, is more probable.

The patterns etched on the surface of the copper electrode are not pertinent to this present investigation except insofar as they give an indication of current densities. The immediate conclusion to be drawn from the patterns is that the ionic current densities at the surface of the receiving electrode are not uniform. This was regarded as being serious enough to warrant deeper study.

3.7.3 Assessment of the Electric Field within the Corona Chamber

The extremely discontinuous etched pattern discussed in the preceding paragraph was quite worrisome. Naturally, it was desired to establish around the periphery of the centrifuge head the most uniform possible field of E and J. Any attempt at a full analysis of the situation would require a numerical solution of a Poisson equation of considerable complexity, quite unjustified at such an early stage of design.

Meanwhile it was decided to make a quick examination of the electrostatic field prior to corona onset, to see if there was anything which might account for possible later discontinuities in J.

Since the system was guarded, attention could be confined to the plane central between the end plates, so reducing the problem to one of two dimensions. Tests had indicated that the Pyrex insulating system of Fig.3.5 carried negligible leakage current, allowing it to be idealised as a perfect insulator. The uncertainty of the nature of the azimuthal boundary suggested an analogue approach to the field

problem to be much prefered over a mathematical one based upon doubtful assumptions.

Accordingly, Teledltos (conducting) paper was prepared with a cross section of the Corona Chamber drawn to full scale. Conducting surfaces, e.g. the inner receiving electrode and the discharge wires were painted in with a silver solution with fine lead wires attached. A print of the completed plot is shown in Fig.3.7. The discharge electrodes could not be drawn to scale and in fact the resulting drops of silver were not quite regular as a study of the print discloses. Such imperfections in the drawing would have little effect at the earthed electrode.

Five basically different boundaries were studied corresponding to Sectors 1-6, in every case the receiving electrode being earthed (V = 0), and the discharge electrode set at V = 100%. Equipotentials were plotted in all six sectors with the orthogonal flux lines in some. The boundaries of each sector, due to symmetry, must be flow lines, so a radial cut was made in the paper there, indicated by the heavy radial black lines. The several models were set up because it was not certain how the Pyrex container would behave.

Sector (1) : The outer cylinder was taken to be a conductor at earth potential. The field strength at the inner cylinder was then found to be closely uniform, azimuthally. The 50% equipotential, but for irregularities in the discharge electrode, would have been circular and nearly concentric with that electrode.

Sector (2) : The equipotentials were drawn in simply to confirm the sketch of Sector 3.

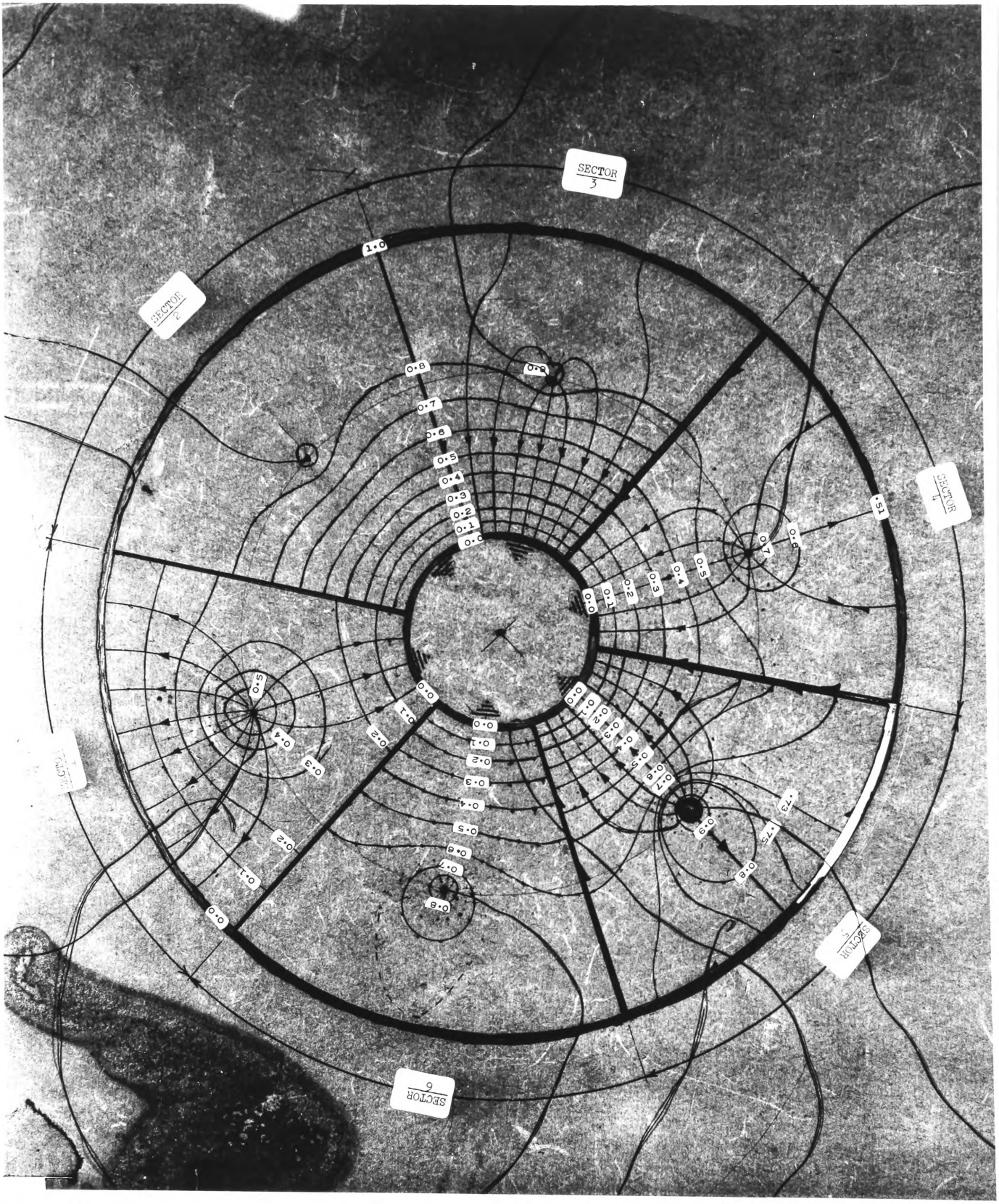

FIG. 3.7 ELECTROSTATIC FIELD PATTERN IN THE CORONA CHAMBER

An analogue electrostatic flux distribution in the corona chamber of the Precipifuge. Teledeltos conducting paper is used. Equipotential surfaces painted on with silver paint. Flow line boundaries established by cutting the paper. In all cases the discharge electrode is at 100% potential.

Sector (3) : The outer cylinder was taken to be an equipotential at 100% potential, i.e. the same as that of the discharge electrode. Again the azimuthal field strength around the inner periphery was found to be uniform. The voltage gradient around the discharge electrode has been seriously diminished by the presence of the neighbouring H.T. Electrode. (i.e. the outer cylinder)

Sector (4) : The outer culinder was taken to be a conductor, but floating. It was found to adopt a potential of 51%. The field intensity at the surface of the receiving electorde was once again found to be uniform. The 70% equipotential was closely circular and nearly concentric with the H.T. electrode.

Sector (5) : The outer periphery was held to be the boundary of a flow-line. Accordingly the paper was cut around the periphery. The H.T. electrode diameter was greatly enlarged. Again the field strength at the surface of the inner electrode is uniform. The 90% equipotential is circular but eccentrically situated.

Sector (6) : A repeat of the flux plot of Sector 5 but this time with the discharge wire of pinhead size. The field strength around the inner periphery is uniform. The 80% equipotential is a circle concentric with the discharge electrode. As compared with the configuration 5, the equipotentials are of the same shape, but predictably shifted in magnitude.

Since the glass might become charged in practice, the true boundary might best be represented by sectors 4 and 5.

A careful examination of the five plots in Fig.3.7 shows the electric field around the inner earthed electrode to be remarkably uniform in all cases. There is no hint of any singularity in E which might later lead to discontinuities in J. Therefore the causes of the apparent discontinuities suggested by Fig.3.6 were still entirely unexplained.

The situation remained serious on two scores. The corona chamber of Fig.3.5b, though working perfectly well from the point of view of macroscopic currents and voltages might be actually behaving poorly on a microscopic level. Secondly, if there really were discontinuities in J over the anode of Fig.3.5b, then might there not be discontinuities in other electrode geometries such as the concentric cylinder of Fig.1.5 or the wire in duct geometry of Fig.1.6?. If the investigators in these cases, e.g. Pauthenier and Moreau-Hanot, and Penney and Klingler, together with a host of others who have worked with coronas, were unaware of the presence of such discontinuities, then what effect did these have on their experiments? What did their measurements actually mean? For the particular technology of electrostatic precipitation, the consequences of current density discontinuities could only be serious, adversely affecting dust precipitation.

The writer felt that the matter was on the one hand disturbing - and on the other extremely interesting, certainly worthy of investigation. It was therefore decided to divert attention from the Precipifuge meanwhile to an examination of the phenomena. Such an examination has been carried out in C6. As matters turned out, the misgivings over the discontinuities observed in Fig.3.6 proved to be well founded, for the whole of the anode surface of a wire-in-duct corona system contained the discontinuities disclosed in Fig.3.6.

3.7.4 Accommodating the Discontinuities

Since the studies of C6 indicated that the corona discontinuities were of a rather fundamental origin, there was nothing whatever that could be done to an electrode geometry to avoid them.

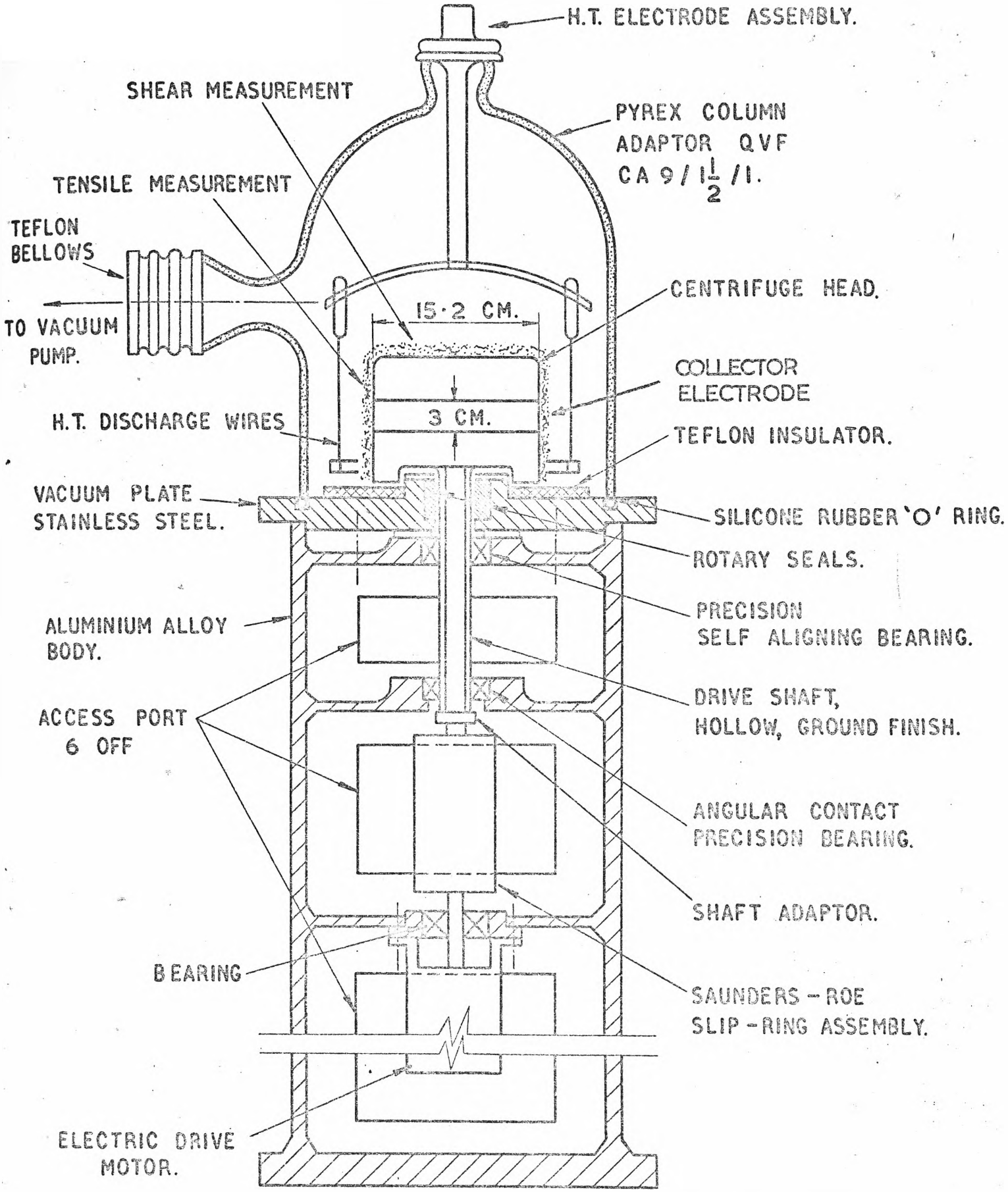

SCALE : 1/4 FULL SIZE

FIG. 3.8 FINAL PRECIPIFUGE ASSEMBLY

In the Precipifuge, during precipitation, the head was quite slowly rotated so that a smooth, uniform deposit was achieved, and ill effects of the discontinuities avoided.

During high speed rotations, the head would sweep rapidly past the six corona zones so that a good average field of both E and J would be applied to the dust surface.

3.8 Final form of the Prototype

The final form of the prototype illustrated in Fig.3.5c reached a speed of 5000 rpm with corona currents flowing, and with good mechanical balance.

3.9 A Complete Precipifuge

With the experience gained in the design, construction and operation of the prototype; construction of the final form of the Precipifuge proceeded with some confidence.

The engineering effort invested in the apparatus was very great. The reader experienced in the art of the construction of electro-mechanical apparatus with special thermal and vacuum constraints applying, will be able to judge from the drawings and photographs the sorts of obstacles which were met with. Accordingly in the description which follows, minutae of mechanical, thermal and vacuum design have been omitted for reasons of space.

The complete, final form of the Precipifuge is illustrated in Fig.3.8, in the photographs of Fig.3.9 (with the corona chamber removed) and Fig.3.10 (with the corona chamber in position).

All the various machining operations were effected outside the University campus, much by the courtesy of the writer's industrial colleagues. It was a serious setback to this project when all Wollongong University workshop facilities were withdrawn; construction, to a cosmic deadline, of a stella telescope absorbed the entire W.U.C. workshop facilities during the period of the Precipifuge development.

The generous help of the writer's industrial colleagues, many of whom took a personal interest in the Precipifuge concept, were a great practical encouragement.

3.9.1 Driving Motor and Speed Monitoring

The variable speed motor finally adopted was a 10,000 rpm universal AC/DC machine of 1.5 kw output, built by H. T. Clements, Instrument Makers of North Sydney and used by them in medium speed medical laboratory-type centrifuges. At the time of writing it is being placed on closed loop control.

Speed measurement indication is by Racal Digital Counter, triggered from the Saunders-Roe slip ring assembly with integral photo-transistors and shaper (illustrated in Fig.3.4 and described in para 3.6.2)

3.9.2 The Head - Mechanical and Thermal Considerations

The Head, visible in Fig.3.8, 3.9 and 3.11, is designed to be able to carry out tensile measurements on dust on the vertical outer curved surface and shear measurements (not simultaneously) on the top flat surface.

On its outer surface, the maximum acceleration produced is 7700g.

There was no particular problem in the mechanical stress design using forged, high tensile strength aluminium supplied by Commalco with the following typical characteristics:

Type 2011T6

Ult. Tensile Strength	57,000 psi
Yield strength	47,000 psi
Elongation	12%
Brinnel Hardness	100
Shear Strength	35,000 psi
Youngs Modulus	10.2×10^6

After much experimentation, a suitable enclosure vessel was found to be a standard Pyres Glass column adaptor shown

in Fig.3.10. Its electrical and thermal characteristics are excellent, while providing adequate visibility. The mechanical strength is sufficient to support the suspended HT electrode system under full vacuum conditions.

A thermal heating mantle took the glassware and enclosure up to 230°C - considerably in excess of that normally contemplated.

A miniature temperature sensitive resistor, Mullard Type VA 3406, is mounted inside the rotating head, adjacent to the collector ring. It may be seen in Fig.3.11, embedded in a ball bearing which had been hollowed out for the purpose. Teflon insulated leads run down the hollow drive shaft to the slip-ring assembly. In this way, the Head temperature may be accurately determined while it is rotating at high speed.

3.9.3 Corona Chamber

The pyrex vessel enclosing the corona chamber proved to have ideal electrical, thermal and vacuum properties. It did however allow considerable residual charge build-up inhibiting corona when the emitters were too close. After shifting the latter inwards, the trouble was cured.

Three forms of high-voltage electrodes are used separately, all hung from the top orifice of the column-adaptor. Two of them are illustrated, each in half-section in Fig.3.11. On the RHS, the six discharge electrodes are at 21.6cm pitch diameter. On the LHS is shown a plain, non-emitting electrode, 19.4 cm dia, intended to set up a uniform field in the gap without corona. The third electrode shown in Fig.3.12 is of mesh type to allow visibility, to provide a comparatively free passage of dust after detachment, and at the same time to set up a uniform electric field at the head. The large teflon sheet on the top of the vacuum plate is to prevent sparkover to earth.

The collector electrode, 15.2 cm dia and 3 cm wide, has a surface area of 143 cm^2. Insulated from earth by a teflon

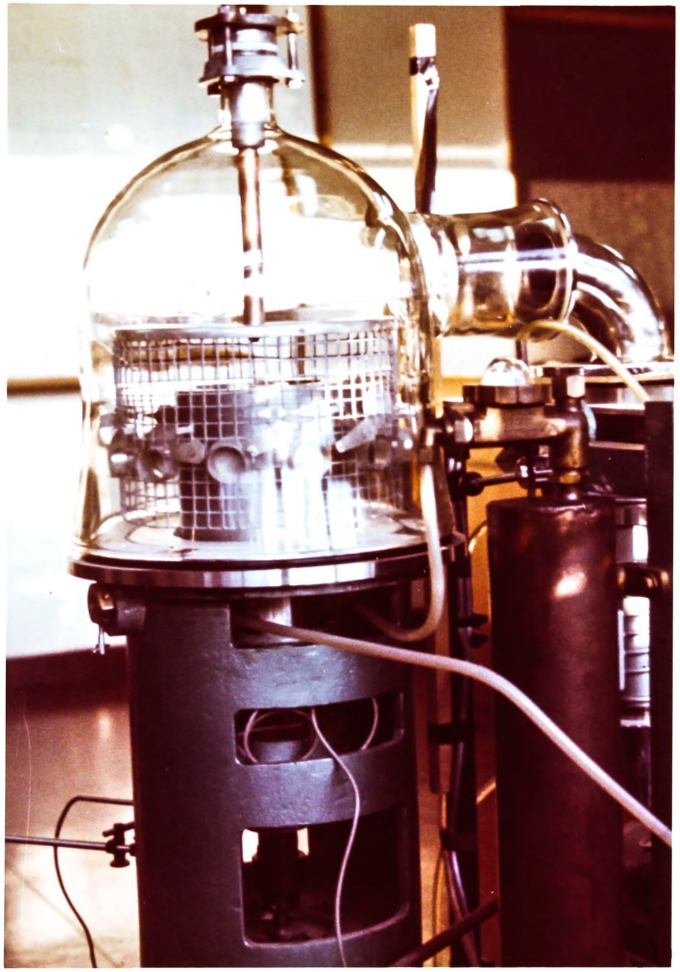

FIG. 3.9 FINAL ASSEMBLED PRECIPIFUGE

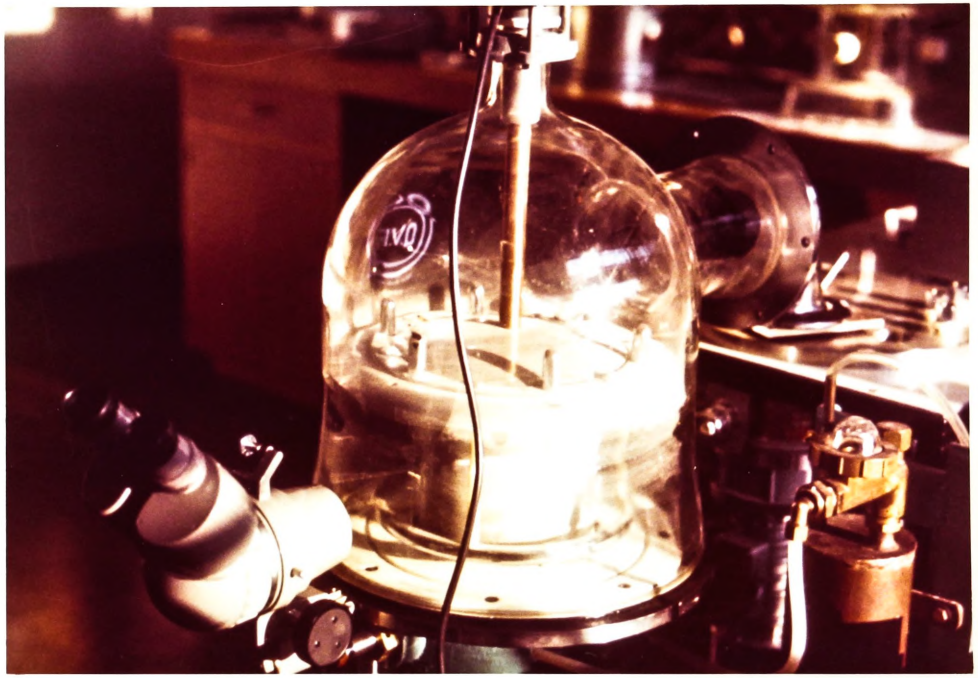

FIG. 3.10 CORONA CHAMBER ASSEMBLY

HT electrodes and binocular zoom microscope are visible.

sleeve, current is conducted from the collector through a teflon insulated wire, down the hollow drive shaft, and finally via the slip rings to monitoring instruments and earth.

3.9.4 Slip Ring Assembly

This has already been fully described in para 3.6.2

3.9.5 Bearing, Seal and Vacuum System

The search for a suitable seal which would hold a decent scientific vacuum of say 10-6 torr. at a rubbing speed of 10,000 rpm and at elevated temperature, was an extremely time consuming task. The file on this aspect of the project rapidly outgrew any other.

All possible materials and schemes for using them were considered. None of the five or six seal manufacturers contacted in 1967 had any experience with high speed vacuum seals, and none would even suggest that their seal might stand up under such conditions. One company, John Crane Mauri Bros and Thompson claimed to have a mechanical face seal irrigated with silicone oil, which performed well under high pressure, but they had no idea as to what the performance would be under high vacuum conditions. An associate company, Morganite (Aust) which produced the PTFE carbon faces, also had experience with the special grades of carbon used in rotating machinery in high altitude aircraft. That some sort of seal could be made, however uncertain the performance, now appeared possible.

Accordingly the writer was able to bring the following parties together with responsibilities as indicated:

Mr P. Rowney of John Crane, Mauri Bros & Thompson	Mechanical Face Seals and Heat Exchanger
Mr K. Strickland of Dynavac High Vacuum Pty Ltd	Vacuum Pump, shaft, bearing, seal, vacuum plate assembly
Mr R. Jeffcoate of SKF(Aust)	Self Aligning bearings
Mr T. Gawn of Vernier Eng.	Construction of Head and General Assembly.

In Fig.3.11, two mechanical face seals in tandem are shown. The actual rubbing takes place between the lapped and honed surfaces of the carbon-loaded PTFE and the loaded phosphor bronze. The space between the two seals is irrigated with silicone oil which serves to remove heat and also to provide a lubricating film on the rubbing surfaces. The top self-aligning bearing operates in a vacuum and was therefore sealed with silicone grease.

Friction was expected to generate about 1000 watts, so that it was necessary to remove it from the seal and housing with forced silicone oil circulation. An external pump and heat exchanger were provided.

The vacuum design of the corona chamber was inevitably a compromise since at other times it had to operate in a gaseous environment. There were certain unavoidable gas 'traps' resulting in slow pump-down beyond certain pressures.

The vacuum pump, manufactured by Dunavac comprised a backing pump and oil diffusion pump. In two stages, the backing pump is capable of pumping 50 litre 1 min. at 760 mm Hg or 44 litre/min at 0.1 mm Hg. The diffusion pump is of 3 stages with 2" dia bore and capable of an ultimate vacuum of 5×10^{-8} torr.

The pumping system is connected to the column adaptor via a teflon bellows to take up slight mechanical misalignment.

There was a sense of keen anticipation by all concerned when the plant was first commissioned. After the head had been run up to speed, backing pump was used for rough evacuation. When the diffusion pump was applied, the ion gauge steadily fell in pressure, finally reaching 5×10^{-6} torr where it remained for some hours. This good vacuum was better than had been hoped for and immensely gratifying to all concerned with the project. Such a vacuum, with heat as well, is more than adequate for out-gassing the specimens under consideration. It became clear that the apparatus could adequately account for the influence of adsorbed gaseous

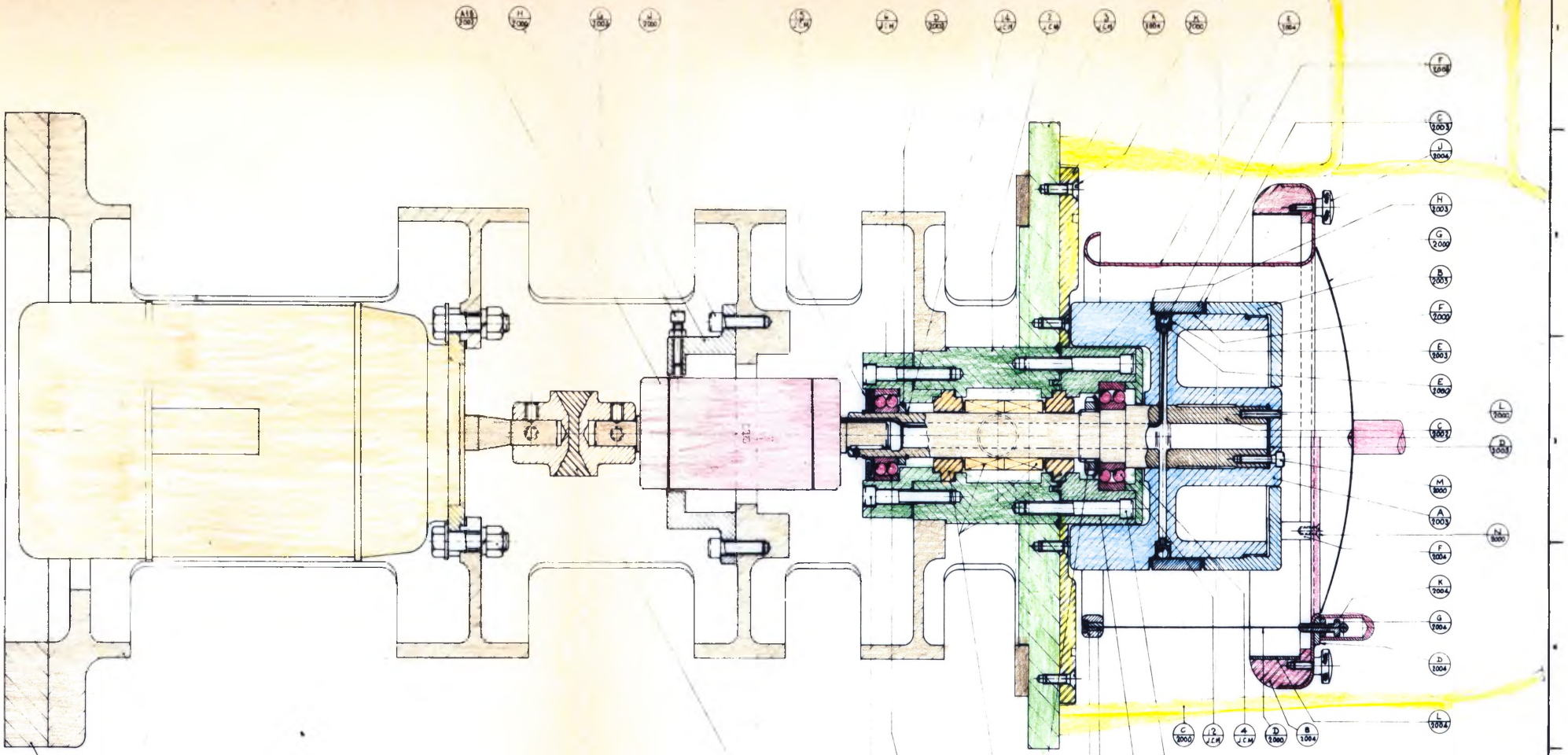

No OFF	ITEM	DESCRIPTION	MAT'	REMARKS
1	15	25 M/M Z TYPE WASHER	SKF	
1	14	CIRCLIP	"	
1	13	VACUUM PLATE	ST/STN	
1	12	BEARING 1206 30 M/M	SKF	
4	11	5/16" WHIT CAP HD SCR × 2½ LONG	ST*	
1	10	LOCKNUT & WASHER KM6 & LM6	SKF	
2	9	SEAL CRANE T109-1"ø QP1	Crane	
1	8	BEARING 1206 25 M/M	SKF	
4	7	5/16" WHIT CAP HD SCR × 1¾" LONG	ST*	
1	6	CLAMP PLATE HOUSING (LOWER)	ST/ST	
1	5	" " " (TOP)	"	
1	4	CAP	"	
1	3	SEE C-PRF 2002	"	
1	2	BODY SEAL HOUSING	"	
1	1	DETAIL OF FLUSHING PORTS		

4	D	5/16" HEX HD SET SCR × 1½" LONG	M.S.	WITH NUT & SPRING WASHER CAP PLATE
3	N	2 BA C/SUNK HD SCR × ⅜" LONG	M.S.	CAP PLATE
3	M	2 BA CAP HD SCR × ⅜" LONG	ST.	" "
1	L	3/16 STD DOWEL × 1" LONG	M.S.	
8	K	⅜ BSF C/SUNK HD SCR × ¾" LONG	M.S.	CAP PLATE
4	J	5/16 BSF CAP HD SCR × 1" LONG	ST.	" "
3	H	¼ BSF CAP HD SCR × 1" LONG	ST.	WITH NUT CAP PLATE
1	G	SUPPORT DOME	ST.	SUPPLIED BY Wm. Cleet CORP.
1	F	INSULATING SLEEVE	TEFLON	
3	E	O RING ¼" × ⅜"	NEOPRENE	
6	D	ELECTRODE N° CHR WIRE	-	COMPLETE WITH BALL
1	C	COLUMN ADAPTOR	BRASS	Q.V.F. CAT N° 12/6/12
1	B	FENNER DODGE RESILLABOND CPL	-	N° 4 Bore ⅝ O.D.
1	A	2 HP 10000 RPM MOTOR		SUPPLIED BY Wm. Cleet CORP.

NOTE :-

ITEMS MARKED THUS (JCM) ARE SUPPLIED IN UNIT BY JOHN CRANE MAURI PTY LTD / DYNAVAC SEE BILL OF MATERIALS ON LEFT OF THIS SHEET

GENERAL ASSEMBLY
PRECIPIFUGE

WOLLONGONG UNIVERSITY COLLEGE
DEPARTMENT OF ELECTRICAL ENGINEERING

SCALE FULL SIZE

DRN. G.SYMES
CHK'D
TRC'D
D.A.

DATE 21.5.71

layers on adhesive strength.

Use of mechanical face seals had been based on little more than an engineering hunch that they might prove adequate. The final result entirely vindicated the effort invested in this aspect of the project.

In retrospect, while writing in 1972, rapid developments in high speed seals for vacuum or pressure applications were taking place in several countries over the period '67 to '71. Whilst in 1967-8 when the Precipifuge was commissioned, the seal performance was something of note, it almost certainly is no longer exceptional.

3.9.6 Dust Monitoring

The Precipifuge head may be continuously monitored by the synchronously triggered stroboscope, a GR 1539-A stroboslave, with 1531-P2 flash delay. The latter facility enables the whole dust surface to be scanned. In addition, an Olympus stereo binnocular microscope with zoom lens is shown in position in Fig.3.10. The light output is adequate and the triggering sufficiently stable to allow microscopic examination of the rotating head at all speeds.

By means of the dial type microscope shown in Fig.3.13, the thickness of dust before and after detachment may be measured.

The remotely operable shutters and receptacles illustrated in Fig.3.12 are an interesting innovation. Dust detached per unit area of head may be directly measured as it is retained in the small aluminium receptacles spaced evenly around the periphery of the mesh. Each receptacle has a shutter across its opening which may be operated by hand (see Fig.3.12) from outside the vacuum chamber. A given shutter will be opened over a small speed increment and then closed again. The small receptacle is weighed in a microbalance to determine the dust captured. The use of this shutter arrangement allows a direct determination of the

FIG. 3.12 MESH ELECTRODE

With provision for externally operated shuttered receptacles.

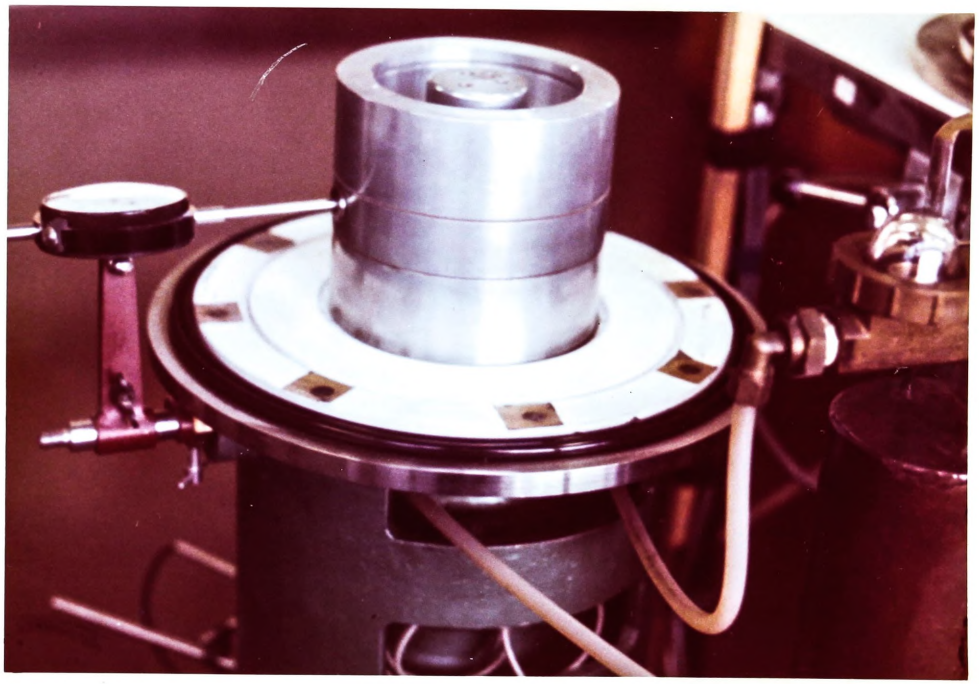

FIG. 3.13 HEAD WITH MICROMETER

Dust thickness is measured before and after deposition.

dust per unit area detached without breaking the corona enclosure until after the test is over. During this operation an electric field may be applied across the gap by energising the wire cage (and receptacles).

3.9.7 Typical Results of Dust Adhesive Strength

During commissioning tests, a sample of Fly-Ash of mixed particle sizing from low sulphur North American Coal was used. Dust was precipitated to a depth of about 2mm with the head slowly turning. The chamber was evacuated to 1×10^{-5} torr for 24 hours. Still under vacuum, the speed was increased by small increments with the dust layer under stroboscopic observation. A small, apparently random proportion of dust detached at speeds below critical speed. At the critical speed, a large proportion of dust detached, leaving a relatively tenacious underskin clearly visible as in Fig.3.14. The vertical wipe was to provide a micrometer reference point on the clean head.

From eq.2.37, the adhesive strength is:

$$P = (F/A) = (M/A)\ \omega_o^2 r \qquad .....(2.37)$$

where r = radius of centrifuge head

ω_o = angular velocity of detachment

(M/A) = mass per unit area of dust detached at the head.

Initially all receptacle shutters were open but were closed one at a time at certain speeds, indicated in the Table 3.1.

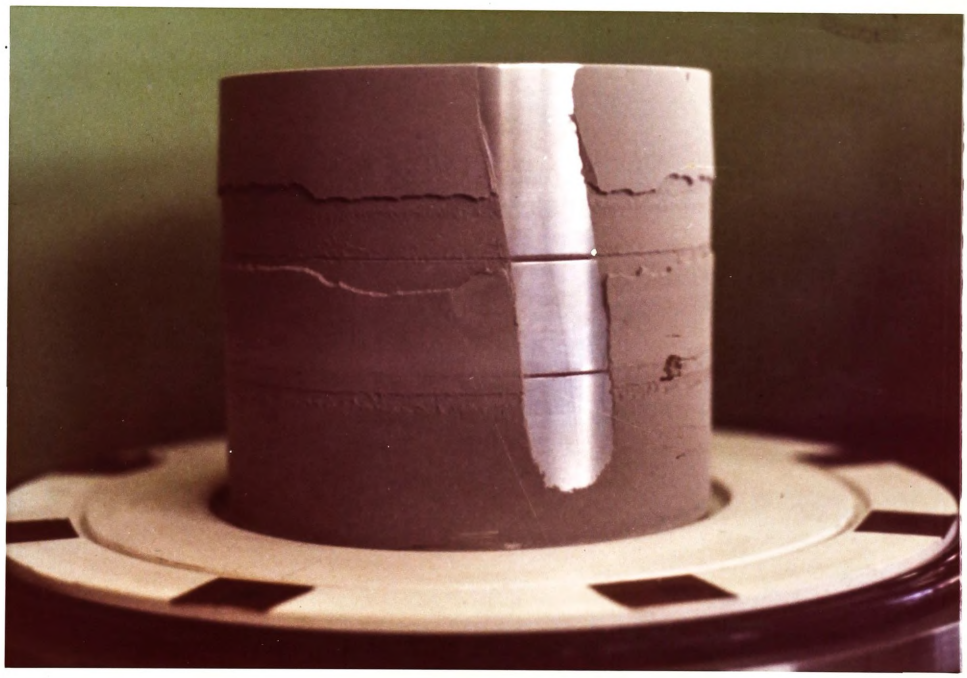

FIG. 3.14 HEAD WITH DUST

Horizontal strata has been centriguged off.
Underskin is clearly visible.
Vertical wipe made manually for micrometer depth reference.

TABLE 3.1

DETACHMENT OF DUST AND ADHESIVE STRENGTH

N RPM	$\frac{\omega^2 r}{g}$	$\frac{\Sigma m}{grm}$	$\Sigma(m/A_o)$ grm/cm^2	$\Sigma(M/A)$ grm/cm^2	(M/A)	% Detach	P grm wt/ cm^2
600	30.3	.03	.0032	.00534	.00534	5.6	.162
650	35.5	.03	.0032	.00534	0	5.6	0
700	41.1	.03	.0032	.00534	0	5.6	0
750	47.3	.04	.0043	.00716	.00182	7.4	.086
800	53.8	.04	.0043	.00716	0	7.4	0
825	57	.26	.0277	.0461	.03904	48.3	2.23
850	61	.26	.0277	.0461	0	48.3	0
875	64.3	.48	.0513	.0856	.0395	89	2.54
900	68	.48	.0513	.0856	0	89	0
2010	340	.5424	.058	.0968	.0112	100	3.8

Col. 1 - Speed, RPM
Col. 2 - Acceleration, G
Col. 3 - Dust Collected in Receptacle, grm (cumulative)
Col. 4 - Dust Collected/Unit Area Orifice, Grm/cm^2
Col. 5 - Dust Detached (Cumulative) from Rotor Surface, grm/cm^2
Col. 6 - Increment of Dust/Unit Rotor Area Detached, grm/cm^2
Col. 7 - Cumulative Fraction Detached
Col. 8 - Adhesive Strength, grm/cm^2

In the second column of this table, the acceleration in g is calculated. In column 3 the cumulative weight of dust collected in a receptacle before its shutter was closed, is shown. The cumulative weight per unit orifice area is shown in column 4; the quantity referred to the rotor surface,

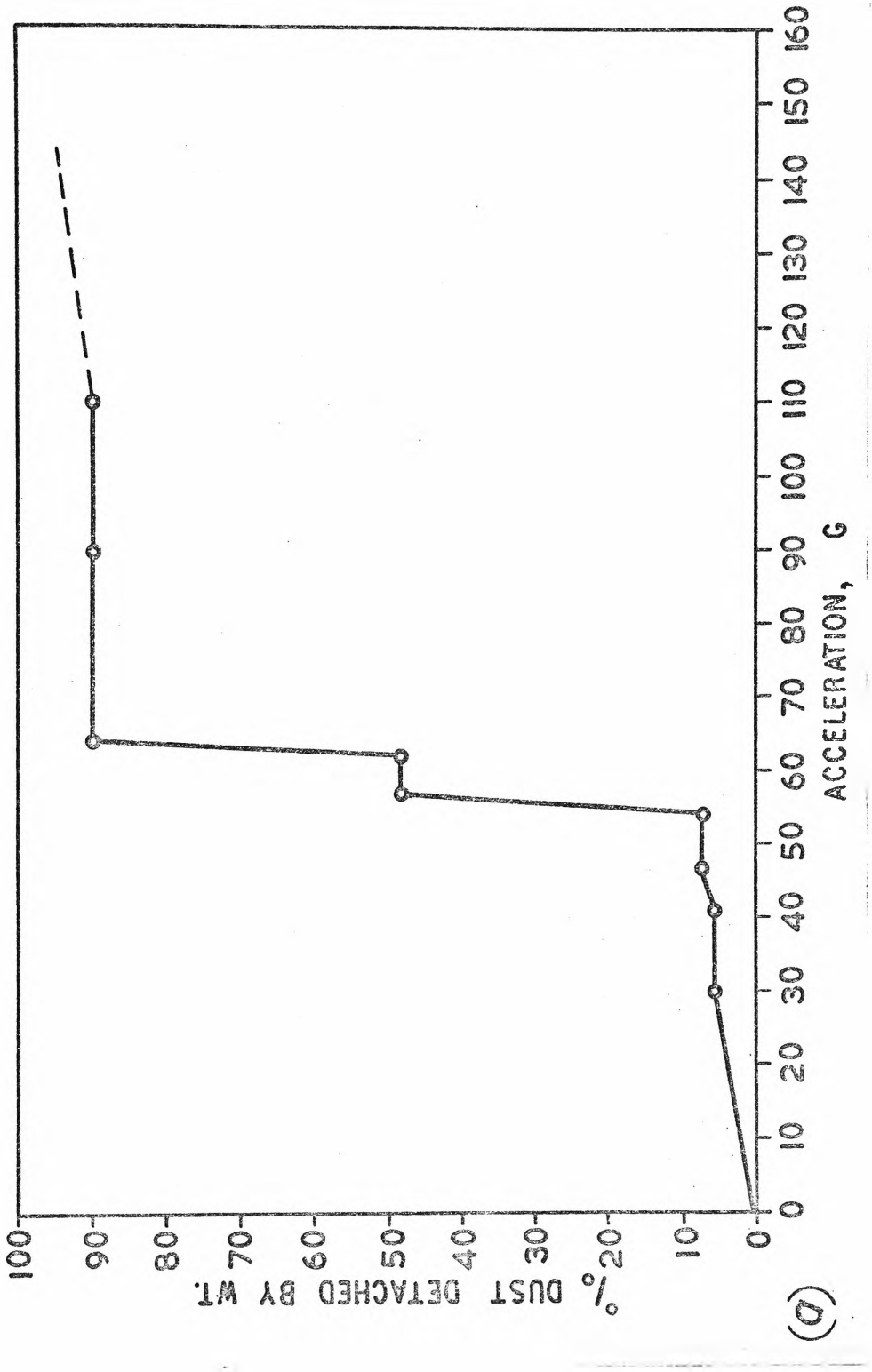

FIG. 3.15(a) ADHESION OF FLY-ASH

Measured in the Precipifuge. Percent dust detached as a function of normal acceleration. North American Ash (Jim Bridger seam)

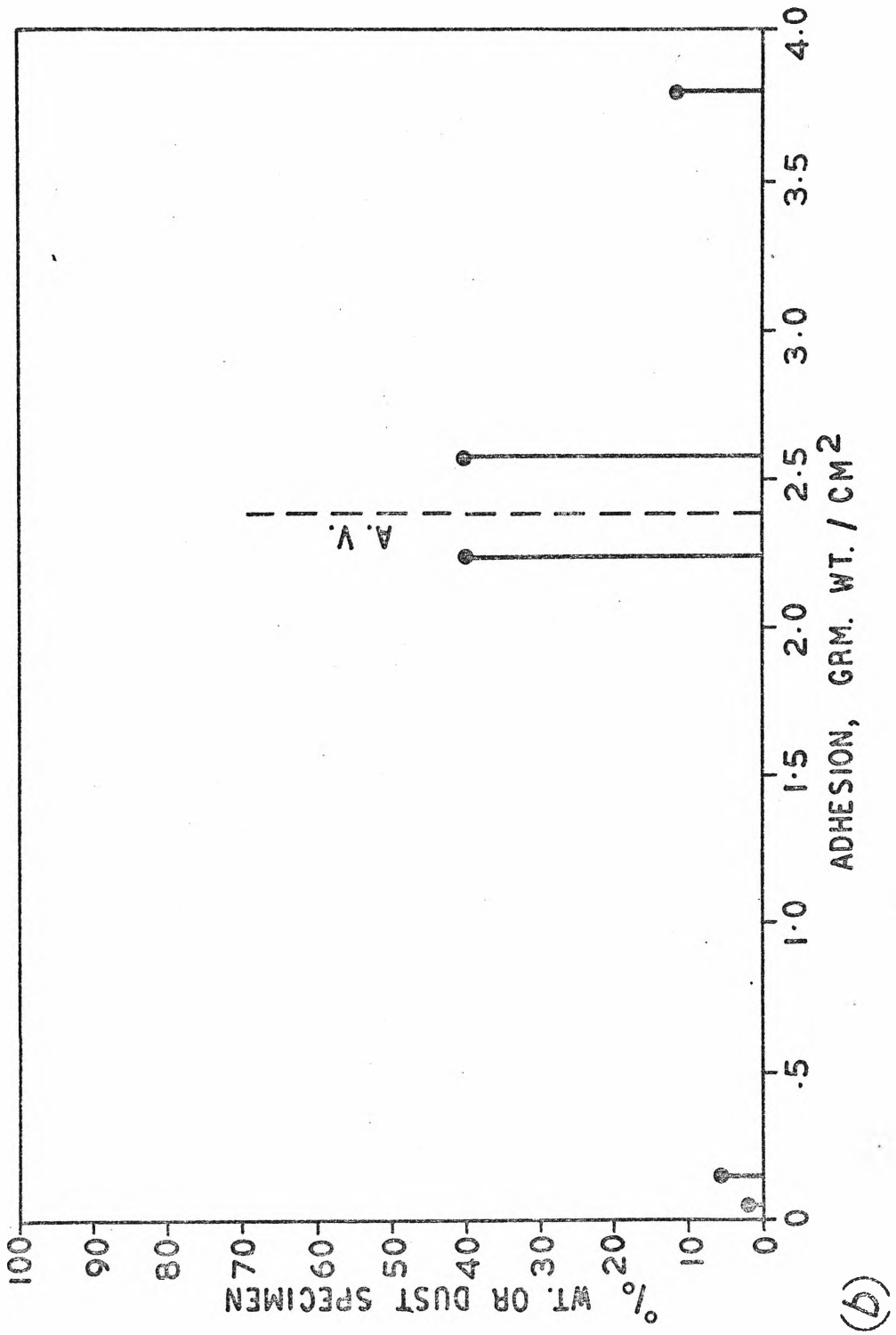

FIG. 3.15(b) ADHESION OF FLY-ASH

Data reduced from Fig.3.15(a). Adhesive pressure as a function of the proportion of the specimen.

i.e. the cumulative dust weight per unit area of rotor surface* is shown in column 5. The incremental dust weight detached from the rotor surface is tabulated in column 6, the percent detachment in column 7 and finally the adhesive strength P in column 8.

Two forms of simple graphical display of the data are of value. The first shown in Fig.3.15a is really a cumulative distribution histogram, showing that an acceleration of 65g has caused 90% detachment. The layer has effectively fractured between 55g and 65g. The Fig.3.15b is really a frequency distribution histogram relating the important fundamental parameter, adhesive strength to proportion of population. Some small pieces, poorly held, detached at low speed. The bulk of the material detached with an adhesive strength of 2.4 grm wt/cm^2. A small proportion, some 10%, had a markedly higher strength. This result is comparable with values published by Sproull, and Penney et al for composite fly-ash specimens.

3.9.8 Future Programme for Precipifuge

The sorts of experiments which may be performed with the Precipifuge are endless.

The theory of general powder technology might possibly benefit by data gained from this machine.

Certainly, data valuable to the Precipitator technology is likely to be gained by a systematic exploitation of the

---

* by elementary geometry from fig.3.12 and 3.8,

$$(M/A) = (m/A_o)R/r$$

where A_o = orifice opening
R = receptacle orifice pitch radius
m = mass of dust in receptacle

Precipifuge.

As for the writer, such work must fall outside this dissertation, for the engineering investment of time and effort in the successful development of the Precipifuge has exceeded all reasonable ceilings. Accordingly, the project must be closed off by the writer at this point. Hopefully, his own post-graduate students will carry on in the coming years where the writer has left off.

CHAPTER 4

THE MICRO AREA BOUNDARY PROBE

4.1 The Micro Area Boundary Probe

The probe to be described in this chapter was developed in order to investigate the apparent discontinuities in corona currents over the anode, noted during the development of the precipifuge corona chamber. The discharge emanated from plain, smooth, round stainless steel discharge electrodes which had been polished (along with the anode) prior to application of the negative high potential. The resulting anode pattern observed in Fig.3.6 gave rise to suspicions of the presence of discontinuities in J.

The implications being both serious and intriging, the precipifuge development was slowed down while the present investigation was undertaken.

The probe consists of a small, flat electrode insulated from the surrounding earthed electrode and well polished. It thus causes negligible perturbation on the existing surface. It will be shown to measure not only J, but E as well, at any point on the boundary.

In a study of impulse phenomena in rod gaps, Meek and Collins[101] first* described such a probe, using it to measure electric field strength as an ion cloud approached it. This mode was only applicable in the absence of conduction currents, using the behaviour of displacement currents to determine transient E.

In observations on impulse corona discharge in a rod/plane gap, Waters, Rickard and Stark[102] used an electrostatic field mill to determine current density and electric field strength. Sets of rotating and stationary vanes 15cm in diameter allow the sampling of slow transients to 0.5ms time resolution. This elegant method, however much the

---

* The present writer's development of this probe was quite independent. Professor L.B.Loeb in December 1967, by which time the writer's probe was well developed, during a discussion, pointed out to the writer that Meek and Collins had a similar mechanical arrangement; but with a different electrical objective and principle.

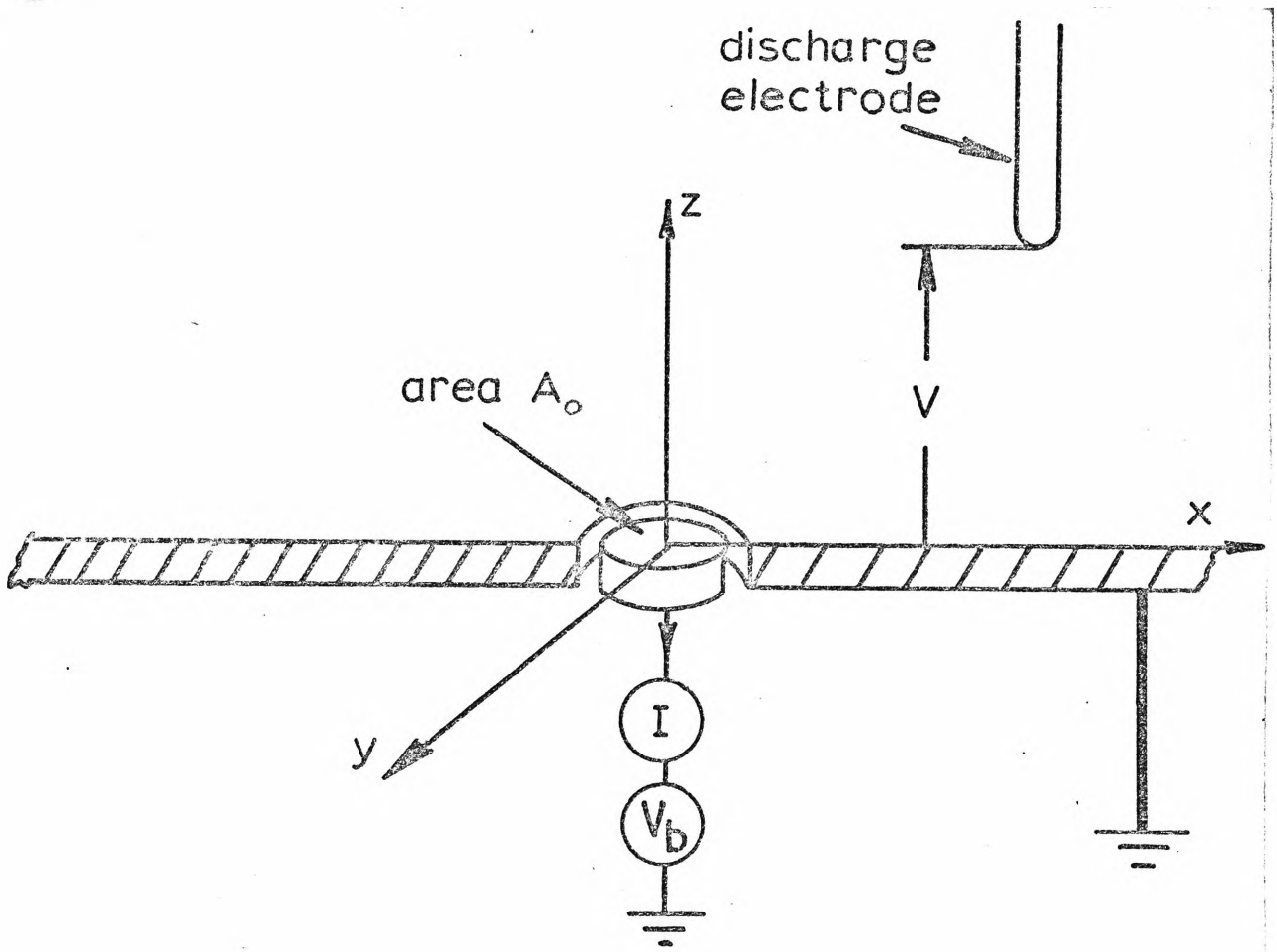

FIG. 4.1 MICROAREA BOUNDARY ELECTRODE WITH PROVISION FOR BIAS

apparatus was miniaturised, would never be compact enough to investigate the pattern of Fig.3.6, which in places is only one or two mm in extent.

The probe and technique to be described provide high spatial discrimination of ± 0.5mm or better. The current density measurement is limited only by the metrology determination of the probe size and by the simple electrical instrumentation. Thus J may be determined to 1%. The accuracy of measurement of E is less, being about 5% absolute and improving for relative observations. The development to be described is for steady-state fields. Experimental verification of the method is described for positive ions in air at NTP and also in an electrolyte.

It appears that a new development has been made here, with extensive possible uses in gas discharges, plasmas, electropheritic deposition and in the technology of electrostatic precipitation.

4.2 Principle of the Boundary Probe

As previously described by Tassicker[103] the probe consists of a small insulated circular electrode inserted into a large plane (or cylindrical) electrode and the whole carefully machined and polished flat. As shown in Fig.4.1, the probe is connected in series with a current measuring device such as a picoammeter. In addition, there is a variable d.c. voltage bias source connected in series with the probe. This bias source was not previously described, but now provides the means for determining the field strength. The high tension electrode system may be moved, while energised, relative to the earthed system in the x,y,z direction with ± 0.2mm discrimination. Since, with V_b set to zero, the probe is at about earth potential, it causes neither electrical nor mechanical perturbation. It therefore correctly samples the current density which is determined quite simply from J = I/A. When the high tension system is moved, the discharge travels with it and the whole of the J

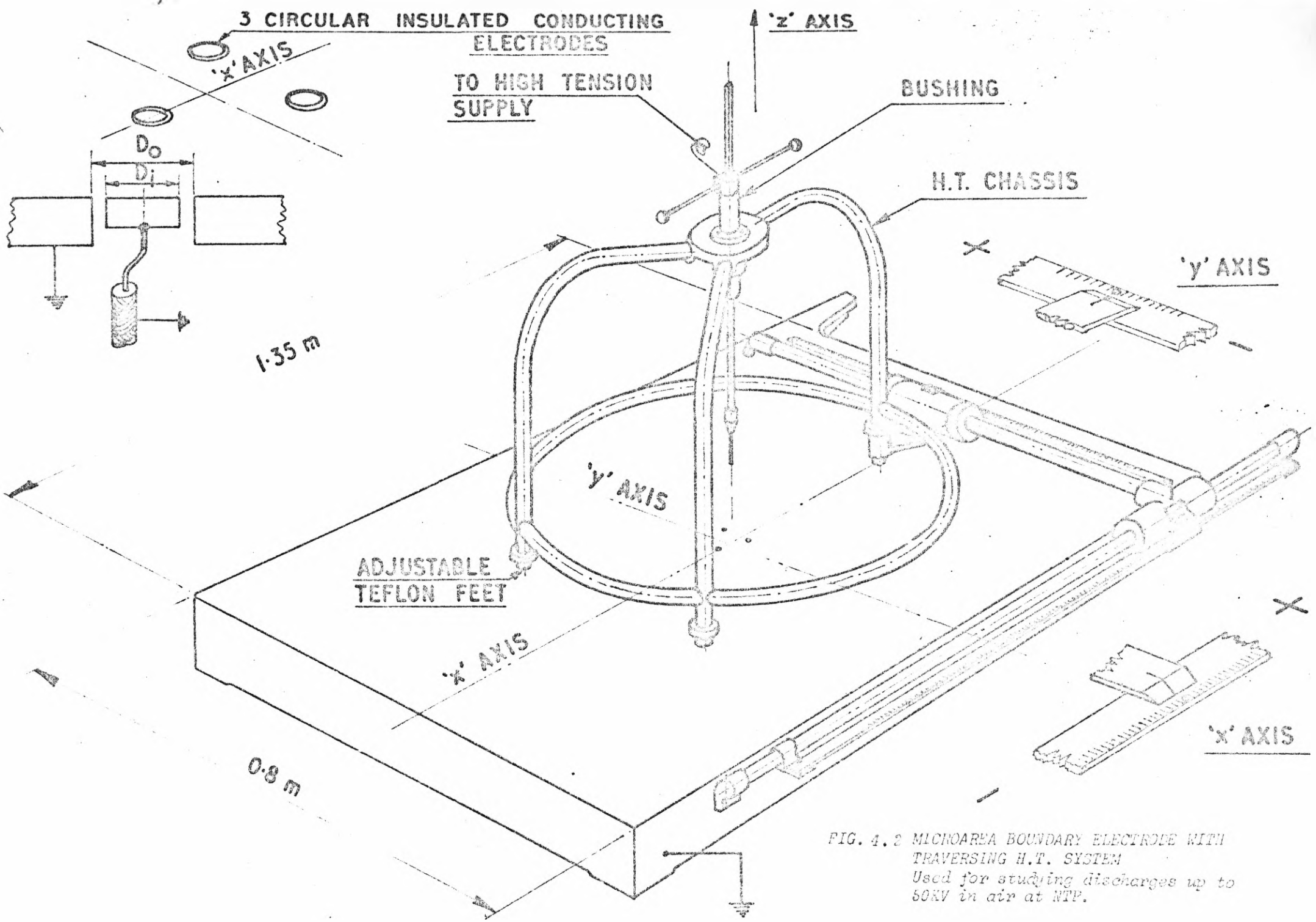

FIG. 4.2 MICROAREA BOUNDARY ELECTRODE WITH TRAVERSING H.T. SYSTEM
Used for studying discharges up to 50KV in air at NTP.

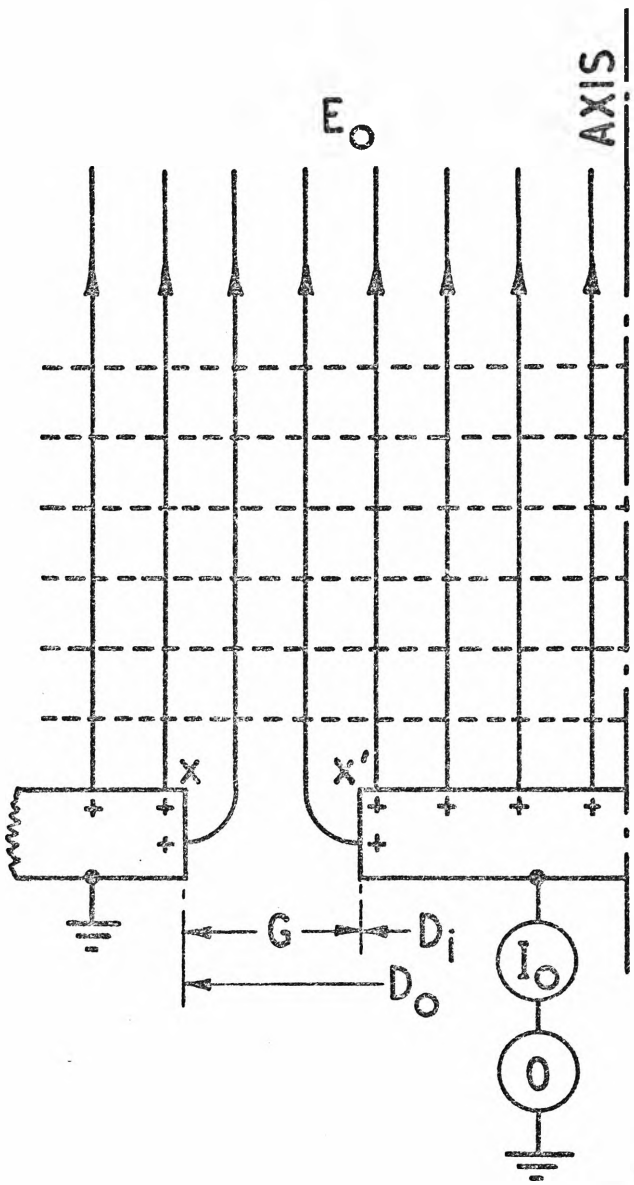

FIG. 4.3 MICROAREA BOUNDARY ELECTRODE IN A UNIFORM AMBIENT ELECTRIC FIELD E_o.

Probe at earth potential - no bias voltage. The proportion of total probe electric flux entering via the gap X-X' is $2G/D_i$, *which is small for a well designed probe.*

profile may be determined.

One form of the equipment used for studying coronas in air at NTP is shown in Fig.4.2. The main electrode, nominally at earth potential is of polished brass supported by a cast aluminium alloy chassis. The H.T. electrode system, used to 50 KV and resting on teflon feet, slides over the earthed electrode. The position of this electrode is fixed by precision guides equipped with vernier scales, in the x,ẏ,z direction. Three insulated electrodes of diameter 0.370mm, 0.875mm and 2.565mm are inserted near the centre of the main plate. Normally used singly, they may however be utilised for mutual checking. Further details of mechanical construction of the apparatus are given in appendix 4.1.

4.2.1 Determination of Current Density - The Unbiased Probe

When it is desired to determine a current density, the bias voltage V_b (Fig.4.1) is set to zero. If the gap between the probe and the surrounding electrode is quite small, then it may be sufficient to simply put $J = I/A$ where $A = \frac{\pi}{4} D_i^2$. More correctly, one should put $J = \frac{I}{\frac{\pi}{4} D_m^2}$, for by reference to the Fig.4.3 it is clear that for a small G/D_i, the flux entering the gap divides equally to the probe and the earth. In Table 4.1* are shown some probe dimensions, the last three of which are typical. Here the gap varies from 1.5% to 6.25%. A simple calculation shows that the proportion of flux entering the side of a probe must be less than $2G/D_i$. Thus for a well constructed probe, this fringing flux could be lower than 3% and at the most about 10%.

4.2.2 Measurement of Electric Field - The Biased Probe

The determination of electric field is a rather more subtle matter than is the determination of current density. The probe is biased first in a positive then negative direction by up to, say 50V. With negative bias, the current

* Para.4.4.1.

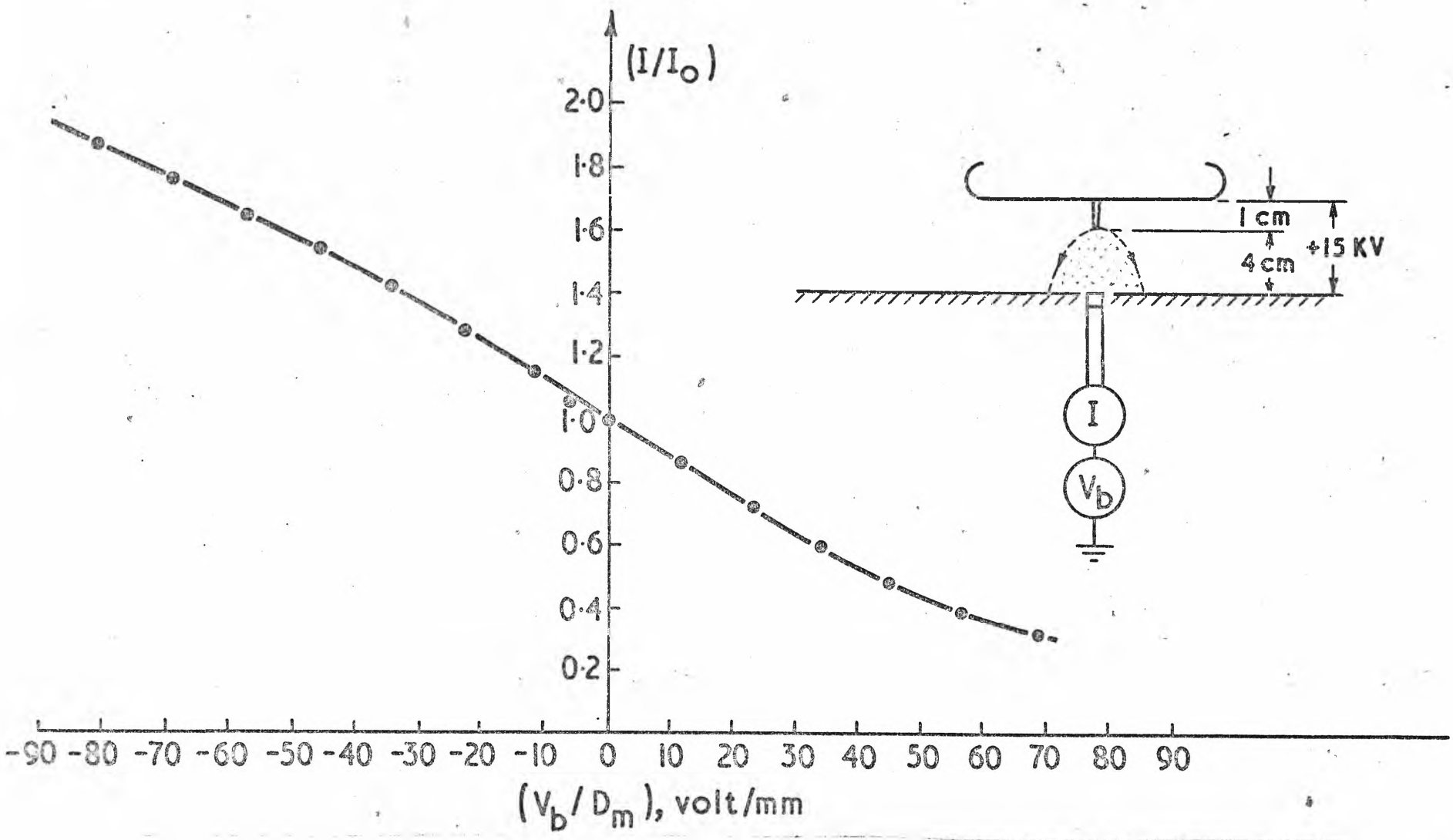

FIG. 4.4 ELECTRIC FIELD DETERMINATION BY PROBE IN THE BIASED MODE

Measurement taken under the centre line of the configuration shown. With incoming positive ions, the current is increased for negative bias and decreased for positive bias. Probe: $D_m = 0.875$ *mm;* $A = 0.602$ mm^{+2}.

flowing increases, while with positive bias, the current decreases. This is plotted, as in Fig.4.4, as I/I_o against V_b/D_m. This typical characteristic always shows a point of inflection and a long straight region about the origin. The slope of this straight line region is proportional to the ambient electric field E_o. In this way, the magnitude of the electric field is determined at each point in the current channel along with the J values. A different technique, utilising displacement current rather than conduction current is used to measure E_o outside the current channel, a matter taken up in para 4.8.

The general theory of the measurement of electric field is given as follows.

4.3 General Theory of the Biased Probe

The biased probe is only operative when current is flowing, since it inherently depends upon the measurement of current. It applies in systems where the electric field is modified by space charges, but it is convenient to first study the electric field configuration in a Laplacian domain and then to extend it to the Poisson case.

Consider that the sketches in Fig.4.5 first represent electrostatic flux in a charge free region, in which there is an ambient electric field E_o constant in the small region under consideration. First observe that, as noted in para 4.2.1, if the gap is small, only a small proportion of the total flux fringes and leaves the electrodes below the top face.

If now a small quantity of negative ions is produced in the space above the probe, they will drift along lines of force and will enter the probe at a rate proportional to D_m^2. The current density will of course be given by eq.1.3, here rewritten as:

$$J = \rho K E_o \qquad \ldots\ldots(4.1)$$

In many situations, diffusion is negligible, the only significant conduction taking place by drift. The role of diffusion is taken up in more detail in Appendix 4.2. If conduction takes place with both positive and negative carriers, then eq.4.1 becomes:

$$J = (\rho_1 K_1 + \rho_2 K_2)E \qquad .....(4.2)$$

and the equation takes on the same form as before. It is noticed that eq.4.2 is an expression of ohms law, viz

$$J = \bar{\sigma} E \qquad .....(4.3)$$

where $\bar{\sigma}$ is the conductivity of the gas or electrolyte.

Returning to the sketches in Fig.4.5 one first observes that Fig.4.5a is a simplified representation of Fig.4.3. If now, the probe is biased negatively, less electrostatic flux leaves the probe as shown in Fig.4.5b and less negative ions drifting down the lines of force, enter the probe. Should the probe be biased positively, then more electrostatic flux leaves the probe and there is a corresponding increase in current. Careful experiments such as that shown in Fig.4.4 demonstrate that the current varies linearly with bias voltage around the origin. If the information contained around the origin of Fig.4.4 is expanded, then the clearly linear relationship illustrated in Fig.4.6 results. It is instructive to enquire into the basis of this relation.

4.3.1 Small Perturbation - Linear Region

It is convenient to examine the origin of the straight line characteristic for (I/I_o) as a function of V_b the bias voltage, by appealing to the Laplace equation:

$$\nabla^2 V = 0 \text{ and } E = -\frac{dV}{dx}$$

We note that in a homogeneous medium, once the solution for this equation has been found for, say, the electrostatic case,

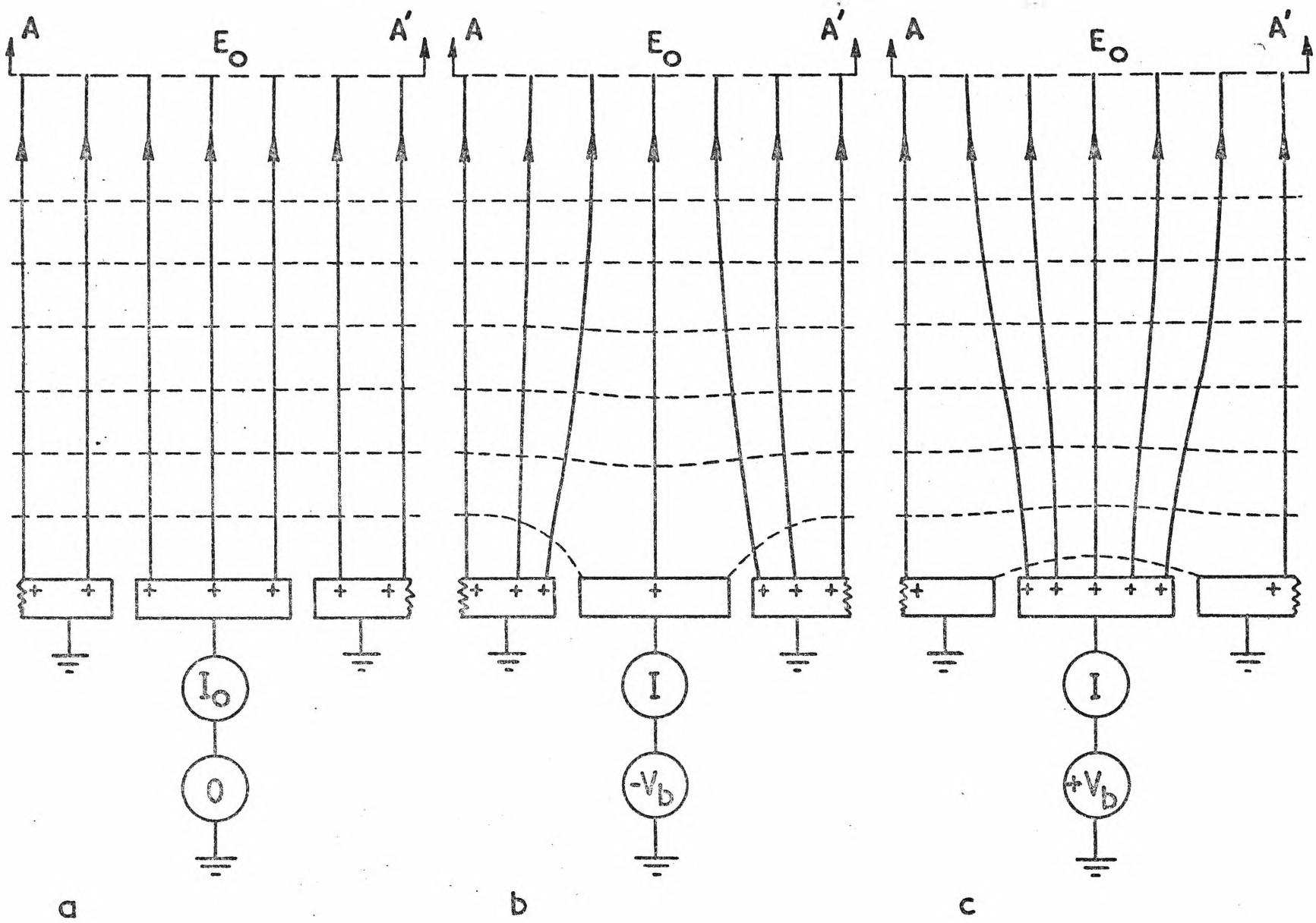

FIG. 4.5 FIELD PATTERN AROUND A PROBE - SKETCHES OF LINES AND EQUIPOTENTIALS, INGRESS OF NEGATIVE IONS.

(a) Unbiased mode, the probe is at earth potential

(b) The probe with negative bias

(c) The probe with positive bias

then the solution for the current conduction case follows immediately by analogy.

In Fig.4.5a, the orthogonal lines represent equipotentials V_1, V_2 etc., and flux lines E_o. One considers a small region of the medium around the probe where the field is uniform. Since fields may be superimposed, one notes that Fig.4.5c may be obtained by adding the fields of Fig.4.5a and Fig.4.5d.

The electrostatic flux leaving the probe of Fig.4.5a is given by

$$\psi_o = A\, E_o \varepsilon_o \qquad .....(4.4)$$

The electrostatic flux leaving the probe of Fig.4.5d is given by the surface integral

$$\psi_1 = \int D.dA = q_1$$

and hence

$$\psi_1 = C_o V_b \qquad .....(4.5)$$

where C_o = capacitance between the top surfaces of the probe and the surrounding plate. It is clear that the capacitance due to the flux in the radial gap is not relevant, since from Fig.4.3, little ambient flux enters by way of the gap. The total electrostatic flux leaving the top surface of the probe is now:

$$\psi = \psi_o + \psi_1$$

and

$$\frac{\psi}{\psi_o} = 1 + \frac{\psi_1}{\psi_o} = 1 + \frac{C_o V_b}{A\, \varepsilon_o\, E_o} \qquad .....(4.6)$$

One now observes that ions enter the probe by drifting down tubes of flux. The perturbation due to the probe is local and does not extend beyond the dotted line A A', a distance of perhaps 1 diameter. Starting from such a cross-section as A A' the current density and total current are proportional to $\frac{E_o}{\varepsilon_o}$ and ψ respectively. By such reasoning

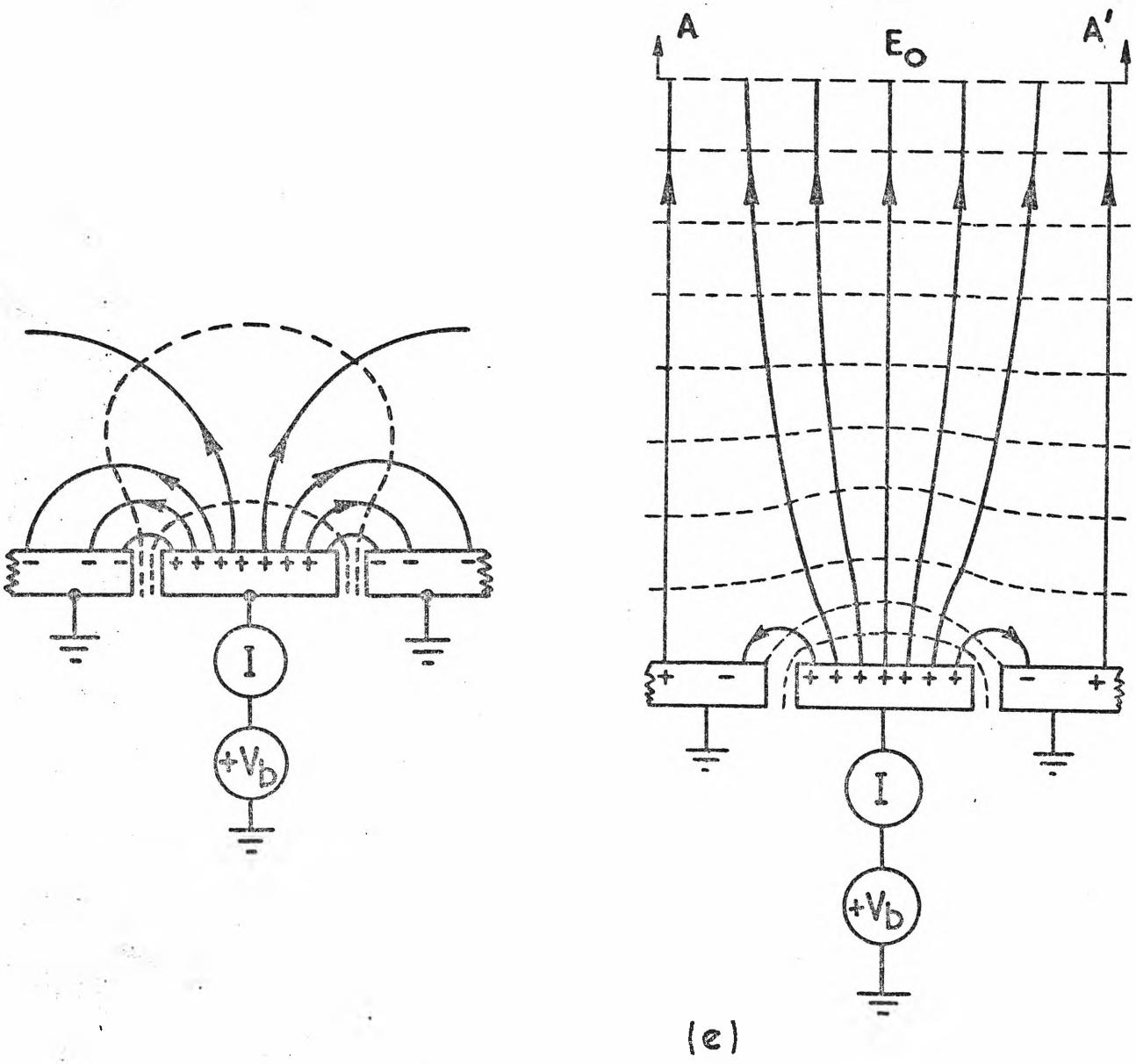

FIG. 4.5 FIELD PATTERN AROUND A PROBE - SKETCHES OF LINES AND EQUIPOTENTIALS

(d) The probe with bias but no external field

(e) The probe with strong positive bias

One may extend eq.4.6 and write

$$\left(\frac{I}{I_o}\right) = 1 + \frac{C_o V_b}{A\varepsilon_o E_o} \qquad .....(4.7)$$

When a negative bias is applied, superposition of Fig.4.5a and 4.5d (with opposite polarity) leadsto the configuration shown in Fig.4.5b. The reasoning which leads to eq.4.7, is identical to that previously given. The careful reader will discern similarities in this approach with that given in appendix 1.2 for the charging of spherical particles.

It is observed that the current/bias-voltage characteristic is a straight line, the slope of which is given by

$$\text{slope} = \frac{C_o}{A\varepsilon_o E_o} \qquad .....(4.8)$$

Since for a given probe, $\frac{C_o}{A\varepsilon_o}$ is a fixed geometrical constant, the value of the ambient electric field E_o may be determined immediately.

One may note that eq.4.8 may be written as

$$\text{slope} = \frac{C_o}{\frac{\pi}{4} D_m^{\,2}\, \varepsilon_o E_o}$$

Now it is clear that as capacitance of geometrically similar probes can depend only on the diameter of the probe, we may with advantage write:

$$\text{slope} = \left(\frac{4C_o}{\pi D_m \varepsilon_o}\right) \frac{1}{D_m E_o} \qquad .....(4.9)$$

so that finally eq.4.7 may be usefully written

$$(I/I_o) = 1 + \left(\frac{4C_o}{\pi D_m \varepsilon_o}\right) \left(\frac{V_b}{D_m E_o}\right) \qquad .....(4.10)$$

The first bracketed term on the RHS is a constant for any diameter of probe in which (G/D) is fixed. For the two smaller probes of Table 4.1 the value of $\frac{4C_o}{\pi D_m \varepsilon_o}$ is found

to be 4.85, by theory and experiment to follow in paras.4.4.1 and 4.6. Hence for the two probes described,

$$(I/I_o) = 1 + 4.85 \frac{V_b}{D_m E_o} \qquad .....(4.11)$$

The constant 4.85 is dimensionless.

4.3.2 Laplacian Field in the Probe Vicinity

The assumption implicit in the previous analysis is that the field surrounding the probe is locally Laplacian. The following approximate analysis shows this to be closely the case.

Consider a single tube of flux in, say, Fig.4.5a. Then in general, the Poisson relation:

$$\nabla^2 V = \frac{dE}{dx} = - \frac{\rho}{\varepsilon_o}$$

holds in one dimension. Hence for a charge density constant in a small region:

$$E_x = \frac{\rho x}{\varepsilon_o} + E'$$

where E' is the field which would be present in the absence of space charge. Since the perturbation of the field around the probe due to ordinary bias voltages does not extend more than a probe diameter, we seek to determine the relative magnitude of the term $\frac{\rho D_m}{\varepsilon_o}$.

The highest value of corona current density shown in Fig.4.9 leads to the following charge density and field strength:

$$\rho = 0.8 \times 10^{-10} \text{ coul/cm}^3$$

$$E_o = 3.42 \text{ kv/cm}$$

Hence for a typical 1 mm probe,

$$\frac{\rho D_m}{\varepsilon_o} = \frac{0.8 \times 10^{-10} \times 10^{+6}}{8.854 \times 10^{-12}} \times 1 \times 10^{-3}$$

$$= .0904 \times 10^{+5} \text{ V/m}$$

Expressed as a fraction of the boundary electric field, this becomes:

$$\frac{E_x - E'}{E_x} = \frac{.0904 \times 10^5}{3.42 \times 10^{+5}} = .026$$

Thus the contribution to the total electric field made by the charge directly above the probe is less than 3%. Of course it is clear that the electric field as a whole for the system shown in Fig.4.9b and at an I'/L of 10μA/cm is space charge dominated; but this is irrelevant to the action around the probe.

By extending this reasoning a little, the product of (ρK) in eq.4.1 is found to be closely a constant within a region of probe dimensions. Hence the conductivity equation is also linear for a moderately distorted field such as illustrated in Figs.4.5b and 4.5c.

For the small region under consideration then, the system is closely Laplacian.

4.3.3 Deviation from Linearity

At high bias voltages, the characteristic disclosed by Fig.4.4 deviates from linearity due principally to a breakdown in the assumptions of the previous paragraph.

In the first instance, gross errors due to leakage of current over the insulation at the tip of the probe must be eliminated or rendered negligible. All probes used possessed an insulation resistance greater than $10^{+12}\Omega$, which was found to be adequate.

As the bias voltage is increased, the electric field surrounding the probe becomes increased in some regions around the probe and weakened in others as illustrated in Fig.4.5b. Now it is known that the mobility of a gas is slowly dependent upon the field strength. Thus changes in

K begin to affect the linearity of eq.4.1. In addition, at high values of $\frac{d^2E}{dx^2}$, the space charge density ρ ceases to be constant in the region of the probe and the analysis of para.4.3.2 breaks down. That is, eq.4.1 again loses linearity.

The effect of diffusion of ions is taken up in Appendix 4.2 where it is shown to be normally negligible at NTP. However, charge gradients $\frac{d\rho}{dx}$ in the region of a strongly perturbed probe might cause some charge transfer by diffusion. This again violates the assumption of para.4.3 where drift is taken to be the dominant mechanism.

A further cause of the non-linear characteristic of eq.4.5 is also noted.

At high bias voltages, such a flux configuration as that shown in Fig.4.5c will develop as indicated in Fig.4.5e. Here, lines of electric force leave the edge of the probe and alight on the surrounding earthed plate. The surface charge density over the surrounding plate is made up of the superposition of two charge densities viz:

$$\sigma = +\sigma_o - \sigma,$$

The first of these is that due to the fixed ambient field while the second is everywhere proportional to the applied voltage $+V_b$. As V_b is increased, there will come a point, first occurring at the gap edge when

$$\sigma = 0$$

and afterwards becomes negative. This means that fringing flux now enters the top plate surface from the probe. Such a flux cannot contribute to current conduction from ions drifting down from A-A'. Neither is the probe an emitter. This flux leads to a definite change in slope visible in Fig.4.12 to a certain extent and unambiguous in other cases.

4.4 Calibration of Probe in Terms of Capacitance

It is clear from the expressions given in eqs.4.7 to 4.10, that the capacitance of the probe is a key parameter. Since capacitance is a geometrical factor, this encourages one to look for an absolute calibration of the probe in terms of its dimensions. It remains to determine the capacitance between the top flat faces of the electrodes illustrated in Fig.4.5d. The solution of the Laplace equation for such a boundary system has not been solved analytically and it is unlikely that it ever could be. The writer has undertaken a digital solution of the field configuration by finite difference equations and this has reached a preliminary stage of finality. An analytical solution to a model which closely approximates the probe under consideration has recently been derived. A further treatment of probe capacitance is given in Appendix 5.1.

4.4.1 The Capacitance of a Flat Disc in Coplanar Gap

For a flat disc in a coplanar gap, Spence[104] derives the following expression for the capacitance per single side, for small gaps:

$$C = 2D_i\varepsilon_o \{-\tfrac{1}{2}.\log_\varepsilon(1 - \frac{D_i^2}{D_o^2}) + \log_\varepsilon 8 - 1\}$$

Noting that:

$$D_o = (D_i + 2G)$$

and making second order approximations, there results:

$$C = 2D_i\varepsilon_o \{1.07944 + \tfrac{1}{2}\log_\varepsilon (1 + D_i/4G)\} \qquad .....(4.12)$$

For geometrically similar probes in which the ratio of gap to diameter, G/D_i is a constant, then the capacitance is

directly proportional to the diameter, as expected. The bracketed term varies slowly with G/D_i. In Table 4.1 are shown the details of four probes used, together with the calculated capacitance.

Table 4.1

Typical Probes and Capacitances as Calculated From the Spence Relation

D_i mm	G/D_i	C F	C F
10	.075	.03624 ε_o	3.624 $D_i\varepsilon_o$
2.525	.0151	.0127 ε_o	5.028 $D_i\varepsilon_o$
0.821	.0625	.0031 ε_o	3.77 $D_i\varepsilon_o$
0.353	.044	.00143 ε_o	4.06 $D_i\varepsilon_o$

The probes require careful constructing, polishing and metrology determination of the diameters. The insulation is recessed to about one gap in depth. During later testing, the slope characteristic of the 0.821 and 0.353mm probes could not be distinguished and the theoretical constants from col.4 of Table 1 were averaged to give $3.915\ D_i\varepsilon_o$. From eq.4.10 the slope constant is $3.915 \times 4/\pi = 4.98$.

4.4.2 Experimental Check of the Capacitance Relation by Electrolytic Means

The capacitance of the top surfaces of the probe/electrode arrangement shown in Fig.4.5d cannot be directly

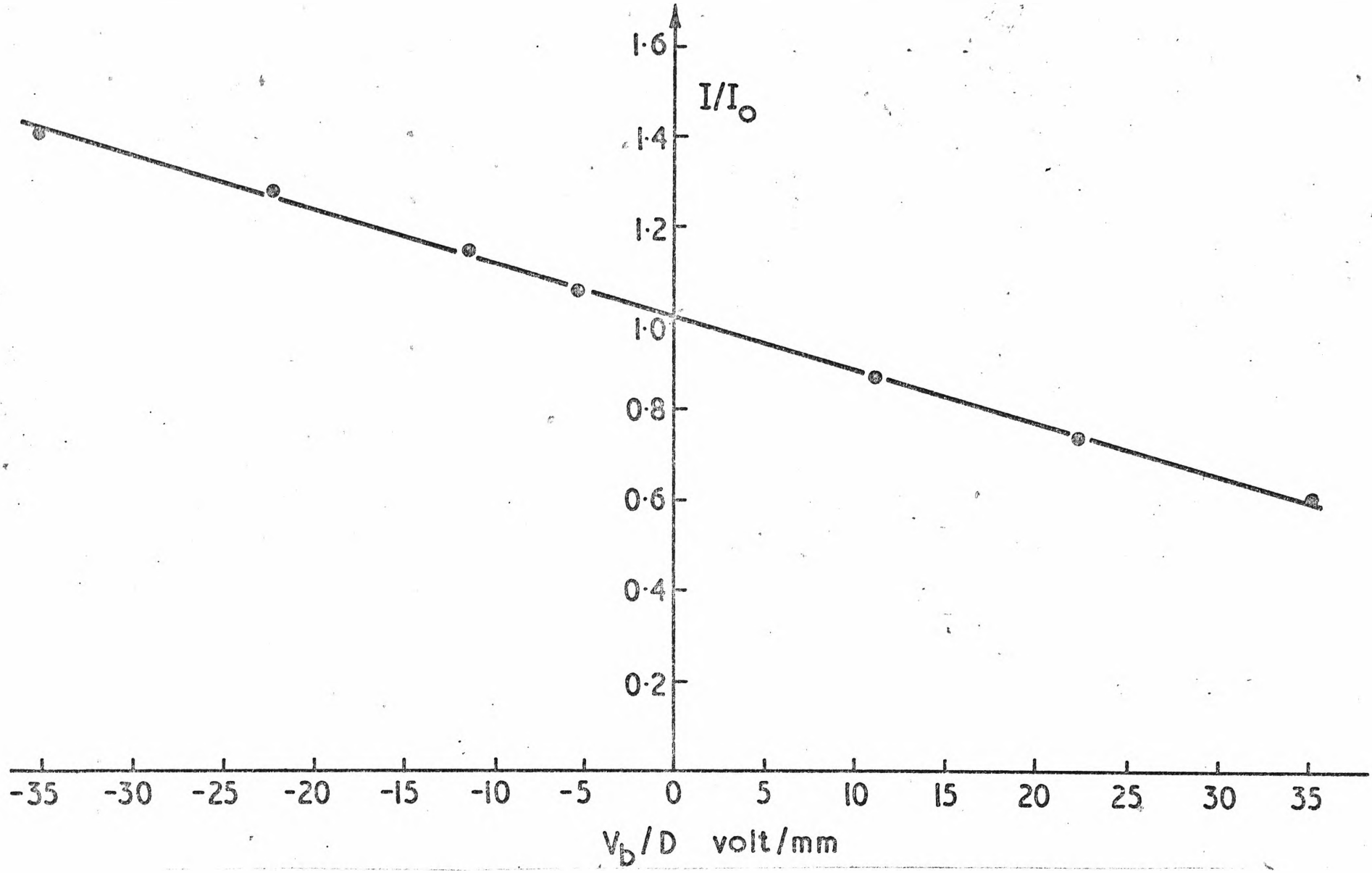

FIG.4.6 STRAIGHT LINE CHARACTERISTIC OF THE RELATIONSHIP $(I/I_o) \sim (V_b/D_m)$

This is an expanded version of Fig.4.4for small perturbations around the origin. Slope = .012 mm/volt.

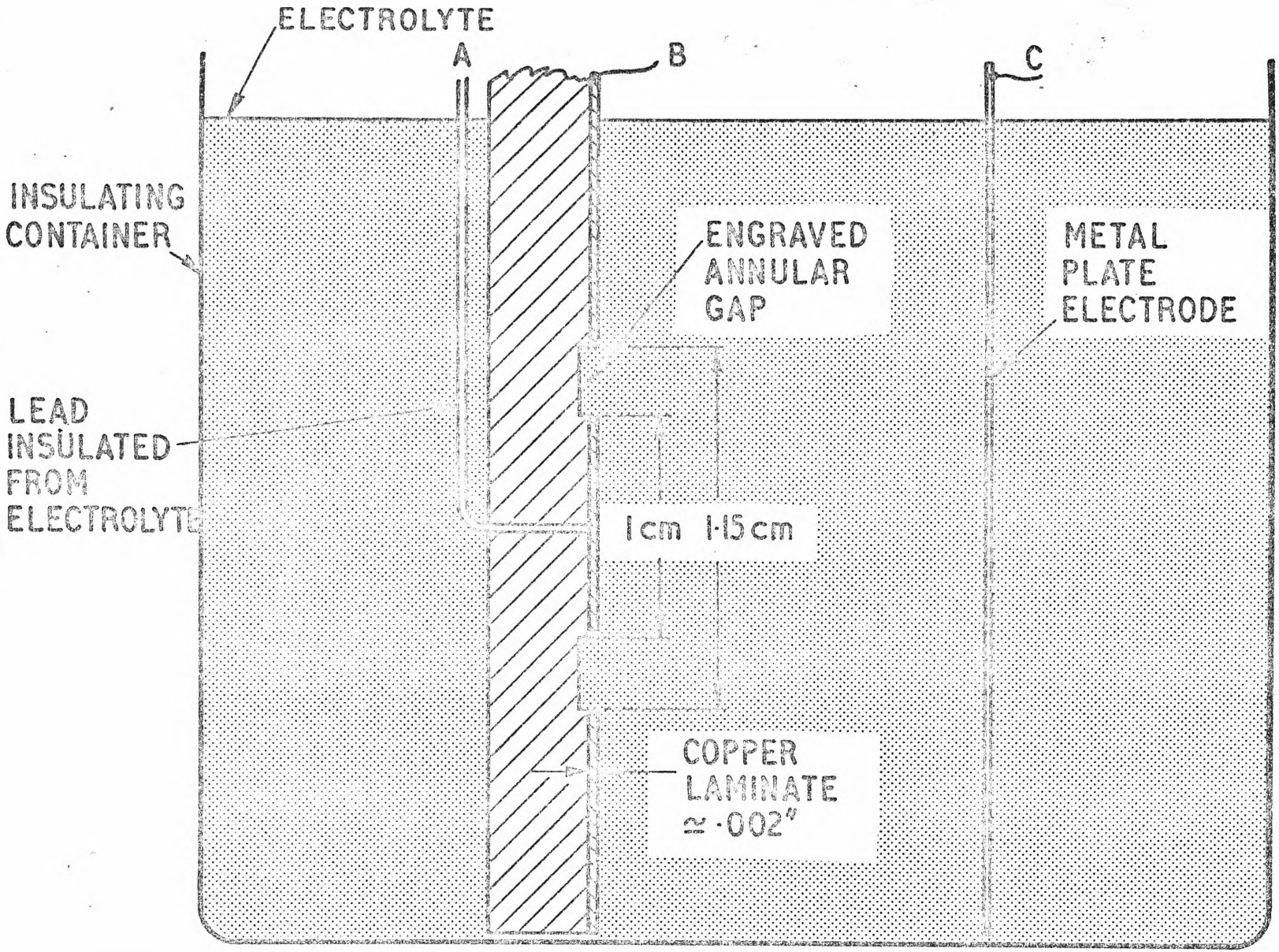

FIG. 4. 7 ELECTROLYTIC DETERMINATION OF THE CAPACITANCE OF THE PROBE

A printed circuit-board copper clad laminate with an engraved disc is immersed in any electrolyte. The conductivity of the solution is first determined between surfaces B and C. Then the resistance between A and B is measured. The capacity C_{AB} follows by analogy.

measured by an electrical bridge since the capacitance of the annular shank dominates. However, it may be approached by a difference method in the following way.
Let the air-spaced capacitance of the probe and shank be measured by an accurate a.c. bridge. Now immerse the active face of the probe in a fluid of high, known dielectric constant ε_r. The difference between the two capacitances is the desired value of the active faces multiplied by ε_r.

It was, however, found more suitable to check out the Spence capacitance relation by an electrolytic method.

The apparatus shown in Fig.4.7 was immersed in an electrolyte. First the resistivity of the solution was measured between the copper laminate and the metal electrode, carried out at 50 Hz to avoid polarisation. Then the metal electrode was removed and the resistance between A and B determined.

Making use of the well known relationship which connects the free space capacitance of a set of electrodes with their resistance when placed in a conducting medium:

$$RC = \bar{\rho}\,\varepsilon_o \qquad \ldots\ldots(4.13)$$

From these tests, $\bar{\rho}$ and R were evaluated, and it was found that:

$$C = 3.75\ D_i \varepsilon_o$$

This is to be compared with the calculated capacitance from the Spence relation taken from Table 1, viz

$$C = 3.624\ D_i \varepsilon_o$$

These constants agree well, and are within the experimental inaccuracies.

The configuration shown in Fig.4.7 closely resembles the model used in the derivation of the Spence Relation. It

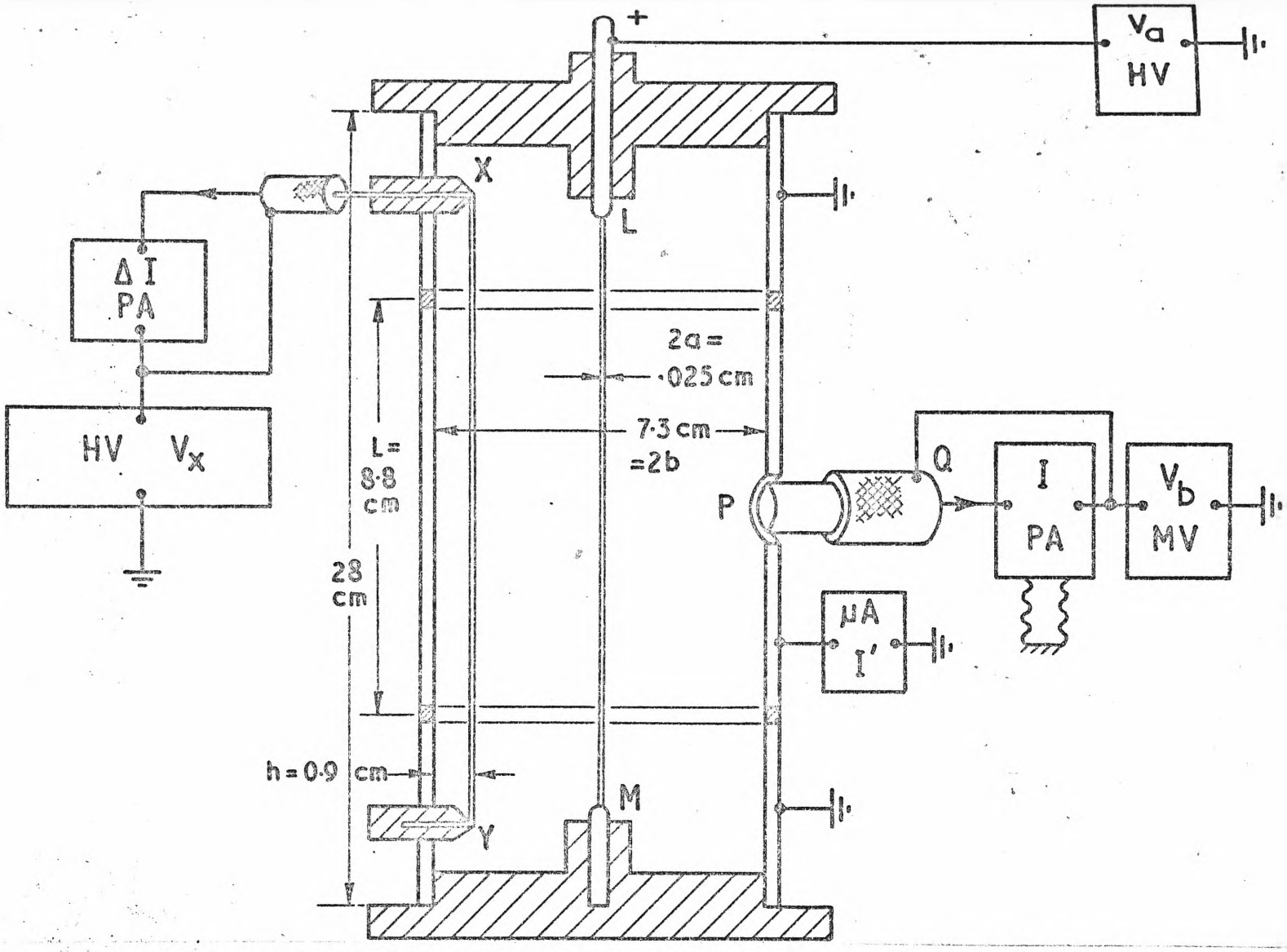

FIG. 4.8 THE PROBE AT THE BOUNDARY OF A CYLINDRICAL ELECTRODE CORONA DISCHARGE

Positive corona is set up between the platinum discharge electrode LM and the earthed, guarded, receiving electrode. Potential gradient at the boundary is measured by the floating electrode XY. The probe PQ samples both E and J on the boundary.

HV = high voltage DC supply, 0-50KV
MV = medium voltage DC supply
PA = chopper stabilised, floating pico-ammeter
μA = micro-ammeter

is interesting to note that this relation may be used to calculate the errors, already observed by Meek and Collins in their earlier work.[101] They found in measurements on displacement current rather than conduction current, that with a 1 cm probe to which a bias of 200 V was applied in an ambient field of 22 KV/cm, an error of 2½% was incurred. The use of eqs.4.6 and 4.11 shows that an error of this order would be expected.

4.5 Experimental Calibration of the Probe in a Unipolar Discharge

In para.4.4.2, an experiment was described in which the probe was immersed in an electrolyte. In this case, the carriers were of mixed and unknown mobilities. Furthermore, the field was alternating so that no space charges could exist. Any part of the conducting medium was therefore electrically neutral, so that the governing equation was Laplace rather than Poisson. A satisfactory experimental check was made on the probe under these conditions.

It was then desired to check the operation of the probe when the surrounding field has strong space charges present. This had already been done in point-to-plane coronas as described in para.4.2.2. At the present time however, E and J cannot be calculated for such a discharge geometry. One looks then for a discharge system which is Poisson dominated, but whose geometry is calculable.

The cylindrical electrode corona system suggests itself because this geometry is fairly readily calculable as already noted, and the discharge may easily be rendered space charge dominated. In the system depicted in Fig.4.8, then, the electric field E and the current density J are both calculable and measurable, as already discussed in para.1.1.

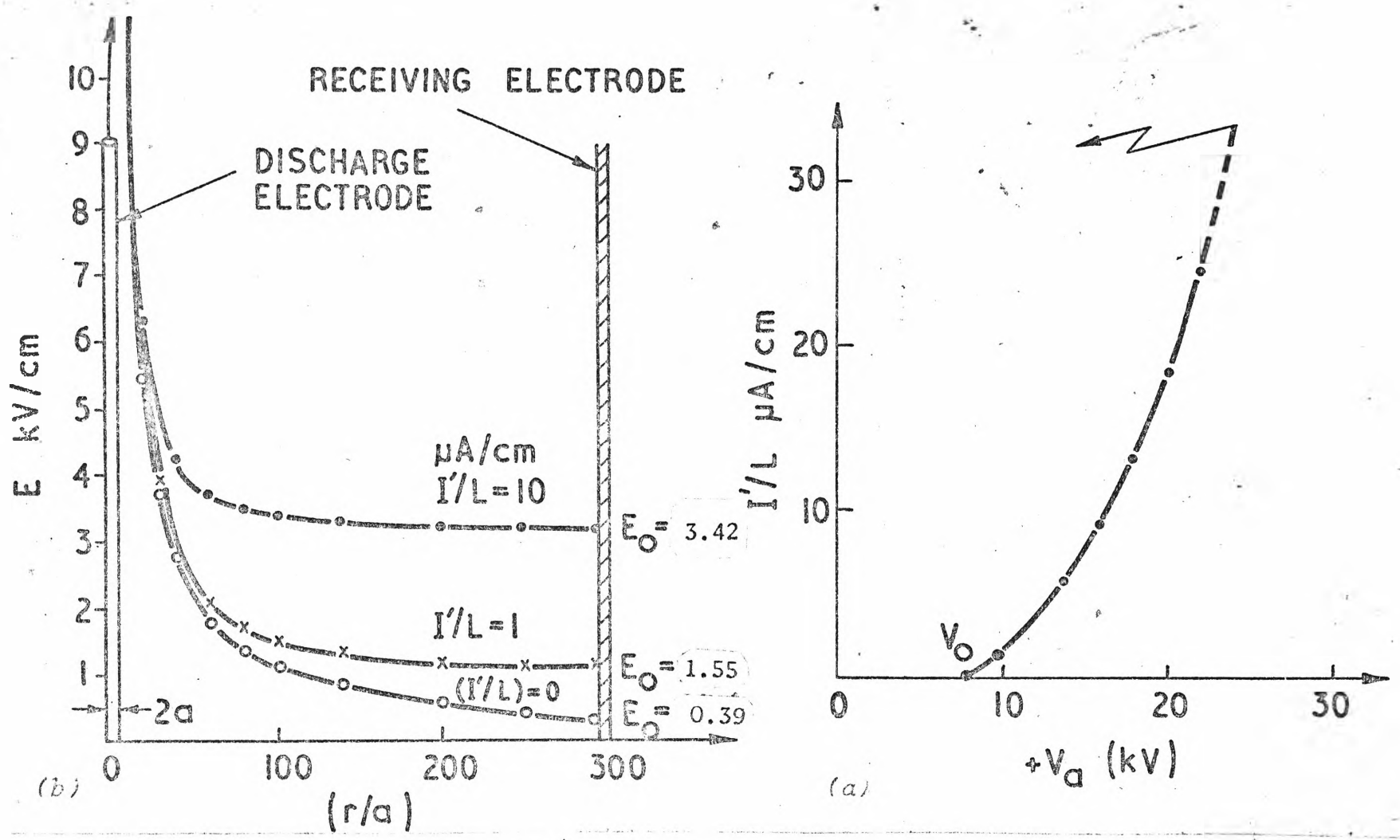

FIG. 4.9 CORONA IN A CYLINDRICAL ELECTRODE SYSTEM

Positive corona is set up in the cylindrical electrode system depicted in Fig.4.9

(a) The relation between corona current/unit length, (I'/L) is closely a parabolic function of the applied potential V_a.

(b) The electric field across the interelectrode space is logarithmic for zero corona current. With increasing current, the space charges cause E_o on the boundary to rise and become uniform across the gap.

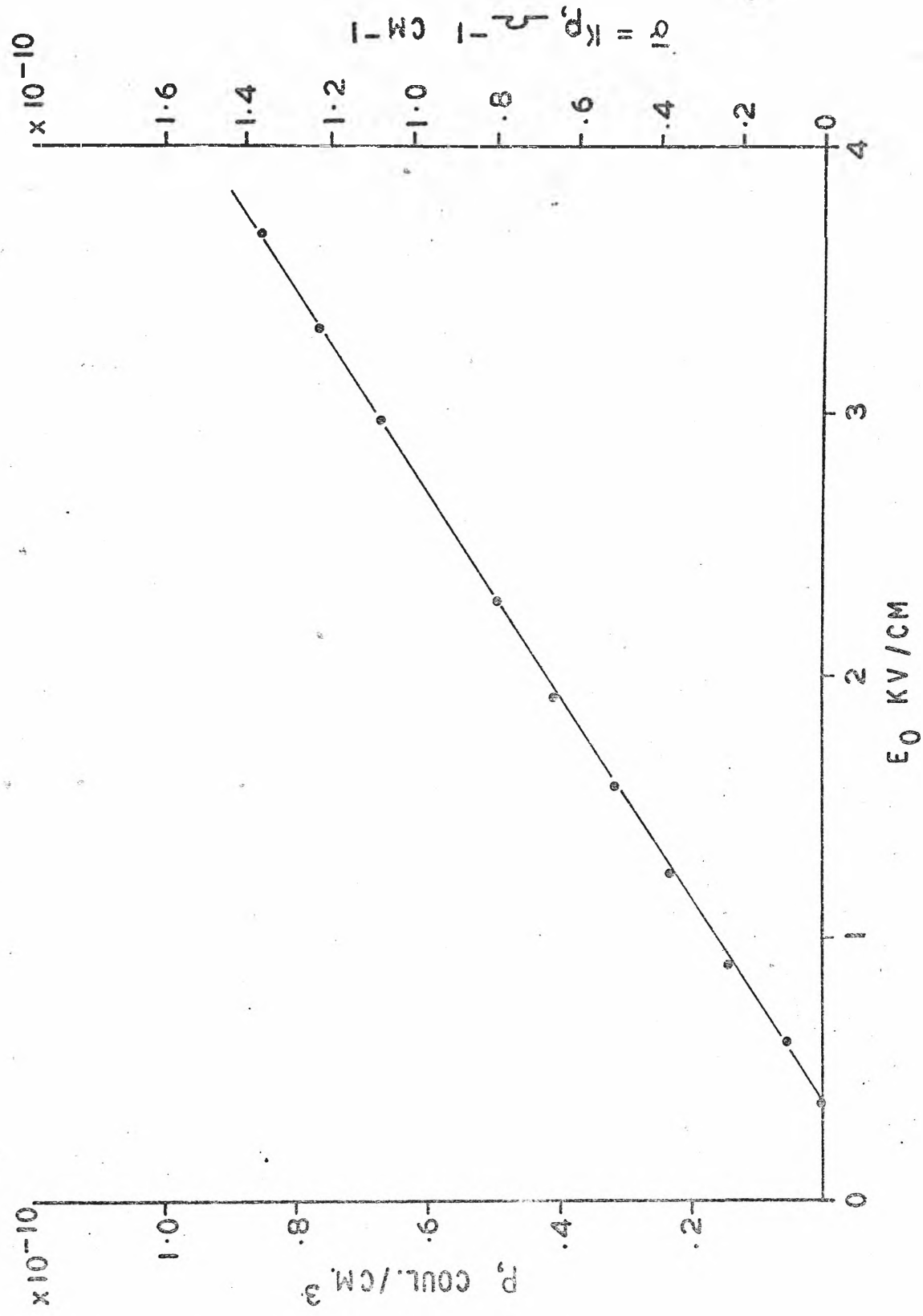

FIG. 4.9(c) CORONA IN A CYLINDRICAL DISCHARGE SYSTEM

Positive corona is set up in the cylindrical electrode system depicted in Fig. 4.8.
The boundary charge density and conductivity of the ionised gas is expressed as a function of the boundary electric field, E_o

The following paragraphs describe the coaxial discharge system, calibration techniques and the various values of J, E and ρ occurring within it.

Attention is again drawn to the characteristics of Fig.4.9a and 4.9b. The charge density ρ present at the outer boundary is shown in Fig.4.9c, there expressed as a function of the boundary electric field E_o. It is calculated from the expression of $J = \rho K E$ using a round value of K^+ of 1.6.

4.5.1 Experimental Determination of Boundary Electric Field E_o

In order to measure the electric field E_o on the boundary, a fine platinum wire X-Y (.25 mm dia) was placed close to the boundary and parallel with the axis. One end of this fine electrode was connected to a digital high voltage supply (readable to 4 figures) via a solid state, floating, chopper-stabilised picoammeter. This is a more sensitive version of the method used by Sato[80] and later by Penney and Matick.[15] The potential V_x is slowly raised until the current ΔI just becomes zero. Ion flow to the electrode X-Y has then ceased, and correcting for the finite size of the wire (ibid p.93), the unperturbed space potential is obtained. The boundary field strength E_o is then obtained as (V_x/h) since on general considerations (Fig.4.9b), E_o is constant for some distance back into the inter-electrode space.

This electric field E_o is then plotted in Fig.4.10 as a function of $\sqrt{I'/L}$. It is there compared with calculated values for E_o obtained from eq.1.6 by inserting various values for the mobility K. The measured curve fits comfortably into the pattern, corresponding to a calculated value of E_o with a K of 1.6. This is an entirely reasonable value for the gas under consideration.[107]

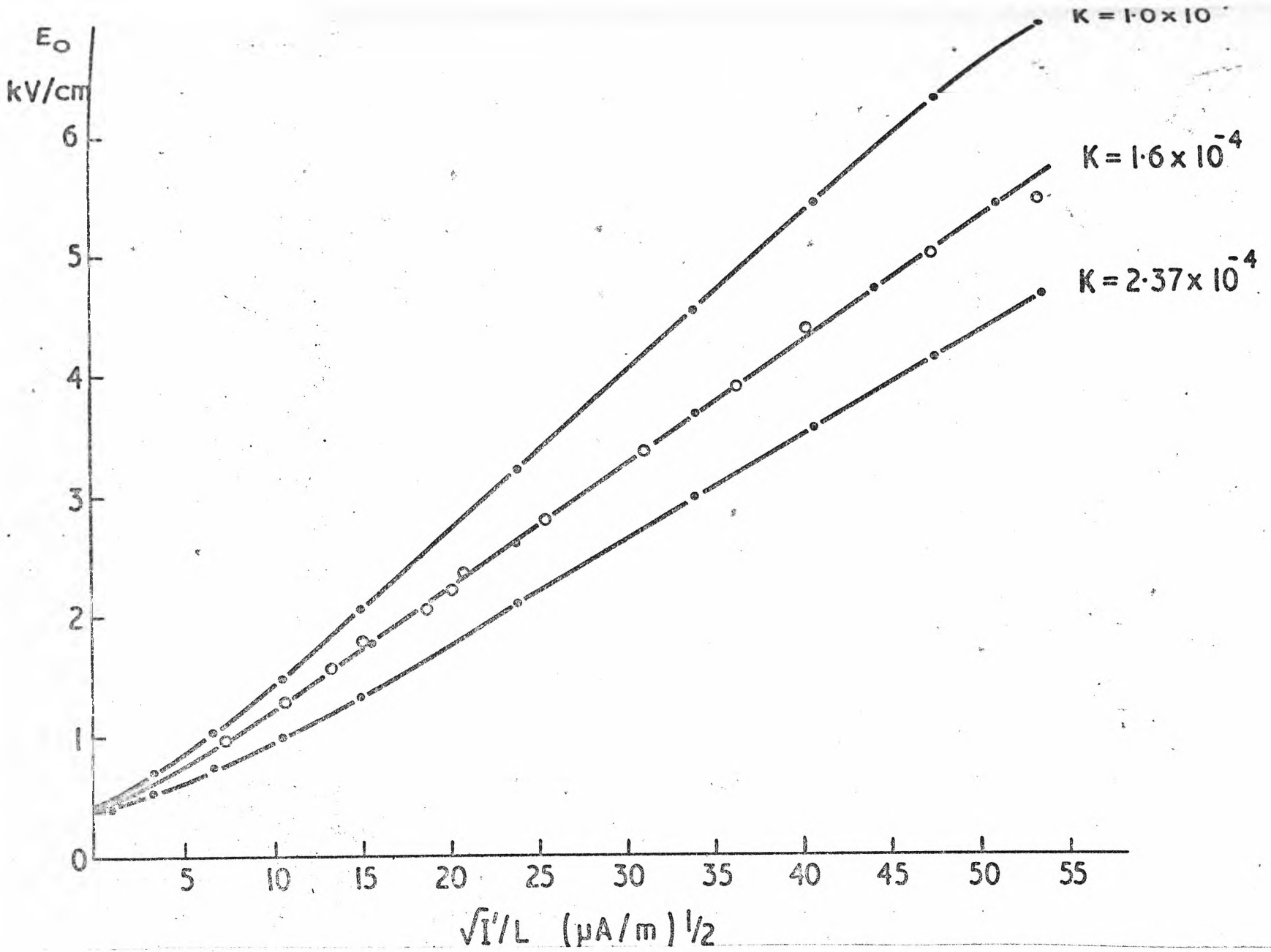

FIG. 4.10 CALCULATED AND MEASURED VALUES OF THE ELECTRIC FIELD ON THE CORONA BOUNDARY

Using the test results from the apparatus of Fig.4.8, a comparison is made with values calculated from Eq. 1.6. The two agree well for a gas mobility of $K^+ = 1.6 \times 10^{-4}$. · *Calculated* o *Measured.*

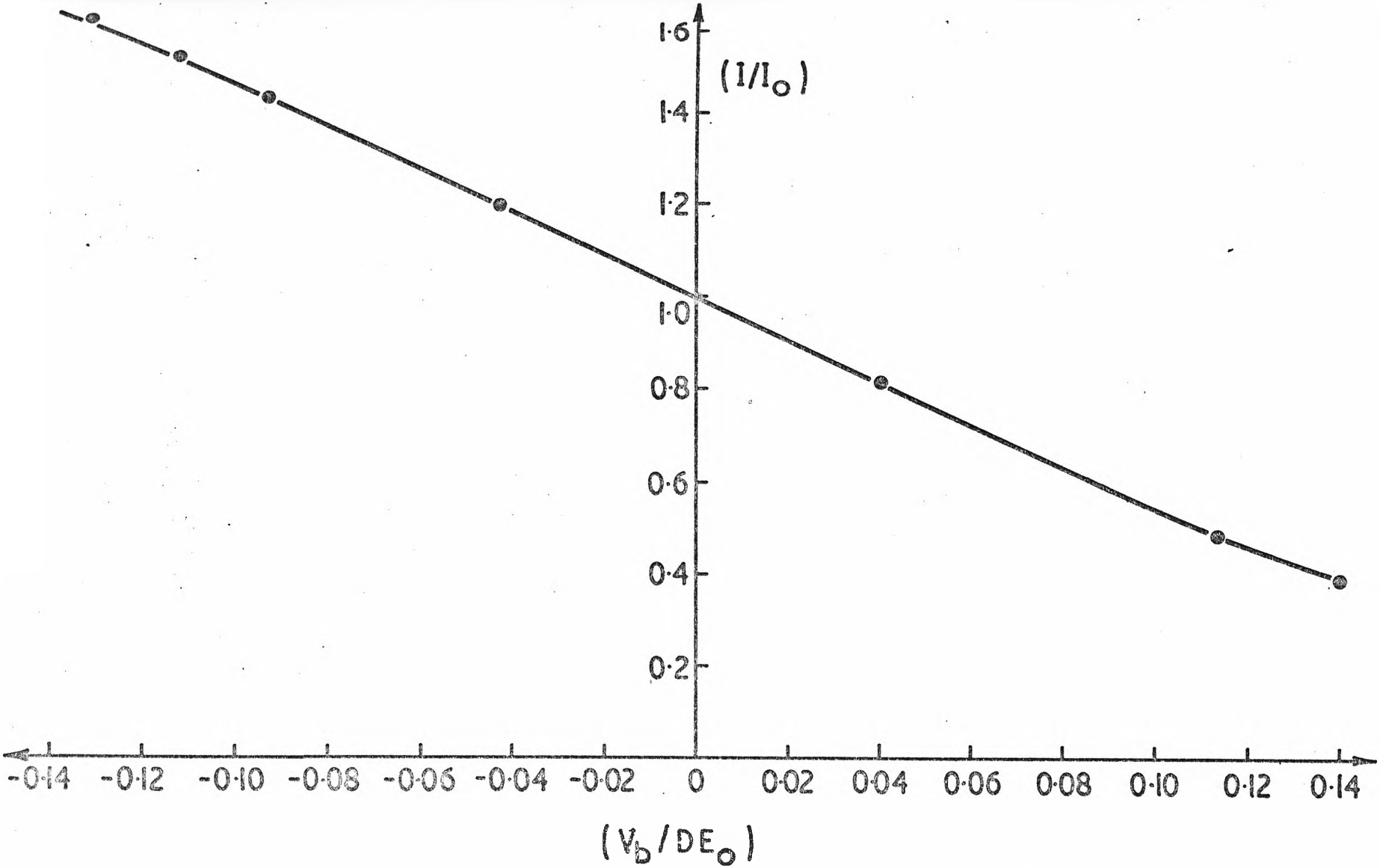

FIG. 4.11 DIMENSIONLESS PROBE CHARACTERISTIC

Dimensionless dependence of the normalised current (I/I_o) upon the normalised bias field (V_b/E_oD). For a single probe; D = 0.832 mm, V_a = 13.6 KV, J_o = .25 μA/cm²; E_o = 2.64 KV/cm. Test apparatus as in Fig.4.8

We therefore conclude that the positive corona system depicted in Fig.4.8 is behaving predictably in all respects. The measured values of electric field E_o on the boundary as depicted in Fig.4.10 are probably correct to within about ± 6%.

4.5.2 The Biased Probe on the Boundary

Firstly, using the instruments to the right of Fig.4.8, the current I_o flowing into the probe PQ with $V_b = 0$ was measured. The current density $J = (I_o/A)$ so determined was compared with the macroscopic current density in the guarded section, viz $I'/(L\ 2\pi\ b)$. With the carefully prepared probes described in Table 4.1, the two values of J checked to within 1%.

Next, the probe was biased positively and negatively, results similar to those described in Figs.4.4 and 4.6 being obtained. The characteristics of several probes of different diameter were obtained at each setting of corona current.

By raising the voltage V_a applied to the HT electrode, a new current condition was reached according to Fig.4.9a and a new boundary electric field E_o established according to Fig.4.9b. The values of I_o and I were again determined.

For these results to be universally applicable, they should be displayed in a dimensionless form, and this is now effected in the subsequent paragraph.

4.6 Generalised Probe Characteristics

The results of any one test with one probe were expressed in the dimensionless form

$$(I/I_o) = f(V_b/E_o\ D_i)$$

where f is the function expressed by the typical curve in Fig.4.11. The independent variable (I/I_o) and the bias voltage V_b are directly measured. The diameter D for the

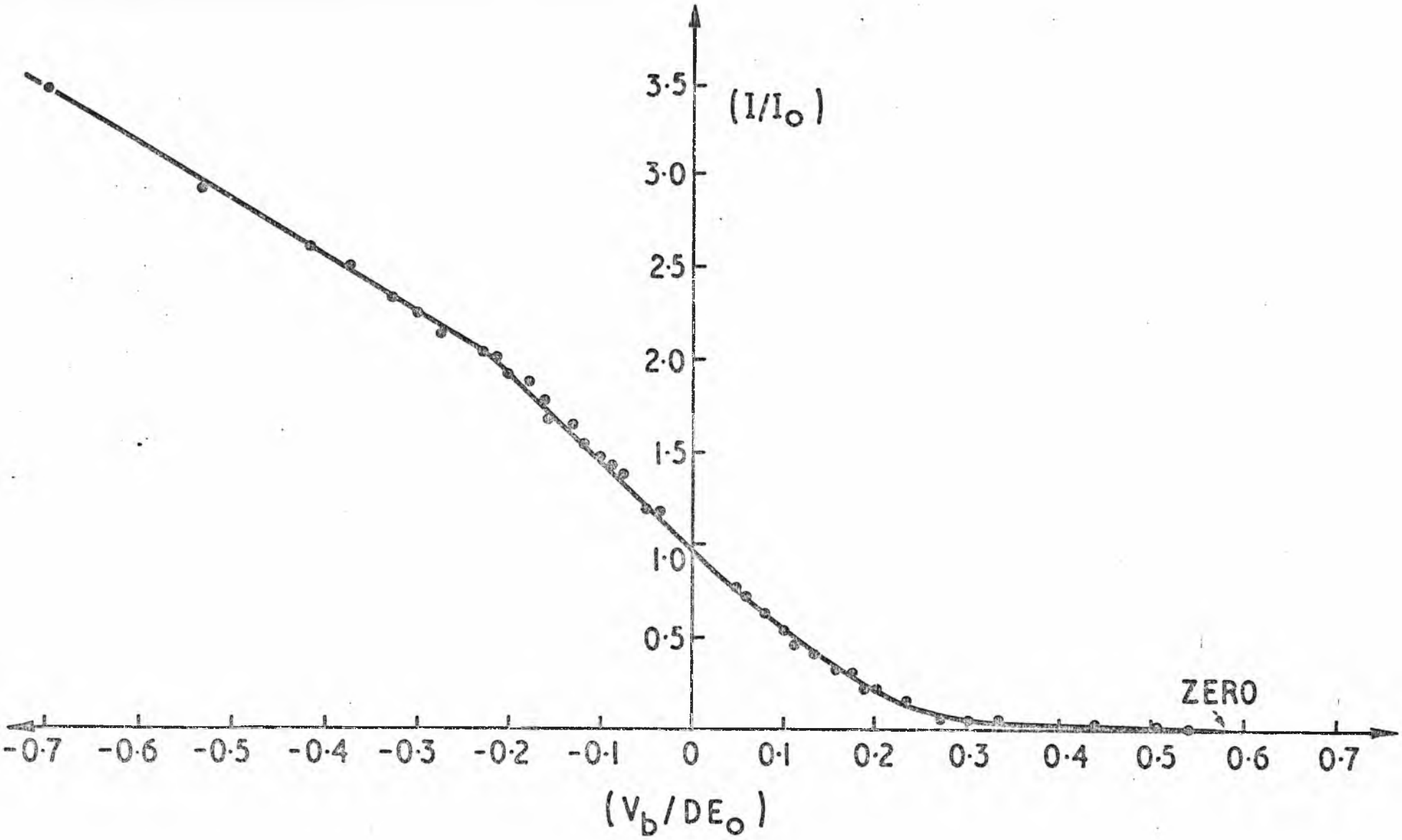

FIG. 4.12 GENERALISED PROBE CHARACTERISTIC

For two geometrically similar probes, D_m = .832 mm and .359 mm. The normalised current density is expressed as a function of the normalised field strength. Current densities J_o were from .05 to 1.25 μA/cm^2 and field strengths E_o from 1.3 to 5.7 KV/cm. Conduction is due to positive ions in air at NTP. Test apparatus as in Fig. 4.8.

appropriate probe was determined by metrology.* The boundary, unperturbed field strength E_o is taken from the values of Fig.4.10.

The mode of expression of the data of Fig.4.11 suggests searching for a greater generality. Two geometrically similar probes i.e. in which the ratio of gap to diameter (G/D_i) were the same, were compared. A range of E_o from 1.3 to 5.7 KV/cm and current densities J_o from .05 to 1.25 $\mu A/cm^2$ were applied to the probe. The results are to be seen in Fig.4.12, which indicates a high degree of correlation between the two probes and the various ambient conditions. The deviations from the mean are within the various experimental errors.

Around the origin, the characteristic is straight for a considerable region, this outcome being expected from the discussion in para.4.3.1. This straight-line region is shown in Fig.4.13, from which the slope is readily measured and found to be 4.72. This value is to be compared with the 4.98 calculated in para.4.4.1 from capacitance considerations. The two values agree within experimental accuracies.

4.6.1 Significance of the Generalised Characteristic

The characteristic portrayed in Fig.4.12 is the result of about a hundred tests on several probes, subjected to a range of current densities, field strength and corresponding charge densities. The gas was however air at NTP. It would

---

* The following gives some idea of the work-effort consumed by this project. The writer's log book shows that the mere measurement of these diameters took him 3 days, plus technician time.

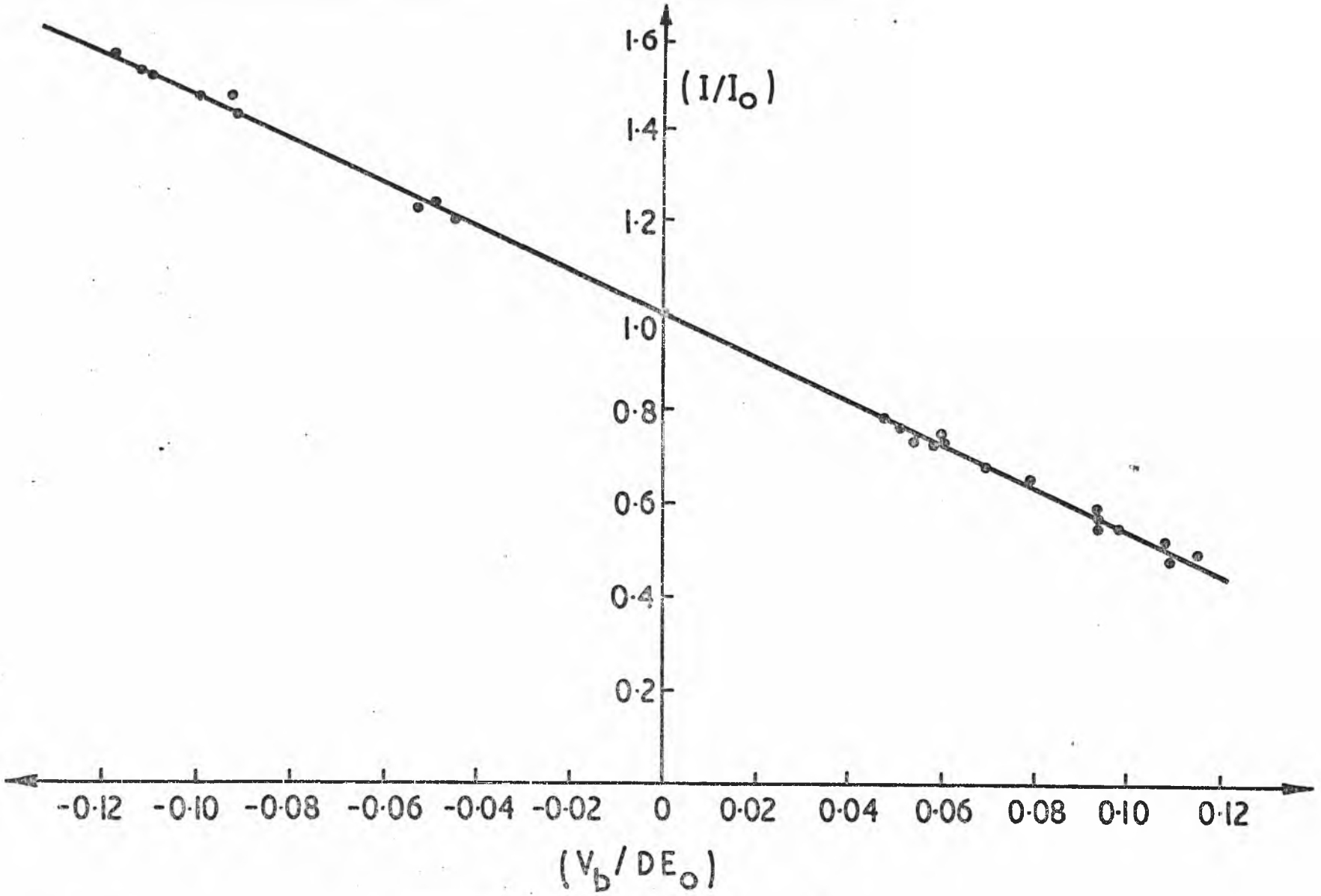

FIG. 4.13 GENERALISED PROBE CHARACTERISTICS, SMALL PERTURBATIONS

The region around the origin in Fig.4.12 is shown here enlarged. The slope of the characteristic is measured as 4.72. Apparatus as in Fig.4.8

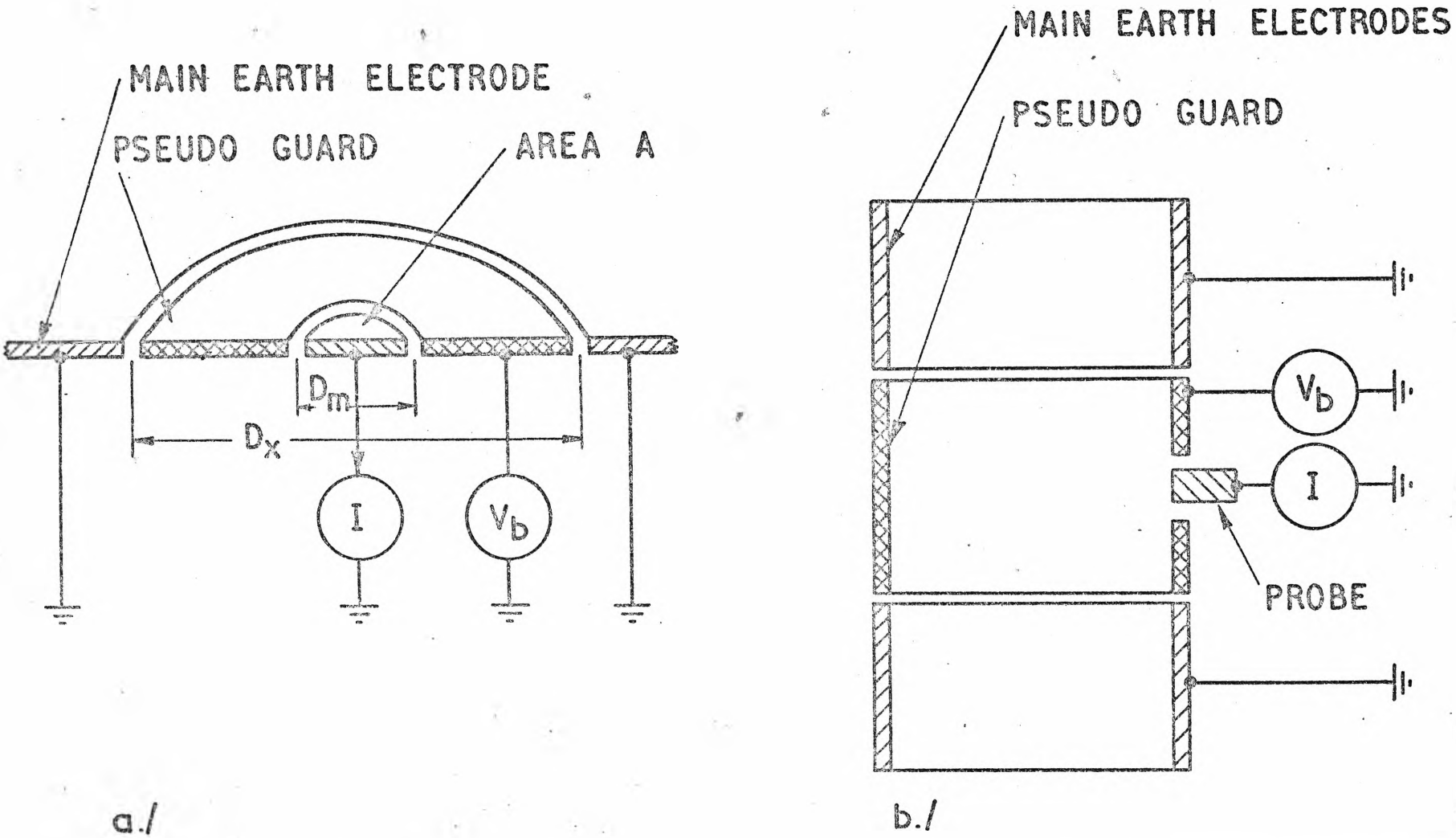

FIG. 4.14 USEFUL PROBE CONFIGURATIONS

In both cases the instrumentation can have one end earthed.

(a) D_x >> D_m and the system replaces that of Fig.4.1

(b) Cylindrical electrode system replacing that of the right half of Fig. 4.8

be interesting to investigate the generality of the characteristic for other gases and electrolytes with differing mobility and diffusivity.

Complete generality of data for all flat probes of whatever shape and area follows from eq.4.7. The dimensionless function

$$(I/I_o) = f(\frac{C}{A\varepsilon_o} \cdot \frac{V_b}{E_o}) \qquad .....(4.14)$$

may prove to have wide validity.

As in the case of a Langmuir probe, in a low pressure gas or plasma, the whole characteristic is of some interest but the vital portions are those which indicate plasma potential and the electron temperature.

In the characteristic presently under consideration, it may prove that the slope at the origin which provides the field strength is the vital part - the remainder may prove to be of marginal value.

4.7 Useful Probe Configurations

There are experimental difficulties associated with the probe arrangements shown in Figs.4.1 and 4.8. It is noted that the picoammeters I (or oscilloscopes in other investigations) must be used in a floating mode with considerable care required for screening. Alternative arrangements which proved satisfactory are shown in Fig.4.14.

4.7.1 Use of Pseudo Guard

In Fig.4.14a, the probe is always held at earthed potential since one end of the pico-ammeter I is earthed. The main receiving electrode is also held at earthed potential. The pseudo-guard is then perturbated by V_b. The action around the probe D_m is then exactly as previously described. However, D_x must be made sufficiently large so that when checked against eq.4.10 or 4.11, the change in

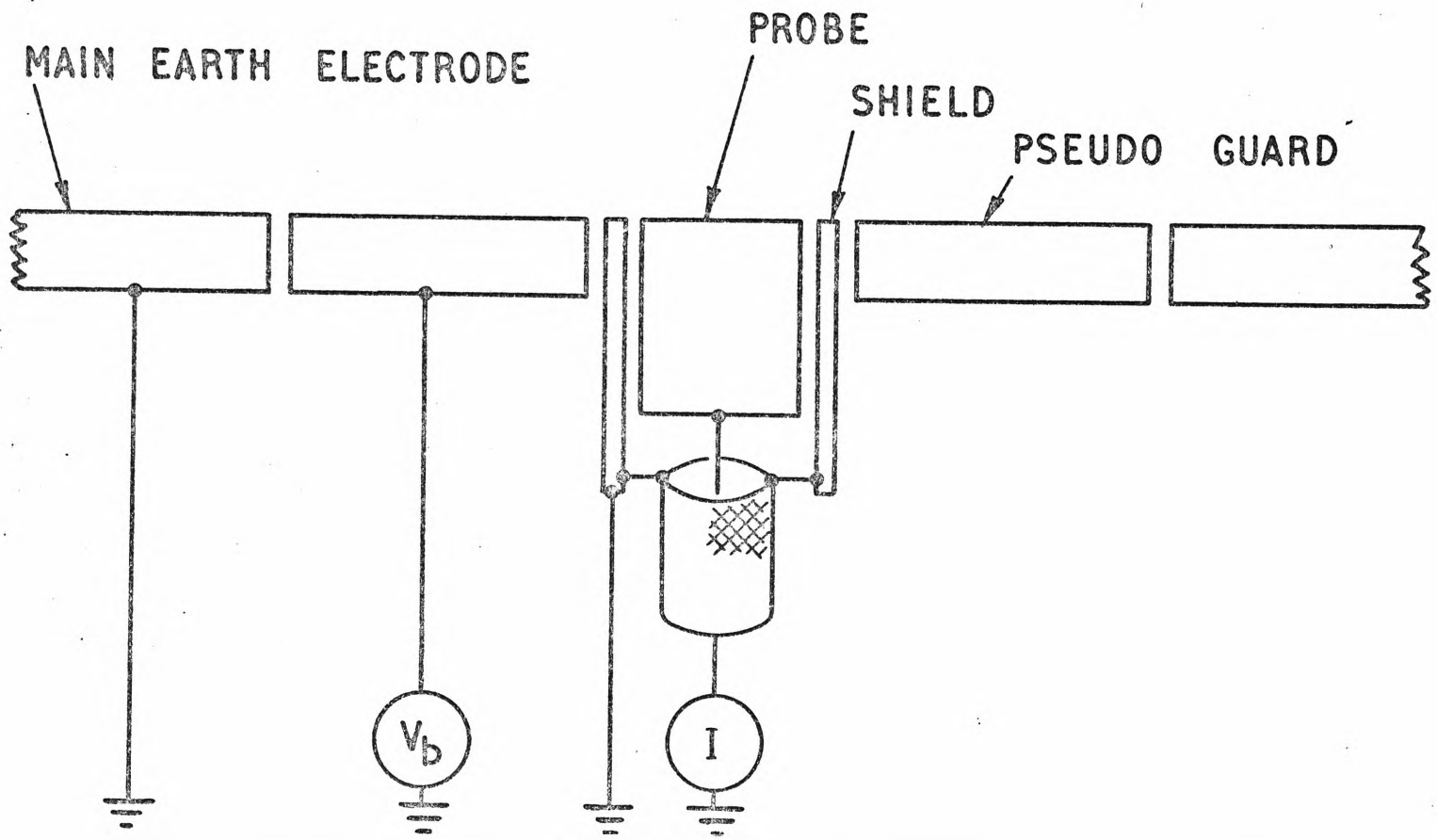

FIG. 4.15 SHIELDED PROBE

The probe is shielded over the whole of its length on up to the active surface. Using a three terminal bridge, the capacitance between the active face and the pseudo guard may be directly measured.

current density across D_x is not altered significantly. As a starting point, a D_x of 10 cm may be chosen. The arrangement of Fig.4.14a then replaces that of Fig.4.1. The cylindrical arrangement of Fig.4.8 may be treated similarly and becomes that shown in Fig.4.14b.

Both the arrangements shown in Fig.4.14 may be found applicable in most cases.

4.7.2 The Shielded Probe

The fully shielded probe illustrated in Fig.4.15 together with the pseudo-guard, is more difficult to construct, but has a number of obvious electrical advantages. All risk of serious leakage from the probe to the surrounding electrode is eliminated. Gases with dew point around the operating temperature may be examined. More important still, the capacitance between the active surface of the probe and the pseudo-guard may be directly measured. Modern bridges are thus able to measure the capacitance C_o of eq.4.6 to better than 1%. Thus absolute calibration of the probe is obtained without the need for any of the calculations described in para.4.4. The three terminal probe is discussed more fully in Chapter 5.

4.8 Electric Field in the Absence of Ionic Currents

The electric field in the absence of ionic currents, or outside a current channel, is determined by the method first described by Meek and Collins[101] but used independently by the present writer for several years without being aware of this prior work on impulse phenomena. As an electrode surface is being charged up, displacement currents flow, and if such currents flowing through a probe are integrated then the field

$$E = \frac{\int i \, dt}{A \, \epsilon_o}$$

and this applies in the transient state. Meek and Collins used a capacitor to integrate their probe displacement currents and displayed the result on an oscilloscope. Large fields and large probes led to adequate sensitivity.

In the present tests, the writer used miniature probes of 2.525, .821 and .353 mm dia. in conjunction with a high gain charge amplifier of the electrometer type using substantial feedback. The sensitivity obtainable is about 50 mV/pico coul with a bandwidth of 400 K Hz. This enables fields as low as 10-100 V/cm to be measured with a 1 mm probe. Moreover, the probe is always held at earth potential within a few microvolts so that no other errors are introduced due to this cause.

To map the static field over the electrode shown in Fig.4.16, an alternating potential Vä of 100 to 500 volts, is applied at any convenient frequency from 50 to 10000 Hz. The ripple from a H.T. D.C. supply is often adequate for this purpose. The output from the charge amplifier is exhibited on an oscilloscope the result being normalised in the form

$$\frac{E_r}{E_o}$$

where E_o is the field in the centre of the electrode. In this way, the field external to, or in the absence of a discharge is quickly and accurately mapped. The result is shown in Fig.6.1 where the field falls away at the edge of the Rogowski profile in the manner expected. Other aspects of this circuit are taken up in Appendix 4.3. The technique as developed has excellent sensitivity and positional discrimination.

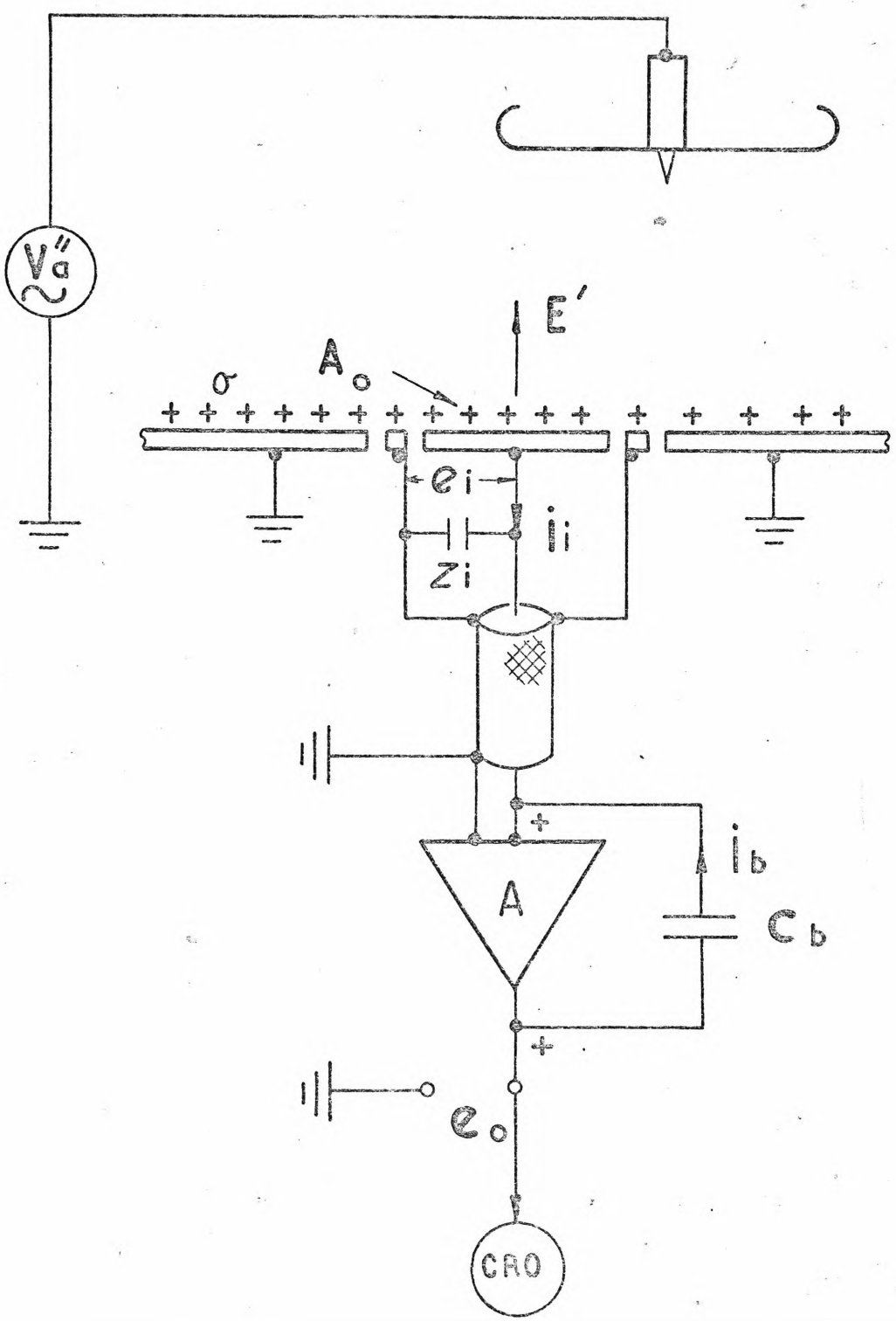

FIG. 4.16 MEASUREMENT OF ELECTRIC FIELD IN THE ABSENCE OF CORONA

The electric field at the boundary of an electrode system comprising a Rogowski Profile with a discharge point (no corona) is mapped. V"a is any low convenient alternating voltage (or transient voltage). Displacement currents are integrated by the fast operational amplifier.

$$E'(t) = e_o(t) \frac{C_b}{A_o \varepsilon_o}$$

4.9 Status of the Probe and Further Developments

A new type of probe capable of measuring steady state J and E over a plane boundary with a mechanical precision of about 0.5 mm has been developed. A small insulated circular area of about 1 mm dia is polished flat and flush with the boundary. Without bias the probe samples the current density at a point. When biassed by V_b, the quiescent current I_o is increased or decreased according to the relation

$$(I/I_o) = 1 + 4.85 \frac{V_b}{D_m E_o}$$

where D_m is the probe mean diameter and E_o the boundary unperturbed field. The constant 4.85 is dimensionless and applies to a gap/diameter ratio $G/D_m = 0.05$; but varies slowly with this ratio. From this expression, E_o may be readily determined.

As matters stand, this new Micro Area Boundary Electrode shows promise of providing valuable information on the boundary of a corona, electrolyte or plasma. In particular it is both small enough and of sufficient sensitivity to be an entirely adequate tool for the investigation of interesting fine structure of negative coronas. It must be emphasised that MABEL requires no axis of symmetry whatever in the corona to be examined, in sharp contrast to the several other probes described in para. 1.1.

In the Chapter 6, the probe will be applied to the coronas from a number of electrode configurations of interest.

CHAPTER 5

DETERMINATION OF THE ELECTRIC FIELD CURRENT DENSITY AND CONDUCTIVITY OF AN IONISED GAS BY MEANS OF AN A.C. BOUNDARY PROBE

5. Determination of the Electric Field, Current Density and Conductivity of an ionised gas by means of an a.c. boundary probe

In this chapter, the writer describes how the three terminal boundary probe MABEL, using an a.c. diagnostic signal and an a.c. bridge as sensor, may be used to determine the current density J, electric field E, conductivity $\overline{\sigma}$ and complex permittivity $\varepsilon = \varepsilon' - j\varepsilon''$ of an ionised gas at a point on its boundary.

Previously in C4, the writer described how the micro area boundary electrode could be used first to find J over the receiving electrode, and later, by d.c. perturbation of the probe to determine E the local electric field. The same information may be obtained much more quickly and accurately by carrying out the perturbation at audio or radio frequencies and using a bridge to eliminate the unwanted quadrature displacement currents.

5.1 Principle of the Boundary Probe

It was previously shown (para.4.2.2) that if a probe of the sort shown in Fig.4.1 on the boundary of a gas discharge were biassed by a direct potential V_b that the resulting characteristic would be typically as shown in Fig.4.4. At zero bias, the quiescent condition

$$J_o = I_o/A_o \qquad \ldots\ldots(5.1)$$

held. The equation of the straight line region about the origin was found to be:

$$(I/I_o) = 1 + \frac{C_o V_b}{A_o \varepsilon_o E_o} \qquad \ldots\ldots(5.2)$$

where C_o was the capacitance between the top face of the probe and the surrounding electrode.

For several probes used, the dimensionless constant

$$\frac{C_o}{\frac{\pi}{4} D_m \varepsilon_o}$$

was found to be 4.85 by theory and experiment.
Hence for a wide range of probes

$$I/I_o = 1 + 4.85 \frac{(V_b/D_m)}{E_o} \qquad .....(5.3)$$

The above equations were based upon the assumptions of local Laplacian action with drift as the mode of ion transport. At high perturbation voltages, space charge distortion, diffusion and changes in ion mobility all contributed to the non-linear characteristic of Fig.4.4.

To determine J_o and E_o at a given point on the boundary of an unknown field, several values of d.c. bias V_b were chosen and the $I \sim V_b$ characteristic around the origin plotted. The desired values of J and E_o followed from eqs.5.1 and 5.3. This did however require stable conditions for a minute or two and the method was only applicable to steady state.

5.1.2 Probe with small Signal a.c. Excitation

It is tempting to enquire what would happen if an a.c. excitation voltage were applied to the probe. Making reference to Fig.4.1 and 4.6, the quiescent d.c. current I_o would still flow and be measured by an average-reading ammeter. Ignoring for the time being displacement currents due to capacitive effects, then a small voltage increment $+\Delta V_b$ will lead to a current decrement $-\Delta I$ in positive corona and the ratio is:

$$\frac{\Delta I}{\Delta V_b} = G, \quad \text{a conductance.}$$

This conductance may be evaluated as follows from eq.5.2:

$$I = I_o + \frac{C_o V_b I_o}{\varepsilon_o E_o A_o}$$

$$\text{hence } G = \frac{dI}{dV_b} = \frac{C_o I_o}{\varepsilon_o E_o A} = \frac{C_o}{\varepsilon_o} \frac{J_o}{E_o}$$

Now for any medium of conductivity $\bar{\sigma}$,

$$J = \bar{\sigma} E \qquad .....(5.4)$$

which is ohm's law at a point. In the present case, for a conducting gas,

$$J = (Kne)E \qquad .....(5.5)$$

where K is the ionic mobility, and ne is the charge density. In general there could of course be several carriers of different mobility and sign contributing to conduction.

Hence we find that:

$$G = \frac{C_o}{\varepsilon_o} \bar{\sigma}$$

from which the resistivity of the gas becomes

$$\bar{\rho} = \frac{C_o}{\varepsilon_o G} \qquad .....(5.6)$$

Summarising then, we conclude that the slope of the $I \sim V_b$ characteristic around the origin leads immediately to that important parameter - the conductivity of the ionised gas.

5.1.3 Conductivity in the absence of Current Density

The result given by eq.5.6 could have been found from a different point of view. Suppose that the gas (or indeed any other medium) is conducting by mixed carriers and that there is neither space charge nor current flow J_o. A fundamental property of Laplacian fields relates the free-space capacitance and the resistance between a pair of arbitrary electrodes immersed in a conducting medium by the relation:

$$RC_o = \bar{\rho} \varepsilon_o$$

Noting that G = I/R and eq.5.6 follows at once.

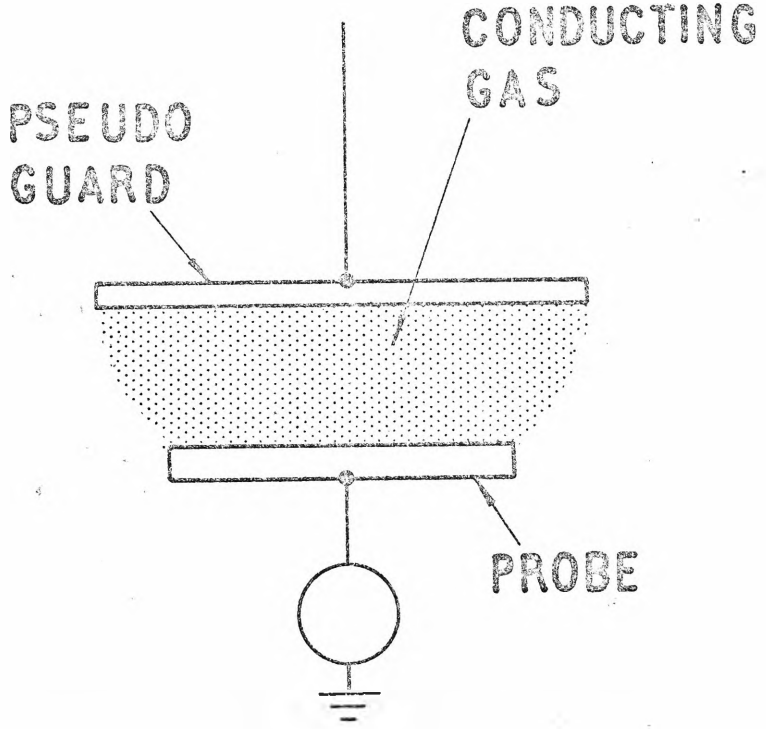

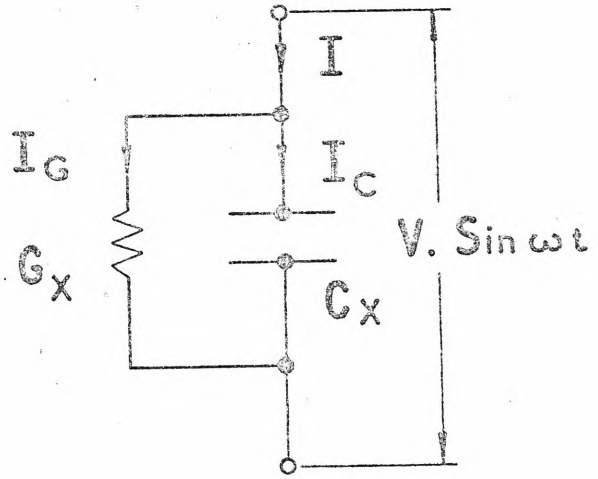

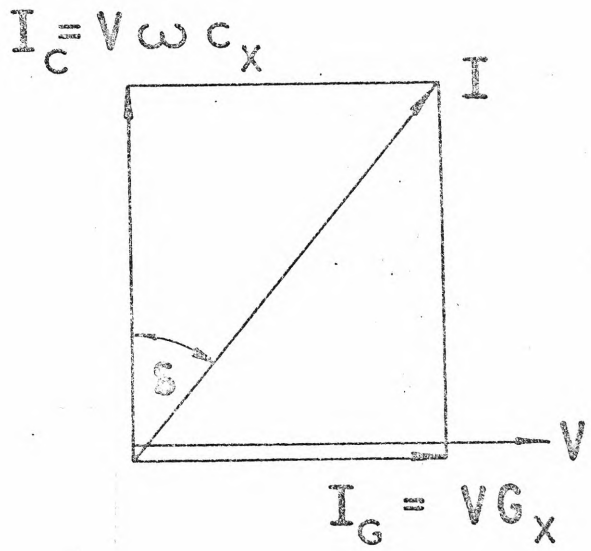

FIG. 5.1 EQUIVALENT CIRCUIT OF ACTIVE PROBE SURFACE

When surrounded by ions, the probe active surfaces become equivalent to a lossy capacitor with C_x and G_x in parallel. With sinusoidal excitation V sin ωt applied, the phasor diagram is as indicated with loss angle δ.

5.1.4 Elimination of Unwanted Displacement Currents - two terminal equivalent

If an alternating potential is applied to the electrode system of Fig.4.1, gross capacitance effects dominate, and the currents of interest cannot be distinguished from such large displacement currents. The difficulty may be resolved when it is observed that the probe and its surroundings may be treated exactly as a leaky condenser. Referring then to the system of Fig.4.1, the equivalent circuit of the probe becomes that of Fig.5.1. One may then obviously apply bridges of the transformer ratio or schering type to determine both the in-phase and quadrature components. Note that C_x is not the capacitance of the active faces alone, but because of the construction depicted in Fig.4.1 contains leads and other unwanted capacitances in parallel.

5.2 The Guarded Probe with a.c. Excitation

The use of a guarded probe, so creating a three terminal device, has a number of advantages foreshadowed in para.4.7.2. Such a probe is depicted in Fig.5.2(a). The probe and screen are at virtual earth, while the convenient pseudo guard is at an active alternating potential of from 1 to 40 volt rms. The voltage appearing between the pseudo guard and the main earth plate causes no difficulty and does not enter into subsequent readings.

Direct leakage over the surface of the insulation separating the probe and main surrounding electrode is entirely eliminated by the shield. All stray capacitances between the probe and earth due to leads etc are similarly eliminated.[108,109,110,111]

The capacitor when 'transformed' as in Fig.5.2(b) takes on the more familiar three terminal configuration in which all fringing and edge effects are eliminated. The measuring system therefore 'sees' only the lossy capacitance appearing between its active face and the main electrode (pseudo guard).

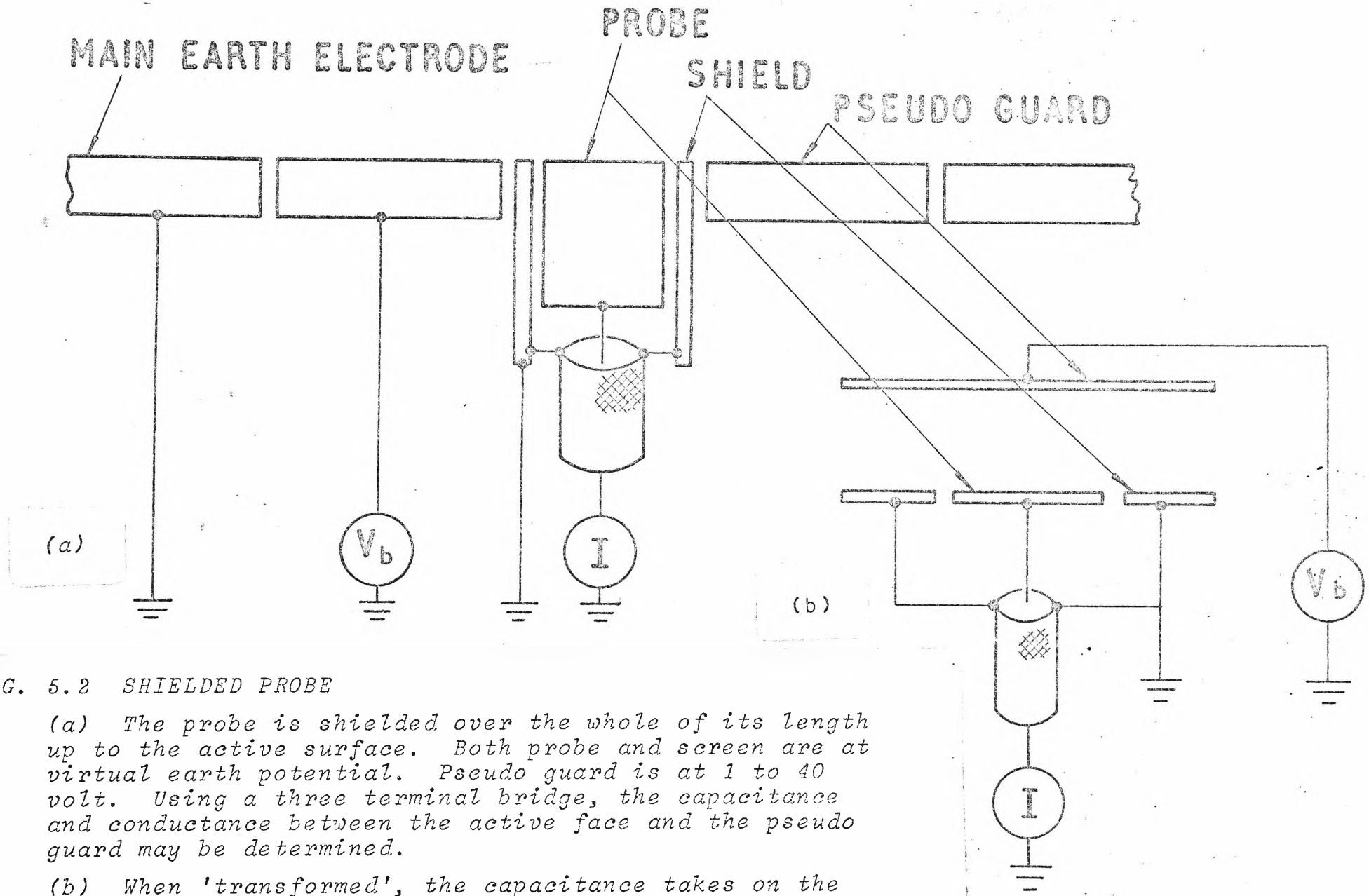

FIG. 5.2 SHIELDED PROBE

(a) The probe is shielded over the whole of its length up to the active surface. Both probe and screen are at virtual earth potential. Pseudo guard is at 1 to 40 volt. Using a three terminal bridge, the capacitance and conductance between the active face and the pseudo guard may be determined.

(b) When 'transformed', the capacitance takes on the more familiar three terminal configuration in which all edge and fringing effects are eliminated.

A more detailed consideration of the capacitance of the flat probe is given in appendix 5.1.

5.2.1 Diagnostic Signal and Relaxation Frequency of Ions

The ions in a gas at NTP under the influence of an alternating electric field of audio or radio frequencies, behave as in a d.c. field. That is, they show no frequency dependent properties. The relaxation frequency for ions or electrons in a gas at NTP is in the order of several hundred MHz . Any convenient diagnostic frequency below these values may be used, typically from 1 KHZ to 1 MHZ.

If the pressure of the gas is reduced and the frequency increased, then charge oscillations within a mean free path will follow and both the real and imaginary parts of the dielectric constant will be reduced. This effect is described in works on the physics of fully ionised gases and is not under discussion in the present paper.

5.2.2 Transformer-Ratio Bridge Measurement of Three Terminal Capacitance

The principles of measuring small three terminal capacitors such as those shown in Fig.5.2 by transformer ratio-arm bridge, have been documented in the references already cited. Since it is believed that the present probe is an important new application of the three terminal transformer ratio arm bridge, the essential concepts are briefly recapitulated.

A three terminal capacitor C_x with terminal H (high), L (low) and G (ground) is shown in Fig.5.3(a). One imagines a small capacitor in a solid earthed enclosure G, so that C_{HG} and C_{LG} are unwanted strays. The standard capacitance C_s with its two strays is similarly placed across the secondary winding of a transformer N_x. Since the transformer is wound on a high permeability core, the volts/turn induced in N_x and N_s is the same. At balance, indicated

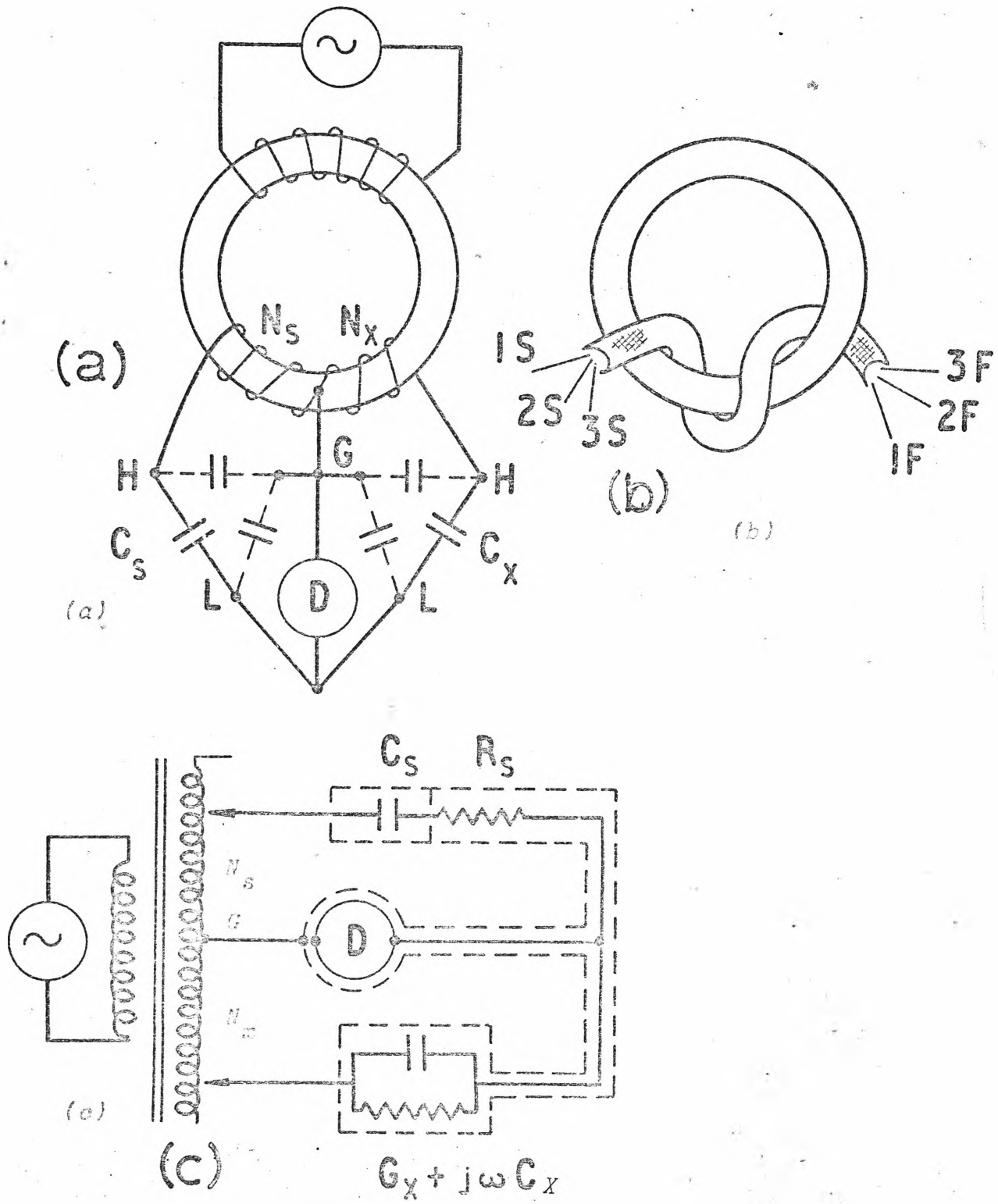

FIG. 5.3 BASIC PRINCIPLES OF TRANSFORMER RATIO ARM BRIDGE FOR DETERMINATION OF THREE TERMINAL CAPACITANCE

(a) Simple bridge with standard C_s and strays C_{SHG} and C_{SLG}; detector D; unknown C_x with strays C_{XLG} and C_{XHG}

(b) Screened multi-cored cable used for transformer winding

(c) Transformer bridge showing series standard, balancing out a shunt equivalent unknown. At balance $N_x z_s = N_s z_x$

by a null in D, the two strays C_{GL} being in parallel with the detector, carry no current. The two strays C_{GH} are both across the source windings and do not enter into bridge balance. Hence at balance:

$$N_s C_s = N_x C_x$$

and the strays are eliminated.

The success of this arrangement depends upon the meticulous care taken in shielding the various transformer windings and in reducing leakage inductance. One way of effecting this is by the arrangement shown in Fig.5.3(b) where a screened multicore cable is used for the transformer windings. A more conventional circuit diagram is illustrated in Fig.5.3(d) where an unknown lossy capacitor $G_x//C_x$ is balanced by an equivalent series standard capacitance. Both sides of the transformer winding are tapped, an arrangement providing for great range and versatility.

The three terminal transformer ratio arm technique has reached the peak of commercial development in the several Wayne Kerr instruments and in the General Radio 1620 instrument. The peak of laboratory development appears to have been reached in the Australian National Standards Laboratory under Thompson/Lampard and at the U.S.A. National Bureau of Standards.

5.2.3 Three terminal bridge Connection

A schematic diagram of the manner of using a three terminal bridge with the probe is shown in Fig.5.4. Positive corona is set up in the cylindrical electrode system, at a point on whose outer boundary it is desired to measure J, E and $\bar{\sigma}$. The direct currents associated with the corona cannot be suppressed and must be arranged to flow through the bridge. Terminal L, connected to the active centre of the probe carries the d.c. quiescent current I_o; while terminal G connected to the guard carries I_1. The pseudo-guard joins the bridge terminal H via a

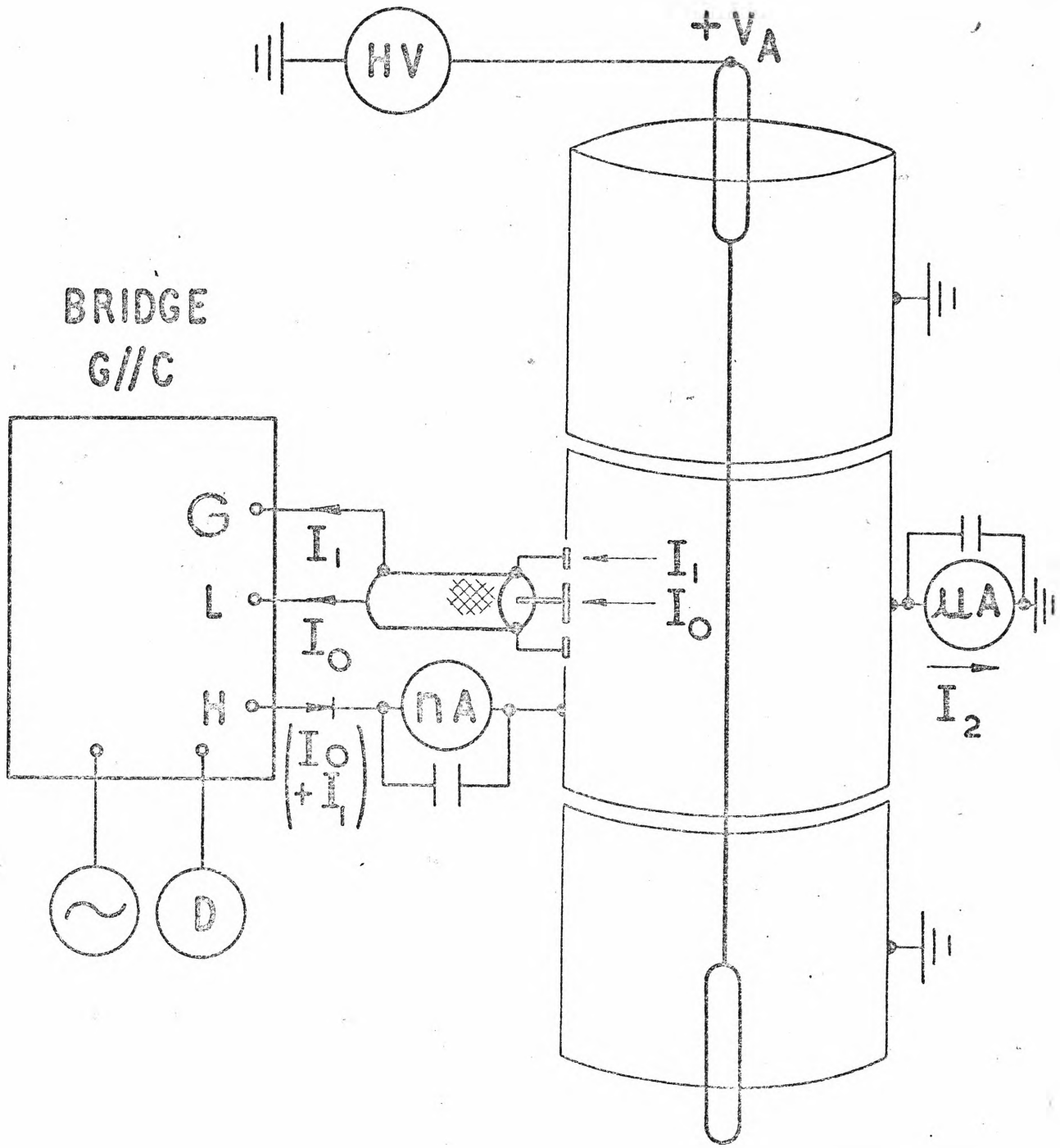

FIG. 5.4 SCHEMATIC DIAGRAM OF THREE TERMINAL BRIDGE MEASUREMENT OF POSITIVE CORONA

The bridge (floating) is connected to the probe, shield and pseudo guard. The system measures $\bar{\sigma}$; J and E on the boundary of the coaxial corona electrodes, which are energised by the positive H.T. d.c. supply. Superimposed a.c. and d.c. are measured separately.

floating d.c. nano-ammeter with by-pass capacitor. It may be useful to measure the total quiescent d.c. I_2 carried by the pseudo-guard. In this configuration, the bridge, the oscillator output, and detector are floating a few mV d.c. around earth.

It must be emphasised that the two d.c. meters operate independently of the bridge and the alternating currents it produces. Likewise the bridge, detector and oscillator operate independently of the direct currents. In this respect, the technique resembles that used to test a capacitor on a.c. but with d.c. polarisation.

Several other configurations are possible to suit a particular bridge. In all cases, careful consideration of the earths and position of the d.c. meters is mandatory.

5.3 Calibration of the Probe in a Corona System

Vindication of the three terminal probe with bridge sensor was carried out in the cylindrical corona system illustrated in Fig.5.4. Since dry air was used, with positive corona, the situation was the same as that depicted in Fig.4.8. Measurements were carried out on the central guarded electrode whose curved surface area was 200 cm^2, and upon which was mounted two screened probes, of capacitance .0162 pf and .049 pf respectively. The Wayne-Ker Bridge type B221 was used at a frequency of $\omega = 10,000$.

5.3.1 Typical Results

Typical results of these calibration tests are shown in Table 5.1, where initially, with the ionising voltage V_a set at zero, the bridge disclosed a loss-free capacitance.

Table 5.1

Calibration of the Probe with Positive Corona

Cylindrical Corona System of Figs. 4.8 & 5.4

Guarded Cylinder				Probe A						Probe B		
V_a kV	I_2 μA	J $\mu A cm^{-2}$	$\sqrt{I_2/L}$	I_o+I_1 nA	J $\mu A cm^{-2}$	C pf	G nmho	$\bar{\rho}$ ohm cm	E kV/cm	C pf	G nmho	$\bar{\rho}$ ohm cm
0	0	0	0	0	0	.0490	0	∞	0	.0162	0	∞
9.5	10	.05	10.66	2.98	.0523	.0490	0.022	2.51×10^{10}	1.26	.0162	0.008	2.29×10^{10}
10.6	20	.10	15.1	5.6	.099	.0490	0.031	1.78×10^{10}	1.78	.0162	0.011	1.67×10^{10}
13.5	50	.25	23.8	14.8	.26	.0490	0.052	1.06×10^{10}	2.65	.0162	0.0185	0.99×10^{10}
16.5	100	.50	33.8	28.5	.50	.0490	0.077	0.72×10^{10}	3.60	.0163	0.0255	0.72×10^{10}
21	200	1.00	47.7	59.6	1.05	.0490	0.112	0.494×10^{10}	4.94	.0162	0.039	0.47×10^{10}

On raising the potential of the stainless steel discharge electrode above corona inception, corona current I_2 flows in the guarded cylinder. (I_o+I_1) flows in the three terminal probe, the larger of the two only being monitored in this way. Both capacitances have now become lossy as indicated by the appropriate value of G. In the Table 5.1, V_a, I_2, (I_o+I_1), C and G are measured quantities, while J, $\bar{\rho}$ and E are calculated.

Typical calculations are illustrated for the case where V_a = 13.5 kV, as follows.

From eq.5.6, and utilising data from the probe A, the resistivity of the gas on the boundary is:

$$\bar{\rho} = \frac{C_o}{G\,\epsilon_o} = \frac{.049 \times 10^{-12} \times 10^{+2}}{.052 \times 10^{-9} \times 8.854 \times 10^{-12}}$$

$$= 1.063 \times 10^{+10} \text{ ohm}^{-1}\text{ cm}^{-1}$$

The current density J on the inside of the guarded cylinder is:

$$J_o = \frac{50}{200} \qquad .25 \ \mu A/cm^2$$

which is to be compared with the value determined from probe A as:

$$J_o = \frac{(I_o+I_1)}{A_{o1}} = \frac{14.8 \times 10^{-9}}{5.7 \times 10^{-2}} = 0.26 \ \mu A/cm^2$$

This is quite good agreement considering that measurement of the area A_{01} of the probe, being on the inside of a cylinder, presented quite a problem in metrology.

Using the better value for the current density, the electric field on the boundary is:

$$E_o = \bar{\rho} J_o = 1.06 \times 10^{10} \times .25 \times 10^{-6} \times 10^{-3}$$

$$= 2.65 \text{ kv/cm}$$

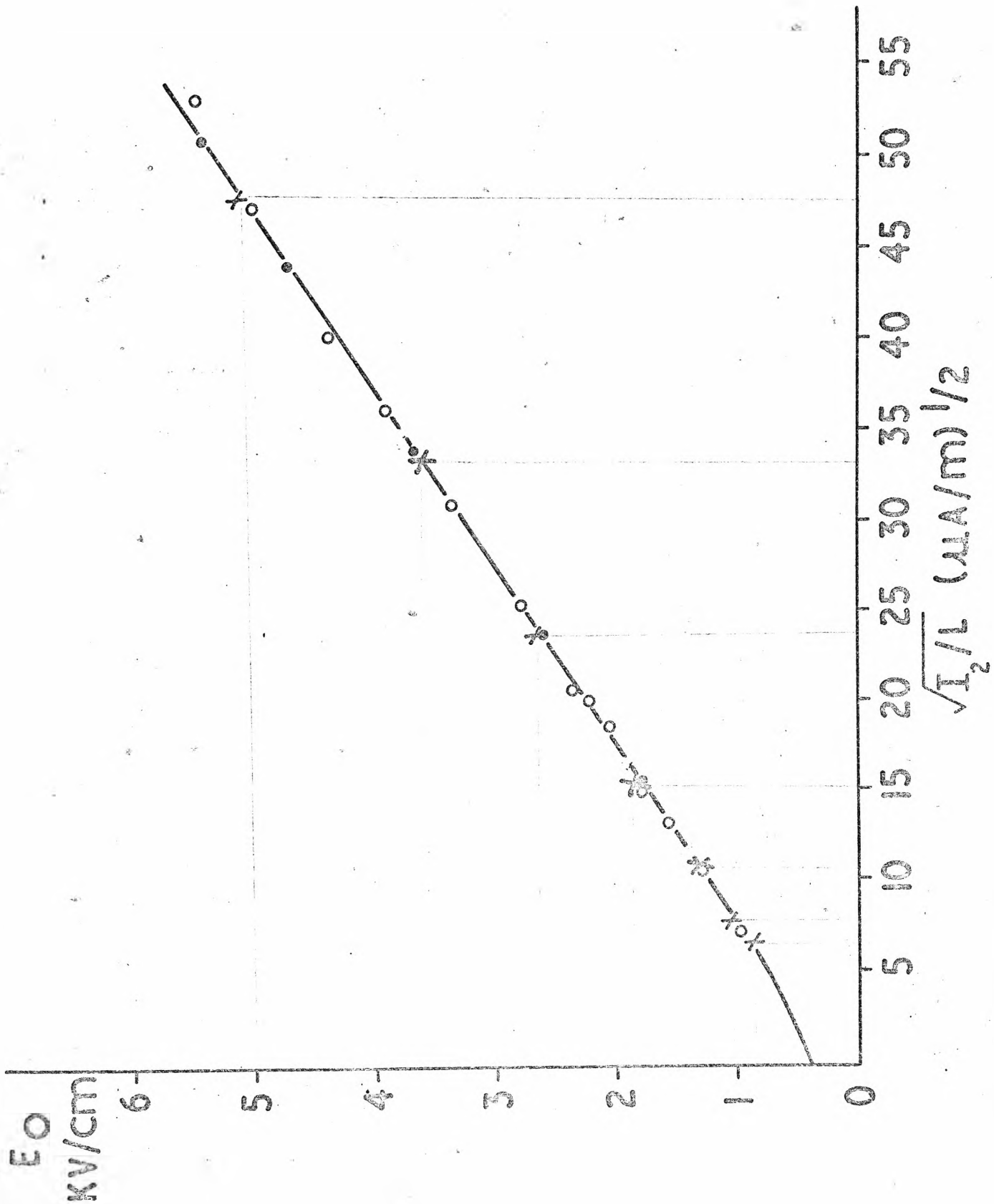

FIG. 5.5 VERIFICATION OF THE A.C. PROBE WITH POSITIVE CORONA

Using the circuit of Fig. 5.4, electric field E_o is measured on the boundary by a.c. probe. Comparison with two other independent methods

X *a.c. measurement*

. *d.c. perturbation*

O *calculations using $K^+ = 1.6$ (air at NTP)*

This value of field strength, indicated by X on Fig.5.5, is there compared with the value of E_o obtained by two other methods viz:

- • d.c. perturbation (vide para.4.5.1)
- o calculations using $K^+ = 1.6$ for air at NTP (vide para.4.5)

As the graph shows, at high values of corona current, the electric field strength becomes proportional to $\sqrt{I_2/L}$, while at zero corona current, E_o tends to the usual electrostatic case for cylindrical electrodes. These and other points were amply demonstrated in appendix 1.1 and used already in Fig.4.10.

Interest now centres on the field strength E_o as determined by the a.c. perturbation method. It is seen from Fig.5.5 that the correlation between the three sets of results is remarkably* close. It may be taken that the a.c. perturbation approach has been thoroughly vindicated for the probe used.

5.3.2 Comparison of Probes

One therefore enquires as to whether such excellent results would have been obtained with another probe. An inspection of Table 5.1 allows a comparison of the two probes within the limit of the sensor, used. The highly regarded Wayne Kerr Bridge, though having ample sensitivity and range for the capacitance measurement on the smaller Probe B, was inadequate for the G determination, particularly at low ionisation level. As the instrument was reading right at the limit of the conductance arm, values of G

---

* Even more remarkable considering that the experiments were performed a world away; the d.c. perturbation being carried out on good North Oxford air, while the a.c. results were with (even better) North Wollongong air!.

FIG. 5.6 ANALOGUE REPRESENTATION OF ELECTROSTATIC FIELD AROUND A BIASSED PROBE

Analogue plot on conducting paper in two dimensions, of a biassed probe.

$$(V_b/D_m)/E_o = 0.15$$

below .02 x 10^{-9}mho were rough. In spite of this, values for gas resistivity $\bar{\rho}$ determined from the two probes are fairly close, and converging rapidly with increased ionisation. Within the limits of the bridge therefore, measurements of E_o derived from the two probes agree.

The extremely promising performance of the technique and the fresh vistas which it opens up of new measurements on both partially and fully ionised gases, led the writer to search for a still more sensitive bridge. The General Radio Bridge Type 1620A provided the answer (though a much more expensive one!) Now properly a part of another continuing project, it will not be described in detail in this dissertation, except to say that this bridge with a vastly increased conductance range, has allowed the use of still smaller probes and has thoroughly vindicated the a.c. perturbation technique.

5.3.3 Constancy of the Real Part of the Capacitance

Though the bridge had ample capacitance sensitivity on both probes, it was very noticeable that there was no measurable shift whatsoever in the capacitance arm, from zero ionisation to the highest values used.

The charges in the ionised gas being swept to and fro in the electric field, do not therefore affect the capacitance, but only the effective shunt conductance.

5.3.4 Dissipation Factor

Since the three terminal probe behaves in all respects as a lossy capacitor, it is instructive to calculate the dissipation factor. Based upon the usual definition and the phasor diagram of Fig.5.1, there is, using the data cited in Table 5.1 at I_2 = 50μA;

$$D = \tan \delta = \frac{G}{\omega C_o} = \frac{.052 \times 10^{-9}}{10^4 \times .049 \times 10^{-12}} = .106$$

Thus for the bridge operated at an angular frequency of 10^4 rad/sec, the capacitance is comparatively 'lossy' for this intensity of corona.

5.4 Complex Permittivity of an Ionised Gas

It is observed that in a more general sense, what has in reality been contrived, is a determination of the complex permittivity of an ionised gas at a point on its boundary.

Viewed in this way, and using the common definition for complex permittivity,

$$\varepsilon = \varepsilon' - j\varepsilon''$$

$$= \varepsilon' - j \frac{\overline{\sigma}}{\omega \varepsilon_o}$$

For an ionised gas at NTP and up to low radio frequencies, the real part remains constant at 1, while the imaginary part is proportional to the conductivity for the reasons pointed out in para 5.1.2 and 5.2.1.

Using the present technique, but at high radio frequencies, the probe might prove useful for examining sheath effects in low pressure plasma, since different species respond more readily to particular excitation frequencies.

5.5 Thermal EMF in relation to d.c. Quiescent Currents

Normally, in an audio or radio frequency bridge, thermal emfs are of little consequence. However, in the present situation, thermal emfs must be of a very low order, since the bridge carries probe direct currents of from 10×10^{-12} to 10×10^{-9}A, which must be metered accurately.

The best qualities of a.c. bridges and of d.c. potentiometers are therefore needed in the present

exercise.*

5.6 Uses of the a.c. boundary probe

In the next chapter, C6, extensive uses of the a.c. boundary probe are discussed in the evaluation of positive and negative corona from various electrode systems.

5.7 Conclusion

The complex permittivity, conductivity, current density and electric field strength on the boundary electrode of an ionised gas may be measured with considerable precision by means of a flat probe and an a.c. bridge as sensor.

Probes as small as 1 mm dia. have already been constructed. As the electric perturbation extends no more than about a probe diameter, a volume of gas no more than a few mm^3 may be interrogated.

The small size of the probe will enable it to document interesting fine structure in negative corona in which discontinuities an mm or two in extent may be present.

The small size of the probe may enable it to be used in the study of sheath phenomena at the boundaries of plasmas and arcs. Over a range of frequencies, the complex permittivity may disclose the behaviour of free electrons and ion species.

The conductivity of an ionised gas at a point on the

---

* ...as the writer found to his cost. A spurious d.c. thermo current of many nanoamp appeared in the a.c. bridge circuitry. After a frustrating search of every junction, the trouble was traced to a temperature gradient of a couple of degrees across an epoxy insulator, which then became slightly active. When this was remedied, residual thermal currents of up to a hundred picoamp remained. This was finally traced to a silver/silver H.F. plug, the friction in which on removal, was sufficient to generate troublesome thermal currents for twenty minutes. The writer's log discloses two weeks of time spent in tracing and remedying such faults.

receiving electrode is a most valuable parameter in the evaluation of electrical adhesive forces between a dispersoid and the substrate as demonstrated in para 2.1.1. In another context not considered in this dissertation the gas conductivity is most useful in evaluating the onset of back-corona. It is when the resistivity of a substrate rises above the level of gas conductivity that back corona becomes likely.

The probe and sensor are now condidered to be a completely engineered system, adequately described, and ready to be exploited in many fields.

6. ELECTRODE CONFIGURATIONS, CORONA PROFILES AND DISCONTINUITIES

Uses to which the Micro Area Boundary Electrode as developed in C4 and C5 may be put, have already been foreshadowed in several places in our discussion so far. MABEL has considerable uses in the examination of some fundamental processes in positive and negative coronas. For an evaluation of various commercial electrode configurations, the device is invaluable. The original purpose of the instrument, it will be recalled, was to examine possible anode current discontinuities and for this it is ideal.

In this chapter a small selection only of the information which the writer has obtained will be presented. A selection of corona characteristics for point to plane, double point to plane, plate emitter, parallel wire in duct, barbed wire in duct will be described. Anode discontinuities in negative corona will be documented and an explanation advanced.

Implications of some of the E and J profiles in electrostatic precipitation of dusts will be considered.

6.1 Long Hemispherically Capped Cylinder to Plane[103]

This oft quoted geometry seemed a good starting point from which to test Mabel. Using a 1 mm dia. stainless steel rod with a hemispherical cap at a height above the plane of 4 cm, the L/r = 80 which is a common ratio. At an applied voltage of -15 kV, the current density profile is shown in Fig.6.1. Since the apparatus has ± 0.1 mm positional accuracy and current sensitivity to ± 2 pA, fine structure may be easily examined.

At the periphery of the discharge, the current does not fall gradually to zero as one would imagine. A sharp cut-off at R_o = 11½ cm is shown in the X10 magnified curve.

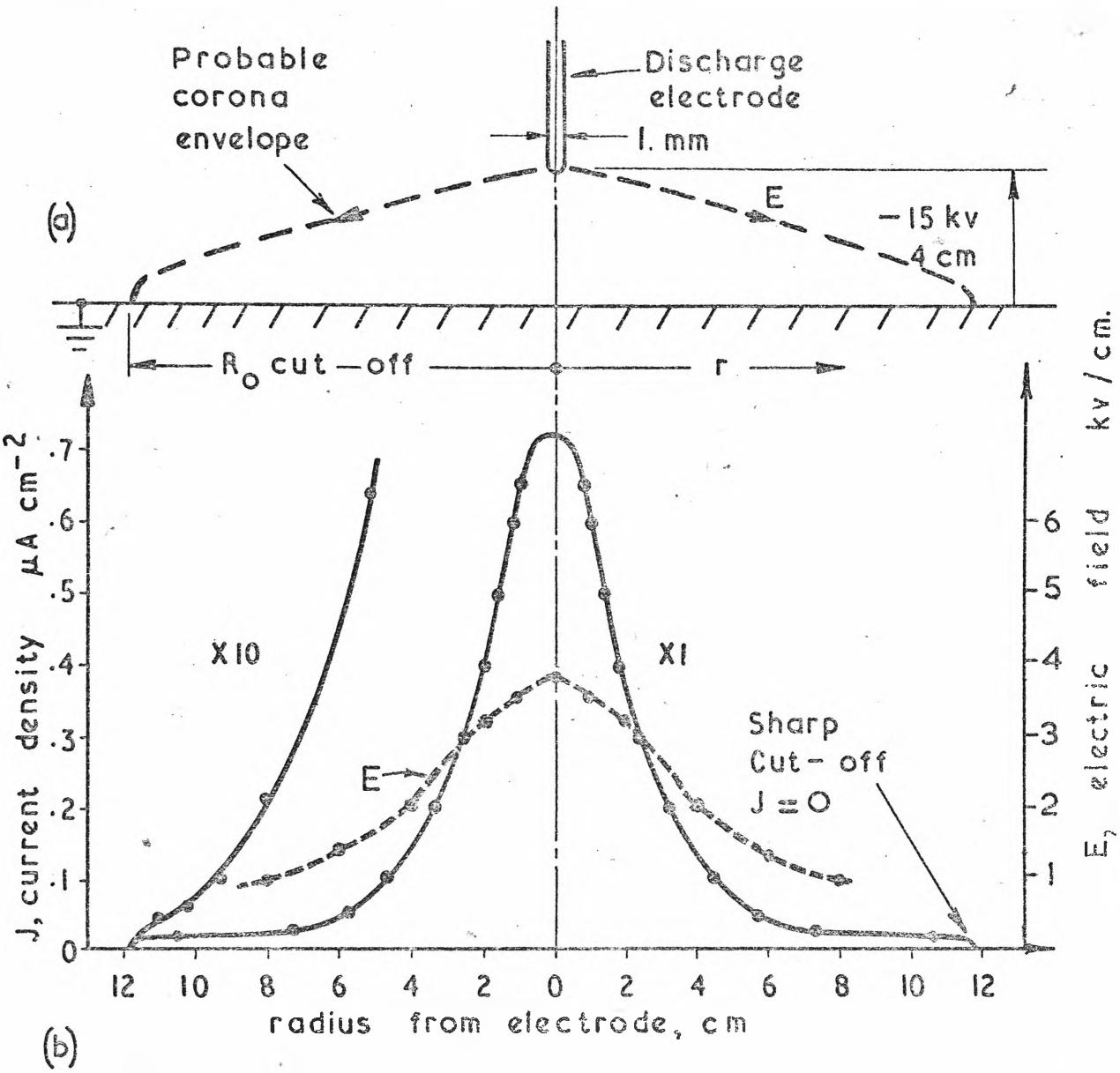

FIG. 6.1 CORONA CURRENT DISTRIBUTION ALONG THE ANODE

Negative corona from a himispherically-capped stainless-steel discharge electrode to plane

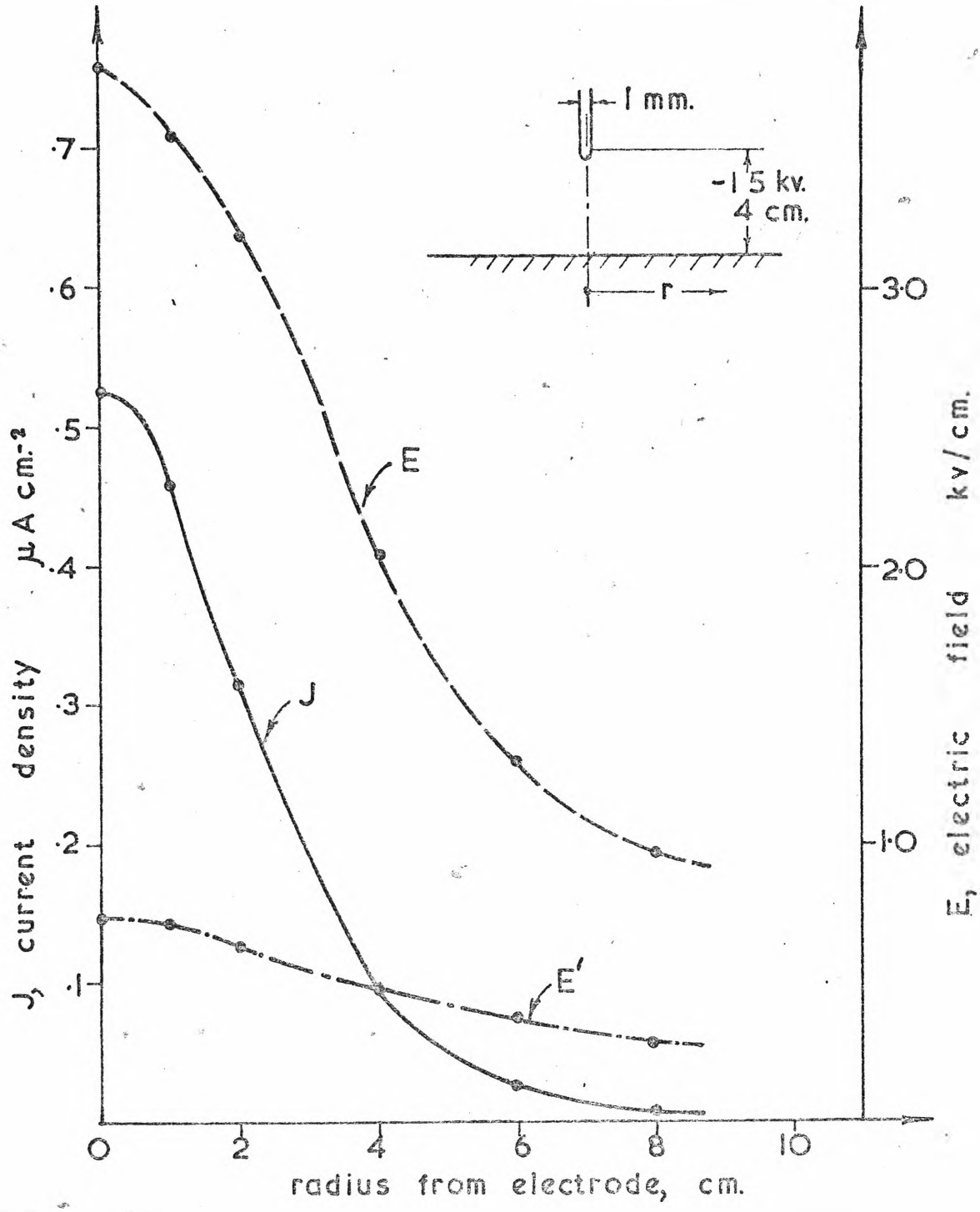

FIG. 6.2 ELECTRIC FIELD AND CURRENT DENSITY DISTRIBUTION ALONG THE ANODE

Same case as in Fig.6.1. Shows primarily the variation of: electric field strength E' in absence of discharge, E in presence of discharge J.

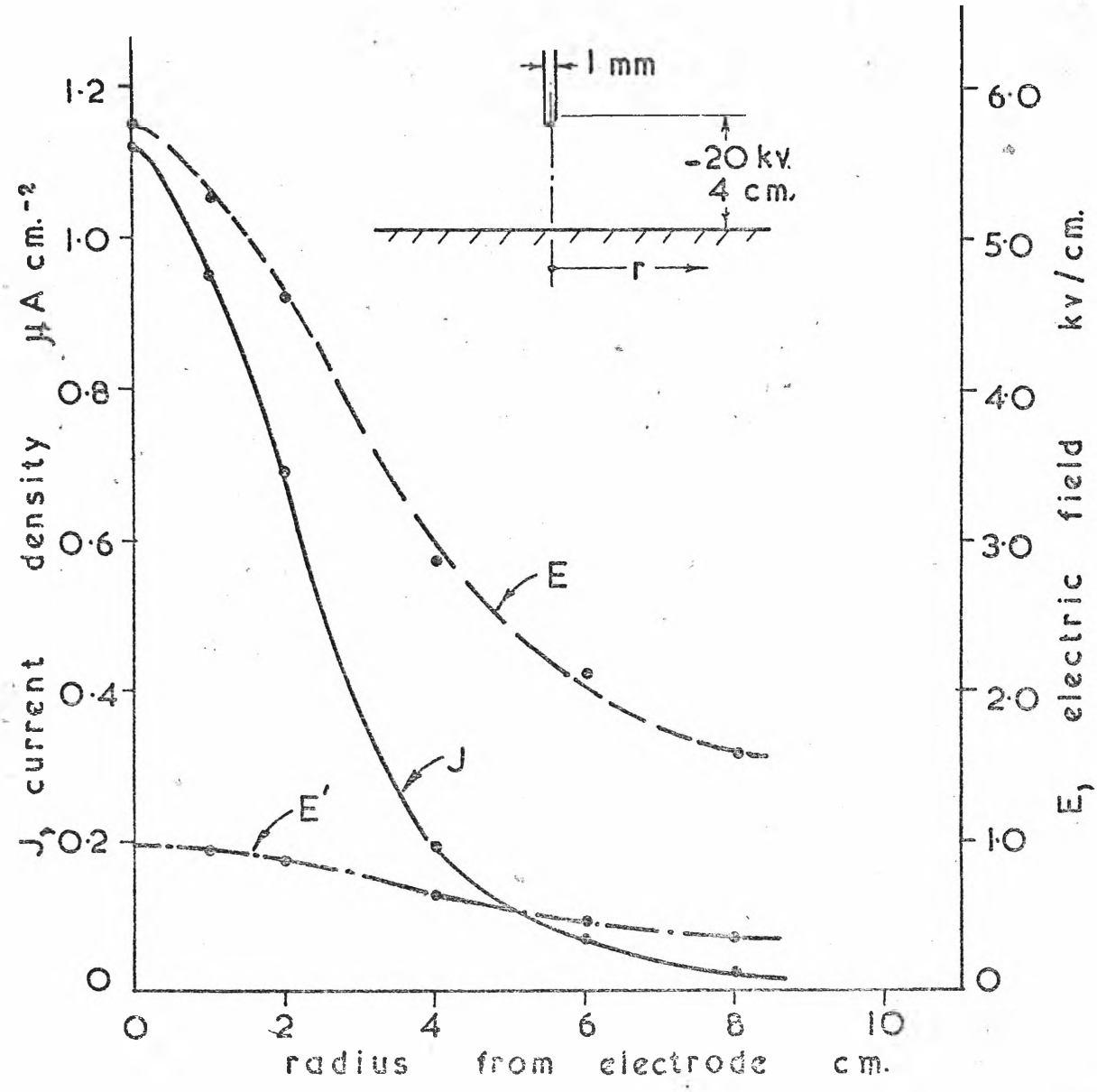

FIG. 6.3 ELECTRIC FIELD AND CURRENT DENSITY DISTRIBUTION ALONG THE ANODE

Same case as in Fig.6.2 but with a higher applied voltage.

TRIM

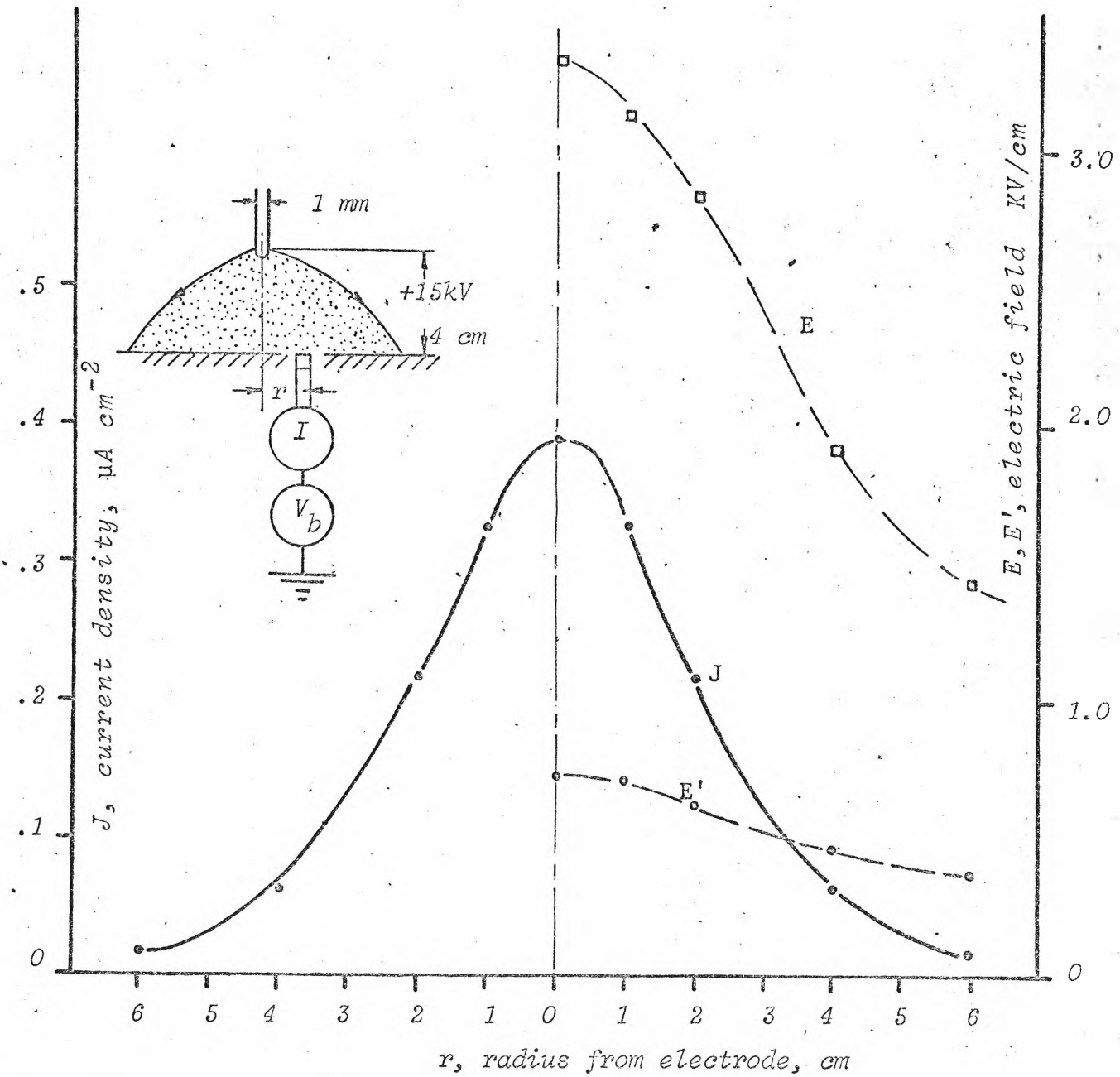

FIG.6.4 POSITIVE CORONA FROM HEMISPHERICALLY CAPPED STAINLESS STEEL DISCHARGE ELECTRODE TOPLANE.

The electric field and current density distribution along the cathode is shown. Total current 12.2 μA in air of N.T.P.

E = electric field with corona.
E'= electric field in absence of corona.

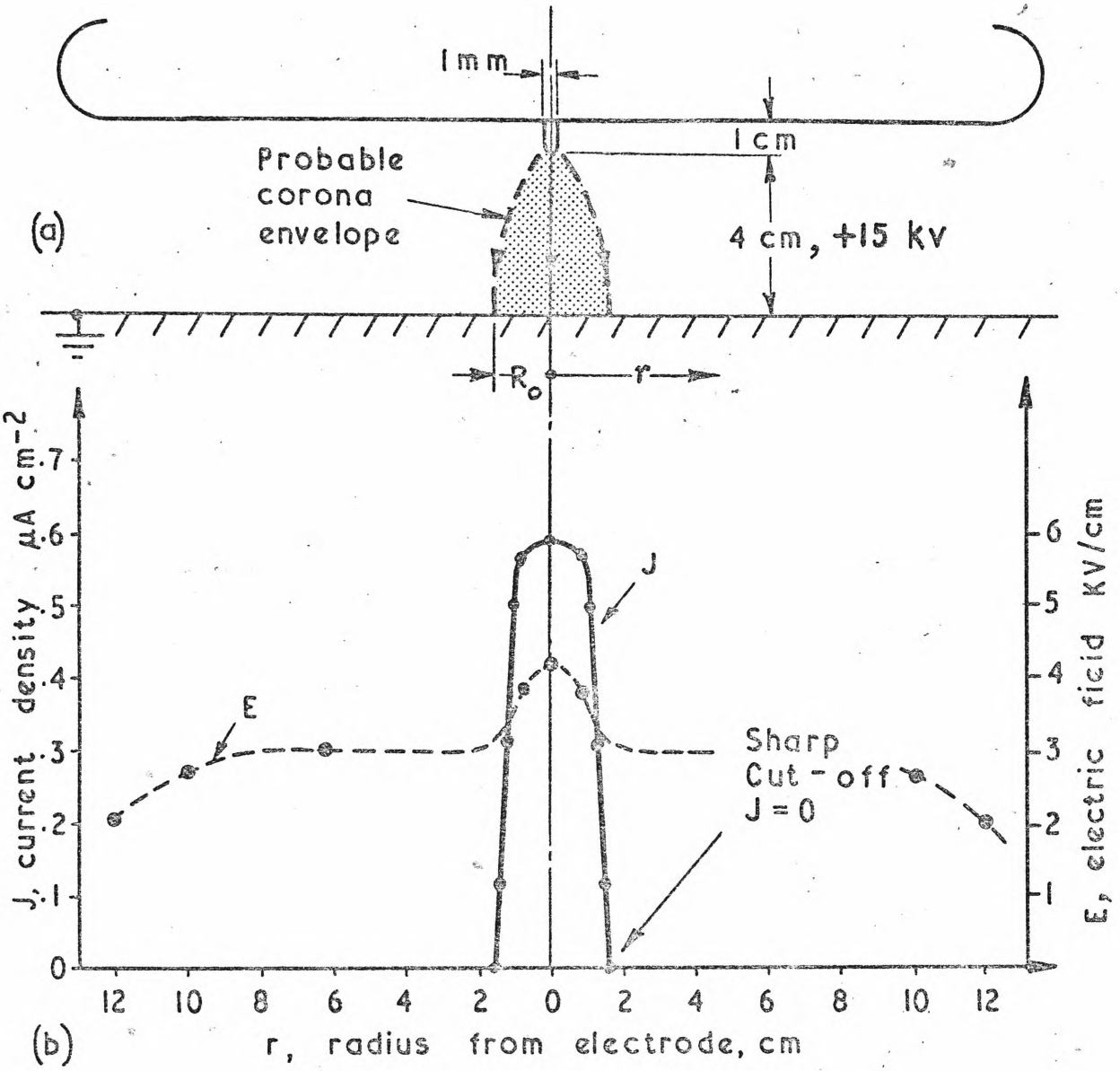

FIG. 6.5 POSITIVE CORONA FROM A PLATE EMITTER

Positive corona from a single point supported in a Rogowski Profile is concentrated into a narrow channel.

Every case examined showed this interesting discontinuity.

For the same geometry and voltage of -15 kV, the electric field levels are illustrated in Fig.6.2. Higher atmospheric humidity leads to lower mobility, lower total current and smaller J_{max}. The electric field E' in the absence of corona, but at the full applied potential shows a maximum value of 0.75 kV/cm. At a current density of 0.53 $\mu A/cm^2$, space charge effects have increased the electric field under the centre line of the probe to 3.75 kV/cm.

In Fig.6.3, with the applied voltage increased to -20 kV, the electric field under the probe has been increased from 1kV/cm to 5.7 kV/cm by space charge effects.

The E and J profiles for positive corona shown in Fig.6.4 are in all respects similar to those found for negative corona. Boundaries show the same sharp J cut-off. Actual values of J_{max} and E_{max} are a little lower than those shown in Fig.6.2 because of the more sluggish motion of the positive ions.

In all respects, the point-to-plane corona system is behaving in a predictable fashion. Electric field enhancement due to space charges is quite marked. The current channel shows well defined edges.

6.2 Point in Rogowski Profile to Plane

The so called "plate emitter", sometimes used in commercial precipitators, consists of a flat plate with spikes spaced at intervals. This rugged construction raps well, and never suffers from outages due to broken wire emitters. There have however been some spectacular failures of this geometry when used with New South Wales fly-ashes. The results depicted in Fig.6.5 help to explain some electrical disadvantages of this geometry.

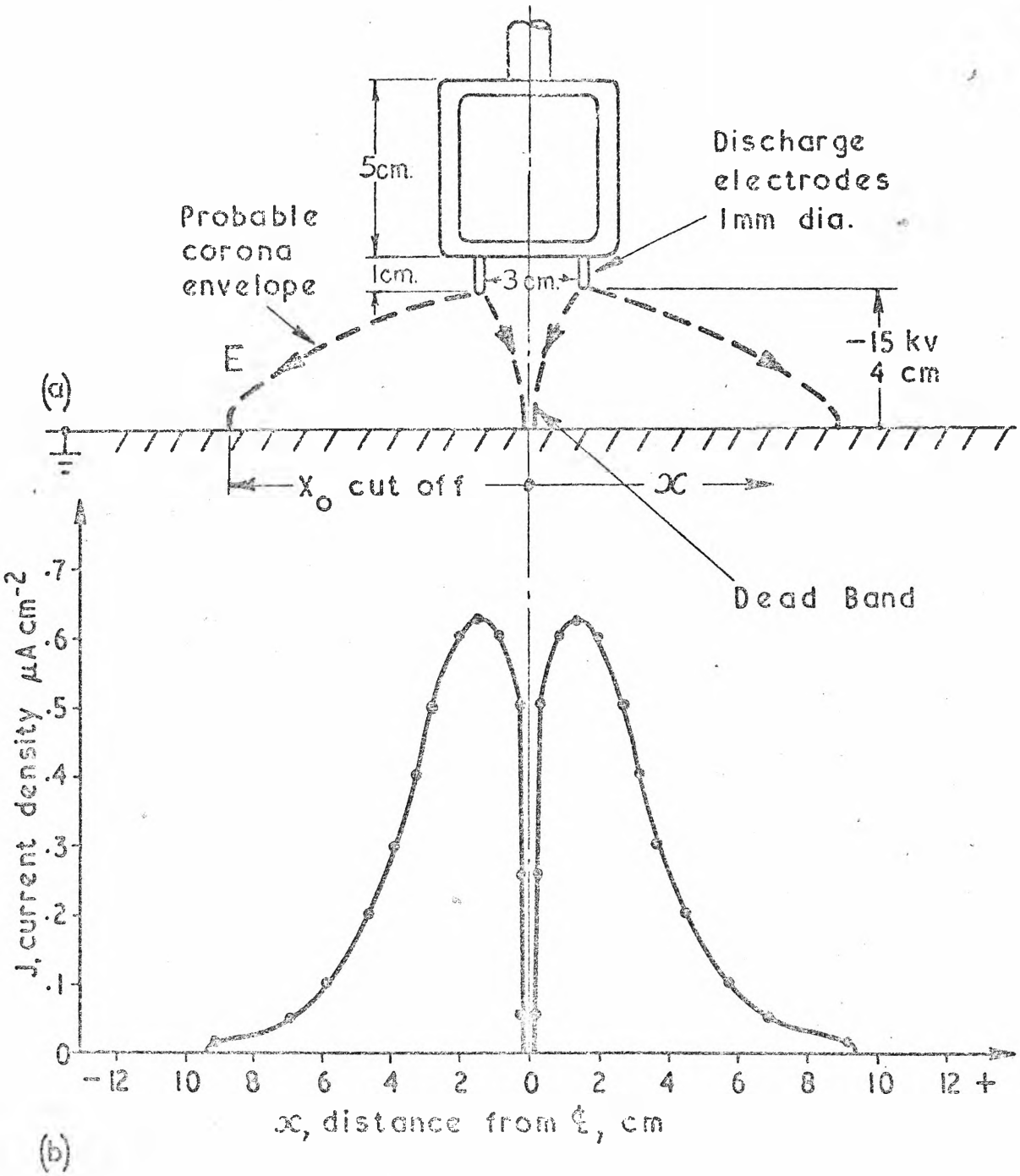

FIG. 6.6(a) NEGATIVE CORONA FROM TWIN POINTS

The two corona channels show discontinuities both in the centre and at the outside edges.

The corona is seen to be concentrated into an extremely narrow channel, no doubt a result of the high ambient electric field of 3 kV/cm. The cut-off radius at R_o = 1.8 cm is remarkably sharp, the current density changing by several orders of magnitude in the space of 1 mm. The electric field increased from 3 kV/cm without discharge to 4 kV/cm with discharge, a more modest increase than that observed in other cases.

If other spikes were placed at say 5 cm centres, the discharges would hardly interact so that the corona current would comprise a series of bars with poor charging characteristics. Current density on the collecting electrode would consist of a set of spots strongly conducive to the production of back ionisation.

6.3 Double Point to Plane

The two electrodes in Fig.6.6 were not supported by a plate but by a simple square grid. In the absence of a discharge, the electric field E' resembled that of Fig.6.2 rather than Fig.6.5.

Without the presence of a strong ambient electric field to concentrate the discharge, it spread out to a radius of R_o = 9.5 cm, at which point the current channel stopped abruptly as in all other cases.

A second remarkable discontinuity was readily measured centrally between the needles. There was complete dead band of a little more than 1 mm in extent, an interesting observation to be found only with the writer's smallest probe.

On another occasion (when the needles had not been inserted quite symmetrically), the more extensive data of Fig.6.6b was obtained. This shows a series of equal current density contours in the plane of the flat plate. The zero band in the centre is seen to be bounded by an almost vertical wall of current filament.

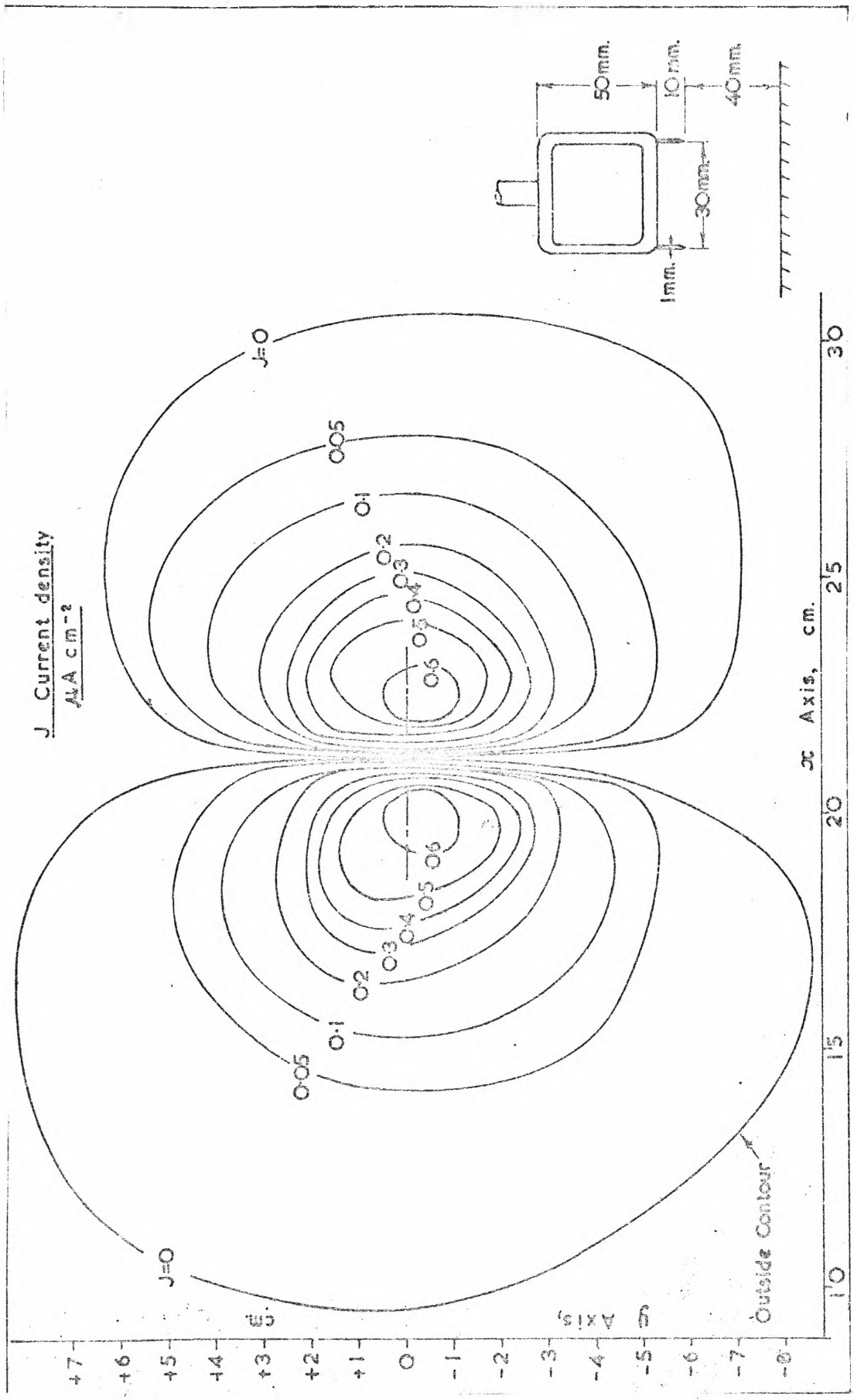

FIG.6.6(b) NEGATIVE CORONA FROM TWIN POINTS

For the case of Fig.6.6(a), current contours at constant J levels are shown. Strong space-cloud interaction is evident.

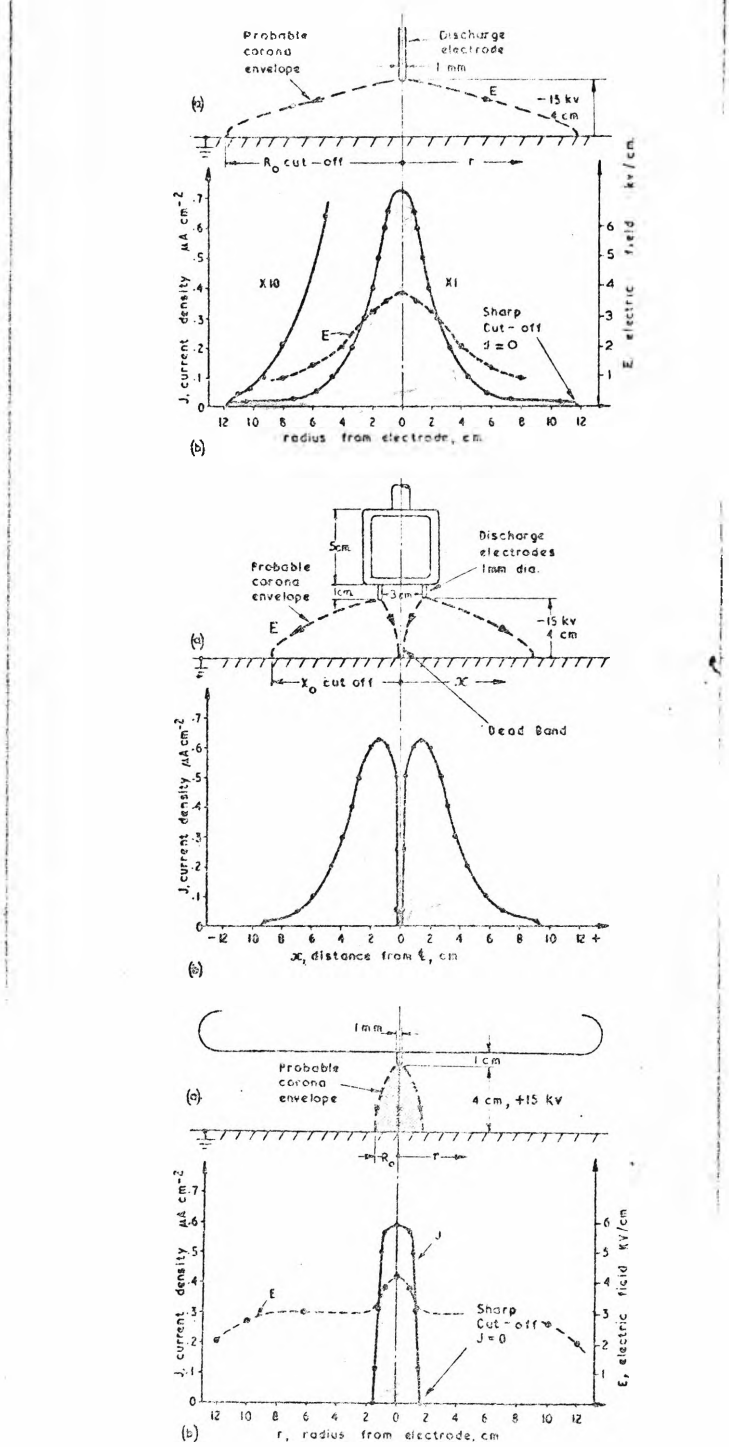

FIG. 6.7 INTERCOMPARISON OF THREE DISCHARGE GEOMETRIES

Three cases previously considered are here compared to the same scale on the same drawing.

The interaction between the two channels displayed in Fig.6.6b bears striking resemblence to the Lichtenburgh figures obtained from the klydonograph, a device used for determining the strength and duration of HV lightning impulses, e.g. Cobine.[112] In this instrument, photographic emulsion, placed on a flat earthed plate, is activated when needles above it are energised. This action, though at one time widely used, has not been adequately explained. If blackening of the emulsion is due to electrons emanating from an impulsive discharge at the needles, then the resultant patterns are likely to be similar to that of Fig.6.6b.

6.4 Comparison of Three Cases

An intercomparison of three cases considered so far, is displayed in Fig.6.7. Moving from L to R, the discharge becomes progressively more concentrated, which underlines the importance of the supporting discharge electrode structure.

6.5 Parallel Wire in Duct

Three parallel stainless steel wire discharge electrodes were placed centrally between parallel plates spaced 23 cm apart. The geometry was therefore closely comparable with that of Penney and Mattick[15] and Cooperman[16].

With the discharge electrodes at -26 kV (one of the two values used by Penney and Mattick), the interesting pattern of current density shown in Fig.6.8 a, b & c was found. Taking a traverse in the x direction at the centre of the Y axis, irregular current density was found. A large dead band between interacting current channels is clearly visible in 6.8a. Such irregularities were found at every Y section. The truly remarkable measurements of Fig.6.8b were taken along the axis of a discharge wire and directly underneath it. Repeated dead bands and a large

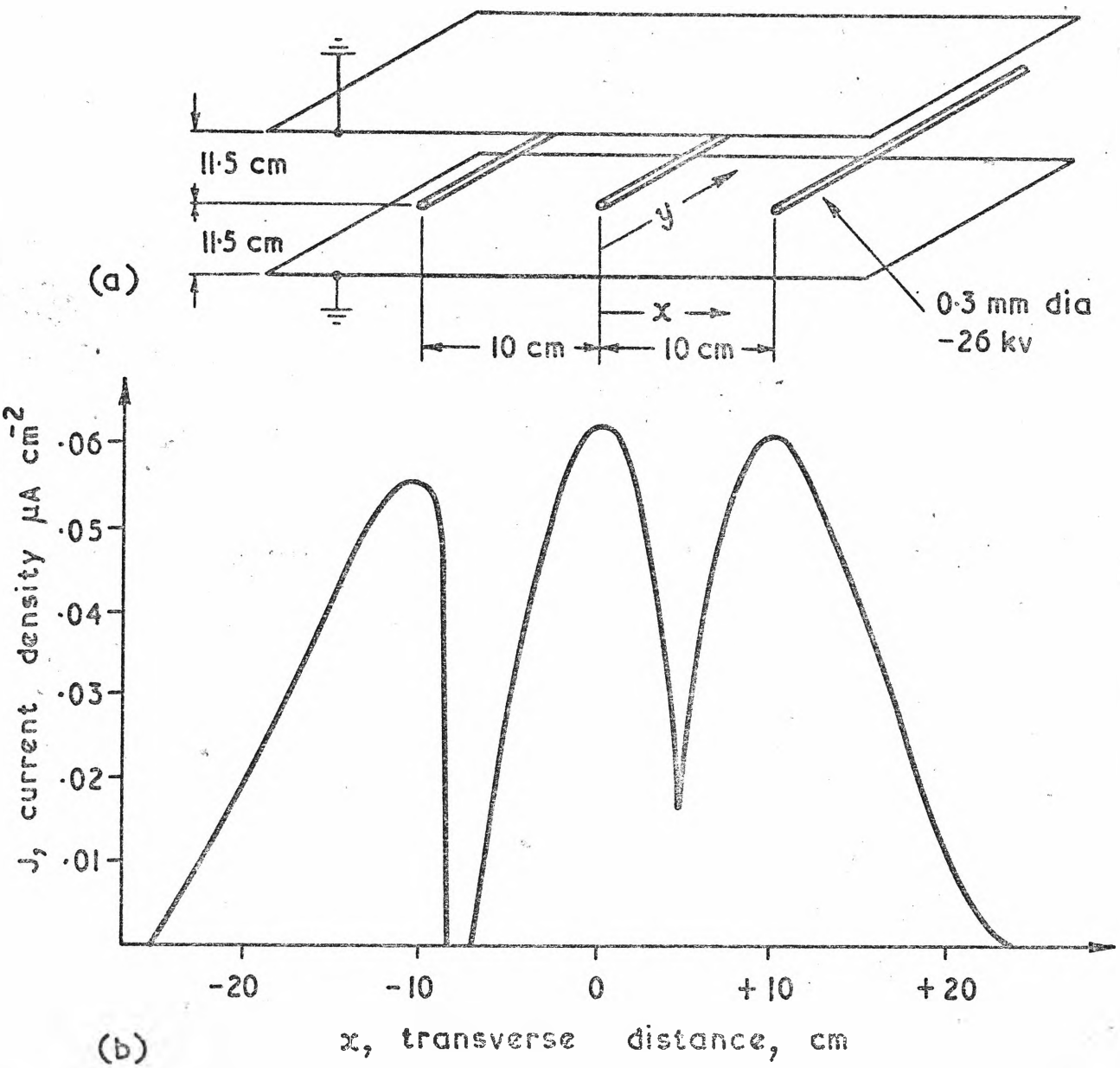

FIG. 6.3(a) NEGATIVE CORONA-PARALLEL WIRE IN DUCT ELECTRODES

Traverse in the x direction discloses substantial irregularities in current density.

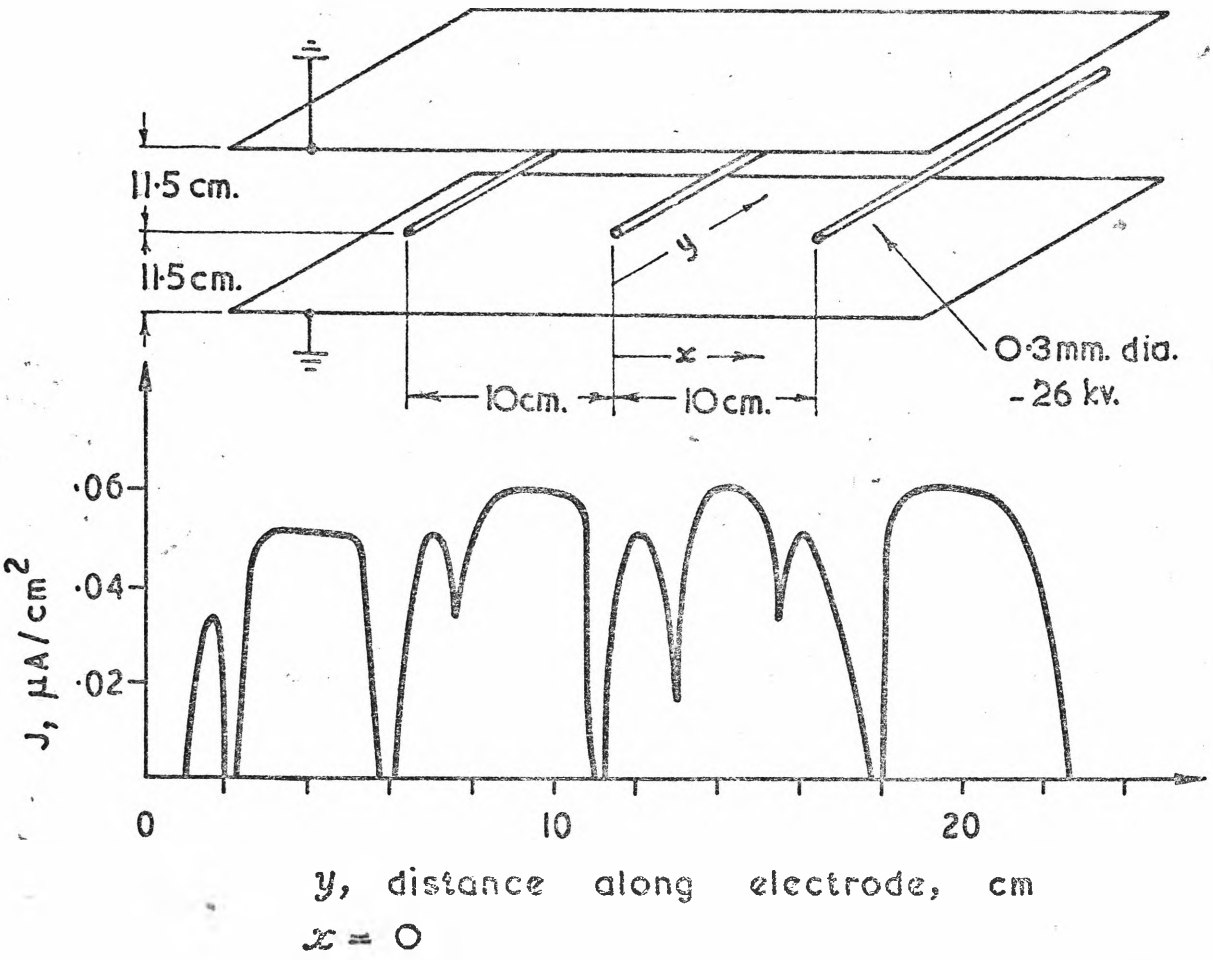

FIG. 6.8(b) NEGATIVE CORONA-PARALLEL WIRE IN DUCT ELECTRODES

Traverse in the longitudinal direction directly underneath a discharge electrode discloses irregularities in J along the whole length of the discharge electrode

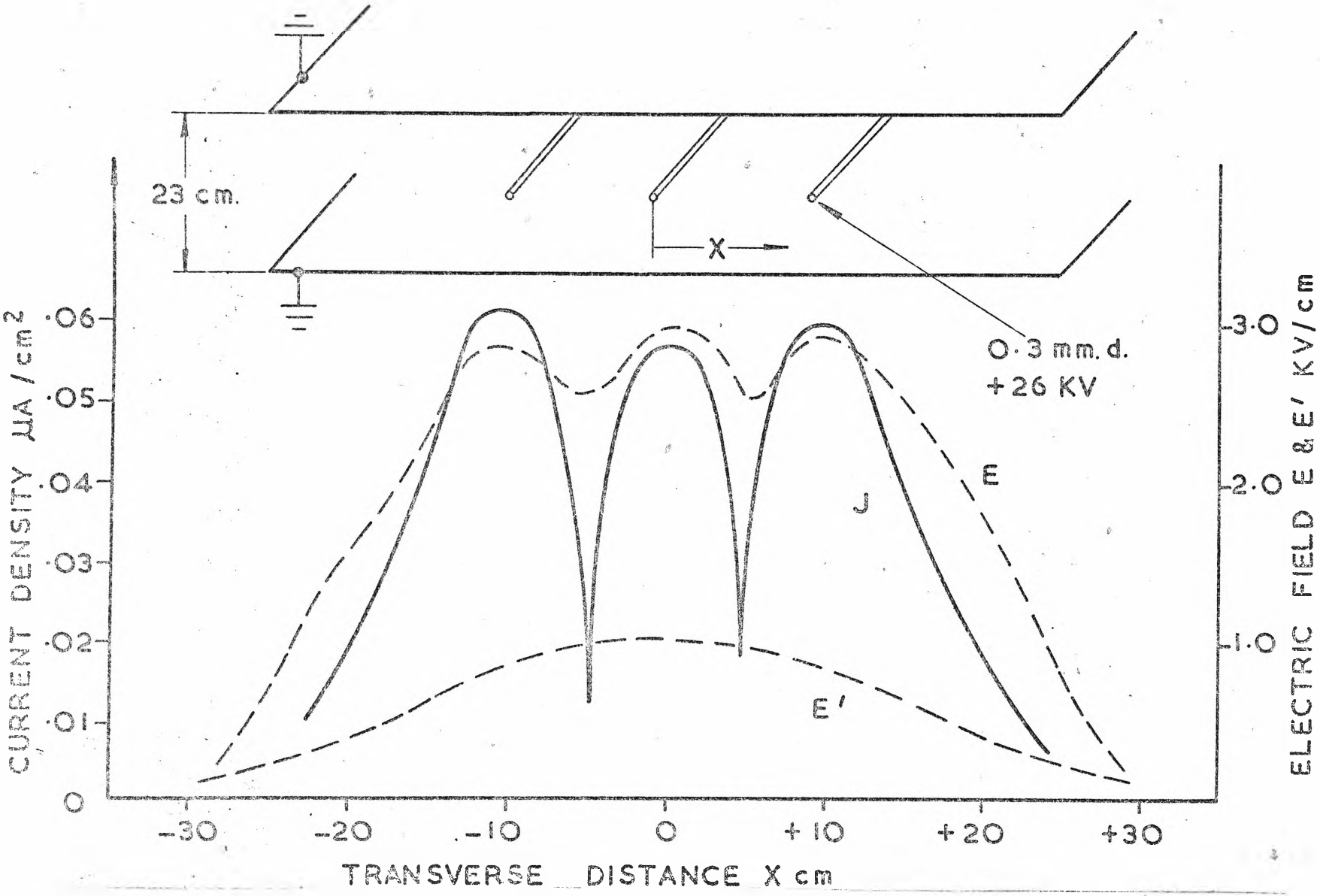

FIG. 6.8(c) POSITIVE CORONA-PARALLEL WIRE IN DUCT ELECTRODES

Illustrating J, E' (in the absence of discharge) and E (with discharge) for positive corona. No singularities in the longitudinal direction.

number of irregularities were measured. It is a sobering reflection that such discontinuities could emanate from a perfectly smooth stainless steel wire, polished and cleaned with carbon-tetra-chloride before each run. Each current increment appeared to emanate from a tuft[9] of light on the wire in accordance with the size of each. A still smaller boundary probe might actually have disclosed a zero band between every current tuft. Miller and Loeb extensively documented visual phenomena on the discharge wire, but did not, apparently, suspect that discontinuities would extend to the anode.

One now comes the full circle, refering back to the point much earlier in this dissertation where the whole question of irregular current densities began. In para. 3.7.1 during the development of the Precipifuge Corona Chamber; the anode pattern of Fig.3.6 was found. Each reduced segment corresponded to a stainless steel discharge electrode. There can no longer be the slightest doubt that Fig.3.6 does indeed represent a form of corona current pattern shown in greater detail in Fig.6.8a and b. Our earlier suspicions were justified and the considerable effort in developing MABEL, vindicated.

Tests made with positive corona and displayed in Fig.6.8c disclosed no irregularities whatsoever in a longitudinal direction under the wire. Perfectly uniform current density under the wire was invariably measured. Interaction in the x direction is seen to be regular.

Also shown in Fig.6.8c are the electric field strength profiles, E' without discharge, E with discharge. Space charge effects increase the electric field threefold, with dips midway between the electrodes, following the J pattern there.

A close scrutiny of the Penney and Mattick data contained in Fig.1.6 is revealing. Although theirs was

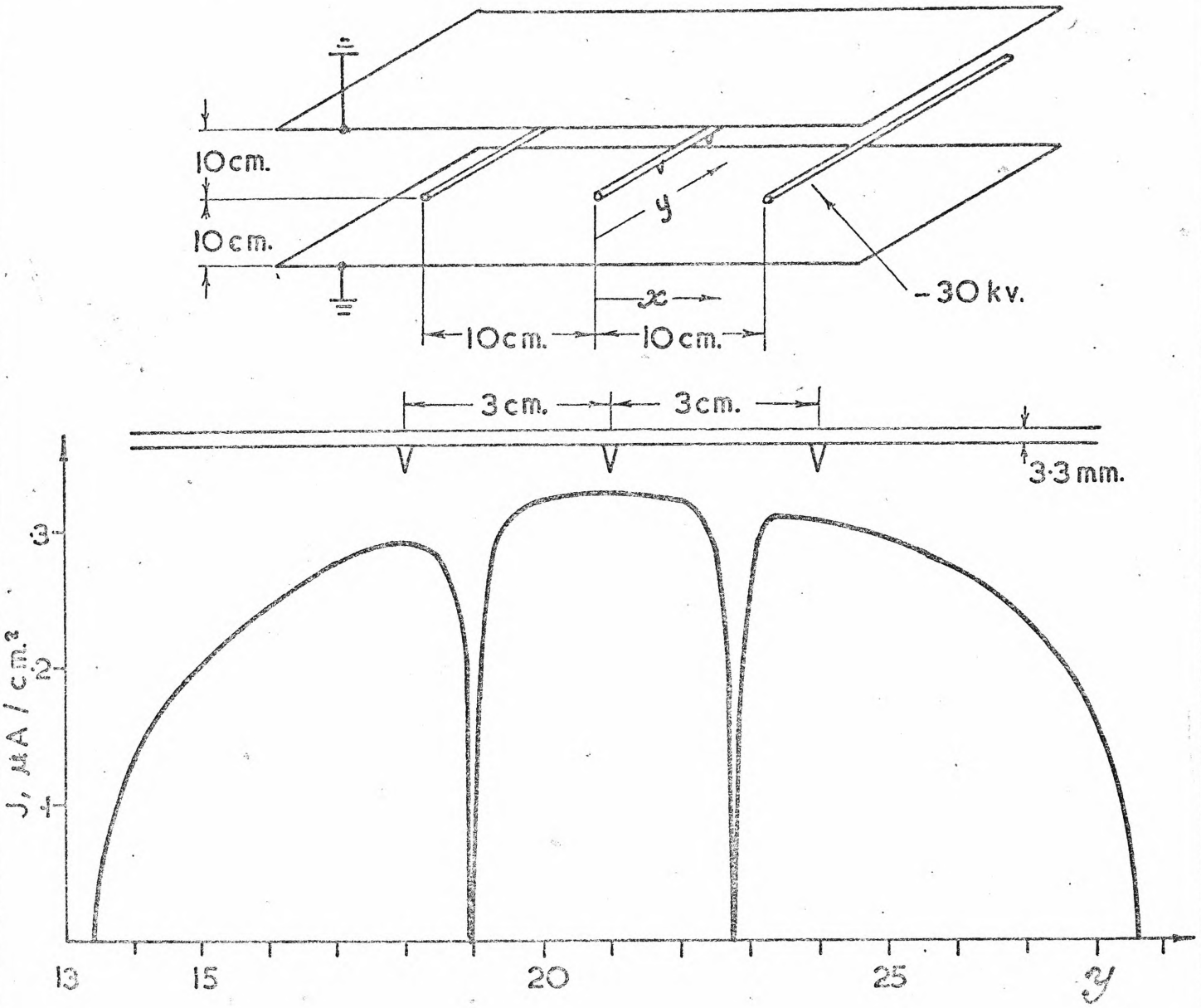

FIG. 6.9 BARBED WIRE IN PARALLEL DUCT

Positive corona from three points inserted in a non-discharging rod. Discharge pattern similar to that of Fig.6.8(b).

measured with negative corona and the writer's of Fig.6.8c determined for positive corona, some conclusions are possible. Elsewhere, as for example in the geometries of Fig.6.7, the writer found little difference in the behaviour of positive and negative corona. J and E patterns for positive and negative corona differed only to the extent expected from a 20 to 30% difference in mobility.

Penney and Mattick measured potentials, and converting the latter to gradients, one observes from 1.6c that underneath a wire, the gradient $\frac{\partial v}{\partial z}$ is nearly constant through 90% of the gas space. Midway between the wires, $\frac{\partial v}{\partial z}$ is roughly constant through half the gas space, falling to zero on the line joining the discharge wires* From Fig.1.6c, this boundary gradient $\frac{\partial v}{\partial z}$ varies from 2.5 kV/cm between the wires to 3 kV/cm opposite the wires.

From the writer's Fig.6.8c, $\frac{\partial v}{\partial z}$ varies from 2.6 kV/cm midway between the wires to 3 kV/cm opposite the wires.

The similarity between the writer's results and those of Penney and Mattick is astonishing. The writer's three curves for J, E and E' are all self-consistent and fully to be expected from his work on prior geometries. He therefore is bound to dispute Cooperman's[16] results which show higher field strengths between the wires than opposite them, and to take sides with Penney and Mattick and Lagarias.[17]

6.6 Barbed Points in Parallel Duct

Three barbed points with 3 cm centres were placed on a 3 mm rod (non discharging) between parallel planes. The resulting discharge with positive corona shown in Fig.6.9 was much the same when negative corona was used instead. The general appearance of the discharge is similar to that of Fig.6.8b. From this, one concludes that a series

---

* Field strengths in the gas space may thus be inferred from boundary measurements.

of barbs on a rod could closely simulate the tufted discharge from a smooth round wire.

6.7 Nature of the discontinuous negative discharge from a smooth wire

One seeks in this paragraph to advance an explanation for the anode current density discontinuities observed. Three types of discontinuity may be distinguished; the sharp cut-off at the edges of the J profile in the three cases of Fig.6.7; the zero band at the centre of 6.7b; and the irregularities of Fig.6.8b.

6.7.1 Effect of Diffusion[113]

The first question to be answered is the apparent absence of diffusion in blurring the edges of the corona channels in each of the three cases of Fig.6.7. On the surface it would appear that charge gradients in a radial direction at these discontinuities ought to be large.

At the edge of the channel of Fig.6.7c, one estimates the radial diffusion current to be:

$$J_r = D\frac{\partial(ne)}{\partial x} \simeq .04 \times (10^{-9} \text{ to } 10^{-10})$$

$$= 4 \times (10^{-11} \text{ to } 10^{-12}) \quad \text{amp/cm}^2$$

which is quite small. Further, (see appendix 4.2) the time of flight of an ion is:

$$T \simeq (0.5 \text{ to } 1) \text{ m sec},$$

hence the mean random walk of such an ion is:

$$\bar{r} = \sqrt{2\,D\,\tau} \not> .01 \text{ cm};$$

a distance which is entirely negligible; therefore diffusion can play no significant part in the movement of the ion cloud.

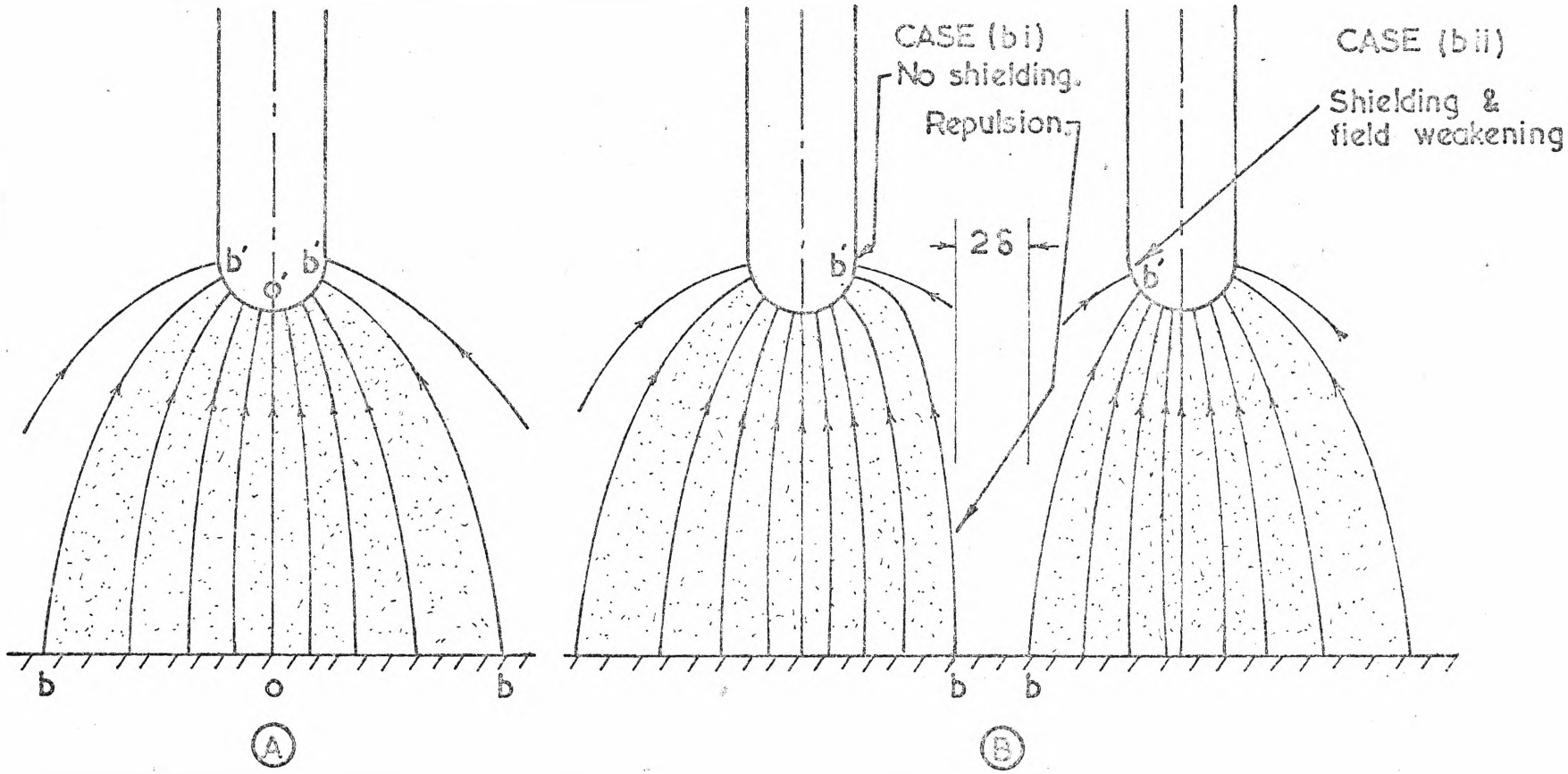

FIG. 6.10 ORIGIN OF DEAD BANDS BETWEEN CORONA CHANNELS

(a) A single discharging spike has a corona channel bounded by bb'.

(b) LHS:- A neighbouring discharge repels the original channel, moving it to a new b. RHS:- A neighbouring discharge causes shielding at the electrode surface, moving discharge boundary to b'.

6.7.2 Townsend Criteria

In the absence of diffusion, ions thus drift down lines of electric force.

Consider, for instance, the Fig.6.10a. Discharge will first begin along line OO' in accordance with Townsend's Integral:

$$\gamma\{\varepsilon^{\int_0^{O'} \alpha \, d\ell} - 1\} = 1$$

As the voltage V_a is raised, so the discharge will spread around the surface of the point until a line of force bb' becomes a boundary of the current channel. The Townsend Integral must always be satisfied along the current boundary.

6.7.3 Interaction of Two Discharges

If now a second discharge point is added a distance 2a from the first (b), we have repeatedly measured channel separation (2δ) at the anode. This means that the boundary points b have been shifted bodily towards the centre line of the respective spike. The two possible interpretations of this phenomena are illustrated in the two halves of Fig.6.10b.

In the RHS of (b) it has been assumed that the shielding effect of the nearby probe has so weakened the electric field on the surface of the spike, that the discharge boundary b' has been shifted (back towards its centre line) and with it, the other end of the flux tube b.

In the LHS of (b) shielding by the other spike has been taken to be negligible and the current boundary b' considered to be fixed. Space charge repulsion between the two channels has

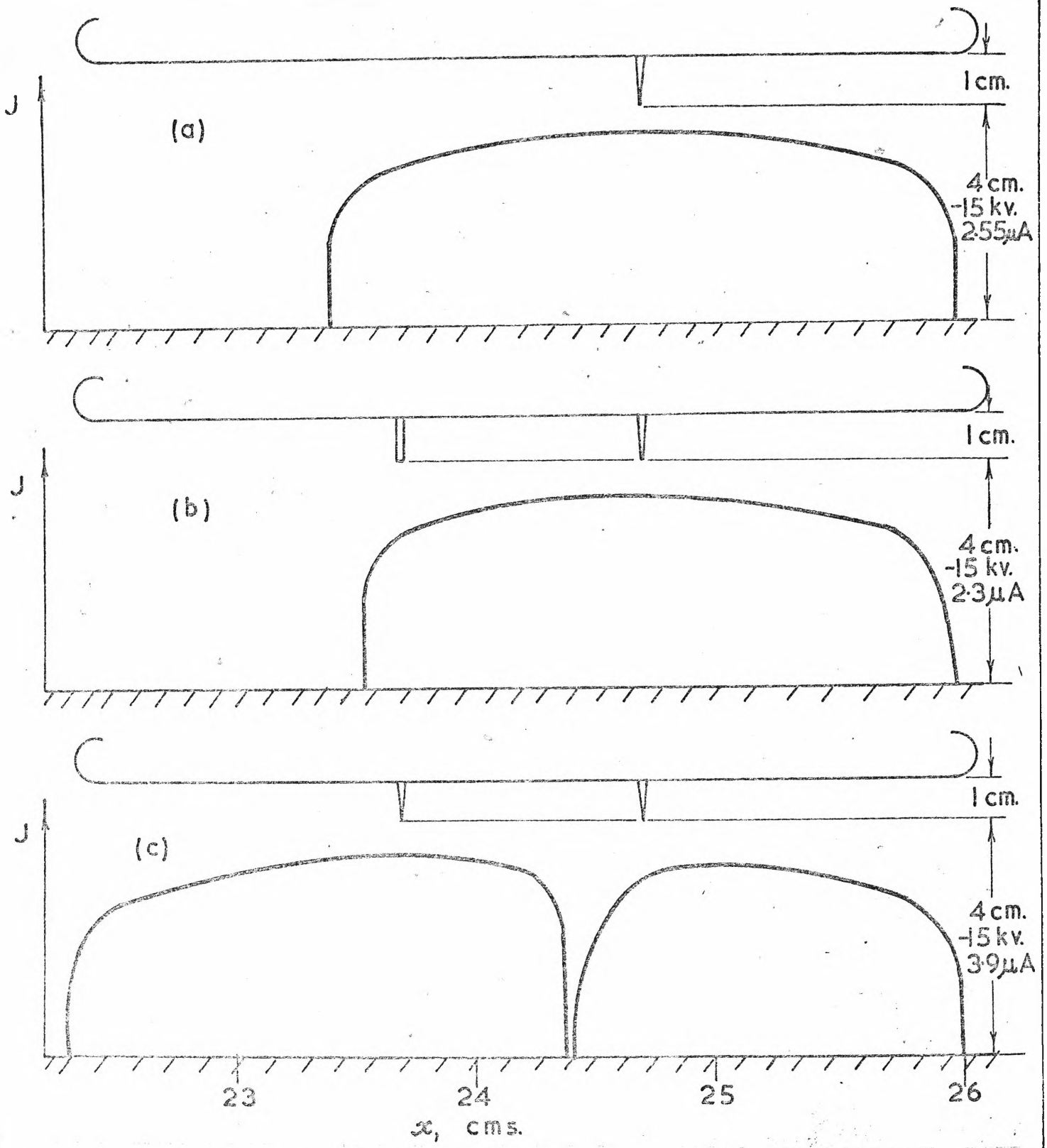

FIG. 6.11 NEGATIVE CORONA FROM POINTS IN A ROGOWSKI PROFILE

(a) One discharging point

(b) One discharging point, one blunt point

(c) Two discharging point.

distorted the field, bending b back towards the centre line of the spike.

It is now of interest to carry out experiments which will distinguish between two explanations advanced.

6.7.4 Distinguishing Space Charge Repulsion and Shielding

The experiment was conducted with two spikes separated by 1cm in a flat plate with Rogowski profile. With one spike only at -15 kV, the current channel on the anode is 2.6cm dia. as illustrated in Fig.6.11a.

One neighbouring spike, blunt and non-discharging, is seen in Fig.6.11b to exert a slight shielding effect on the original discharging spike. The discharge has been shifted .15cm and the total current reduced from 2.55 to 2.3μA.

When the sharp end of the second electrode was used instead, it discharged and obviously affected the first discharge, shifting it to the right a full 1.0cm as in Fig.6.11c.

With the experiment repeated with positive corona, as shown in Fig.6.12; a blunt neighbouring spike causes a slight shielding effect, while a second discharging spike causes a large shift.

Thus for both positive and negative corona, dead bands between current channels are certainly caused by space charge repulsion.

The writer considered that others[9] had adequately described why negative corona from a smooth wire should emanate from discrete points. He believes that his own contribution is in showing that, once tufts are established from any cause whatever, resultant current channel discontinuities will penetrate right to the plane receiving electrode.

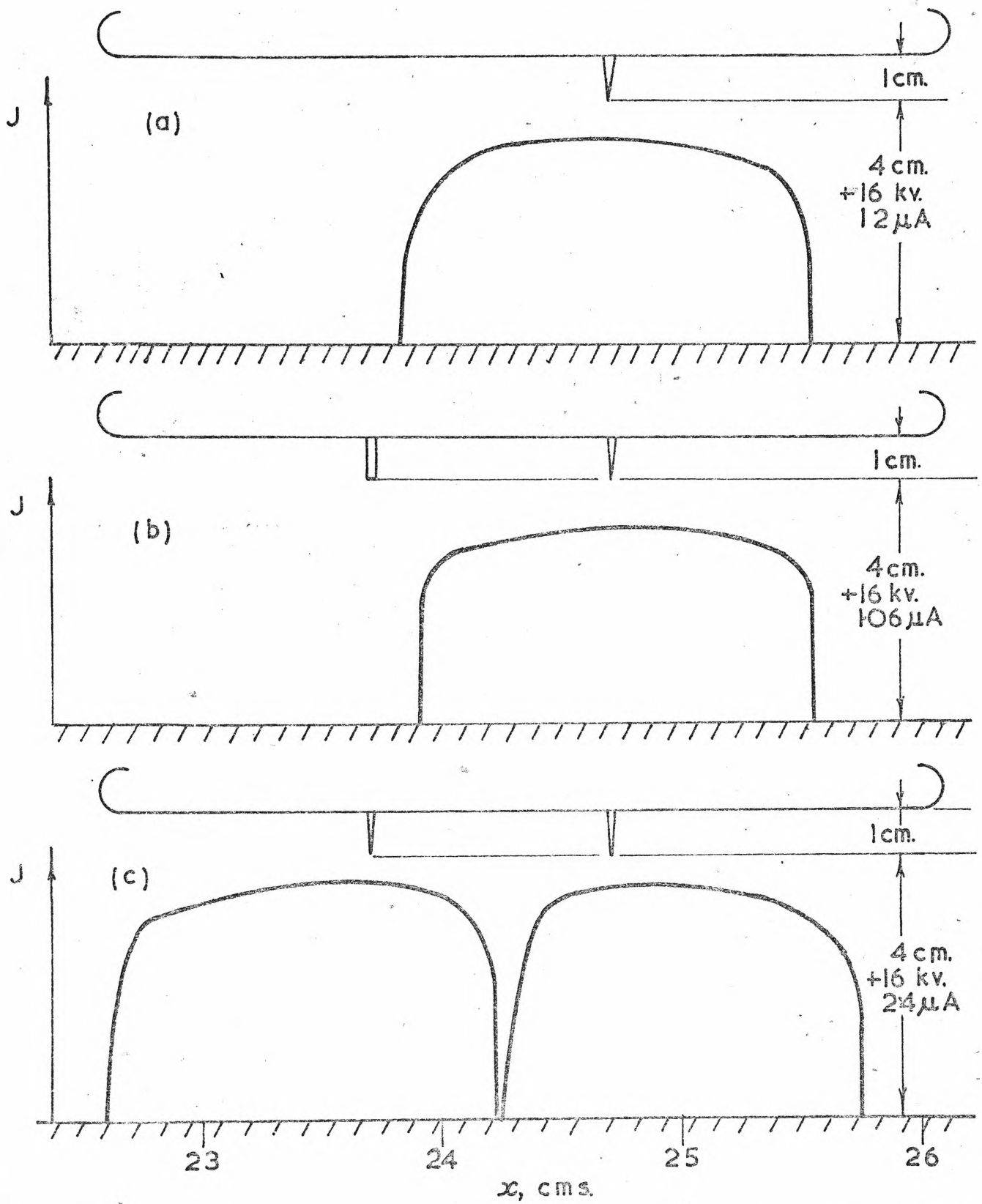

FIG. 6.12 POSITIVE CORONA FROM POINTS IN A ROGOWSKI PROFILE

(a) One discharging point

(b) One discharging point, one blunt point

(c) Two discharging points.

6.8 Further Studies with MABEL

Possibilities of further studies with MABEL immediately suggest themselves. A systematic search for most favourable electrodes for commercial precipitators might well be undertaken.

There is some evidence, from the data taken, that a relation between field strength and current density similar to eq. 1.6 for the coaxial geometry, may hold for all electrode geometries whatsoever. If so, this could prove to be a useful generalisation.

Such studies must now be undertaken outside this dissertation. Hopefully, the apparatus will be put to use by the writer's own postgraduate students.

6.9 Dust Deposition and Electrode Geometry

There seems to be widespread evidence that dust deposition on the receiving electrode is closely related to the shape of the HT electrode above it.

Rose and Wood[114] report that dust built up in ridges opposite the discharge electrodes in a parallel-wire-in-duct precipitator; due, they supposed, to the higher electric field there.

The writer observed interesting dust deposit in the corona chamber of the prototype Precipifuge of Fig.3.5c. With the inner copper receiving electrode fixed, and a uniformly dusty gas in the corona chamber, dust deposited in precisely the patterns shown in Fig.3.6. Down to the smallest detail, the dust lodged in accordance with the etched copper configuration. This provides more evidence that uneven current distribution leads to lack of uniformity in dust deposition.

Schiedel and Eishold[115] compared the deposition of dusts in a bench scale apparatus which had been equipped with smooth wires, barbed and double barbed discharge

electrodes respectively. With smooth wires, dust patches on the receiving electrode formed underneath tufts of discharge and moved about with a tuft as the latter shifted on a wire. With barbed discharge points, dust gathered in well defined round patches underneath them. Migration velocity and overall collection efficiency depended strongly not just on the electrical power input, but on the electrode geometry as well. For equal power inputs, collection efficiency thus depended markedly on the distribution of current density and electric field.

One could cite further cases which emphasise the importance on precipitation efficiency of the manner in which the corona power is distributed over the receiving electrode.

For an examination of such corona power distribution, the Micro Area Boundary Probe is a valuable aid.

CHAPTER 7

THE TEMPERATURE AND FREQUENCY DEPENDENCE OF THE DIELECTRIC CONSTANT OF POWER STATION FLY-ASH

7. THE TEMPERATURE AND FREQUENCY DEPENDENCE OF THE DIELECTRIC CONSTANT OF POWER STATION FLY-ASH.

In C2 dealing with forces of adhesion the writer made the point that there was a need for information on both components of the dielectric constant of industrial dispersoids. The real component was needed for the determination of the force component present when the HT supply was switched on. The imaginary part was needed for the determination of the Van der Waal forces by the London-Lifshitz criteria. The writer could find little, if any data on either component for industrial powders, in the literature.

The present investigation was begun very tentatively indeed. At the outset, the writer had no idea whether meaningful, repeatable measurements could be made on such a powder as say fly-ash. The investigation was begun in a low key; really in the first place to see if the writer's bridge methods were valid for a powder and if repeatable data could be found.

The results to follow were much more useful and encouraging than the writer could have hoped. It did transpire though, that his frequency range was not high enough to provide data on the imaginary constant which could be used for the Lifshitz-Landan calculation. It does appear that information on the imaginary constant is needed in the UHF - or indeed possibly as high as ultra-violet frequencies.

The way has nevertheless been opened up for much further work on industrial dispersoids.

The writer has nothing to add to his paper published[116] in Staub-Reinholt Luft, the English version being appended, except for the following note dealing with Debye Time Constants.

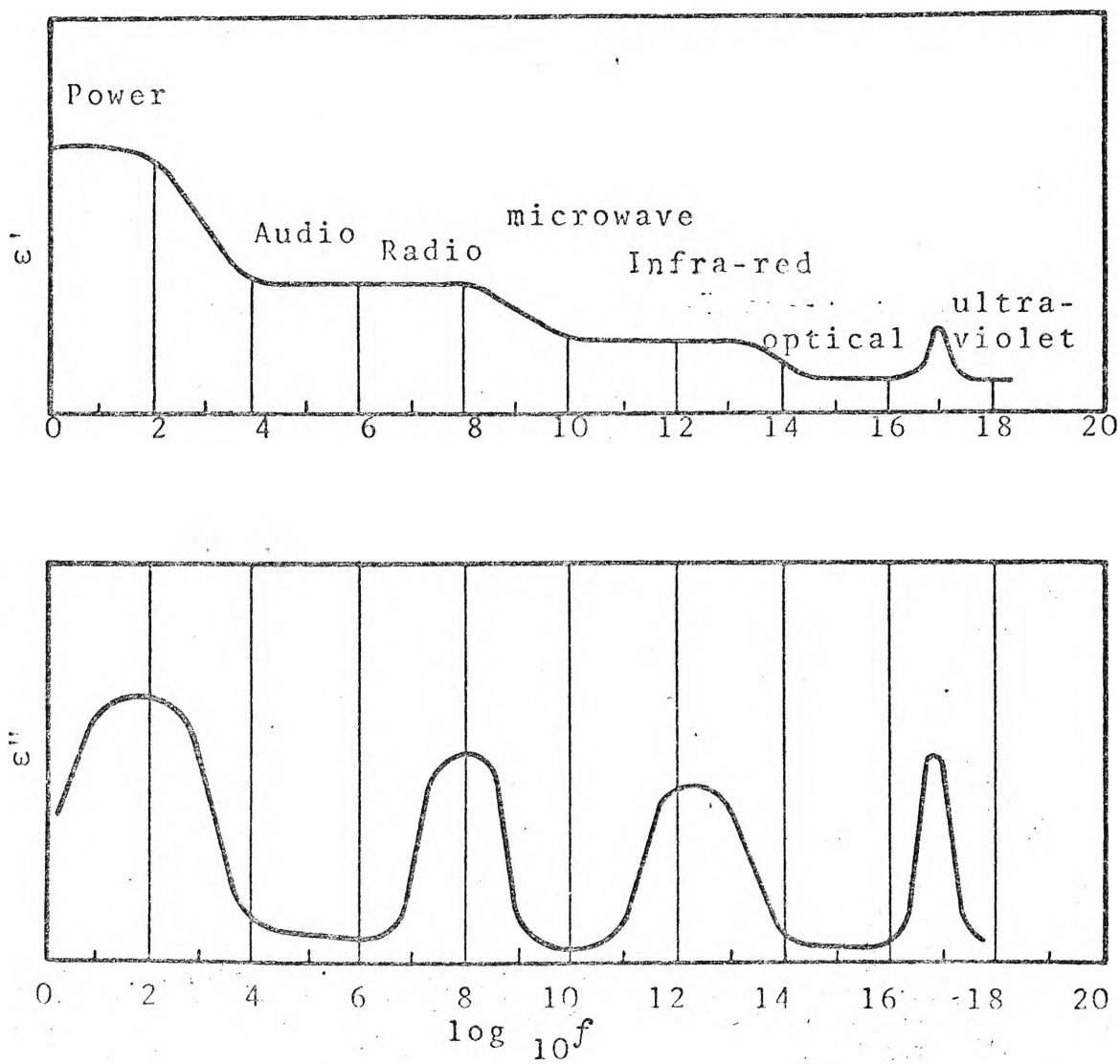

FIG. 7.1 DIELECTRIC RELAXATION AND ABSORPTION

The typical variation of the components of dielectric permittivity $\varepsilon = \varepsilon' - j\varepsilon''$ *as a function of frequency*

7.1 The Debye Model - Relaxation Absorption[6]

When ε' and ε'' are plotted as a function of frequency, the curves show characteristic regions from power to optical frequencies. At optical and infra-red frequencies, the material absorbs energy quite sharply in what is known as resonance absorption and the dielectric losses rise abruptly.

At audio and power frequencies there is a wide band of absorption relaxation which is present in all inhomogeneous dielectrics. In the crystalline powder dielectrics which we are considering, we expect to find strong relaxation absorption.

When the external potential is applied to dusts of mixed size and shape, we expect currents to flow temporarily as the individual particles are charged up. Current flow eventually stops at crystal interfaces. As the space charges due to such interfacial polarisation are swept to and fro by an alternating field, they constitute a large alternating current. As this frequency falls towards d.c., the only conductivity remaining is represented by the residual d.c. resistance. These facts are shown by the curves of Fig.7.1, in which σ_o is the d.c. conductivity, ε_∞ is the permittivity at very high frequency, and $\tau_N = \frac{\varepsilon_N}{\sigma_N}$ represents a number of Debye time-constants. This circuit shows that at d.c., it is only σ_o which can conduct. However at intermediate frequencies, τ_1 to τ_N may dominate the behaviour and contribute to the losses. At a single frequency, the circuit of Fig.7.2 becomes equivalent to that of Fig.1 (in the paper appended).

The magnitude of the various Debye time-constants τ_N depends upon the shape and orientation of the crystal interfaces and their temperature. It is clear that an impurity elongated in the direction of the applied electric field will have a larger dipole moment than one flattened in the direction of E. The effect of the former will be larger and will occur at a lower frequency.

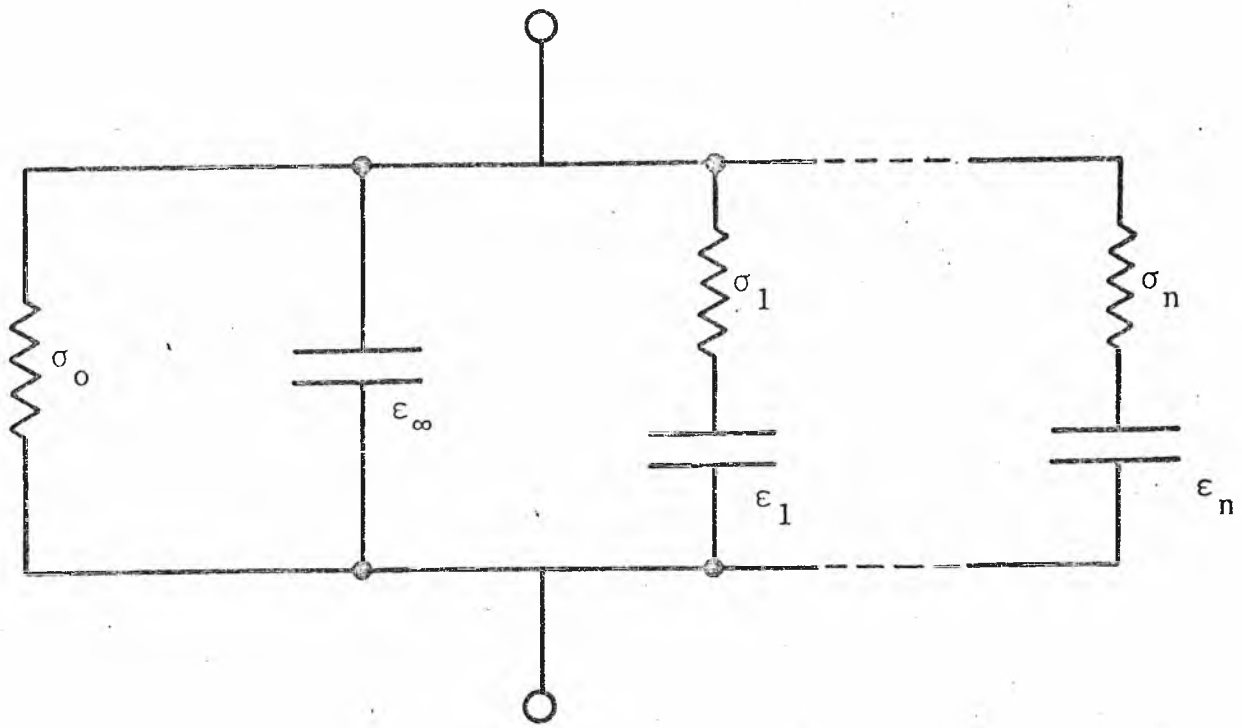

FIG. 7.2 EQUIVALENT CIRCUIT OF A DIELECTRIC

Showing several Debye time constants $\tau_n = \varepsilon_n/\sigma_n$, the d.c. conductivity σ_o and the residual real permittivity ε_∞

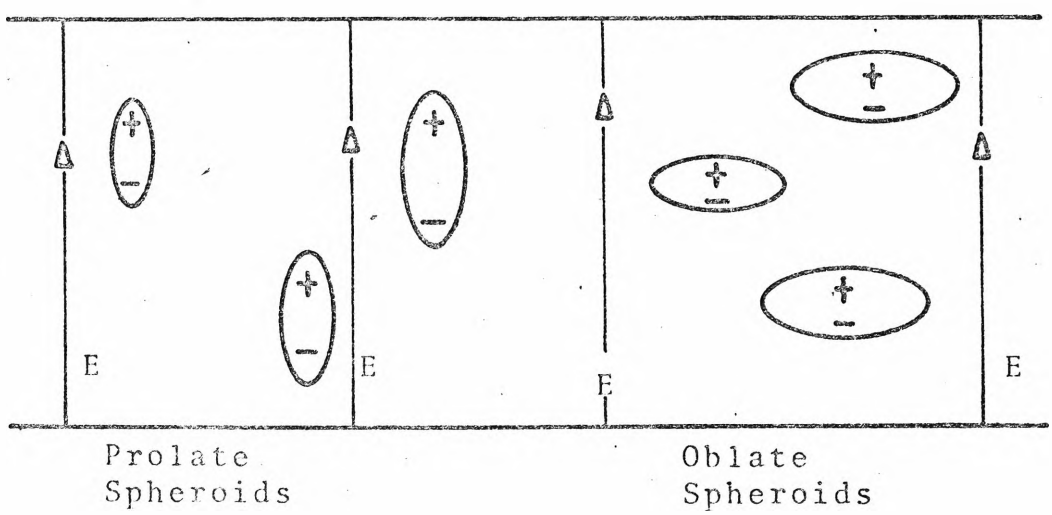

FIG. 7.3 TYPES OF PARTICLE IN AN ELECTRIC FIELD

Electric field applied to heterogeneous dielectric containing particles of various shapes and orientation

An industrial dispersoid may be expected to have all possible shapes, arrays and sizes. Some of the resultant Debye time constants may be very long - a matter of minutes. Such principles are illustrated by the diagrams of Figs.7.1, 7.2 and 7.3.

The paper appended;"The Temperature and Frequency of the Complex Dilectric Constant of Fly-Ash", should now be read.

Staub-Reinhalt. Luft Vol. 31 No. 8 August, 1971

UDC 628.511.1:537.226.2:537.226.8
621.311:621.359.4.002.68

THE TEMPERATURE AND FREQUENCY DEPENDENCE OF THE DIELECTRIC CONSTANT OF POWER-STATION FLYASH

by Owen J. Tassicker*

Wollongong University College, The University of New South Wales, Australia

1. INTRODUCTION

The ac and dc properties of typical industrial dusts (in the case at hand – power-station flyash) were investigated. The usual methods for determining the dielectric constants of solids were adapted to pulverulent material and the complex dielectric constant was measured in the range from 50 Hz to 50 kHz and from 20°C to 220°C. Investigations of this type are important for electrostatic filters, since the layer adhering to the collecting electrode forms a powder dielectric /1, 2, 3/.

Hitherto the dc properties of this layer were mainly of interest /4, 7, 8/. However, since now alternating current /5/ and pulse excitation are also applied in electrostatic filters for separating troublesome dust, the ac properties have gained in importance. The different values are arranged in such a way that the dielectric properties of the dust can be readily compared with those of known dielectric solids, such as aluminum, ceramics, glass and polymers.

Power-station flyash

The tests to be described were performed on flyash from a pulverized-coal fired power station. The ash was collected in a pilot precipitator during test giving of a new coal seam. The parent black coal had the following composition:

moisture	4.4%
volatile matter	23 %
ash	11.1%
fixed carbon	61.5%
sulfur	0.43%

The ash consisted of alumina and silica with 7.4% carbon. The carbon content was abnormally high due to special conditions imposed by the test firing.

2. THE COMPLEX DIELECTRIC CONSTANT

In the study of dielectric materials it is common to divide the dielectric constant into two components, namely the real part ε' and the imaginary part ε'' which accounts for the losses

$$\varepsilon = \varepsilon' - j\,\varepsilon''. \tag{1}$$

When the capacitor is air-spaced, then the capacitance is given by

$$C_0 = \varepsilon_0 \frac{A}{L}. \tag{2}$$

For an imperfect dielectric the current is

$$I = V\,j\,\omega\,C_0\,(\varepsilon' - j\,\varepsilon''), \tag{3}$$

where the second term represents the losses. Considering the equivalent circuit and the conductivity σ, the following relations apply (Figure 1)

$$C = C_0\,\varepsilon' \tag{4}$$

and

$$G = \omega\,C_0\,\varepsilon'' = \sigma\frac{A}{L} = \sigma\frac{C_0}{\varepsilon_0}. \tag{5}$$

Finally, the loss tangent $\tan\delta$ is obtained from the phase diagram:

$$\tan\delta = \frac{\varepsilon''}{\varepsilon'}. \tag{6}$$

List of symbols

ε	complex dielectric constant,
ε'	real part of the complex dielectric constant,
ε''	imaginary part of the complex dielectric constant,
ε_0	$8.854 \cdot 10^{-12}$ = dielectric constant of vacuum,
ε_c	composite dielectric constant,
C_0	capacitance of the air-spaced, annular test cell (F),
A	surface area of the test cell (m^2),
L	annular gap of the test cell (m),
ω	$2\,\pi\,f$ = angular frequency (rad/sec),
G	conductance of dust (Ω^{-1}),
σ	conductivity of dust ($\Omega^{-1}\,m^{-1}$),
$\tan\delta$	loss tangent of the dielectric,
$\varrho\,d\cdot c$	dc resistivity ($\Omega \cdot m$),
T	absolute temperature,
k	Boltzmann constant ($J°K^{-1}$),
E	activation energy (eV),
q	electron charge (C),
I	alternating current
V	ac voltage applied to sample,
δ	volume of dielectric consisting of spheres and voids.

* Address of the author: Wollongong, N. S. W. 2500/Australia.

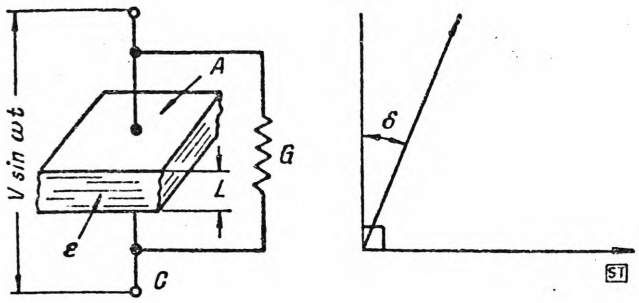

FIGURE 1. Capacitor with dielectric and loss tangent tan δ in a phase diagram

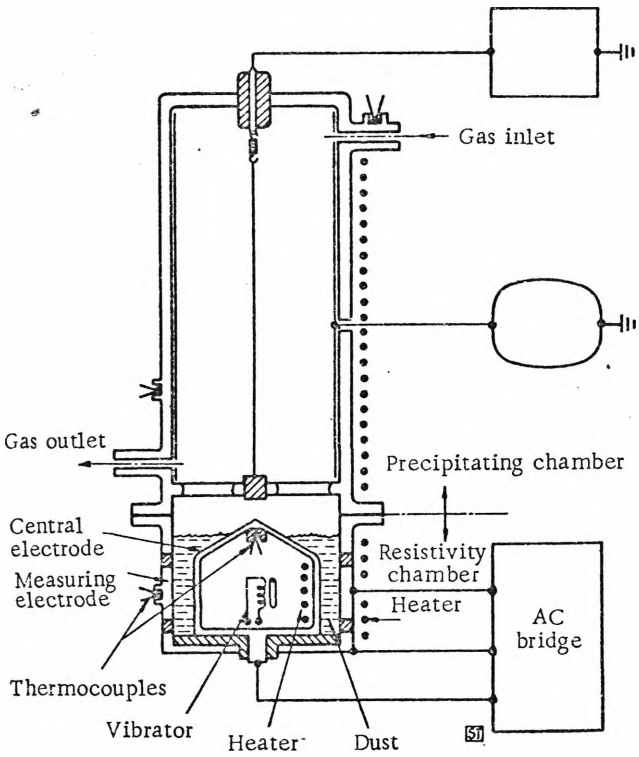

FIGURE 2. Dielectric measuring cell

It is expected that an inhomogeneous material, such as the power-station flyash considered here, exhibits a strong Debye relaxation absorption with a large time constant.

3. TEST PROCEDURE

The requirements of the test apparatus are that it shall have a close temperature control, that the particles to be examined shall be in a well-defined electrode geometry, the gaseous environment shall be controlled, and the degree of compaction of the powder shall be known. It should be capable of operation with a modern ac bridge.

3.1. Test apparatus

The measuring apparatus used, illustrated in Figure 2 and now marketed under the name "KEVATRON 223" was originally developed by the author and colleagues for measuring the in-situ dc resistivity of dispersoids, and for corona characteristics of flue gases. However, it proved to be ideal for ac measurements.

Dust to be examined was deposited by hand into the lower measuring cell. The internal vibrator compacted the specimen into the 2-mm annular gap. Edge effects were eliminated by the use of the three-electrode system. A modern transformer ratio-arm bridge was connected to the three active electrodes. The bridge gave readings of equivalent C and G in parallel as indicated in Figure 1.

3.2. Reduction of the bridge readings

The stainless-steel electrodes are so proportioned that $A/L = 300$ cm. Thus, from equation (2) we obtain

$$C_0 = 26.56 \text{ pF}$$

and

$$\varepsilon' = C/C_0 \text{ from (4)}$$

and

$$\sigma = G/3000 \text{ from (5).}$$

It was thus easy to find $\sigma, \varepsilon', \varepsilon''$ and tan δ from the bridge readings.

4. THE COMPLEX DIELECTRIC CONSTANT AS A FUNCTION OF TEMPERATURE AND FREQUENCY

Varying the temperature of the specimen from ambient to 220°C and the frequency from 50 Hz to 50 kHz, results were obtained as described in the following paragraphs.

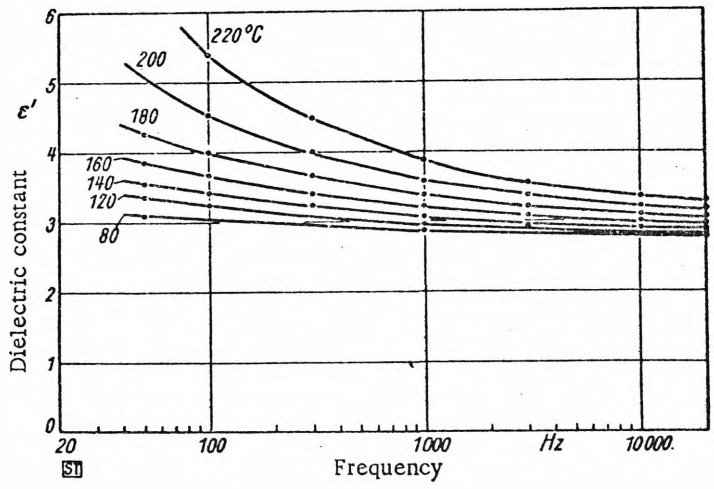

FIGURE 3. Dielectric constant ε' as a function of frequency and temperature for dry, compacted flyash

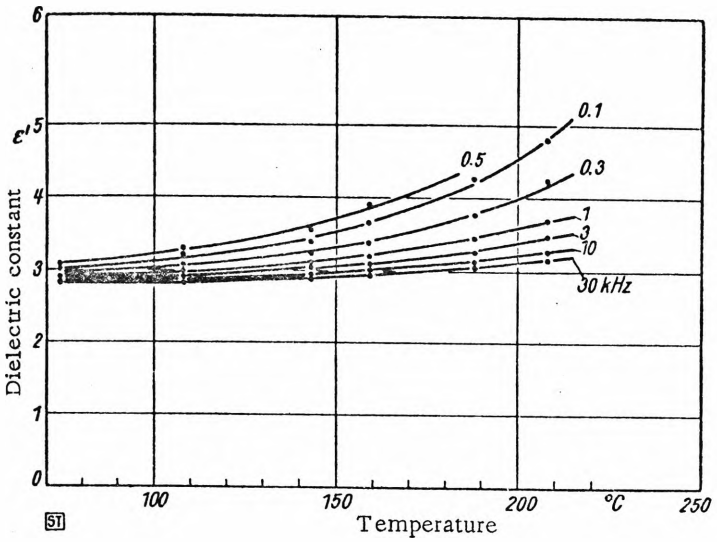

FIGURE 4. Dielectric constant ε' as a function of temperature and frequency for dry, compacted flyash

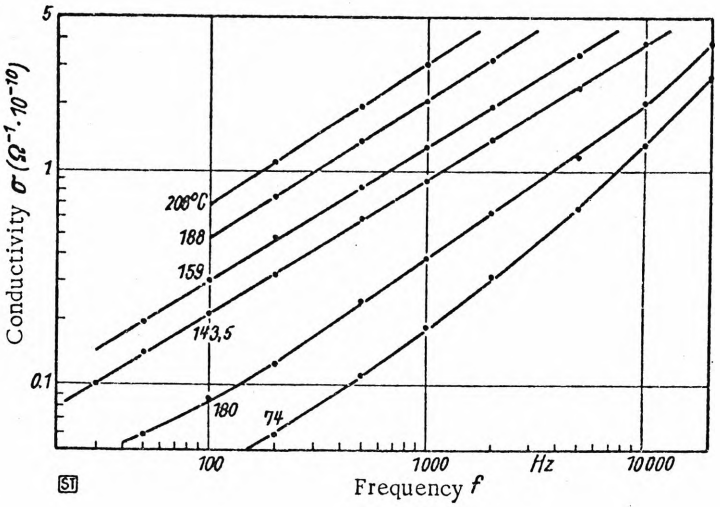

FIGURE 6. The conductivity σ of dry flyash as a function of frequency and temperature

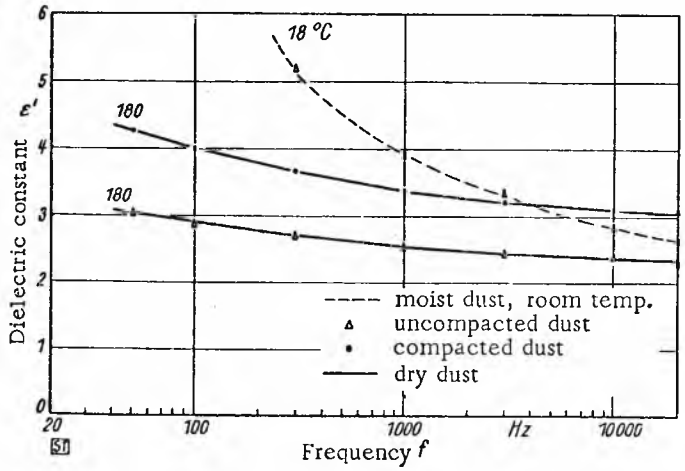

FIGURE 5. Effect of compaction and moisture on the dielectric constant of flyash

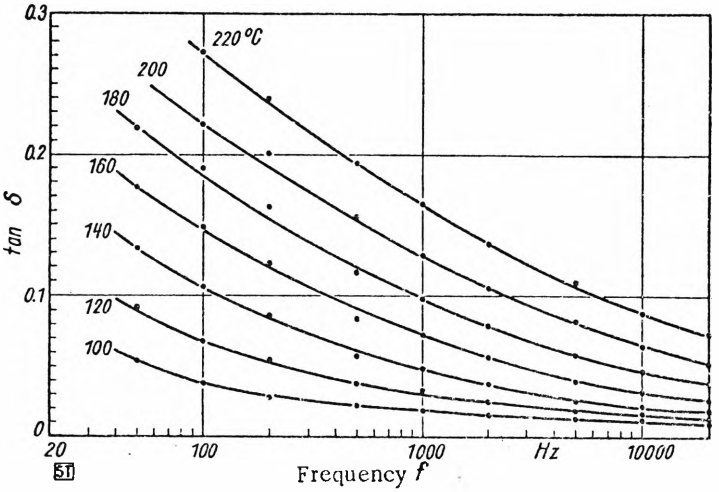

FIGURE 7. Loss tangent tan δ of dry flyash as a function of frequency and temperature

4.1. Temperature and frequency dependence of ε'

The results are shown in Figures 3, 4 and 5. At a fixed temperature, the values of ε' fell from their low frequency values at 50 Hz, and leveled out to about 3 at 50 kHz. The higher values of ε' at power frequencies are attributed to the presence of dielectric relaxation absorption effects with long time constants which respond at low frequencies but cut off at R.F. This behavior is the same as that commonly found in ceramics.

At a fixed frequency, ε' steadily increases with a rise in temperature as shown in Figure 4. Again the same behavior is observed in both glasses and ceramics.

The effects of moisture and compaction on the dust are shown in Figure 5. In the case of the uncompacted specimen, the dust was just run into the annular cavity at room temperature and later heated. The same specimen when warm and dry was then vibrated at 100 Hz by the compactor fitted inside the central dome, after which the frequency-response test was repeated. The greater density of packing is seen to increase the dielectric constant by 30 to 40%. A specimen, damp after being exposed to ambient humidity for some days, shows values of ε' in excess of 5 at power frequencies, decreasing to about 3.0 at high frequencies.

4.2. Conductivity as a function of temperature and frequency

Figure 6 shows that at a given temperature, the conductivity of the ash increases with frequency in a linear fashion

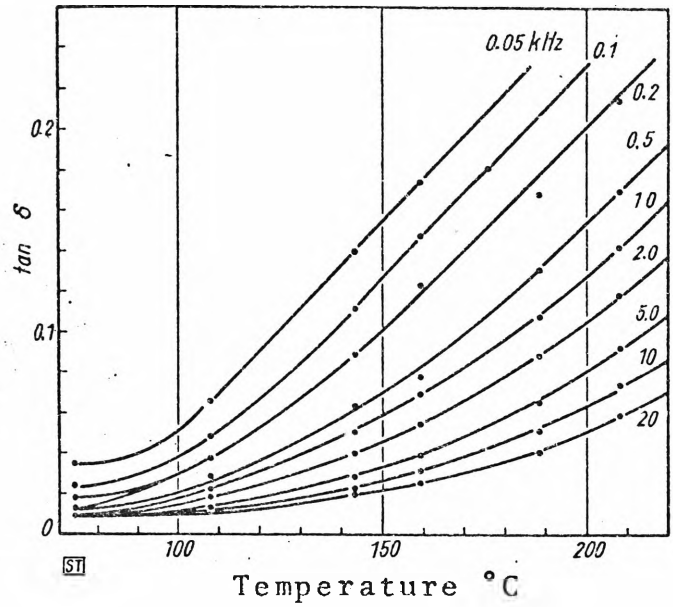

FIGURE 8. Loss tangent tan δ of dry flyash as a function of temperature and frequency

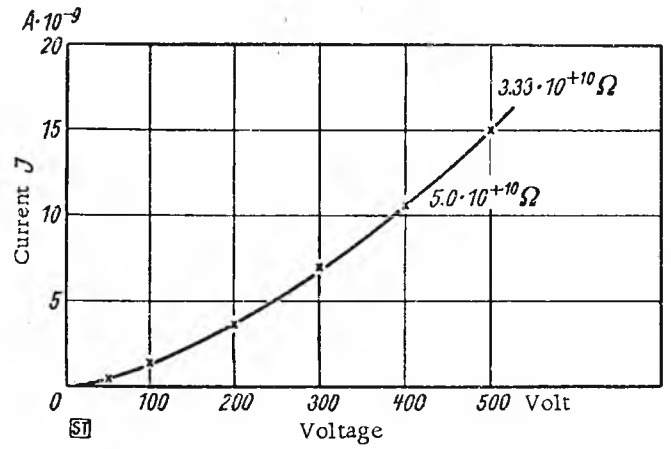

FIGURE 9. DC resistivity of dry flyash

on a log-log scale. Apart from the two lower temperatures where it is believed the specimen was slightly affected by atmospheric humidity, it is found that $\sigma \sim f^{0.63}$. The conductivity σ is to be understood in conjunction with the equivalent circuit in Figure 1. It is shown in 5. 2. that σ is related to the absolute temperature in an exponential manner.

4. 3. The loss tangent tan δ

The loss tangent falls steadily with increasing frequency, for the whole range of temperatures considered, as shown in Figure 7. The fall is attributed to relaxation absorption effects at low frequency. In Figure 8 the power factor is seen to rise with temperature. It is likely that carriers contributing to current flow must overcome potential barriers distributed in the body of the material. The higher the temperature, the

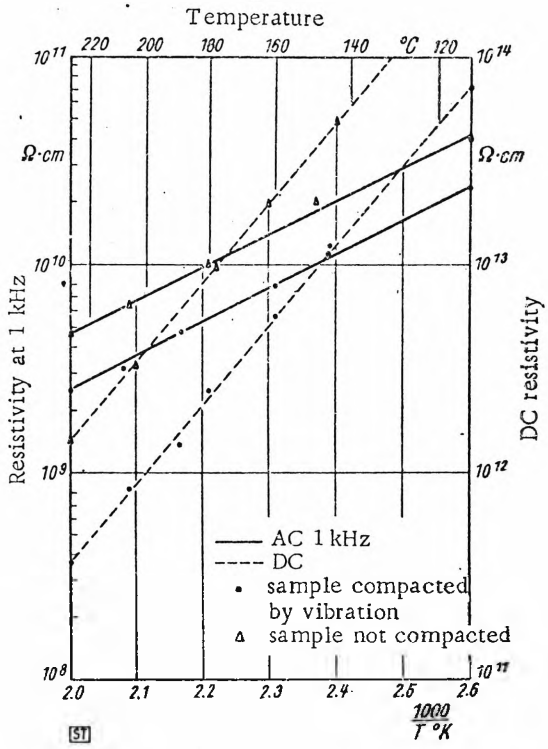

FIGURE 10 Comparison of ac and dc resistivity of flyash

greater the number of carriers which have sufficient energy at a given time. That is, the conduction may be interpreted in terms of statistical mechanics. Therefore we shall examine the temperature dependence more closely.

5. COMPARISON OF AC AND DC RESISTIVITIES

5.1. DC resistivity

The apparatus depicted in Figure 2 was originally designed for dc measurements, so it was a simple matter to obtain dc resistivity along with the ac values. The current voltage dc characteristic is not linear, but is of the form shown in Figure 9. For dc resistivity to have any meaning, it is necessary to specify it at a given voltage or current density. The author and colleagues have adopted 1.5 kV/cm as a standard potential gradient in all their work, corresponding to 300 V in the test cell. Such a nonlinear relationship between the voltage and current was not observed during the ac measurements. When plotted on semi-log graph paper as in Figure 10, the relationship between the reciprocal of the absolute temperature and the dc resistivity is a straight line. From this it may be shown that

$$\varrho \cdot d \cdot c = 0.95 \cdot 10^4 \, \varepsilon + \left(\frac{q\,E}{kT}\right) (\Omega \cdot \mathrm{cm}),$$

where T is the absolute temperature, k is Boltzmann's

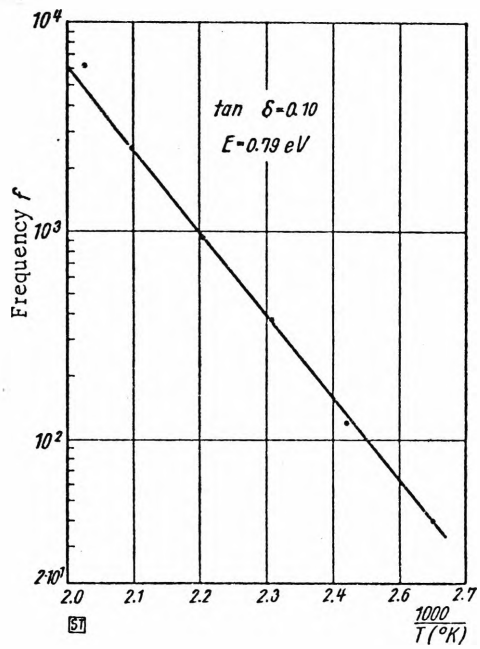

FIGURE 11. Activation energy for flyash on ac at a fixed loss tangent tan δ

constant, $E = 0.75$ eV is the activation energy for the specimen, $qE/kT = 8{,}750/T$.

It is observed that the same activation energy applies whether the sample is compacted or not.

5.2. AC resistivity

If the results for the ac tests at 1 kHz are plotted on the same coordinates, the relationship is also exponential. As in the dc case, the degree of compaction does not affect the activation energy E which is now found to be 0.32 eV.

Over the range of measurements, it is found that

$$\varrho\,(1\text{ kHz}) = 1.53 \cdot 10^6\,\varepsilon + \frac{3700}{T}\,(\Omega \cdot \text{cm}).$$

It is to be noted that in the working range of temperatures, the ac resistivity is about three orders of magnitude smaller than the dc resistivity. At low power frequencies the resistivity is still orders of magnitude lower than the dc values.

5.3. Relation between dc and ac activation energies

It is of considerable fundamental interest to examine the data contained in Figure 7 more closely. For a given tan δ, if f is plotted against the reciprocal of absolute temperature, it is again observed that an exponential relationship holds (see Figure 11). Now the activation energy E is found to be 0.79 eV. This, within experimental error, is the same as the dc activation energy of 0.75 eV found above.

6. DISCUSSION OF RESULTS – RELATION TO OTHER HETEROGENEOUS DIELECTRIC STUDIES

A limited amount of work on the dielectric properties of powders of various shapes has been carried out. Böttcher has surveyed work in this field /9/. Wiener, Bruggeman, Polder and Van Santen have considered powders consisting of spheres, cylinders, laminae and arbitrary shapes. Böttcher's relation

$$\frac{\varepsilon'_c - 1}{3\,\varepsilon'_c} = \delta\,\frac{\varepsilon'_1 - 1}{\varepsilon'_1 + 2\,\varepsilon'_c} \qquad (7)$$

is valid for powders consisting of spheres of dielectric constant ε'_1 occupying a volume proportion δ of the whole. The composite or bulk dielectric constant is ε'_c. For low values of ε_1, the relation has been found to hold reasonably well for particles of any shape. Equations such as (7) could be valuable in further studies of industrial dispersoids, since they relate the packing density δ to the bulk dielectric constant. Where there are conducting particles distributed at low density throughout a continuous loss-free dielectric, the composite material is found to have losses. This situation bears strong similarities to the flyash under consideration in these tests, where there is a low concentration of carbon. The material then behaves as it had only Debye time constant.

7. BACK CORONA AND THE AC CONDUCTIVITY

The results obtained in this series of tests throw some light on the phenomena of reverse ionization in electrostatic filters which separated high-ohmic dust /5/. Even at low power frequencies, the resistivity has been found to fall by several orders of magnitude – enough to take some dusts out of the range known as 'difficult.' This helps to explain the beneficial results obtained with irregular voltage waveform which has been commonly noted but described by White /10/: "Cottrell in his early experiments, tried both the pulsating voltages obtained from unfiltered rectifier sets and the steady, or dc voltage obtained by adding a filter condenser to the rectifier output. The pulsating voltages proved definitely superior, chiefly because of the unsatisfactory spark characteristics of dc voltage. This result has been confirmed by long experience ..." Very conductive particles are precipitated best by voltages which approach dc, and high-resistance particles respond best to fairly impulsive voltages.

Acknowledgements

Dr. J. S. Dryden and his colleagues of the Dielectrics Group, Commonwealth Scientific and Industrial Research Organization (C. S. I. R. O.) provided valuable advice. The National Coal Research Advisory Committee and the electricity Commission of New South Wales financed the project.

Bibliography

1. Rohmann, H. Messung der Grösse von Schwebeteilchen (Measurement of the Size of Suspended Particles). — Z. Phys., 17, p. 253. 1923.
2. Krupp, H. and G. Sperling. Theory of Adhesion of Small Particles. — J. Appl. Phys., 37, No. 11, p. 4176. 1966.
3. Penney, G.W. and E.H. Klingler. Contact Potentials and the Adhesion of Dust. — A. I. E. E. Trans. p. 200. July 1962.
4. Eishold, H.G. Eine Messvorrichtung zur Bestimmung des spezifischen elektrischen Staubwiderstandes (A Measuring Device for Determining the Specific Electrical Resistance of Dust). — Staub-Reinhalt. Luft, 26, No. 1, pp. 11-14 [Engl. Translation]. 1966.
5. Lau, H. Mit Wechselspannung betriebene Elektrofilter (AC Electrostatic Precipitator). — Staub-Reinhalt. Luft, 29, No. 8, p. 10-14 [Engl. Translation]. 1969.
6. "Dielektrika," Handbuch der Physik, Edited by S. Flügge, Vol. XVII, Springer-Verlag, Heidelberg. pp. 119-132. 1956.
7. Tassicker, O.J., Z. Herceg, and K.J. McLean. A New Method and Apparatus to Assist the Prediction of Electrostatic Precipitator Performance. — Elec. Eng. Trans. I.E. Aust., pp. 277-279. September 1969.
8. Pauthenier, M. Back Corona and the Bi-Ionised Electric Field in Electrical Precipitators. Colloques Internationaux du Centre National de la Recherche Scientifique. 1960.
9. Böttcher, C.J.F. Theory of Electric Polarisation. Elsevier, Amsterdam. pp. 414-420. 1962.
10. White, H.J. Industrial Electrostatic Precipitation. Addision-Wesley. p. 213. 1963.

Summary

Flyash has been examined as a complex dielectric constant over the range of temperatures of 20°C to 220°C and of frequency 50 Hz to 50 kHz. The behavior is similar to that of known ceramic, glass and polymer dielectrics. Important conclusions may be drawn regarding its behavior in an electrostatic precipitator. There remains much scope for studies of this kind on other industrial dusts, especially with regard to the influence of humidity and conditioning agents.

UDC 577.4:614.7
061.3.055.1(43-2.3) "1971"

PROTECTION OF THE ENVIRONMENT — A TASK OF OUR TIME

On the occasion of its 15-year existence the Institut für gewerbliche Wasserwirtschaft und Luftreinhaltung e. V. (IWL), Cologne, held a symposium on the theme "Protection of the Environment — A Task of Our Time" on 18 May 1971 in the newly built "House of the German Industry" in Cologne, which at the same time became the permanent seat of IWL. On 19 May 1971, a tour was made of several industrial enterprises. After a welcoming address and an inspection of the new offices and laboratories four lectures were given.

Dr. Werner Best, Hessen Minister for the Economy and Environment, expanded on his theme "Protection of the Environment from the Standpoint of the States with Special Emphasis on the State of Hessen" and pointed out, among other things, that the current state of affairs requires immediate action, since, for example, it takes some time before the Federal government will arrive at definite resolutions regarding this problem. Thus, in Hessen, considerable advances have been made as regards clean air maintenance in the industrial domain over the past years. The percentage of emissions produced by industry could already be decisively limited by implementing technological measures. The main problem of clean air maintenance is currently the waste gases produced by motor vehicles and oil furnaces.

According to an article which appeared in the publication "Zeit" of 27 February 1970 the following amounts of pollutants were annually emitted: 2.5 million tons of dust, 2.5 million tons of nitrogen, 3 million tons of hydrocarbons, 5 million tons of sulfur oxide and 7 million tons of carbon monoxide; 60% of the above amounts are discharged via the exhaust pipes of internal-combustion engines, whereby diesel engines produce heavier pollution than gasoline engines. The health hazard inherent in air pollutants has been established. It ranges from nausea and asthma to chronic bronchitis and lung cancer. Here, in the nearest future decisive measures must be implemented. The pollution of the environment cannot be effectively combatted by merely spending the tax payers money. Here it is necessary to get to the root of the problem. Every industrial enterprise should be required to implement the proper measures to curtail air pollution. The same applies to the citizens.

In combatting hazardous influences on the environment safety measures do not take precedence (these merely serve as a means of protection), but rather the state of the environment.

Dr. Best treated in an analogous manner the less pressing problems of water resources, water supply, noise suppression.

CHAPTER 8

CONCLUSION

8. CONCLUSION

Some Areas for Further Investigation

There are a number of areas in electrostatic precipitator technology and theory which are in need of investigation in depth.

In the first place, a refined theory of particle collection is needed which will embrace the transition from large to fine particles and which will fully account for modern concepts of turbulent diffusion. Such a theory would need to accommodate such effects as re-entrainment of previously captured particles, and the effects of back corona.

New means are needed to cope with the collection of high resistivity particles and for the amelioration of back corona. A deeper study of the surface chemistry of particles is mandatory in order to open up new possibilities for gas conditioning agents. A thorough exploration of all types of pulse and asymmetrical a.c. energisation needs a high priority. A proper alternative to the present practice of building mammoth size precipitators for the capture of high resistivity particles is urgent.

The least understood aspect of precipitator technology is possibly that of rapping and the resultant re-entrainment. A further study of the various components of adhesion in a layer of deposit and of the dynamics of their dislodgement is mandatory.

A systematic study of discharge electrode shape is indicated. It is not enough to ensure that maximum electrical power is put into the gas. Ample evidence is available to indicate that the distribution of power in the inter-electrode space and on the receiving electrode is important, especially for high resistivity material.

Adhesive Forces in a Powder and Rapping

The forces of adhesion between solid particles principally comprise; short range Van der Waal, electrostatic due to the externally applied corona, capillary due to a vapour in the ambient gas; and secondarily, dipole attraction/repulsion and triboelectric forces.

Agglomerates in a gas stream will probably cohere in spite of the disruptive effects of Brownian motion and gas turbulence.

Small particles adhere to a substrate more tenaciously than large particles when subjected to vibration, impact or gas scouring. Agglomerates of small particles are more stable than those comprising large particles.

The tensile and shear strength of a layer of deposit on a precipitator plate are derived from the forces between individual particles as listed above. The tensile strength, P (adhesion) of a layer depends sharply on the density of packing of the particles α_b/α_s (or porosity) for this parameter determines the interparticle spacing. Some quantitative relations may be synthesised from diverse sources. Some of the elementary forces between a pair of spheres are proportional to the diameter viz:

$$\Delta F = A_v d \qquad \text{Van der Waal}$$

$$+ A_c d \qquad \text{Capillary}$$

where both constants depend upon the nature of the particles, surface roughness, and surface states. Some values for industrial powders are available. A_c is negligible below a gas RH of 80%, rising steeply at such water vapour contents. The tensile pressure in a layer due to these two sources is given by:

$$P = +H'(\alpha_b/\alpha_s)^m \Delta F/d^2 \qquad \text{Van der Waal and Capillary forces}$$

$$= +H'(A_r+A_c)\ (\alpha_b/\alpha_s)^m/d \qquad N/m^2$$

where H' and m are constants for the material and (α_b/α_s) is the relative bulk density. If such a layer of dispersoid is subject to a corona field, there are additional electric forces which tend to detach a low resistivity deposit or to hold more tenaciously a high resistivity one. The additional electric pressure is given by:

$$P = + \frac{\varepsilon_o}{2} \left[\left(J\bar{\rho}_\ell \frac{d}{d'k} \right)^2 - Eg^2 \right] \quad N/m^2$$

where; $(J\bar{\rho}_\ell)$ is the average electric field in the layer, $(\frac{d}{d'k})$ a stress concentration factor and E_g is the electric field in the adjacent gas. Some experimental support for the above results has been found from miscellaneous sources.

When an electrode coated with a deposit is rapped, it is principally the normal modes of vibration which are effective in dislodging deposit. There is a certain minimum depth of deposit given by:

$$T < P/(\alpha_b \ \ddot{z}) \quad m$$

where P = total tensile pressure N/m^2

α_b = bulk density KG/m^3

$\ddot{z}$ = normal acceleration m/s^2

below which no material is detached and above which the whole depth T will be removed except for a thin underskin.

The Precipifuge

A new machine, known as a Precipifuge, which as the name suggests is a combination of a precipitator and a centrifuge, has been designed, constructed and commissioned. Dust may be precipitated uniformly onto the rotor head at any convenient current density and electric field strength. Precipitation takes place in a closed chamber, which may contain any desired gas at a range of temperatures. Dust so deposited may be centrifuged off by spinning the rotor up to 10,000 RPM when an acceleration of 7700 g is reached. Detachment of the whole

layer of dust (except for a thin underskin) occurs at a definite speed which is determined by observing the surface stroboscopically. The adhesive strength of the layer of deposit follows immediately. During centrifuging, the dust may be subjected to an electric field or to a vacuum.

A Micro Boundary Electrode

The corona current density J_o and the electric field strength E_o at a point on an electrode boundary may be determined by means of a new probe known as MABLE - a micro area boundary electrode. A small element of current I_o is sampled by means of a flat, smooth insulated area A of about $1mm^2$ which is at earth potential. The current density J_o is simply $(\frac{I_o}{A})$. If the probe is biassed by a voltage V_b, then the current changes in accordance with the equation:

$$(I/I_o) = 1 + \frac{C_o V_b}{\varepsilon_o A E_o}$$

where C_o is the capacitance of the active surface of the probe. From this, the electric field at the boundary E_o may be readily determined.

The three terminal screened version of the flat probe uses an a.c. diagnostic signal rather than d.c. perturbation and utilises a conductance/capacitance bridge as a transducer. By these means, the conductivity $\bar{\sigma}$ of the ionised gas at a point on the boundary is determined from the expression:

$$\bar{\sigma} = \frac{G}{C_o} \varepsilon_o$$

and the electric field follows immediately from the known current density:

$$J_o = \bar{\sigma} E_o$$

Viewed in a more general fashion, this technique measures the complex permittivity of an ionised gas at a point on its boundary.

The screened probe has thus been developed to a high

degree of electrical precision and mechanical discrimination.

Corona Patterns and Discharge Electrodes

MABEL has considerable uses in the examination of fundamental processes in positive and negative coronas, and also in the evaluation of commercial precipitator electrodes. Interesting fine structure in J over the anode of a negative corona system has been observed. Discontinuities originating from the cathode have been found to penetrate right through the gas space to the anode. The electric field and current density profiles on the boundary of various corona systems have been measured. In every case examined, viz the point-to-plane, multiple wire-in-duct, barbed wire in duct, plate emitter, etc have all shown strong enhancement of the boundary electric field due to the presence of space charges.

A.C. and D.C. properties of Fly-Ash

The a.c. and d.c. properties of a typical fly-ash have been determined and compared over a range of temperatures from 20°C to 220°C. The complex dielectric constant of compacted fly-ash has been measured from 50Hz to 50KHz. The real part E' over this range and at a temperature of 220°C, falls from 6 at low frequencies to 3.5 at the high frequency end. The behaviour is generally similar to that of known ceramic, glass and polymer dielectrics. The resistivity on a.c. is several orders of magnitude smaller than the d.c. resistivity at the same temperature, thus explaining the observed field result that high resistivity dispersoids are collected more effectively with an impulsive discharge electrode energisation. The way is clearly indicated for fruitful investigation of a.c. energisation of precipitators.

CHAPTER 9

ACKNOWLEDGEMENTS

9. ACKNOWLEDGEMENTS

The writer's special thanks is due to Professor L. W. Davies of the University of New South Wales who has rendered constant counsel, criticism and encouragement during the whole course of this long project.

The writer's colleagues K. McLean and Z. Herceg have always been ready with background support from their own specialist studies.

The Electricity Commission of New South Wales has provided financial support for the project, and its officers, especially B. Kirkwood, K. Watson and N. Lamb have frequently brought their long field experience to bear during discussions.

The National Coal Research Advisory Committee has provided funds for some parts of the project.

Dr. A. H. Von Engel of Keble College, and Dr. J. E. Allen of University College Oxford, both rendered valued criticism on Chapter 4.

The National Standards Laboratories, C.S.I.R.O., particularly Mr M. C. McGregor, took a keen interest in the a.c. bridge techniques used in Chapter 5, generously loaning the writer some of their own specialised bridge apparatus.

Dr. G. Dryden of the Dielectrics Group of the C.S.I.R.O. allowed the writer to complete certain experiments of Chapter 7 in his own laboratories.

Lysaghts Pty Ltd and Australian Iron and Steel, both of Port Kembla carried out certain machining operations for the Precipifuge and MABEL respectively, and the latter provided considerable computer time. Mr G. W. Sykes produced engineering drawings with skill and dexterity.

Professor C.A.M. Gray and Professor B. H. Smith of Wollongong University College readily allowed their facilities to be used in the course of the project.

CHAPTER 10

APPENDICES

Appendix 1.1

The Cylindrical Electrode Corona System

Considering the cylindrical electrode system depicted in Fig.4.8, if the potential $+V_a$ is raised above a critical voltage V_o, a stable, space charge limited discharge takes place. Immediately surrounding the discharge electrode there is at NTP, a softly luminous plasma sheath. The remaining 99% of the interelctrode space contains positive ions and neutral gas. These drift under the radial electric field to the outer boundary, constituting the corona current.

Since there is axial symmetry, Poisson's Equation

$$\nabla^2 V = - \frac{\rho}{\varepsilon_o}$$

becomes:

$$\frac{d^2V}{dr^2} + \frac{1}{r}\frac{dV}{dr} = -\frac{\rho}{\varepsilon_o}$$

where

$$E = - \frac{dV}{dr}$$

The equation of continuity is:

$$\nabla . J = - \frac{\partial \rho}{\partial t}$$

which for the steady state leads to:

$$(I'/L) = 2\pi r K E \rho$$

These equations, when integrated by elementary means, and making second order approximations, yield[4,11]

$$(I'/L) = 4\pi\varepsilon_o K \left[\frac{(V_a - V_o)^2}{2b^2} + \frac{V_o(V_a - V_o)}{b^2 \ln(b/a)} \right] amp^{+1}{}_m{}^{-1} \qquad \ldots(1.5)$$

for the current per unit length, arithmetical corrections having here been made to the White expression and

$$E = \sqrt{\frac{2(I'/L)}{4\pi\epsilon_o K}\left(1-\left(\frac{a}{r}\right)^2\right) + \left(\frac{V_o}{r\ \ln(b/a)}\right)^2}\ \text{Volt}^{+1}\ \text{m}^{-1} \qquad \ldots(1.6)$$

for the electric field at any radius.

Three principal assumptions are made here, viz:

(a) The plasma sheath is not larger than two or three times the discharge electrode, a, and may be approximately taken to be a.

(b) The field strength at the edge of the plasma sheath is constant at the Peek[105] inception value, which is for air, $E_i = (30n + .9\sqrt{n/a})\text{KV}^{+1}\ \text{cm}^{-1}$ where n is the density of air relative to NTP.

(c) The mobility of the gas K^+ has been regarded as constant for the wide range of field strength indicated in Equation 1.6. Since for the geometry of Fig.4.8, E varies from 110 KV/cm to 1 KV/cm, the strict constancy of K^+ cannot be expected.[107] However, from Fig.4.9b and the numerous experiments cited, the field strength E is constant over most of the space, albeit at high values. Cobine[106] points out (p.41) that the break-up of ion 'clumps' at values of E/P above about 10 leads to larger than normal K^+. This accounts for high values of K^+ (1.6 to 3.0) determined by the present writer and others using coaxial electrode corona.

It is noted from the equation of continuity that:-

$$\rho = \frac{(I'/L)}{2\pi r K E}$$

which gives a ready means for the determination of charge density.

Appendix 2.1

Mechanical Forces at a Dielectric Interface

It is shown in texts, (for example: Smythe "Static and Dynamic Electricity", 1950, McGraw Hill, P.18) on electricity that the pressure over any section of a tube of electric flux is given by:

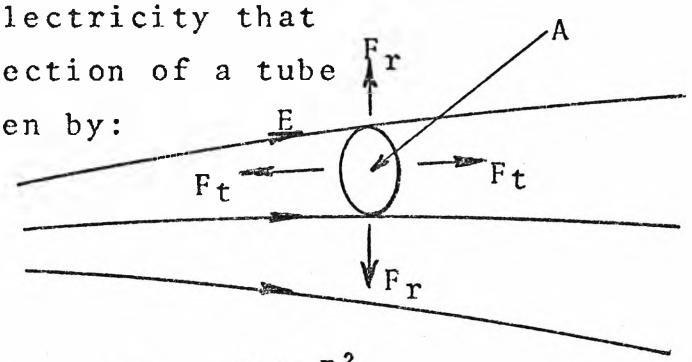

$$(F_t/A) = P = \frac{D \cdot E}{2} = \frac{D^2}{2\varepsilon_o\varepsilon_r} = \frac{\varepsilon_o\varepsilon_r E^2}{2} \quad \text{(tension) N/m}^2$$

The lateral pressure between adjacent tubes of flux is also:

$$(F_r/A) = P = \frac{\varepsilon_o\varepsilon_r E^2}{2} \quad \text{(repulsion) N/m}^2$$

Where there is a dielectric boundary with normal electric fields then the nett normal stress is:

$$P_n = \frac{(D')^2}{2\varepsilon_o\varepsilon_r'} - \frac{(D'')^2}{2\varepsilon_o\varepsilon_r''} \quad \text{N/m}^2$$

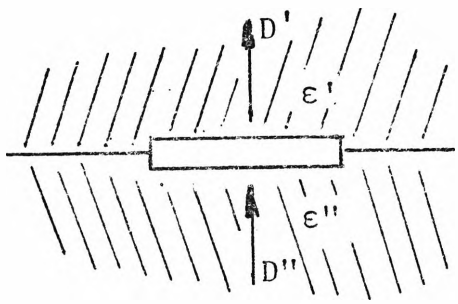

(If in addition there is no surface charge, then D' = D''.)

In a situation where there are tangential fields at the dielectric boundary, then the nett normal pressure is:

$$P_n = \tfrac{1}{2}\varepsilon_o\varepsilon_r'(E')^2 - \tfrac{1}{2}\varepsilon_o\varepsilon_r''(E'')^2$$

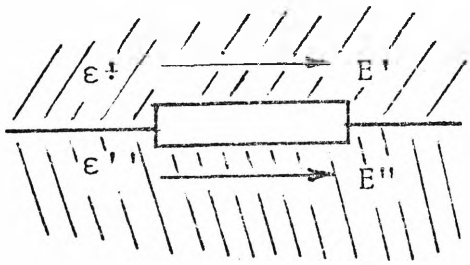

This is really a special case of the Maxwell Electromagnetic Stress Tensor.

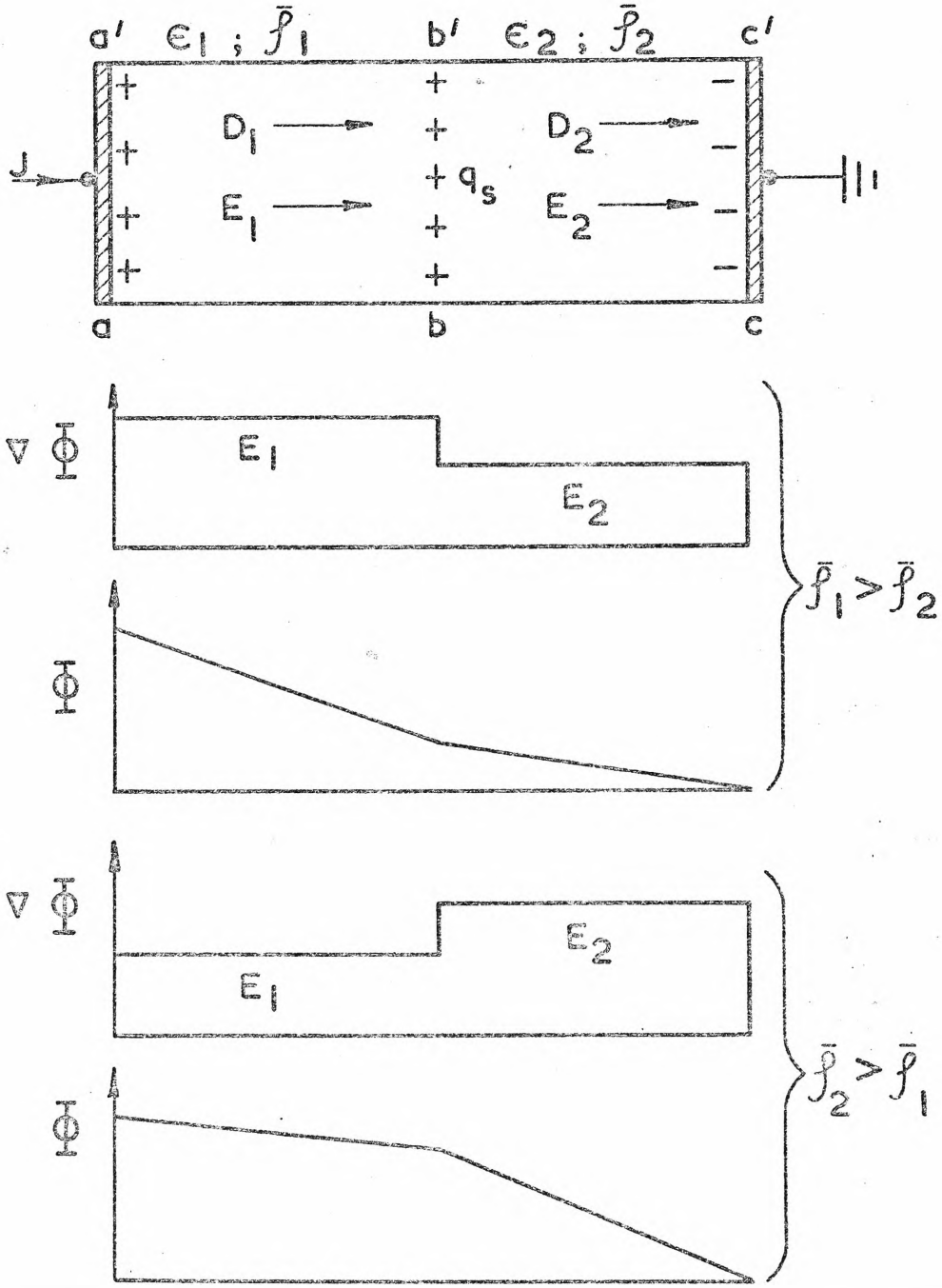

FIG. 2.13 ELECTRIC FIELD IN LEAKY DIELECTRICS

Two dielectrics are in series carrying a common current density J. A surface charge q_s will always exist at the boundary bb' except when $\rho_2 \varepsilon_2 = \rho_1 \varepsilon_1$

The case pertinent to the electrostatic precipitator is depicted in Fig.2.13 where a conducting dielectric media carries a constant current density J normal to the interface. A constant current density J enters the dielectric $\varepsilon_1/\bar{\rho}_1$ at aa', crosses the interface bb', crosses dielectric $\varepsilon_2/\bar{\rho}_2$ and leaves via electrode cc'.

It is necessary to postulate the presence of a surface charge density q_s at the interface.

$$\text{Then} \quad D_2 = D_1 + q_s$$

$$E_1 = \bar{\rho}_1 J$$

$$E_2 = \bar{\rho}_2 J$$

$$\text{Hence} \quad E_2\varepsilon_2\varepsilon_o = \bar{\rho}_2\varepsilon_o\varepsilon_2 J = D_2$$

$$E_1\varepsilon_1\varepsilon_o = \bar{\rho}_1\varepsilon_o\varepsilon_1 J = D_1$$

$$\text{and} \quad q_s = (D_2 - D_1) = J\varepsilon_o (\bar{\rho}_2\varepsilon_2 - \bar{\rho}_1\varepsilon_1)$$

It is readily shown that the summation of the pressure in the system

$$F_{aa'} + F_{bb'} + F_{cc'} = 0$$

as it should.

If dielectric 1 id an ionised gas and dielectric 2 is a particulate layer, then

$$P = (F/A) = + \frac{\varepsilon_o}{2} (\varepsilon_\ell E_\ell^2 - E_g^2) \quad \text{(adhesion)} \quad N/m^2$$

The Fig.2.13 shows how the potential and potential gradient vary in the media for two resistivity cases.

Appendix 2.2

Lifshitz (1956) evaluation of the Van der Waal force[72,82]

The pressure between flat parallel surfaces of the same material is:

$$P = \frac{h\bar{\omega}}{8\pi^2 Z_o^3}$$

where $$\bar{\omega} \equiv \int_o^\infty \frac{(\varepsilon(i\xi)-1)^2}{(\varepsilon(i\xi)+1)^2}\, d\xi$$

an integral carried out in the complex plane along the imaginary frequency axis ($i\xi$).

The value of $\varepsilon(i\xi)$ to be used in the above may be found from the imaginary part $\varepsilon''(\omega)$ of the complex dielectric constant, as a function of real frequency ω, by the Kronig-Kramers relations:

$$\varepsilon(i\xi)-1 = \frac{2}{\pi}\int_o^\infty \frac{\omega\varepsilon''(\omega)}{\omega^2+\xi^2}\, d\omega$$

In a few cases, the several integrals may be found analytically for materials with simple structures. Generally, they must be evaluated numerically from experimental data.

Appendix 2.3

A General Theory of Adhesion of Dry Particulates

A general theory of the adhesion of dry particulates has been advanced by Cheng[93] after drawing from all other published work. The theory connects tensile strength P with the fundamental particle and size distribution parameters; $\bar{S}$ the mean surface area/particle, v mean volume/particle, $\bar{d}$ mean diameter, α_b bulk density of powder, α_s density of a particle, α_b' density of bulk powder at which tensile strength disappears, Z_o' particle separation at which interparticle force vanishes. Determination of the particle parameters $\bar{S}$, $\bar{v}$ and $\bar{d}$ were carried out by a Coulter Counter in accordance with established practice. Density α_s was determined by the well known air displacement pycnometer. Tensile strength P was determined by the inclined plane method.

Cheng, following Rumpf, considers, Fig.2.9b, that the actual cleavage is an irregular line through the main plane of the break. The particles, as shown in the sketch below, though possessing an irregular surface nevertheless have mean diameters $d_j > d_i$. The mean surface separation is Z_o, dependent on the size of surface asperites. The origin of interparticle forces was not discussed beyond assuming that they were short range and a function of particle separation Z_o. From the theory, there develops,

$$Z_o = Z_o' - \frac{\bar{d}}{3}\,(\alpha_b/\alpha_b' - 1)$$

and

$$P = (abc)\left(\frac{1}{2}\,\frac{\bar{S}}{\bar{v}}\,\frac{\alpha_b}{\alpha_s}\right) f(Z_o)$$

where $f(Z_o)$ = interparticle force per unit contact area and (abc) = closely constant for one material.

The results of 25 tests on each of 5 different powders were compared with the above equation, with fair correlation.

The value of Z_o' was within order of magnitude agreement with known values for the average height of aspersites.

The writer considers that Cheng's treatment, as it becomes more fully developed, may prove to be an important synthesis. As yet it is not in a form that could be applied to the tensile strength of deposits in a precipitator, but future developments from this group of workers merits watching.

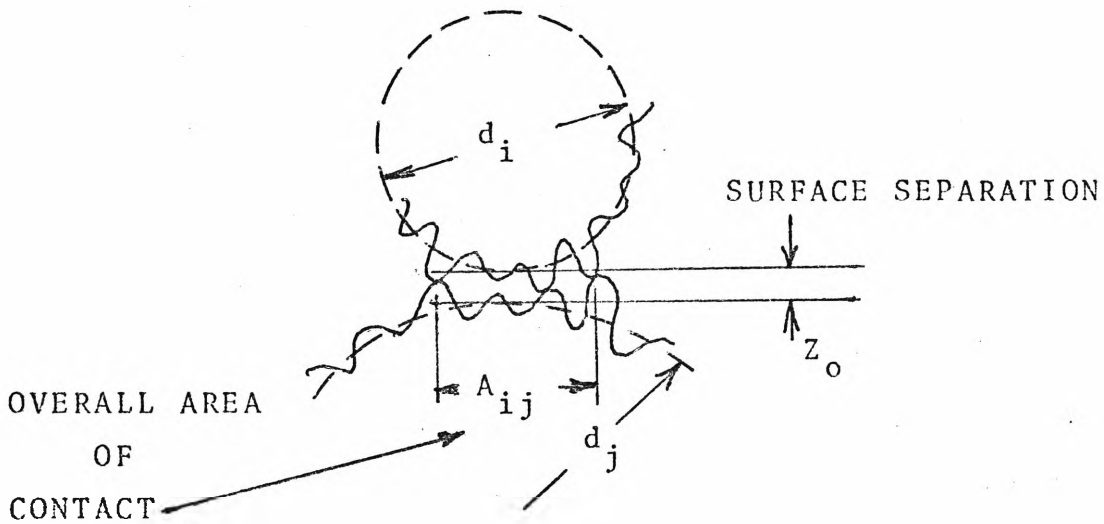

Appendix 4.1

Mechanical Development of the Micro Area Boundary Probe

The drawing of Fig.4.2 shows the mechanical layout.

(a) The basic casting was poured from an aluminium 96% and magnesium 4% alloy. Traces of titanium were added to improve the grain structure. Great care was taken in the construction of the pattern and sand mould to assure even cooling in the casting. In spite of these precautions, the casting was almost a failure, with chill indentations $\frac{3}{4}$" deep occurring in the principal face. These indentations were welded over in aluminium and the casting annealed at 350°C. The resultant casting was so imperfect that it could only be used as a chassis. The flat surface could not me machined up to a proper finish for corona studies. A further working surface was needed. The casting was machined to the best finish possible, and a sheet of bright finished stainless steel was glued on by means of epoxy resin. Pressures of 300 psi were applied to ensure flatness. Unfortunately, the sheet lifted due to failure of the epoxy to bond the stainless steel and aluminium surfaces together After attempting to effect a proper bond three times, the idea was abandoned.
A $\frac{3}{8}$" brass plate was screwed to the aluminium casting in 36 separate places. The screw holes were plugged with brass. The whole surface was ground to a flatness of 0.002" and to a surface finish of 15 μ inch. This was regarded as being the limit of capacity of a grinding wheel.

(b) The High Tension structure was deliberately built with the largest possible diameter of 26" P.C.D. so that

(b) cont.

disturbing surfaces would be as far away from the corona point as possible.

However, the large diameter resulted in lack of mechanical rigidity. A further stiffening ring was added and this stopped flexing of the legs. Teflon pads were provided at the base the legs so as to reduce friction. However, it was found that there was still enough friction to cause position errors due to flexing of the X-Y traversing system. The teflon pads were replaced with three different types of rollers. Although these were most effective in reducing friction, they all marked the surface of the polished brass and had to be abandoned. The teflon pads were finally adopted as the best compromise.

The verniers in the X and Y directions may be read to ±0.1 mm. However, owing to slight mechanical flexing of the system, the overall positioning accuracy is approximately:

x direction ±0.25 mm

y direction ±0.5 mm

In a single traverse, these accuracies are improved upon.

(c) Three micro conducting areas were inserted at 5 cm pitch, with the following dimensions -

	A	B	C
Hole dia.mm.	0.956	0.938	0.932
Conductor dia.mm.	0.860	0.867	0.863
area conductor $mm.^{+2}$	0.582	0.590	0.586

These three similar areas were mutually checked one against the other in terms of corona current density from a standard point. Before polishing the surface, such a comparison test showed 10% difference in current density as measured between the three areas. Extensive careful polishing brought this down to ± 2%. Precision, sturdy Swiss jewellers drills were used to drill the flat electrode surface. At a later stage, probes of 0.3mm dia were successfully inserted.

To reach this stage of development, a great amount of engineering effort was expended. It required the resources of the largest engineering workshop in Port Kembla and the skill of experienced instrument makers.

Appendix 4.2

Effects of Diffusion

Where conduction takes place by both drift and diffusion, then the governing equation becomes for a single carrier:

$$J = \rho KE + D \frac{\partial \rho}{\partial x}$$

where $\frac{\partial \rho}{\partial x}$ is the space charge density gradient. In many situations it is easy to check and show that the second term representing diffusion is negligible and that the conduction is essentially drift from the first term.

For example, in Appendix 1.1, the corona field calculations have been made considering drift only using mobility $K = 1.6\ cm^2\ sec^{-1}\ volt^{-1}$. Now an expression is there given for space charge density in cylindrical co-ordinates, viz

$$\rho = \frac{(I'/L)}{2\pi r K E}$$

If the gradient $\frac{d\rho}{dr}$ is found from this, and using a diffusion coefficient $D = .043\ cm^2\ sec^{-1}$ for ions in air at NTP, the contribution to current flow due to the diffusion term is found to be negligible*.

Using the approximate Einstein expression:

$$\frac{D}{K} = \frac{kT}{e}$$

where T is the absolute temperature, one can determine for such a gas when the diffusion term might stand to become significant.

Viewed a little differently, we may calculate $\bar{x}$, the average (rms) movement by diffusion of a single ion during its time of flight between the electrodes by means of the equation*:

$$\bar{x} = \sqrt{2D\tau}$$

where the time of flight for the configuration of Fig.6.1 is

---

* Ref.12 P.140

approximately;

$$\tau = \frac{4}{1.6 \times 3000} \simeq 1 \text{ m sec.}$$

Hence

$$\overline{x} \simeq \sqrt{1 \times 10^{-3} \times 2 \times .043} \simeq .01 \text{ cm}$$

This is negligible.

Appendix 4.3

Charge Amplifier for the Measurement of Transient Electric Field

Meek and Collins[101] have described how they measured transient electric fields on an electrode boundary. In conjunction with a comparatively large probe and fairly substantial fields they evidently found a good quality oscilloscope amplifier to be adequate.

The extremely small probes used in the present developments together with low fields rendered the best oscilloscope amplifier useless. Moreover the slightest movement in the connecting cable from probe to amplifier gave rise to unacceptable noise. After days of delay, a small vacuum pump in another part of the building was found to be a contributing culprit, in one instance of elusive noise.

Accordingly, a new approach was required to provide adequate charge integration without noise. A miniature solid state operational amplifier A with FET input which could be mounted right on the probe itself, was found. A high quality variable feedback capacitor C_b integrated the input currents in the usual manner. It was necessary to ascertain the effect of capacitance in the input connectors as follows.

Referring to the equivalent circuit shown in Fig.4.16 and applying transformed nodal analysis to the input of the amplifier;

if

$$i_i = \frac{d(A_o\sigma)}{dt} = A_o \frac{dD}{dt} = A_o\varepsilon_o \frac{dE'}{dt}$$

then

$$+i_i - \frac{e_i}{Z_i} + \frac{(e_o - e_i)}{Zb} = 0$$

where Z_i = total input impedance (principally capacitance).

Since

$$e_i = \frac{e_o}{A}$$

then

$$i_i = \frac{e_o}{A\ Z_i} + \frac{e_o}{A\ Z_b} - \frac{e_o}{Z_b}$$

$$= -\frac{e_o}{Z_b} + \frac{e_o}{A}\left[\frac{1}{Z_i} + \frac{1}{Z_b}\right] \qquad .....(4.15)$$

To first approximation the second term is small because A is large, so that:

$$e_o \simeq -Z_b i_i = -\frac{i_i}{S\ C_b}$$

and

$$e_o(t) = \frac{1}{C_b}\int i_i\ dt$$

$$= \frac{A_o \varepsilon_o E'}{C_b} \qquad .....(4.16)$$

and

$$e_o(t) = \frac{1}{C_b}\int A_o \varepsilon_o \frac{dE'}{dt}\ .\ dt$$

or

$$E'(t) = e_o(t)\ \frac{C_b}{A_o \varepsilon_o} \qquad .....(4.17)$$

This is the looked for result, namely that the transient electric field is proportional to the integrated displacement current.

We return to eq.4.15 to check the effect of input capacitance.

$$i_i = e_o S\ [C_b - \frac{C_i}{A} - \frac{C_b}{A}\ ]$$

Suppose $C_i = C_b$ and $A = 1000$

Hence

$$i_i = -e_o p\ [C_b - \frac{C_b}{1000} - \frac{C_b}{1000}\ ]$$

which indicates an error of .2% by comparison with eq.4.16 and 4.17.

In practice, since we have designed an amplifier to mount right on the probe, and $C_b \not< 20pf$, we expect that $C_i << C_b$.

We conclude that errors in eq.4.17 due to input capacitance and finite amplifier gain are less than 0.2%. The amplifier, in conjunction with advanced techniques for constructing precision probes, has provided us with extremely sensitive means of measuring transient electric fields.

As far as the writer can judge from subsequent published works, his measurement of electric field in the absence of ionic charge as described above has been taken an order of magnitude or two beyond (as to sensitivity and positional accuracy) that described by Meek, Collins, Stassinopoulos* et al.

---

* Stassinopoulos, C.A. Proc.IEE, 1968, 115, pp.1225-6.

Appendix 5.1

Capacitance and Electric Field around a Co-Planar Disc

In C4 and C5, the capacitance between the active probe surface and the earthed surround, emerged as being of key importance. Therefore independently of the experimental work, a mathematical examination of the electric field in the half-space surrounding the probe, was begun in three directions.

The first approach to the field configuration was an analogue one using conducting paper; the second was by mathematical analysis in both cylindrical and prolate spheroidal co-ordinates; the third a digital solution based upon iterative procedures with finite difference equations.

Meanwhile the very successful development of the three terminal probe whose active capacitance could be accurately and directly measured, mitigated the urgency of the mathematical approach. Accordingly, while the analysis was taken as far as possible, the digital solution was taken to a certain level and then adjourned meanwhile.

Analogue Field Representation

The results of this approach, strictly a two dimensional representation and presumably an approximation to the actual problem which has axial rotational symmetry, are seen in Fig.5.6. Here, the dimensionless ratio

$$(V_b/D_m)/E_o = .15$$

which, from such experimental results as those shown in Fig.4.12 would correspond to that bias voltage above which non-linearity develops.

Inspection of Fig.5.6 shows that at a height D_m above the probe, perturbation of the ambient electric field has become imperceptible.

We therefore conclude from this preliminary analogue study that biassing the probe within the limits of linearity leads to no significant distortion of the ambient electric field beyond a height of one probe diameter.

Mathematical Analysis

An intensive mathematical analysis of the axi-symmetric Laplacian electric field surrounding the probe was carried out by the writer and his Oxford colleague D. A. Spence who is a mathematician well known for his original contributions to boundary value problems. The writer in a letter to Spence defined the problem as follows:

24th June, 1969

"It would be very valuable, if as discussed verbally, you applied your expertise in boundary value potentials, to the probe described.

The new probe which we have developed over the past year, embodies a flat disc in a hole in an infinite plane. Given that in sketch (a):

$\phi(r,0) = 0$ for $r > b$

$\phi(r,0) = 1$ for $0 < r < a$

$\frac{\partial\phi(r,0)}{\partial z} = 0$ for $a<r<b$

We require

(i) Potential $\phi(r,z)$ for $z > 0$

(ii) The capacitance

$$C = \frac{\int_0^a (2\pi r) \cdot \frac{\partial\phi}{\partial z}(r,0).\, dr}{1}$$

(a) Model

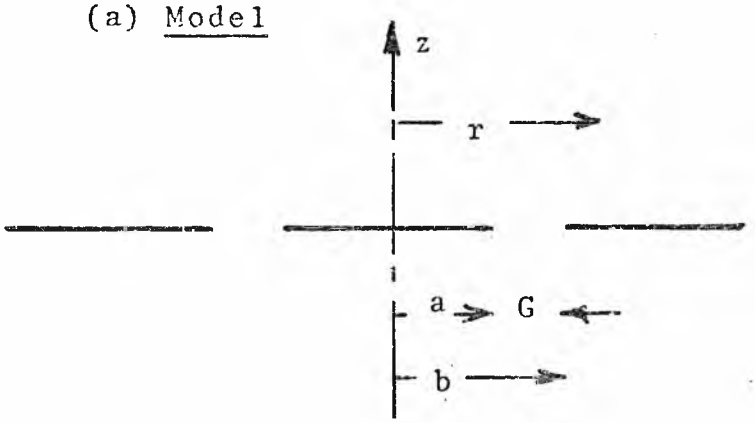

(b) Actual Probe

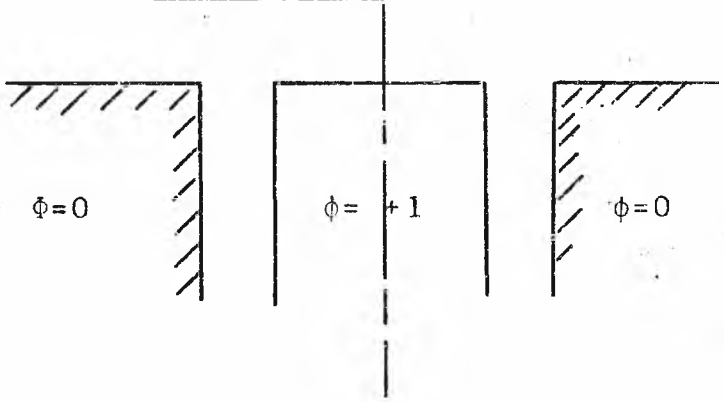

Yours sincerely,

O. J. T."

The model proposed for mathematical study by the writer was thus somewhat simpler than the actual probe. However, the field within the annular shank plays no part in the probe action. Accordingly, it was felt by the writer that the surface capacitance of the co-planar disc, for which mathematical difficulties appeared formidable enough anyway, gave promise of being an acceptable approximation, particularly if $G \to 0$.

Spence chose to express Laplace's equation in cylindrical co-ordinates; the writer considered oblate spheroidal co-ordinates were more promising, choosing to work in them. After several months work, the writer, had come within a hairs breadth of a proper solution containing an infinite series of Legendre functions of the second kind. Of the four boundary conditions, the writer was able to close three, but to his keen disappointment, the fourth could not be closed. His final solution was thus frustrated on the very last line.

Meanwhile to the immense gratification of all interested parties, Spence[104] succeeded in producing a final solution after applying several elegant transformations.

Spence's solution was quite general. However, he derived two important asymptotic simplifications viz:

for $\frac{a}{b} \to 1$:

$$C = 4a\left[-\tfrac{1}{2}\ell n\left(1-\frac{a^2}{b^2}\right) + \frac{1.0794}{3\ell n 2-1}\right]$$

for $\frac{a}{b} \to 0$:

$$C = 4a\left[1+\frac{4}{\pi^2}\,\frac{a}{b}\right]$$

A further outcome of the Spence derivation is that the capacitance of the three terminal probe of Fig.4.15 may also be determined, provided the gap between the probe

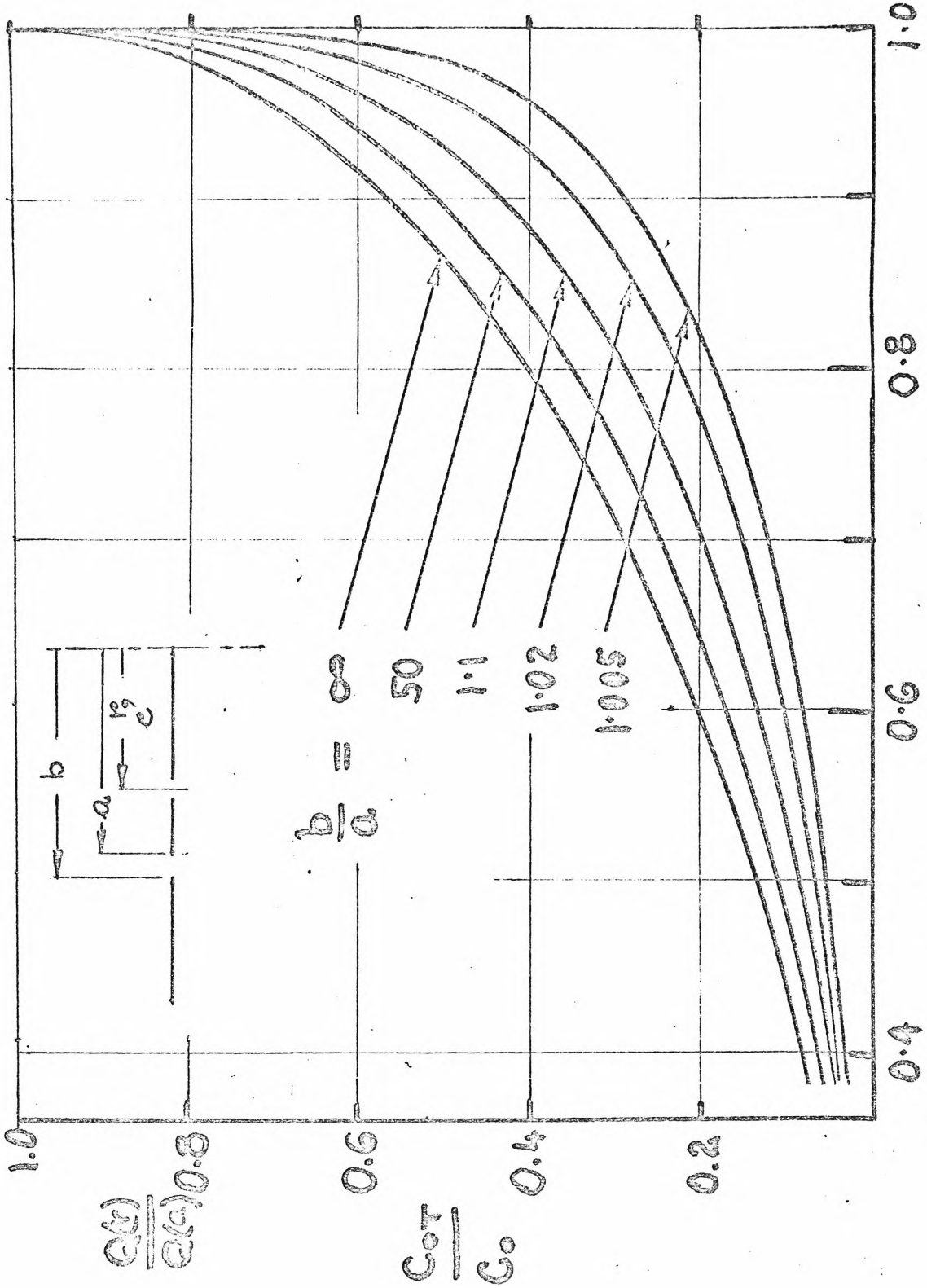

FIG. 5.7 CHARGE DISTRIBUTION ON AN ELECTRIFIED DISC (after Spence)

C_o = *Capacitance of total active face without screen, 0-a.*

C_{OT} = *three terminal capacitance of active face with screen*

and screen is small (which in practice it invariably is).

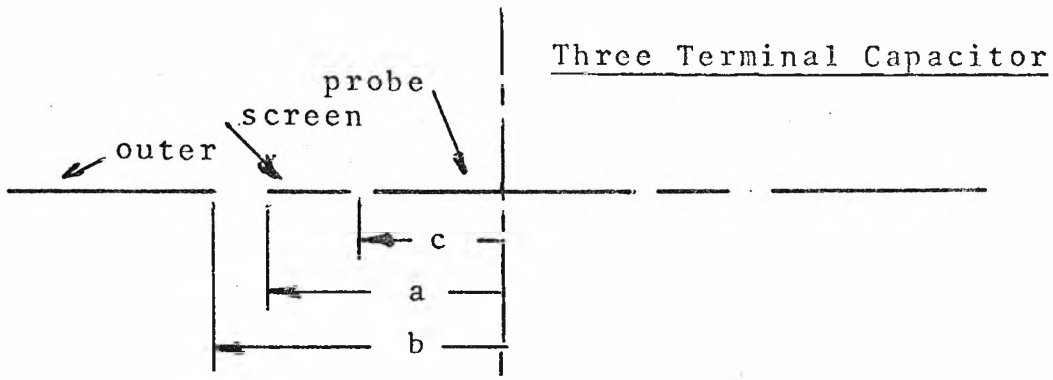

The dimensions now become:

c = radius to the mid-point of the gap between probe and screen.
≃ radius of active face of probe.
a = radius over the screen
b = radius of hole in the outer

The presence of the screen predictably lowers the capactiance of the active face in the fashion shown in the Fig.5.7 in which:

C_{oT} = three terminal capacitance
C_o = two terminal capacitance of the whole face.

For a typical probe in which

$$(b/a) = 1.02$$

and

$$c/a = 0.90,$$

the curves of Fig.5.7 disclose that:

$$C_{oT}/C_o = 0.35$$

Thus the shielding has reduced the active capacitance by 65%.

Altogether, the Spence analysis for the electrified co-planar disc has provided useful support for the experimental programme.

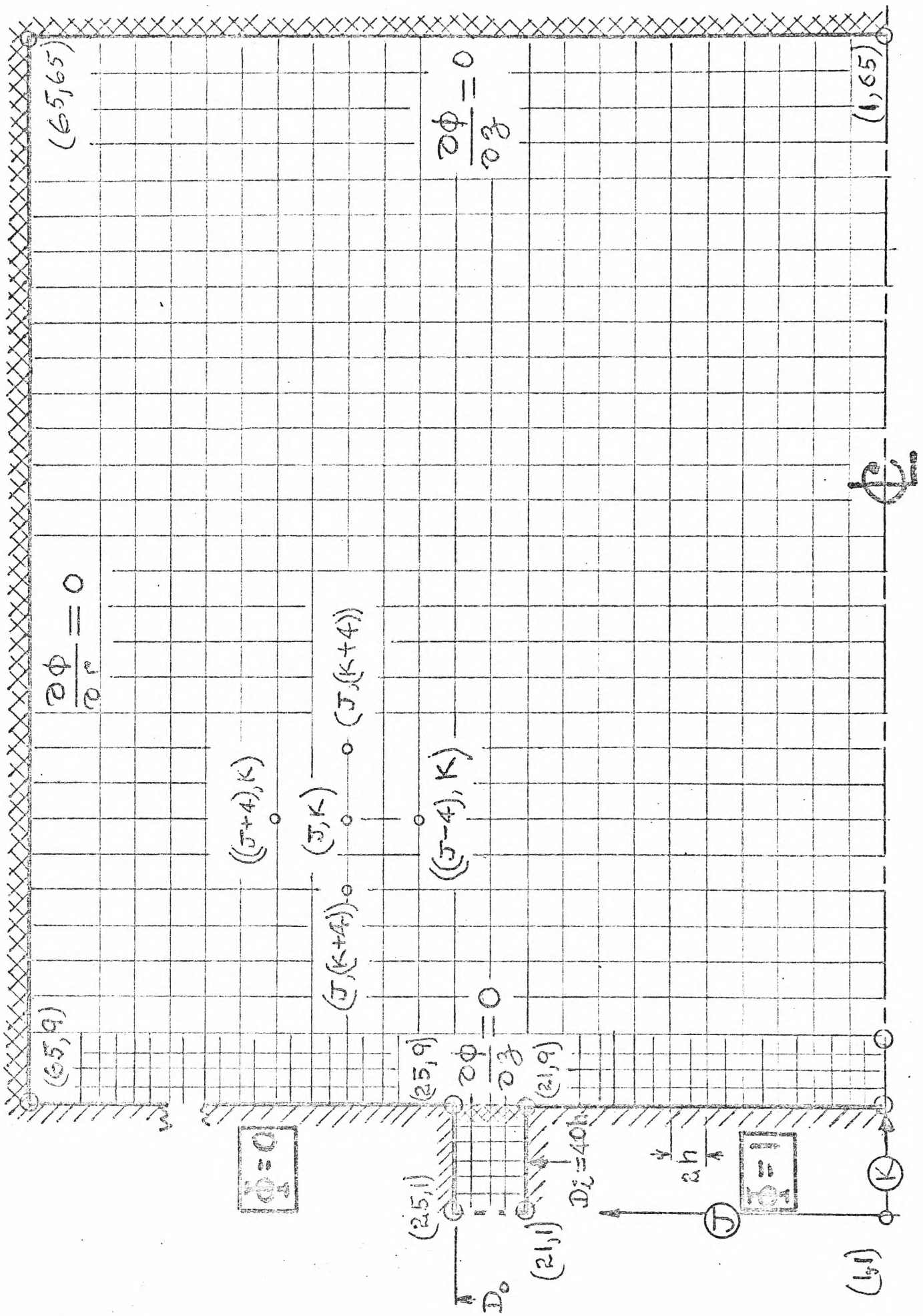

FIG. 5.8 DIGITAL SOLUTION OF PROBE FIELD

Half probe with two zero flux boundaries. $G/D_i = 0.1$
Mesh co-ordinates: $z = (J-1)h$; $r = (K-1)h$

Digital Computer Solution of the Field Problem (Preliminary)

The writer decided to commence a digital solution of the electric field around the probe. Though not a matter of immediate necessity, the writer believed that when finally developed, such a programme would enable a complete study of shank effects to be made, for which the Spence solution was inapplicable. Though not mandatory for the present dissertation, a preliminary programme appeared desirable.

The writer established a mesh system around the probe as shown in Fig.5.8 in which the axis of rotation is shown as being horizontal. In the case chosen for examination, the ratio of gap to diameter:

$$G/D_i = 0.1$$

By symmetry, a quarter space only was chosen. The area of examination was originally taken to be two probe diameters in the z direction and two in the r direction. It was soon found that if the boundaries were reduced to one probe diameter in the z direction and one in the r direction that no perceptible error in the surface capacitance was incurred.

The two arbitrary boundaries were established as zero flux boundaries in which:

$$\frac{\partial \phi}{\partial z} = 0 \quad \text{and} \quad \frac{\partial \phi}{\partial r} = 0$$

They thus became boundaries of tubes of flux, so that all positive flux leaving the central probe was constrained to return to the earthed plates. Such a procedure ensured that the capacitance found by integrating flux over the probe, i.e.:

$$\psi_{o\text{-}a} = {}^{+}\int_{o}^{a} \frac{\partial \phi(r,0)}{\partial z} (2\pi r)\, dr$$

would, on programme convergence, become equal to the flux entering the earthed plate, viz

$$\psi_{b-\infty} = -\int_{b}^{\infty} \frac{\partial\phi(r,0)}{\partial z}\,(2\pi r)\,dr$$

hence at programme convergence,

$$\psi_{oa} + \psi_{b\infty} = 0$$

The mesh points were indicated by J in the radial direction and by K in the z direction.

The Liebmann iterative procedure for the solution of the Laplace's equation was used. In rectangular co-ordinates the upgraded potential of point O at (J,K) is:

$$\phi_o = \tfrac{1}{4}[\phi(J,K-1) + \phi(J+1,K) + \phi(J,K+1) + \phi(J-1,K)]$$

which was of course adjusted for cylindrical co-ordinates in the actual programme.

Every point in the mesh, is scanned in a regular manner some scores of times until all potentials are sufficiently steady as indicated by the residues. Convergence proceeds asymptotically with the number of iterations, N. For a large number of mesh points, this process becomes prohibitively slow, so accelerating factors W were introduced which aimed to extrapolate the potential of a given mesh point to convergence. By such means the process is considerably speeded up.

A suitable flow diagram (with certain house-keeping operations omitted) is shown.

A print-out of an early elementary programme in Fortran, carried out on the Oxford University Computing Centre's KDF9 machine, is attached.

The test of convergence, namely that:

$$\psi_{oa} + \psi_{b\infty} = 0$$

was not quite met. However, it was clear that potentials were very nearly steady.

Accordingly the potential matrix was put onto a curve plotter, which produced the very interesting potential pattern shown in Fig.5.9. This is the field pattern, with some degree of accuracy, which was earlier postulated in Fig.4.5d.

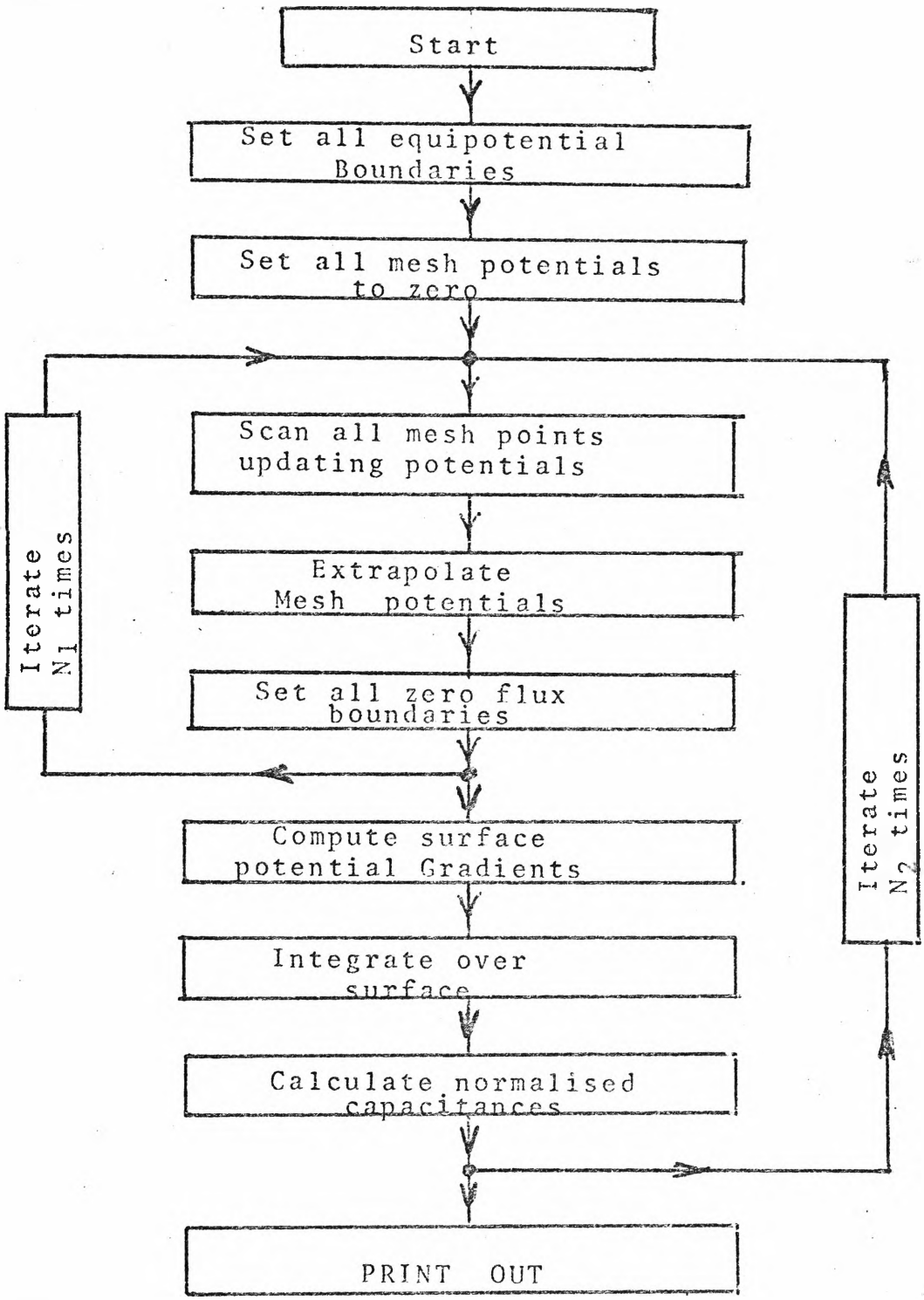

COMPUTER PROGRAMME FOR MESH POTENTIALS AND CAPACITANCE INTEGRALS

```
EGTRAN COMPILER        MAP, NO. 302        DATE    05/11/69        TIME
      DIMENSION POT(65,65),E(65),CA(5),DIA(21),POTA(5,65),C(64),
     1CAP(5,21),CAPN(5,21),ITERAT(5),CB(5),POTB(5,65)
C   SET ALL EQUIPOTENTIAL BOUNDARIES
      DO3J=1,21
      POT(J,9)=1.
    3 CONTINUE
      DO4J=25,65,1
      POT(J,9)=0.
    4 CONTINUE
      DO5K=1,9,1
      POT(21,K)=1.
    5 CONTINUE
      DO6K=1,9,1
      POT(25,K)=0.
    6 CONTINUE
C   SET ALL INITIAL VALUES TO ZERO
      DO50K=8,9,1
      DO51J=22,24,1
      POT(J,K)=0.
   51 CONTINUE
   50 CONTINUE
      DO10J=1,65,1
      DO11K=10,65,1
      POT(J,K)=0.
   11 CONTINUE
   10 CONTINUE
      DO1L=1,5,1
C   ITERATE AROUND WHOLE MESH 10 TIMES
      DO19M=1,10,1
      DO20J=22,24,1
      I=J-1
      K=9
  201 POT(J,9)=0.25*(POT(J,K+1)+POT(J,K-1)+(1.+0.5/I)*POT(J+1,K)+
     1(1.-0.5/I)*POT(J-1,K))
   20 CONTINUE
      DO22K=10,64,1
      DO21J=1,64,1
      IF(J-1)23,24,23
   24 POT(1,K)=1./6.*(POT(1,K-1)+POT(1,K+1)+4.*POT(2,K))
      GO TO 21
   23 I=J-1
      POT(J,K)=0.25*(POT(J,K+1)+POT(J,K-1)+(1.+0.5/I)*POT(J+1,K)+
     1(1.-0.5/I)*POT(J-1,K))
   21 CONTINUE
   22 CONTINUE
C    SET ZERO FLUX BOUNDARIES
      DO62J=22,24,1
      POT(J,8)=POT(J,10)
   62 CONTINUE
      DO7K=10,64,1
      POT(65,K)=POT(63,K)
    7 CONTINUE
      DO8J=1,65,1
      POT(J,65)=POT(J,63)
      POTA(L,J)=POT(J,10)
      POTB(L,J)=POT(J,60)
    8 CONTINUE
   19 CONTINUE
C     FIELD STRENGTH OVER SURFACES
      DO25J=1,21,1
      E(J)=(1.-POT(J,10))*40.
   25    CONTINUE
      DO26J=25,65,1
      E(J)=(-40.)*POT(J,10)
```

```
      7 CONTINUE
        DO8J=1,65,1
        POT(J,65)=POT(J,63)
        POTA(L,J)=POT(J,10)
        POTB(L,J)=POT(J,60)
      8 CONTINUE
     19 CONTINUE
C      FIELD STRENGTH OVER SURFACES
        DO25J=1,21,1
        E(J)=(1.-POT(J,10))*40.
     25    CONTINUE
        DO26J=25,65,1
        E(J)=(-40.)*POT(J,10)
     26 CONTINUE
C      CAPACITANCE SURFACE INTEGRALS
        CA(L)=0.
        DO27J=2,21,1
        C(J)=3.1416*.025*.025*(J-1.5)*(E(J)+E(J-1))
        CA(L)=CA(L)+C(J)
        CAP(L,J)=CA(L)
     27 CONTINUE
        CB(L)=0.
        DO28J=26,64,1
        C(J)=3.1416*.025*.025*(J-1.5)*(E(J)+E(J-1))
        CB(L)=CB(L)+C(J)
     28 CONTINUE
C      NORMALISED CAPACITANCE
        DO29J=5,21,4
        CAPN(L,J)=CAP(L,J)/CAP(L,21)
     29 CONTINUE
        ITERAT(L)=10*L
      1 CONTINUE
        DO30J=5,21,4
        DIA(J)=(J-1)*.05
     30 CONTINUE
        PRINT(3,100)
    100 FORMAT(1H1,///,22H          POTENTIAL MATRIX)
        PRINT(3,101)(ITERAT(L),L=1,5 ),(ITERAT(L),L=1,5)
    101 FORMAT(///,1I20,9I12)
        DO104J=1,65
        PRINT(3,103)J,(POTA(L,J),L=1,5),(POTB(L,J),L=1,5)
    103 FORMAT(///,I12,10X,10F12.4)
    104 CONTINUE
        PRINT(3,102)
    102 FORMAT(1H1,///,39H                CAPACITANCE SURFACE INTEGRALS)
        PRINT(3,108)(CA(L),L=1,5)
    108 FORMAT(//,1F24.4,4F12.4)
        PRINT(3,105)(CB(L),L=1,5)
    105 FORMAT(//,1F24.4,4F12.4)
        PRINT(3,106)(DIA(J),(CAPN(L,J),L=1,5),J=5,21,4)
    106 FORMAT(/////////,6F12.4)
        CALL EXIT
        END
```

REFERENCE TABLES

0	00000/0	3	00004/4	4	00012/5
51	00041/3	50	00044/1	11	00054/5
20	00107/0	23	00125/5	24	00115/2
62	00157/2	7	00167/0	8	00204/5
26	00226/0	27	00250/2	28	00266/4
30	00316/1	100	00322/4	101	00340/5
102	00370/4	108	00400/3	105	00410/2

```
      ROUTINE COMPILED
      TIME  LESS THAN 11 SECS
      NUMBER OF INSTRUCTION WORDS 281
```

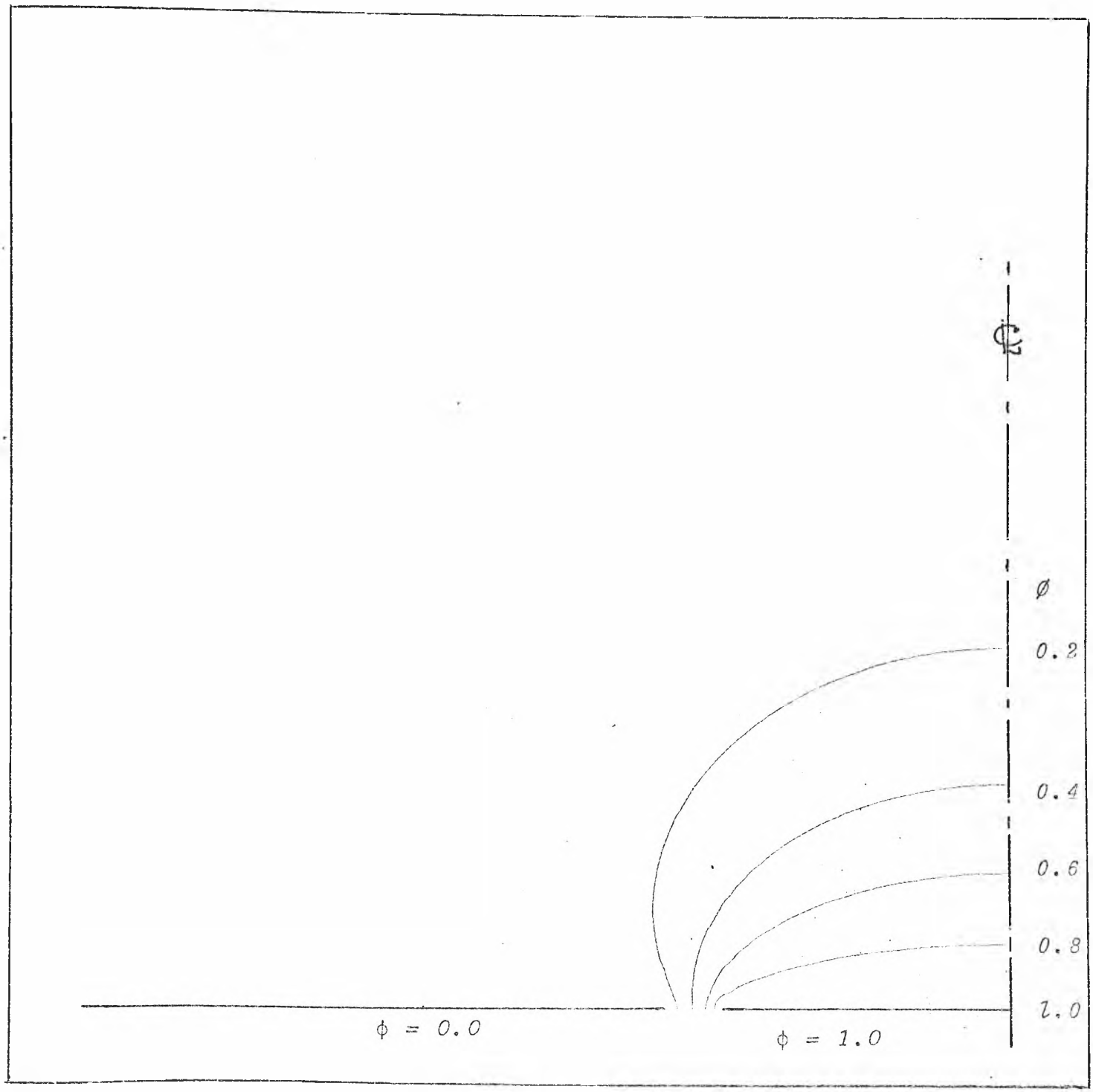

FIG. 5.9 DIGITAL SOLUTION OF POTENTIAL PATTERN

A curve tracer, programmed to draw equipotentials, draws the potential system around a biassed probe. This result compares with Fig.4.5d.

CHAPTER 11

REFERENCES

11. REFERENCES

1. WHITE, H.J. 'Industrial Electrostatic Precipitation' Addison-Wesley, 1963, 1st edition. p.26
2. ROSE, H.E. and WOOD, A.J. 'An introduction to Electrostatic Precipitation in Theory and Practice' Constable & Co. Ltd, 1966, 2nd edition.
3. TOWNSEND, J.S. 'Electricity in Gases' Oxford, Clarendon, 1915, pp.260-336
4. WHITE, H. Ibid. pp.89-109
5. *TASSICKER, O.J. 'Experiences with an Electrostatic Precipitation Analyser' Proc. of International Clean Air Conference, May 1972, Melbourne University, Proc.P.88
6. HENRY, B. M.Sc. Thesis 'A Study of the Effect of Process Variables upon Electrostatic Precipitator Performance' Uni. of New South Wales, 1967, p.82
7. BOYLETT, F.D.A. and LOOMS, J.S.T. 'Effect of Discharge Products upon Corona Discharge and Spark Breakdown Voltage' Proc.I.E.E., Dec.1963, Vol.110, No.12 p.2292
8. MILLER, C.G. and LOEB, L.B. 'Positive Coaxial Cylindrical Corona in Pure N_2, O_2 and Mixtures Thereof'. Jnl.App.Phys. April 1951, Vol.22 No.4, p.494
9. MILLER, C.G. and LOEB, L.B. 'Negative Coaxial Corona Discharges in pure N_2, O_2 and Mixtures Thereof' Jn. App. Phys., May 1951, Vol.22 No.5, p.614
10. SHALE, C.C. 'Electrostatic Precipitation at High Temperatures and Pressure', Bureau of Mines Report (U.S.A.), 1964.
11. PAUTHENIER, M. and MOREAU-HANOT, M. 'La Charge Des Particules Sphériques Dans Un Champ Ionisé' Jnl. Phys. et Radium, 1932, Vol.3 No.7, p.591
12. COOPERMAN, P. 'A Theory for Space-Charge limited currents with Application to Electrical Precipitation' Trans. A.I.E.E. 1960, vol.79 p.47

---

* References so marked are appended in the Thesis

13. LOEB, L.B. 'Electrical Coronas', Univ. of Calif. press, 1965, P.45
14. BOOTH, Phys.Rev., 1917, Vol.10 p.266
15. PENNEY, G.W. and MATICK, R.E. 'Potentials in D.C. Corona Fields' AIEE Trans.Comm. & Elect. May 1960, P.91
16. COOPERMAN, P., 'A New Technique for the Measurement of Corona Field Strength and Current Density in Electrical Precipitation' AIEE Trans., 1956, Vol.75 p.64
17. LAGARIAS, J.S., 'Field Strength Measurement in Parallel Plate Precipitators', Trans.AIEE, 1959, Vol.78, p.427
18. GOSHO, YASUSHICHI, 'Measurement of Potential Distribution across Discharge Gap by Electrostatic Probe Method' SCI. papers, I.P.C.R. (English), 1967, Vol.61, No.3, p.61.
19. ROSE and WOOD, Ibid, p.49
20. ROHMANN, H., 'Messung der Grösse von Schwebeteilchen' Z. Phys., 1923, Vol.17 pp.253-65
21. WHITE, H.J., 'Particle Charging in Electrostatic Precipitation' AIEE Trans., 1951, Vol.70, p.1189
22. MOON, P. and SPENCER, D.E. , 'Field Theory for Engineers' Van Nostrand, Princeton, 1961, 1st edition, p.225
23. ARENDT, P. and Kallman, H., 'The Mechanism of Charging Mist Particles', Zeitschr,f. Phys., 1925/6, Vol.35 p.421
24. MURPHY, A.T., ADLER, F.T., PENNEY, G.W. 'A theoretical Analysis of the Effects of an Electric Field on Charging of Fine Particles' AIEE Trans., 1959, Paper 59-102 p.318
25. PENNEY, G.W. and LYNCH, R.D., 'Measurements of Charge Imparted to Fine Particles by a Corona Discharge' AIEE Trans., 1957, Vol.76, p.294
26. HIGNETT, E.T., 'Particle Charge Magnitudes in Electrostatic Precipitation', Proc. IEE, 1967, Vol.114, No.9, p.1325

27. COCHET, R. "Lois de Charge des Fines Particules Etudes Théoretiques - Controles Réchents Spectre de Particles" Colloque International - La Physique des Forces Electrostatiques et Leurs Applications Grenoble, 1961.

28. LOWE, H.J. and LUCAS, D.H., "The Physics of Electrostatic Precipitation", Brit.Jnl. App.Phys., 1953, Supp.2, p.40.

29. PAUTHENIER, M., "The Charging of Spherical Conducting Particles in a Bi-ionised Electric Field", Colloque Internationaux du Centre National de la Recherche Scientifique; Grenoble, 1961.

30. SATO, Y, "Measurement of Space Potential and Density of Space Charge in d.c. Corona Discharge" JIEE of Japan, 1933, 53, 182-200.

31. OGLESBY, S. and NICHOLS, G., "A Manual of Electrostatic Precipitator Technology Part 1 Fundamentals [for NAPCA] Southern Research Institute, Alabama, Aug.1970, p.69.

32. SEMAN, G.W. and PENNEY, G.W., "Photographic Studies of Particle Behaviour under Varying Precipitator Conditions" Trans. IEEE, 1967, Vol.PAS-86, No.3, p.365.

33. ROSE, H.E. and WOOD, A.J., ibid, pp.90-96.

34. PAUTHENIER, M., DEMON, L. and VARSHNEY, M.P. La Tech. Mod. 1953, Vol.45, p.245.

35. HIGNETT, E.T., "Particle Charging in Electrostatic Precipitation", IEE Colloquium on Electrostatic Precipitation (London), Feb.1965.

36. DEUTSCH, W. Ann. Phys. [Leipzing], 1922, Vol.4, No.68 pp.335-44.

37. WHITE, H.J., "Modern Electrical Precipitation" Industrial and Engineering Chemistry, 1955, Vol.47, p.932.

38. ROBINSON, M., "Movement of Air in the Electric Wind of the Corona Discharge", Trans.AIEE 1961, Vol.80, part 1, P.143.

39. ROBINSON, M. "Turbulence in Electrostatic Precipitators" Minerals Processing, May 1968, P.13.

40. INYUSHKIN, N.V. and YA.D.AVERBUKH, "Dust Precipitation from a turbulent Gas Stream in an Electrostatic Precipitator", Izv.Vyssihikh Uchebn.Zavedenii Khim.i. Khim.Tekhnol, 1963, Vol.6, pp.1031-1036.

41. PENNEY, G.W., SEMAN, G.W., and PROBST, R.E. , "Some Effects of large Particles in Electrostatic Precipitation" IEEE Int.Convent. Record, Part 4, 1964, pp.164-167.

42. WHITE, H.J. "Industrial Electrostatic Precipitation" Addison-Wesley, 1963, 1st ed., P.331.

43. TROOST, N., "A New Approach to the Theory and Operation of Electrostatic Precipitators for use on P.F. Fired Boilers", Proc.IEE, 1954, Vol.101 part 2, p.369.

44. WHITE, H.J., Ibid. pp.172-176.

45. ALLANDER, C. and MATTS, S., Staub, 1957, Heft 52, p.171

46. ROSE, H.E., "The Measurement of Particle Size in Find Powders", Constable & Co., London (Book).

47. LANG, H.R. (Editor) "The Physics of Particle Size Analysis", Brit. Jnl. App. Phys. Supplement No.3, 1954.

48. ELLISON, J.M. "Light Scattering by Polydisperse Dust Clouds", Brit.Jnl.App.Phys. Supplement No.3, 1954,p.66.

49. DAVIDSON, I.M. and WHITTET, D.R., Engineer, Part 2, 1953, Vol.196, p.211.

50. WATSON, K.S. and BLECHER, K.J. "Further Investigation of Electrostatic Precipitators for Large Pulverised Fuel Fired Boilers", Proc. Clean Air Conference, Sydney, Aust. and N.Z. Clean Air Soc. Aug.1965, paper 10.

51. PENNEY, G.W., "Electrostatic Precipitation of High Resistivity Dust", AIEE Technical paper 51-201, 1951.

52. WHITE, H.J. ibid, p.294.

53. DURIE, R.A. and POTTER, E.C., "Factors Influencing the Efficient Operation of Electrostatic Precipitators for Pulverised-fuel Ash", Australian Chem.Proc and Eng. Sept.1970, p.18.

54. PENNEY, G.W. and HEWITT, J.G., "Some Measurements of Abnormal Corona", AIEE Electronics Trans. July 1958,P.319

55. PAUTHENIER, m., "Back Corona in Electrical Precipitators" Compt.Rend., 1946, Vol.244, pp.1219-20.

56. HERCEG, Z. "Electrical Characteristics of Contaminated Corona Systems" 1970, Doctoral Dissertation, Univ. of New South Wales.

57. PAUTHENIER, M., DUPUY, J, and TRAN AN NHAN; "The Coaxial Cylindrical Electric Field in the Presence of Back Corona", Compt.Rend. 1558, Vol.246, pp.1394-6.

58. WHITE, H.J. ibid, p.150

59. LAKEY, J.R.A. and BOSTOCK, W., "Researches into Factors Affecting Electro-precipitation", Trans.Instn.Chem Engrs, 1955, Vol.33, p.252.

60. BUSBEY, H.G.T. and DARBY, K. "Efficiency of Electrostatic Precipitators as Affected by the Properties and Combustion of Coal". Jour.Inst.Fuel., 1963,Vol.36 p.184.

61. TASSICKER, O.J., HERCEG, Z., MCLEAN, K. "Electrical Resistivity of Fly-Ash from Bayswater and Newvale Coals" No.11 Bulletin, The Wollongong University College, Univ. of New South Wales, 1966.

62. WHITE, ibid, p.309

63. BAXTER, W.A., "Recent Electrostatic Precipitator Experience with Ammonia Conditioning of Power Boiler flue Gas", Jnl. Air Pollution Cntrl. Assn, Dec.1968, Vol.18 No.12, p.817

64. PAUTHENIER, M.M. et MOREAU-HANOT, M., "Etouffement de la Décharge Couronne en Milieu Trouble". Jour. Physique et de Radium, 1935, Vol.6, No.7.

65. BALABANOV, Ye. M., "Particle Charge in the Electric Field of Corona Discharge in very dusty media" Elektrichestvo, 1965, Vol.2, No.57-61, pp.109-121.

66. PROBST, R.E. and PENNEY, G.W., "Some Effects of Particle Size on the Adhesion of Electrostatically Deposited Dust", AIEE Conference Paper, Jan.1963.

67. PROCHAZKA, R., 'Kontinuierliche Staubmessung an Arbeitsplätzen und Industrie anlagen/ (Archiv für Eisenhuttenwesen, June 1968, Vol.39, p.439.

68. PLATO, H., "Über das Klopfen von Niederschlagsplatten im Elektrofilter", Staub-Reinhalt, Luft, Aug.69, Vol.29, P.321.

69. RUCKELSHAUSEN, K., "Removal of Deposits by Vibration"; Doctoral Dissertation, Technischen Hochschule, Stuttgart, No. DK-68511 Giese-Druck, Kg Offenbach/M 1957.

70. SPROULL, W.T., "Fundamentals of Electrode Rapping in Industrial Electrical Precipitators", Jnl. Air Polltn. Cont. Ass., Feb. 1965, Vol.15, No.2, pp.50-55.

71. BRANDT, H., "Der Entwicklungsstand de Electrostatischen Staubabscheider Unter Besonderer Berücksichtigung der Abreinigungsprobleme" Staub, Sept.1961, Vol.21, pp.392-7

72. DZYALOSHINSKII, I., LIFSHITZ, E.M., and PITAEVSKII, L.P. Advan. Phys., 1961, Vol.10, p.165.

73. McLEAN, K.J., "Electrical Conduction in High Resistivity Particulate Solids", Doctoral Dissertation, Uni. of New South Wales, Dec.1969, p.34.

74. SPROULL, W.T., "Minimising Rapping Loss in Precipitators at a 2,000 MW Coal fired power station" Air. Poiln. Control Assn. New Jersey, June/July, 1971.

75. SPROULL, W.T. and NAKADA, Y., "Operation of Cottrell Precipitators", Ind. and Eng. Chem, 1951, Vol.43, No.6, p.1350.

76. *TASSICKER, O.J., HERCEG, Z. and McLEAN, K.J. " A new Method and apparatus to assist the prediction of electrostatic precipitator performance" Trans. I.E. Aust. Sept. 1969, Page 277.

77. FRÖHLICH, H., "Theory of Dielectrics (book), Clarendon Press, Oxford, 1958, 2nd edition,

78. MURPHY, E.L. and GOOD, R. H., Phys. Rev. 1956, Vol.102 Page 1464.

79. LYMAN, E.M. et al, Co-ordinated Science Laboratory Progress Report, Uni. of Illinois, 1962, p.72.

80. KRUPP, H. "Particle Adhesion, Theory and Experiment" Advan. Colloid. Interface Sci., 1967, Vol.1, p.111-239.

81. PENNEY, G.W. and KLINGLER, E.H. "Contact potentials and the adhesion of dust", AIEE Trans., 1962, Vol.81(1) p.200-204.

82. LANDAU, L.D., LIFSHITZ, E.M., "Electrodynamics of Continuous Media", Pergamon, Oxford, 1960, 1st ed.

83. BRADLEY, R.S., Phil. Mag. and Trans. Faraday. Soc.,1932 & 1936, 13th & 32nd ed. pp. 853 and 1088.

84. HAMAKER, H.C., "The London-Van Der Waals Attraction between spherical particles". Physica, 1937, Vol.4, p.1058.

85. KRUPP, H. and SPERLING, G., "Theory of Adhesion of Small Particles", Journ. Appl. Phys., Oct. 1966, Vol.37, No. 11, p.4176.

86. BEISCHER, D., KOll.Zeits, 1939, Vol.89, p.215

87. BOHME, G., KRUPP, H., RABENHORST, H., SANDSTEDE, G. "Adhesion Measurements Involving Small Particles", Trans. Instn. Chem. Engrs., 1962, Vol.40, p.252.

88. JORDAN, D.W., "The Adhesion of Dust Particles", Physics of particle size analysis supplement No.5, Brit. Journ. App. Phys., 1954, p.5194.

89. ASHTON, M.D., CHENG, D.C.-H, FARLEY, R., VALENTIN, F.H.H. "Some investigations into the strength and flow properties of powders", Rheol. ACTA., 1965, Vol.4, p.206

90. FOWLER, R.T., and RADFORD, C.D. "Preliminary studies into the cohesion of granular particles", Mechan. and Chem. Trans. Inst. Eng. Aust., 1965, MC1, p.129.

91. JENIKE, A.W., ELSEY, P.J., and WOOLLEY, R.H. "Flow Properties of bulk solids", Proc. Am. Soc. Test Mats. 1960, Vol.60. P.1168.

92. ASHTON, M.D., FARLEY, R., VALENTIN, F.H.H. "An improved apparatus for measuring the strength of powders" J. Sci. Instruments, 1964, Vol.41, P.763

93. CHENG, D.C.-H, "The tensile strength of powders", Chem. Eng. Sci., 1968, Vol.23, p.1405

94. FARLEY, R., VALENTIN, F.H.H., "Effect of particle size upon the strength of powders", Powder Technol. (Elsevier) 1967/8, Vol.1, p.344-54

95. SMILGA, V.P., DERYAGIN, B.V., Dohl. Akad. Nauk, SSSR, 1958, Vol. 122, p.1049

96. SHAPIRO, I., KOLTSHOFF, I.M., "Studies on the ageing of precipitates and co-precipitates", J. Phys. Coll. Chem. 1948, Vol.52, p.1020

97. McFARLANE, J.S., & TABOR, D., "Adhesion of Solids and the effect of surface films", Proc. Roy. Soc., 1950, Vol. A202, p.224.

98. EISNER, H.S., FOGG, G., TAYLOR, T.W., "Cohesion of Powders and the Effect of Atmospheric Moisture", Int. Cong. Surface Activity (3rd), 1960, Sect. B, p.378.

99. RUMPF, H., "Strength of Granules and agglomerates",in Knepper, W.A. (Ed.), 'Agglomeration' Interscience, 1962. p.379.

100. BRADLEY, R.S., "Polymolecular Adsorbed Films Part II, The general theory of the condensation of vapours on finely divided solids", J.Chem. Soc., 1936, Vol.11, p.1799

101. MEEK, J.M., and COLLINS, M.M.C., "Measurement of electric fields at electrode surfaces", Electron. Lett., 1965, 1, pp.110-111.

102. WATERS, R.T., RICKARD, T.E.S., and STARK, W.B. "Electric field and current density in the impulse corona discharge in a rod/plane gap", Proc. Roy. Soc., 1968, A304, pp.187-210.

103.*TASSICKER, O.J., "Measurement of corona current density at an electrode boundary", Electron. Lett., 1969, 5 pp.285-286.

104. SPENCE, D.A., "A Wiener-Hopf solution to the triple integral equations for the electrified disk in a coplanar gap", Proc. Camb. Phil. Soc. (1970), 68, p.529

105. PEEK, F.W., "Dielectric phenomena in high voltage engineering", 3rd ed., N.Y., McGraw Hill, 1929, p.64.

106. COBINE, D.C., "Gaseous conductors", Dover, 1958, p.38

107. von ENGEL, A., "Ionised gases", 2nd ed., O.U.P. 1965 p.119

108. THOMPSON, A.M. and LAMPARD, D.G., "A new theorem in electrostatics and its application to Calculable standards of capacitance", Nature, 1956, Vol.177, p.888

109. RAYNER, G.H. and FORD, L.H., "Improvements in the Precision Measurement of Capacitance", Proc. I.E.E., Mar. 1960, Vol. B, No. 32, p.185

110. ROGAL, B., "Recent Advances in Three Terminal Bridge Techniques", Proc. Inst. Electronics, 15th Annual convention Vol. 4, No. 2

111. THOMPSON, A.M., "The Precise Measurement of small capacitances", Trans. I.R.E., Dec.1958, Vol.1-7, No. 3, p.245.

112. COBINE, D.C. "Gaseous Conductors", Dover (book), 1958, p.202

113. von ENGEL, A.E., "Ionised Gases", Oxford/Clarendon, (book), 1965, p.139-154.

114. ROSE, H.E. and WOOD, A.J., "Electrostatic Precipitation" (book), Constable, 2nd ed. 1966, p.108

115. SCHEIDEL, C. and EISHOLD, H., "A contribution to the theory of Flue Dust Removal in the Electro-Precipitator" Lurgi (Home Publication), Oct. 1960, Vol. BP 17/I.O.e.R.

116. *TASSICKER, O.J., "The Temperature and Frequency Dependence of the Dielectric Constant of Power Station Fly Ash", Staub-Reinholt. Luft (English version), Aug. 1971, Vol.31, No.8, p.23.

CHAPTER 12

REPRINTS OF SOME REFERENCES.

EXPERIENCES WITH AN ELECTROSTATIC PRECIPITATION ANALYSER IN THE EVALUATION OF DIFFICULT DUSTS

PROCEEDINGS INTERNATIONAL CLEAN AIR CONFERENCE
Melbourne, Australia. May 1972

Owen J. Tassicker

Wollongong University College, The University of New South Wales.

An Electrostatic Precipitator Analyser has been used to conduct in-site measurements at a pulverised coal fired power station. The ash from this low sulphur coal, regarded as being one of the most difficult to collect in Eastern Australia, was subject to both ammonia and sulphuric acid conditioning.

The analyser simultaneously measured both dust electrical resistivity and flue gas corona properties while efficiency tests on the main plant were in progress. With unconditioned dust, the apparatus showed the rapid development of severe back corona with predictable degeneration of performance in the main plant. With acid conditioning, there was a slight reduction in back corona, while with ammonia conditioning there was a modest reduction in back corona. The analyser indicated that performance in the main plant would show slight improvement in efficiency with acid conditioning, and some improvement with ammonia conditioning.

Simultaneous collection efficiency measurements on the main plant disclosed effective migration velocities of 2-3 cm/sec for unconditioned dust, 4 cm/sec with acid conditioning and 5-6 cm/sec with ammonia conditioning.

The present results harmonise with pilot precipitator tests and main plant tests carried out over the past ten years at Tallawarra Power Station.

1. INTRODUCTION

Modern electrostatic precipitators are capable of extracting solid particles from large volumes of hot gases with efficiencies exceeding 99%. If, however, the particles to be collected are of high electrical resistivity (such as fly ash produced from the firing of low sulphur coals) otherwise well-designed plant may suffer a drastic fall in efficiency.

When electrodes are coated with high resistivity particles, the whole of the applied voltage/corona current characteristic changes markedly. Contrary to what commonsense would suggest, the currents actually become very much larger while the maximum applied voltage falls, due to a phenomenon of back ionisation. The dust on the formerly passive receiving electrode glows with bright spots which emit positive ions. Since there is some applied voltage and a large current flowing, the precipitator gives the illusion of being healthy. The dense stack emission however, leaves no doubt about a malfunctioning plant.

Where the trouble has been identified as being back corona due to high resistivity dust, a number of ameliorative measures may be taken. The temperature in the precipitator, the water content in the flue gas, and trace conditioning agents added to the flue gas all have an effect on particle resistivity Proper adjustment of these parameters may reduce resistivity and improve plant performance.

It cannot be too strongly emphasised that it is the chemical composition and the resulting electrical properties of both the gas and the dust which determine the precipitator performance. When conditioning agents are added to the flue gas, it is important to be able to distinguish between the resulting changes in both flue gas and dust characteristics.

2. AN ELECTROSTATIC PRECIPITATOR ANALYSER

The apparatus depicted in Fig. 1., known as the

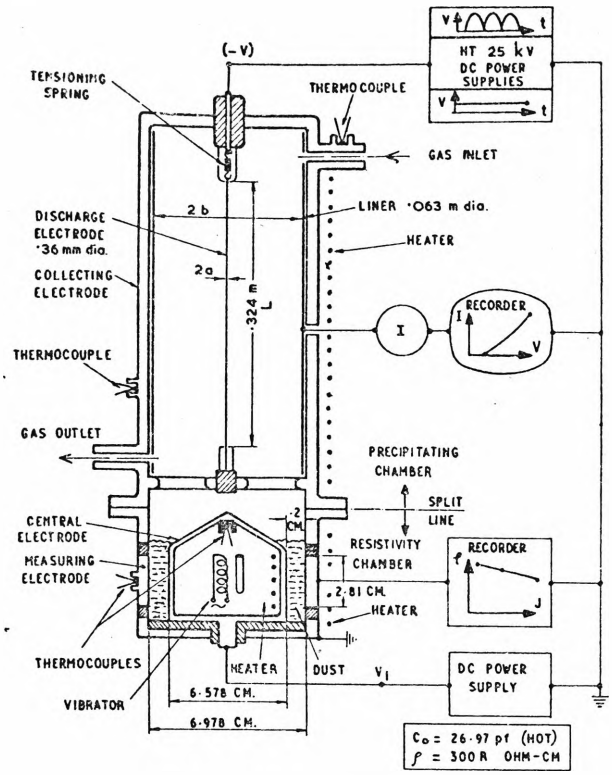

Fig. 1. Kevatron Electrostatic Precipitator Analyser.

Gas to be examined enters the inlet to the precipitator stage where particulates are removed with high efficiency. After rapping, deposit drops into the lower chamber, where after compaction, resistivity is measured.
In this instrument, (2a) = 0.35mm; (2b) = 6.3cm; L = 0.36m.
In regular instruments, (2a) = 0.70mm; (2b) = 6.3cm. L = 0.324m.

Kevatron Electrostatic Precipitation Analyser, is designed to measure those electrical properties of dusts and flue gases which are important to the operation of a precipitator. Since it is described more fully elsewhere[1], a brief description follows.

Dusty gas drawn isokinetically from the main duct into the precipitating chamber is ionised there by the intense electric field established by the discharge electrode. Particles entrained in the gas stream are precipitated onto the receiving electrode with high efficiency.

Since both dust and gas properties are highly sensitive to temperature, close thermal control of the whole apparatus is exercised.

The corona-current applied voltage characteristic is readily measured by taking meter readings of V and I. Corona onset potential V_o is accurately observed from the oscilloscope. The clean electrode (as distinct from contaminated) corona characteristic is readily determined by placing a filter at the gas inlet to remove solid particles.

The lower chamber measures dust resistivity. On rapping the upper chamber, the dislodged dust falls into the annular space where it is compacted by means of a vibrator. Stepped voltages applied to the central electrode cause small currents to flow which are then conditioned by an operational amplifier.

Resistivity is displayed on a light spot recorder.

The apparatus is in two main parts, comprising the measuring chambers and the control console, interconnected by quick release couplings.

3. POWER STATION PRECIPITATORS AT TALLAWARRA

Two precipitators in parallel treat the gas from a 100 MW boiler installation. Each precipitator has three zones; inlet, centre and outlet, each with separate energisation.

4. COAL AND ASH CHARACTERISTICS

Coal from the Wongiwilli seam used to fire Tallawarra power station has the following typical analysis:

Proximate (air dried)	
Moisture	0.5%
Ash	28.6%
Volatile matter	23.2%
Fixed carbon	47.7%
Sulphur	0.4%
Calorific value	10,620 BTU/lb

The resultant ash principally comprises:

SiO_2	64.7%
Al_2O_3	24.5%
Fe_2O_3	7.4%
K_2O	0.85%
MgO	0.57%

5. DUST RESISTIVITY AND MEASUREMENT

A number of articles have been written about the measurement of dust resistivity and the effect of temperature and moisture [1,2,3,4].

The resistance of a specimen of dust of length L, area A and resistivity ρ is given by:

$$R = (V_1/I) = (\rho L)/A \text{ ohm} \quad (1)$$

hence $$\rho = (A/L)R \text{ ohm - cm.} \quad (2)$$

for the resistivity chamber of the analyser.

$$A/L = 300 \text{ cm}$$

$$\therefore \quad \rho = 300\ R \text{ ohm-cm} \quad (3)$$

From (1);

$$(V_1/L) = \rho(I/A)$$

$$\text{or } E = \rho J \quad (4)$$

where J = current density A/cm^2

The voltages V_1 are applied to the dust layer in three set values placing a maximum stress (eq. 4) of 1.5 kv/cm.

Dust does not follow Ohm's law exactly, i.e. the plot of E against J (eq. 4) is not quite a straight line[4]. Hence, to be clear, a resistivity measurement should always be specified at a certain electric field. For the author and his colleagues this stress is commonly 1.5 or 4 kv/cm.

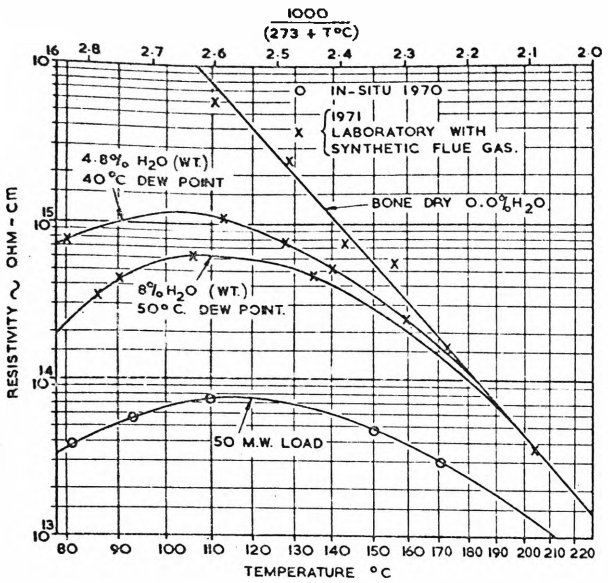

Fig. 2. Resistivity – Temperature Relation.

For Tallawarra fly-ash from Wongiwilli seam. Dry laboratory test is a straight line. Synthetic flue gas conditioning contains all compounds except SO_3. Electric stress E = 1.5 and 4 kV/cm. (See also Busby Darby [11] 1963).

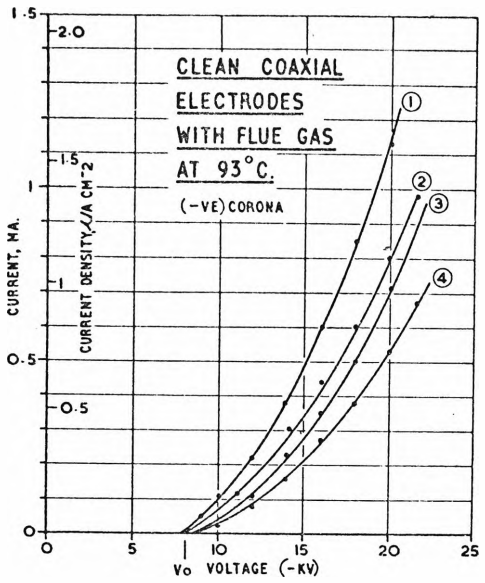

Fig. 3. Corona Characteristic - H_2O Content.
Illustrating the effect of water vapour in air and flue-gas mixture. Increasing H_2O decreases mobility and increases sparkover. Curves are parabolic. Clean electrodes, no back corona.

After the application of V_1, several minutes should be allowed before taking readings, so that dielectric absorption currents, commonly found in glassy structures like dry fly-ash [5], may settle down.

The resistivity – temperature curve for the Tallawarra fly-ash is shown in Fig. 2 for both a dry state and when conditioned with flue-gas. The dry ash resistivity as a function of the reciprocal of the absolute temperature is a straight line – a result found without exception for intrinsic semi-conductors.

As moisture is added to the flue-gas either artificially or as a product of combustion, the resistivity exhibits the well known[2] maximum around 110°C, falling away rapidly at lower temperatures.

Occasionally a carbon chain forms from electrode to electrode giving a spurious low resistivity of $10^4 < \rho < 10^7$ ohm - cm. It is characterised by a low breakdown strength and small temperature dependence.

6. CORONA PROPERTIES OF CLEAN GASES

The upper chamber is an effective device for measuring the fundamental electrical properties of a gas. If filtered flue-gas is admitted to the previously cleaned and polished upper chamber, the corona characteristic is shown in Fig. 3. The typically parabolic shape is found in point-to-plane, wire-to-plane and coaxial electrode geometries. Corona inception potential V_o is accurately determined by the cathode ray oscilloscope.

6.1 The Mobility of a Gas

The mobility K of a gas is the fundamental measure of its ability to conduct electricity[6 7 8]. It bears the same importance to the conductive properties of a gas as does resistivity to conduction in a solid.

From eq. (3) for a solid:

$$J = \frac{1}{\rho} E = \sigma_s E$$

In a gas,

$$J = (NeK)E = \sigma_g E$$

where σ ohm^{-1} cm^{-1} = conductivity of the gas or solid;

(Ne) c cm^{-3} = charge density in the gas.

The mobility of a gas is inversely proportional to its density; therefore at constant pressure, K is proportional to the absolute temperature. The common experience illustrated in Fig. 4, that corona currents

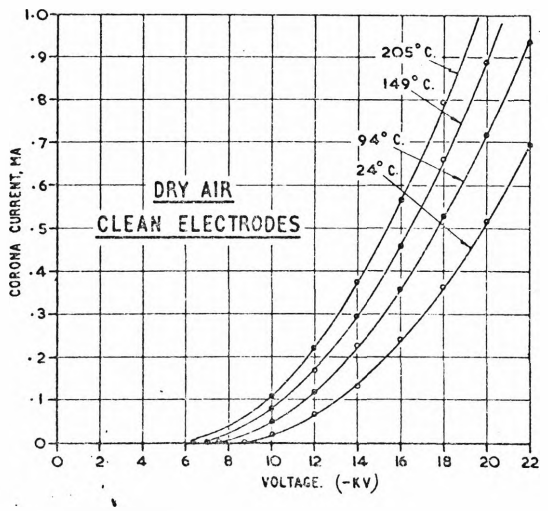

Fig. 4. Corona Characteristics – Temperature.
The effect on the corona characteristics of raising the temperature is to increase current and lower sparkover. Curves are parabolic. Clean electrodes, no back corona.

increase with temperature (while sparkover decreases), is the direct consequence of the increase in ionic mobility.

It is not widely appreciated that the addition of water vapour to dry air or dry flue-gas can decrease gas mobility (and increase its sparkover)[2] to a large extent. In Fig. 3, the corona current characteristic is seen to decrease progressively as moisture content increases from gas 1 down to gas 4.

The curves shown in Fig. 4 (or Fig. 3) may be readily used to determine the mobility K of the gaseous ions in each case. This is carried out in Appendix 1 where it is shown that mobility K is directly proportional to absolute temperature. At 150°C $K = 2.2\ cm^2\ sec^{-1}$, volt $^{-1}$ which is the order of value to be found in tables of physical constants.

7. DEVELOPMENT AND DIAGNOSIS OF BACK CORONA

In rather dramatic fashion, Fig. 5 illustrates the development of back corona in the Kevatron corona chamber as dusty gas is drawn in. Using the clean electrode flue gas as reference, deterioration of the corona characteristic is obvious after only 1½ minutes. Between inception and 14 kV, the corona is suppressed; Thereafter back corona develops, unmistakeably indicated by increasing currents and falling sparkover. After 4 minutes, vigorous back corona has developed — current has increased significantly while sparkover has fallen to 15 kV. The whole characteristic is flat and unstable. It is a sobering thought that so much damage could be done by a dust layer a small fraction of a millimetre in thickness.

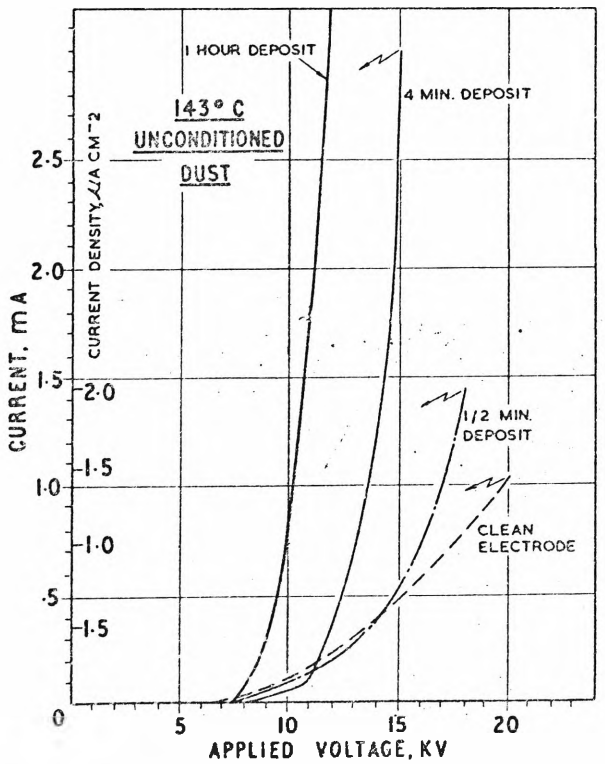

Fig. 5. Development of Back Corona.

Severe back corona develops as high resistivity fly-ash is deposited on electrodes. Current increases rapidly, sparkover is reduced, classical back corona symptons.

This phenomena has already been observed in general terms by Kirkwood[9] in New South Wales fly-ash precipitator installations and specifically at Tallawarra during pilot-plant testing by Watson and Blecher[10].

The gas space, instead of containing negative ions, now contains positive ions as well. Particle charging falls drastically, and with it, collection efficiency.

7.1 Sulphuric Acid Conditioning

Some 40-50 ppm of sulphuric acid was injected into the flue gas after the primary superheater at a temperature of 444°C in an effort to lower particle resistivity and improve main plant performance. The improvement in the corona current characteristic at 143°C is observed in Fig. 6 by the shaded band. Flashover voltage has been raised a little by comparison with unconditioned dust, currents are much reduced and the performance has moved back toward clean electrode conditions.

Tests carried out at Tallawarra, Wangi and Kincardine using SO_3 conditioning of the flue gases both on pilot plant and main plant are described by Busby and Darby[11]. The reduction of back corona (and improvement in collection efficiency) show close similarity to these Kevatron results.

In the Kevatron it was possible to reduce the temperature to 110°C when a remarkable change in the corona characteristic is disclosed in Fig. 7. There, the corona has moved back to the clean electrode condition with both back corona and corona suppression entirely absent.

The main plant, unfortunately, could not be operated at as low a temperature.

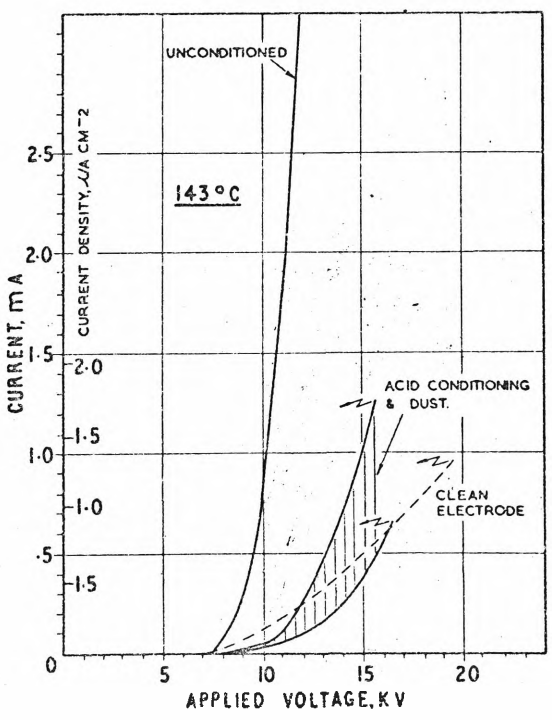

Fig. 6. Acid Conditioning Relieves Back Corona.

Sulphuric acid conditioning (40 ppm) in the flue gas relieves back corona. Shaded area represents range of performance depending upon depth of deposit.

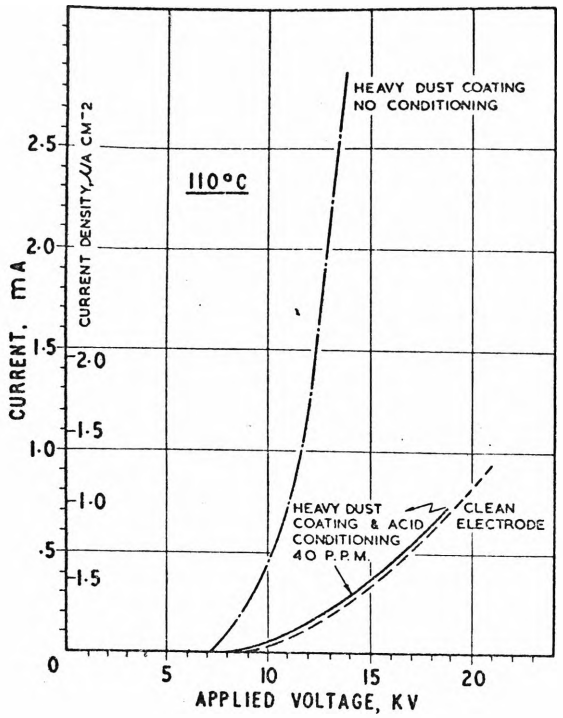

Fig. 7. Back Corona Minimised by Acid Conditioning and Low Temperature.

Surprising result. Combination of heavy H SO conditioning (50 ppm) and low temperature brings corona characteristics back to clean electrode condition.

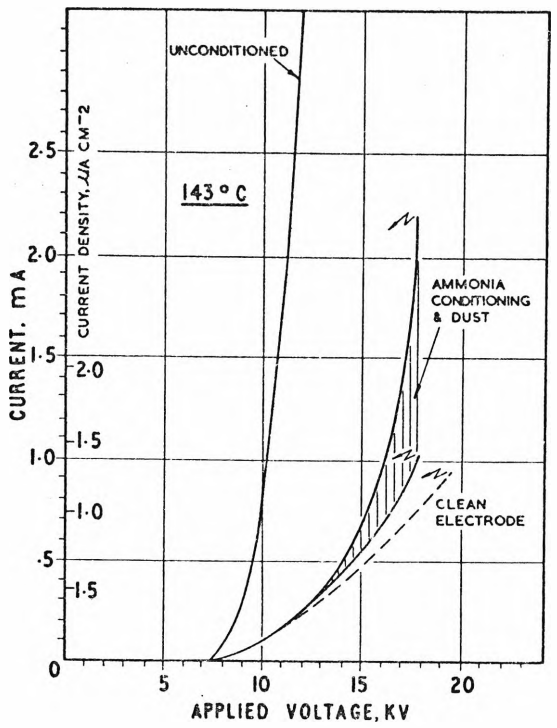

Fig. 8. Ammonia Conditioning Mitigates Back-Corona in Contaminated electrodes.

Ammonia conditioning (47 ppm) in the flue gas reduces back corona, bringing the characteristic back nearer the clean electrode condition.

Analysis of the unconditioned dust samples showed the sulphate content to be 0.06% to 0.1% whereas in the conditioned dust it was 0.2% to 0.3%.

7.2 Ammonia Conditioning

Anhydrous ammonia was injected into the gas stream before the precipitator inlet dampers at a temperature of 144°C and at the rate of 47 ppm with a 60 MW load. The corona characteristic in the corona chamber of the instrument at 143°C showed a marked improvement from that of Fig. 5., rising to that illustrated in Fig. 8 by the shaded zone. A worthwhile rise in voltage level to 17.5 kV has been achieved with a reduction in current. The characteristic bears remarkable correspondence to pilot plant testing with anhydrous ammonia at Tallawarra described by Watson and Blecher.[10]

8. MAIN PLANT PERFORMANCE

On the basis of the corona characteristics in the Kevatron, one could infer that the main plant should show some improvement in collection efficiency at 143°C with acid conditioning. With ammonia conditioning there should be a slight further improvement.

These inferences were indeed borne out by the plant precipitator tests illustrated in Fig. 9. Unconditioned tests show the behaviour of the precipitator to be little better than a settling chamber. The 1970 acid-conditioned tests showed a band of migration velocities between 3.5 and 4.5 cm/sec. With ammonia conditioning, migration velocities rose still further to 5-6 cm/sec.

Since the 1962 unconditioned tests, power station staff made strenuous efforts to optimise plant maintenance and operations schedules, without which conditioning agents would have been of less avail.

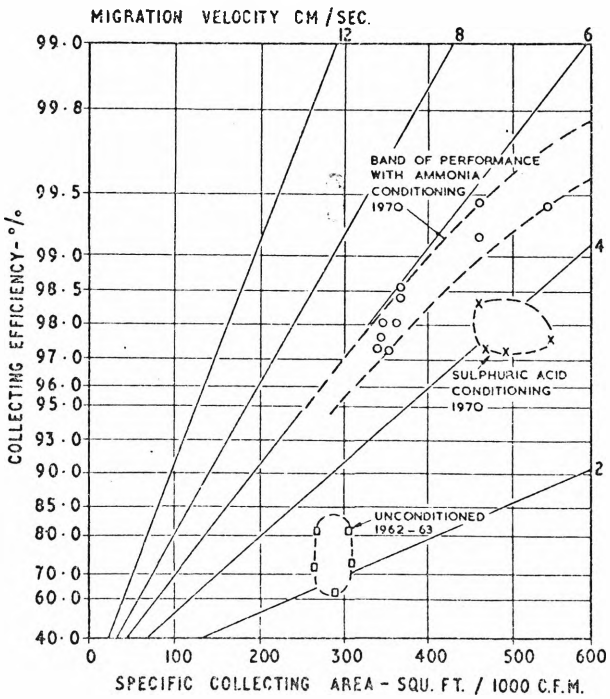

Fig. 9. Precipitator Performance with Conditioning Agents.

Main plant shows poor performance with unconditioned dust, some improvement with acid conditioning, marked improvement with ammonia conditioning,. Analyser results carried out simultaneously confirm this behaviour. After Kirkwood, Watson, Lamb, O'Brien, Blecher.

9. CONCLUSION

For ash from the Wongiwilli seam which is fired at Tallawarra power station, both sulphuric acid and ammonia were found to improve performance. Due to the greater efficacy of ammonia, this conditioning agent (in the form of a by-product from coke ovens), is being used as routine.

A precipitation analyser provided data closely resembling that from pilot plant and main plant testing carried out over a period of years. Use of the instrument confirmed previous diagnosis of high-resistivity ash, back corona, and the corrective value of conditioning agents. In close collaboration with colleagues in the Electricity Commission of New South Wales, such tests have been conducted at other power stations where similar corroborative evidence has been found.

With an increasing credibility being placed in the analyser, ways are being sought to test the effect of conditioning agents in the laboratory. Ash from the appropriate station is injected into the Kevatron corona chamber together with synthesised flue gas. Characteristics similar to the in-situ measurements are emerging. A systematic laboratory programme, moderated by results reported elsewhere, [1,2] for evaluation of conditioning agents is in progress.

10. ACKNOWLEDGEMENTS

The project is being supported financially by the Electricity Commission of New South Wales and with the active collaboration of their officers, in particular, Mr. B. Kirkwood, Mr. K. Watson and Mr. N. Lamb. Permission to use the data contained in Figure 9 is gratefully acknowledged.

APPENDIX 1

Determination of Gas Mobility

The actual shape of the current-voltage characteristics shown in Fig. 3 or Fig 4 is part of a parabola. Indeed, curves of such a shape are found also in point-to plane and wire-in-duct corona. The following analysis is inapplicable if back corona is present.

For the cylindrical system depicted in Fig 1,[6,7,8]

$$I = 4\pi\epsilon_o K L \left[\frac{(V-Vo)^2}{2b^2} + \frac{V_o (V-Vo)}{b^2 \log_e(b/a)}\right] \text{ amp}$$

where

- I = corona current, amp.
- ϵ_o = 8.854×10^{-12} = permittivity of free space.
- K = ion mobility, $m^2\ sec^{-1}\ v^{-1}$
- L = discharge electrode length, m.
- V = applied voltage, V.
- V_O = corona inception voltage, V.
- b = receiving electrode radius, m.
- a = emitting electrode radius, m.

The curves in Fig. 3 and 4 conform to this equation since L, a and b are fixed constants of the instrument. K may be determined as follows:—

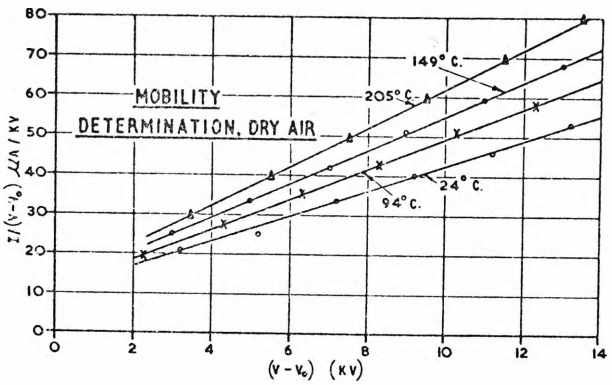

Fig. 10. Correlation Graph for Mobility Determination.

The data for dry air from Fig. 4 is reduced as shown. The slope of each line is multiplied by the Kevatron constant to obtain mobility K.

From one of the curves of Fig. 4 plot:
$(I/(V-V_O))$ against $(V-V_O)$ as is done in Fig. 10.

The resulting straight line is to be expected from the equation above for,

$$I/(V-V_o) = \frac{4\pi\epsilon_o K L}{2b^2}(V-V_o) + \frac{V_o}{b^2 \log_e(b/a)}.$$

If the slope of a straight line from Fig. 10 is, say P, then

$$K = P.\ \frac{2b^2}{4\pi\epsilon_o L}\ cm^2\ sec^{-1}\ V^{-1}$$

= 0.5P (for the dimensions shown in Fig. 1 and used in these tests). Regular instruments have K = 0.55P.

Finally, in Fig. 11, the mobility of the gas at several temperatures is indicated, from which linear dependence on absolute temperature is observed.

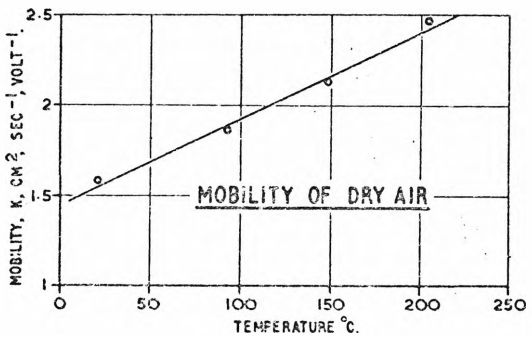

Fig. 11. Mobility of Dry Air as a Function of Temperature.

The slope of each line of Fig. 10 is multiplied by the Kevatron constant of 0.5 to obtain mobility K.

REFERENCES

1. Tassicker, O.J., Herceg, Z., McLean, K. — "A new method and apparatus to assist the prediction of Electrostatic Precipitator Performance". Elec. Eng. Trans. I.E. Aust., Sept. 1969, p. 277.
2. Sproull, W.T. and Nakada, Y. — "Operation of Cottrell Precipitators, Effects of Moisture and Temperature". Industrial and Eng. Chemistry, Vol. 43, No. 6, June, 1951, p. 1350-58.

3. Isahaya, F. and Echizenya, S. – "Some Technical problems for Electrostatic Precipitator and properties of industrial dust". Hitachi Review, Vol. 17, No. 2, 1968, p. 40-45 (English).
4. McLean, K. – "Doctoral Dissertation", The University of New South Wales.
5. Tassicker, O.J. – "Uber die Temperatur-und Frequenzabhängigkeit der Dielektrizitäts-konstante von Kraftwerksstaub". Staub – Reinhalt. Luft 31 (1971) Nr. 8 August.
6. White, H.J. – "Industrial Electrostatic Precipitation", Addison – Wesley, 1963, p. 88-107.
7. Henry, B.D. – "A study of the effect of process variables upon electrostatic precipitator performance". M.Sc. dissertation, The University of New South Wales (1967).
8. Koller, L.R. and Fremont, H.A. – "Negative wire corona at high temperature and pressure". Jour. App. Phys. (1950) *21* (8), p. 741-744.
9. Kirkwood, J.B. – "Electrostatic Precipitators for the collection of fly-ash from large pulverised fuel fired boilers". Proc. Clean Air Conf., Feb. 1962, University New South Wales, Paper 14.
10. Watson K.S., Blecher, K.J. – "Further Investigation of Electrostatic Precipitators for large pulverised fuel fired boilers". Proc. Clean Air Conf., Aug. 1965, University New South Wales. Paper 10.
11. Busby, H.G. and Darby, K. – "Efficiency of Electrostatic Precipitators as affected by the Properties and Combustion of Coal". Jnl. Inst. Fuel, May, 1963. p. 184.
12. Baxter, W. – "Recent electrostatic precipitator experience with ammonia conditioning of power boiler flue gas". A.P.C.A. Jnl., Dec. 1968, Vol. 18, No. 12.

A New Method and Apparatus to Assist the Prediction of Electrostatic Precipitator Performance

By O. J. Tassicker, M.E.E., F.I.E.Aust., Z. Herceg, M.I.E.Aust. and K. J. McLean, M.E., B.D., M.I.E.Aust.*

Summary.—A new method and apparatus is described which provides additional data to that previously obtained from a bench size apparatus, which can be used to assist in the prediction of electrostatic precipitator performance. In addition to measuring the in-situ resistivity of particles suspended in the flue gas, it also measures the corona current and sparkover voltage characteristics of the flue gas in the presence of a collecting electrode either clean, or contaminated with precipitated particles.

1.—INTRODUCTION

The accurate prediction of electrostatic precipitator performance has always been a formidable problem for manufacturers and users. Although the basic principle of operation is simple, there are many secondary effects taking place which make exact prediction of performance very difficult. Some of these are associated with the mechanical construction and gas flow characteristics of the unit, while others are associated with the electrical properties of the gas and deposited particles. Many of these secondary effects are not very well understood and no rigorous mathematical relationship between them and the collecting efficiency of electrostatic precipitators has so far been established.

The design of a new precipitator is still based substantially on the manufacturer's past experience and the designer's skilled judgment. Where the flue gas or suspended particles are expected to have unusual characteristics, additional information is frequently obtained from special large scale pilot-plant tests. On a much smaller scale, in-situ particle resistivity measurements have proved to be very useful. Various methods have been used to carry out these measurements. White and Anderson designed a point-to-plane method and this was used by Sproull and Nakada in their experiments (Ref. 1) and has been adopted by the Air Pollution Control Association of America as a standard (Ref. 2). Cohen and Dickinson (Ref. 3) and Eishold (Ref. 4) have described alternative methods of carrying out the tests. Isahaya and Echizenya (Ref. 5) have refined some of these techniques.

In view of the expense involved in conducting pilot-plant tests and the uncertainty of relating the results to full scale precipitators, some manufacturers are of the opinion that it is hard to justify the expense of this method. On the other hand, the much simpler in-situ resistivity measurements, although very useful, are insufficient as they do not provide any information about the electrical properties of the gas nor of the back corona behaviour of the precipitated particles.

The apparatus described in this paper provides a suitable balance between the more extensive tests involved with the pilot plant and the less extensive, but simpler, test in measuring the particle resistivity. The apparatus proposed in this paper is small and simple to operate. It not only provides an additional and, in some aspects, a superior method for measuring the particle resistivity under controlled environmental conditions but also provides means for determining the voltage current and sparkover voltage charactetistics of the gas in the presence of both clean and contaminated electrodes. The fixed cylindrical geometrical configuration of the precipitating chamber enables easy comparison of different tests and facilitates relating the results to full scale precipitator performance.

2.—DESCRIPTION

2.1 Description of Apparatus:

The apparatus, shown in schematic form in Fig. 1, comprises two main sections. The upper chamber is a small cylindrical type electrostatic precipitator 45 cm. long and 7.5 cm. dia. The discharge wire, situated centrally in the chamber, is fed through a high tension insulated electrode and held at the bottom end by an insulating bar. The wire is kept taut by means of a small spring. The gas inlet is near the top of the chamber and the outlet at the bottom. For some tests guard rings are also provided at each end of the chamber.

The lower section forms the resistivity measuring chamber and is arranged immediately below the precipitating chamber. The central electrode is accurately situated with respect to the outer electrode to give a uniform gap of 2 mm. and is electrically insulated from the rest of the apparatus. To improve the accuracy of the measurements and to eliminate fringe effects, the outer electrode is provided with guard rings.

Since all the measurements are very sensitive to temperature variations, provision is made for accurate temperature measurement and control. Heaters are wound around the precipitating chamber, outer resistivity measuring electrodes and inside the central electrode. The temperature at these points is measured by suitably placed thermocouples. To eliminate temperature gradients the whole of the apparatus is thermally insulated.

The apparatus is supported by a tubular frame to which is attached a suitable vibrator. The main metal components are made of stainless steel and all joints and connections are sealed against air leaks with O-rings. The resistivity measuring chamber can be easily removed from the precipitating chamber by quick release clamps.

Either a full wave or filtered variable D.C. voltage is supplied from a 30-kV power supply and is connected to the high tension terminal. The corona current may be measured by a milliammeter, which is connected to the collecting electrode, or the voltage current characteristic may be displayed on a C.R.O.

For measurement of the particle resistivity, provision is made to connect a variable voltage, low ripple D.C. power supply to the central electrode. The resultant current may be measured directly or a semi-automatic X-Y plotter may be used to record the bulk resistivity as a function of current density or electric field strength. The measuring electrode, terminals and leads are all carefully screened and connected to earth. In the case of high resistivity particles, the presence of spurious positive and negative pulses in the current necessitates the careful design of current measuring instrumentation.

All measuring, thermocouple and heating leads are connected to the apparatus and control console by quick release connectors.

2.2 Description of Operation:

A sample of the flue gas, with its dispersoid, is extracted from the main gas stream by well known sampling techniques (Ref. 6) and after

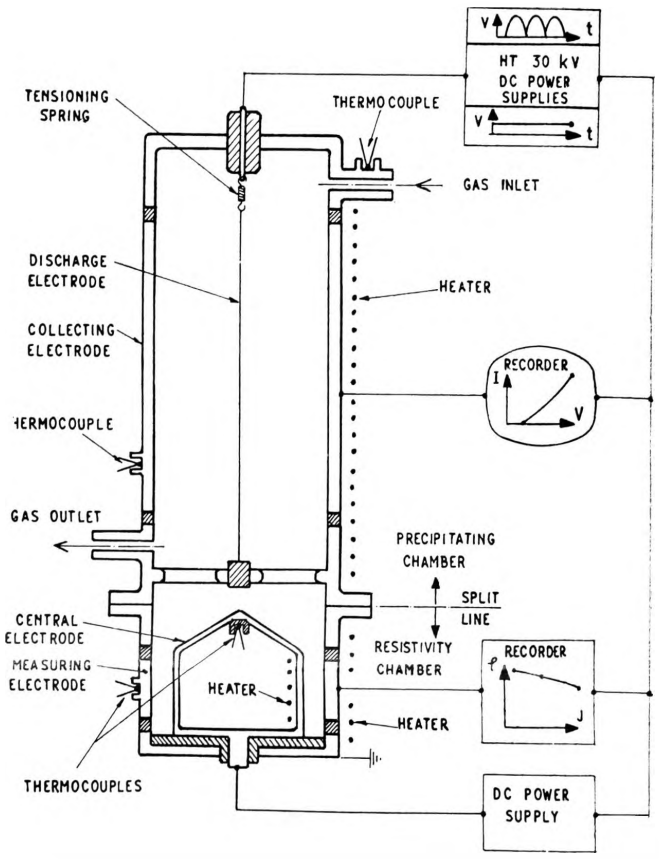

Fig. 1.—A Schematic Block Diagram of the Electrostatic Precipitator Analyser.

*Paper No. 2751, submitted by the authors on 11th November, 1968.

Mr. Tassicker is a Senior Lecturer and Messrs. Herceg and McLean are Lecturers in the Department of Electrical Engineering, Wollongong University College.

passing through a preheater enters the top of the precipitating chamber. A high negative D.C. voltage is applied to the discharge wire causing corona current to flow through the gas to the collecting electrode. The voltage current characteristic of the dust free gas with clean collecting plate may be obtained by initially placing a filter at the input to the chamber to collect any suspended particles before they enter the chamber. If this filter is removed, the gas with the suspended particles then enters the chamber and the particles are precipitated, with high efficiency, on to the collecting electrode. At various points during this stage, corona voltage current and sparkover measurements may be made.

When a sufficient volume of particles is collected, the high tension power supply is switched off and the whole apparatus rapped to dislodge the precipitated particles and deposit them in the resistivity measuring chamber. During this process the flue gas is kept flowing through the apparatus so that the particles are kept in contact with their environment. The apparatus is then vibrated by a known amount and mode to ensure a constant and even compaction in the annular space between the central and outer electrodes. The resistivity may be calculated from a series of voltage current measurements of the compacted particles or the semi-automatic X-Y recorder may be used to give the result directly. Accurate and consistent results are obtained only after observing two precautions:

(i) Measurements must be made over a wide range of electric fields and the resistivity specified for a particular electric field. Extensive tests have shown that the effective resistivity is not constant but that it decreases with increasing electric field strengths (Ref. 7).

(ii) Before beginning measurements it is also advisable to apply initially the maximum voltage before taking any other readings. In the presence of the higher field, the particles seem to realign themselves and improve their compaction.

For some types of measurements these refinements may not be necessary.

3.—RESULTS

The utility of the apparatus was demonstrated during a series of tests, conducted on a three-stage plate type pilot precipitator, which were designed to determine the precipitating properties of a particular fly ash. Gas was extracted from the power station main boiler flues and, after passing through a temperature controller, entered the pilot precipitator. A representative sample of this gas was extracted at a point just before the entrance to the pilot precipitator and then passed through the apparatus. Throughout the tests the chemical and moisture content of the gas remained substantially constant.

Fig. 2 shows the results of the resistivity measurements taken over a temperature range of 200°F. to 350°F. at an electric field strength of 1167 V/cm. The moisture-free curve was obtained by thoroughly drying out the particles in a laboratory oven and repeating the resistivity measurements under the same compaction conditions as before. The results were as expected, having the same shape as obtained by Sproull and Nakada (Ref. 1). At temperatures below 275°F, the in-situ resistivity is lower than the moisture-free resistivity but at higher temperatures the two curves coincide, resistivity decreasing with increasing temperature.

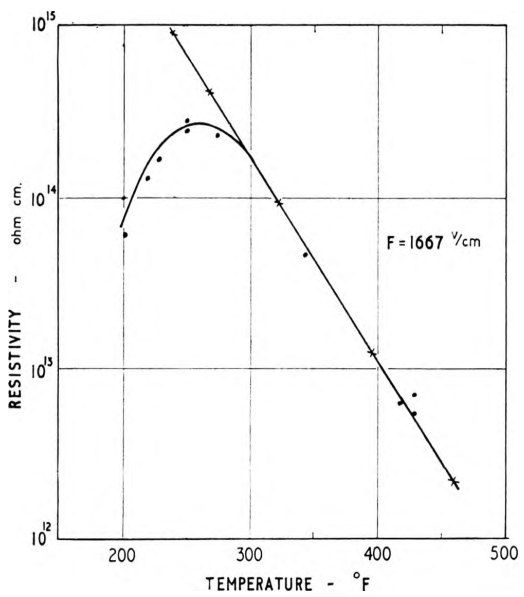

Fig. 2.—Resistivity versus Temperature Relationship of Fly-Ash for a Constant Electric Field Strength of 1,667 *V/cm.*

• In-situ tests in the moist power station flue gas.

x Laboratory tests of dried-out specimen.

Table I shows the variation of the apparatus precipitator and the pilot precipitator sparkover voltages with temperature. As can be seen, the characteristics correlate, differing in magnitude by a constant factor.

The same table shows that the corona current characteristic is similar in shape to that of the pilot precipitator. A voltage of 14 kV was selected as reference for the apparatus and the currents at the different temperatures were recorded. This is then compared with the pilot precipitator currents at the equivalent voltage of 32 kV. This is the average of the currents in the three stages of the pilot precipitator with extreme values ignored.

When the flue gas was conditioned with ammonia and sulphur trioxide, the sparkover voltage and corona currents of the apparatus varied in the same manner as in the pilot precipitator. With both types of conditioning, the resistivity of the particles was substantially lowered.

TABLE I

Correlation between Performance of Large Pilot Plant Precipitator and Bench Scale Precipitator. Sparkover Voltages and Corona Current Characteristics.

Gas Temp. °F.	Sparkover Voltage, kV			Corona Currents, mA		
	Apparatus	Pilot Plant	Pilot Plant / Apparatus	Apparatus at 14 kV	Pilot Plant at 32 kV	Pilot Plant / Apparatus
200	21.0	49.0	2.33	0.10	1.0	10.0
225	19.0	44.0	2.32	0.10	0.7	7.0
250	17.5	40.0	2.29	0.13	0.9	6.9
275	16.5	37.0	2.24	0.20	1.4	7.0
300	15.5	35.0	2.33	0.40	2.7	6.8
325	15.0	34.0	2.26	0.64	4.3	6.7
350	14.5	33.0	2.28	0.90	6.3	7.0

4.—CONCLUSIONS

The apparatus described in this paper is an important advance on other measuring equipment of the same size used to provide data which can be of assistance in the prediction of electrostatic precipitator performance. In addition to measuring the fly-ash resistivity, it also measures the electrical characteristics of the flue gas and precipitated layer.

The resistivity measurements have proved to be more reliable and consistent than those made by other methods. Since a high efficiency electrostatic precipitator is used, a true sample of the particle population is collected. The existence of the guard rings in the measuring chamber and provision of a variable D.C. voltage enables accurate determination of resistivity as a function of current density or electric field strength.

The tests recorded in this paper confirm that the voltage-current and sparkover voltage characteristics obtained from the apparatus have the same general characteristics of the much larger electrostatic precipitator with which it was compared. With these additional tests, more information is readily available to predict full-scale precipitator performance. In some circumstances this may avoid the necessity of pilot plant tests.

ACKNOWLEDGMENTS

The authors wish to thank the Electricity Commission of New South Wales for their financial assistance and for providing facilities for carrying out the in-situ tests.

They also acknowledge the useful discussions they have had with K. Watson and J. Blecher of the Commission, G. E. Tassicker of EEL International, and the assistance of R. Kirkpatrick and H. Lynas in constructing and testing the apparatus.

References

1. Sproull, W. T. and Nakada, Y.—Operation of Cottrell Precipitators, Effects of Moisture and Temperature. *Industrial and Engg. Chemistry*, Vol. 43, No. 6, June, 1951, pp. 1350-58.
2. Walker, A. B.—Information Required for Selection of Electrostatic and Combination Fly Ash Collectors; Methods of Analysis for Chemical Physical and Electrical Properties of Fly Ash? Informative Report No. 2. *Jour. Air Pollution Control Assoc.*, Vol. 15, No. 6, June, 1965, pp. 257-60.
3. Cohen, L. and Dickinson, R. W.—The Measurement of the Resistivity of Power Station Flue Dust. *Jour. Sci. Instruments*, Vol. 40, Feb., 1963, pp. 72-75.
4. Eishold, H. G.—Eine Messvorrichtung zur Bestimmung des spezifischen elektrischen Staubwiderstandes. *Staub-Reinhaltung der Luft*, Vol. 26, No. 1, Jan., 1966, pp. 11-14.
5. Isahaya, F. and Echizenya, S.—Some Technical Problems for Electrostatic Precipitator and Properties of Industrial Dust. *Hitachi Review*, Vol. 17, No. 2, 1968, pp. 40-45.
6. Stairmand, C. J.—The Sampling of Dust-Laden Gases. *Trans. I. Chem. E.*, Vol. 29, No. 1, 1951, pp. 15-39.
7. Lakey, J. R. A. and Bostock, W.—Researches into Factors Affecting Electro-Precipitation, *Trans. I. Chem. E.*, Vol. 33, No. 4, 1955, pp. 252-63.

Reprinted from *Electronics Letters*, Vol. 5, No. 13, 26th June 1969

MEASUREMENT OF CORONA CURRENT DENSITY AT AN ELECTRODE BOUNDARY

A technique and instrument [known as the microarea boundary electrode Langmuirian (MABEL)] have been developed for fine-scale measurement of steady-state corona current to an electrode boundary. The results of measurements of negative corona in air at n.t.p. are described. Sharp cutoff at the edges of such corona have been observed. Dead bands with zero current have been repeatedly measured between interacting space clouds.

The principle of determining the current density over a boundary involves an earthed plane electrode in which is mounted a small circular insulated electrode, machined and polished flat. In this way, provided that the electrode is at earth potential, its presence does not disturb the surrounding field, be it electrostatic, corona or electrolytic. This small electrode, being shielded and protected from vibration, is connected in series with an earthed picoammeter. The current density is simply given by $J = I/A$, where both the symbols and system are illustrated in Fig. 1. The high-voltage electrode

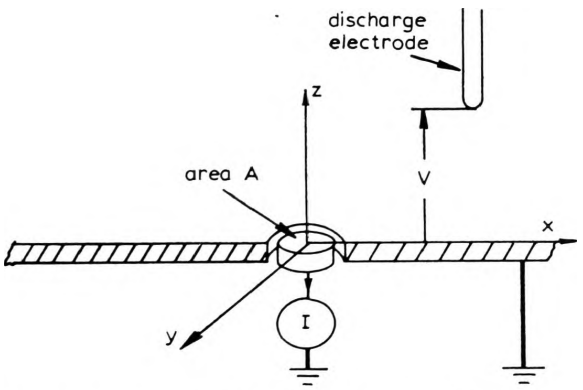

Fig. 1 *Microarea boundary electrode Langmuirian*

may be traversed over the plane surface, so that the whole receiving electrode area (x, y) may be mapped with the system energised. The electrode height z may also be varied with the system energised.

The technique appears to be useful for fundamental studies of corona discharges, such as an examination of the discontinuities common to negative corona. Further, the operating

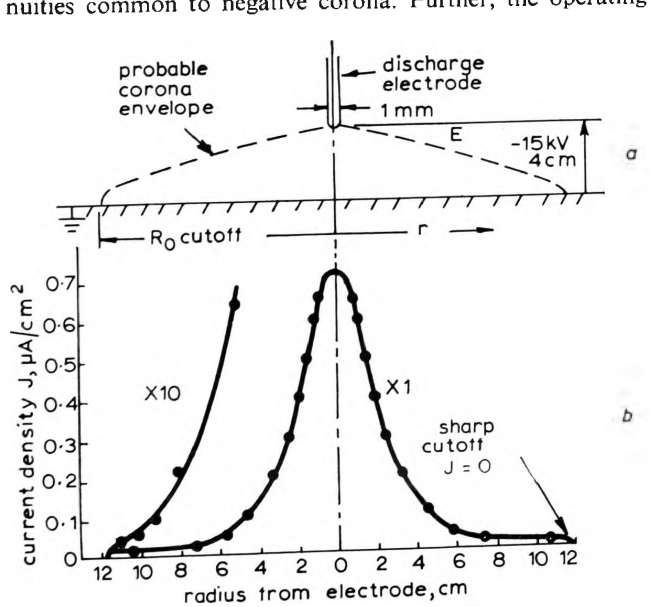

Fig. 2 *Corona-current distribution along the anode*
Negative corona from a stainless-steel discharge electrode to plane

efficiency of electrostatic precipitation equipment is dependent on the effective charging of the particles to be precipitated, in order that they may be collected at an electrode passing through the precipitator with the flow of gas. The spatial distribution of charge, and hence of corona current, is therefore of considerable interest in relation to the achievement of greater efficiency in commercial electrostatic precipitators. An additional value of the present device is that it may be used for an electrode coated with a layer of particles. Other devices are not suitable in such an environment.[1]

The inserted probe electrode is similar to that described by Collins and Meek, and Stassinopoulos,[2,3] who have reported measurements of electric field strength E in a rod-gap/plane electrode system. For this, it was necessary to integrate displacement current only, excluding conduction current from the measurements. In the present results, the conduction current was of prime interest as the means of obtaining J, the current density over the plane electrode. The technique is capable of high positional accuracy and repeatability. The feature displayed surprisingly fine structure in negative corona.

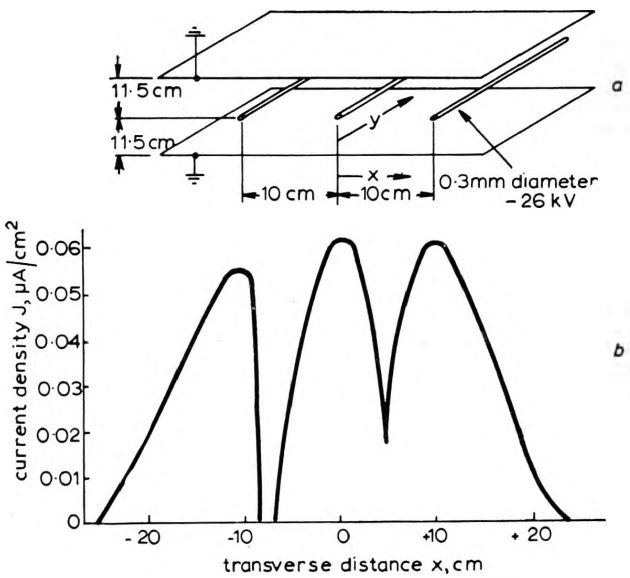

Fig. 3 *Negative corona from three parallel stainless-steel wires to twin planes*

The results for negative corona in a 1 mm-diameter hemispherically capped cylinder/plane electrode system are shown in Fig. 2*b*. The maximum current density along the axis is seen to rise to $0{\cdot}7\,\mu A/cm^2$. At $11\frac{1}{2}$ cm radius, J fell sharply to zero. The mechanical and electrical discrimination was so great that the edge of the corona field was readily studied at an enlarged scale. The probable envelope of ions drifting along a boundary line of force E is shown to scale in Fig. 2*a*.

The corona-current distribution for the multiple wire/plane electrode geometry commonly used in electrostatic precipitators has been studied. Stainless-steel discharge electrodes of 0·3 mm diameter spaced 10 cm apart were situated midway between plane electrodes, as illustrated in Fig. 3*a*. Quality discharge wires, well polished and cleaned before electrical energisation, were used. Profiles of J for a cross-sectional traverse in the x direction are shown in Fig. 3*b*. The discontinuities known to occur with negative corona were clearly measurable. The unexpected zero band ($<0{\cdot}005\,\mu A/cm^2$) at about -8 cm should be noticed, for it is a typical observed irregularity. A traverse made in the x direction, but at other values of y, disclosed irregularities over the entire (x, y) plane. A traverse made in the y direction and underneath a discharge electrode shows that the 'tufts' observed visually as points of light on the wires extend right to the anode. These results will be reported in detail.

By using other geometries, such as multiple point/plane and point-in-Rogowski-profile/plane, the complex phenomena have been illuminated to some extent. Explanation for the sharp cutoff at the boundaries, and for the interesting interaction between adjacent space clouds, will be reported.

The technique is suitable for measurements in gases or electrolytes, and the results are applicable to such technologies as electrofilters and electrophoretic deposition.